Dissertation
submitted to the
Combined Faculties of the Natural Sciences and Mathematics
of the Ruperto-Carola-University of Heidelberg, Germany
for the degree of
Doctor of Natural Sciences

Put forward by

Dipl. Phys. Christoph Federrath
born in: Sonneberg (Germany)

Oral examination: June 7th, 2010

The formation of molecular clouds and stars by turbulent compression and collapse

Referees: Prof. Dr. Ralf S. Klessen

Prof. Dr. Mordecai-Mark Mac Low

Zusammenfassung

Das Ziel dieser Arbeit ist, die Rolle der interstellaren Turbulenz für die Sternentstehung besser zu verstehen. Dazu wurde der Mechanismus der turbulenten Energieerzeugung, das Treiben der Turbulenz, mit Hilfe hydrodynamischer Simulationen untersucht. In einem systematischen Vergleich wurden die beiden Extremfälle turbulenten Treibens betrachtet: solenoidales (divergenzfreies) Treiben und komprimierendes (rotationsfreies) Treiben. Ich zeige, dass sowohl die Dichte-, als auch die Geschwindigkeitsstatistiken für diese beiden Fälle jeweils signifikant unterschiedlich sind. Die fraktale Struktur und die Wahrscheinlichkeitsverteilung der Dichte des turbulenten Gases werden detailliert untersucht. Das Ergebnis ist eine nahezu Gaußsche Wahrscheinlichkeitsverteilung mit einer Standardabweichung, die für komprimierendes Treiben drei Mal größer ist als für solenoidales Treiben. Die Bedeutung dieses Ergebnisses für analytische Sternentstehungsmodelle wird diskutiert. Ein detaillierter Vergleich mit Beobachtungsdaten zeigt, dass verschiedene Regionen in Molekülwolken Anzeichen für unterschiedliches Treiben der Turbulenz aufweisen, wobei komprimierendes Treiben bevorzugt in expandierenden Schalen dichten Gases beobachtet wird. Um den Gravitationskollaps dichten Gases in numerischen Simulationen verfolgen zu können, wurden akkretierende 'Sink Teilchen' in den adaptiven Gittercode FLASH implementiert. Mit Hilfe der Sink Teilchen zeige ich, dass die Sternentstehungsrate durch komprimierendes Treiben um mehr als eine Größenordnung größer ist als durch solenoidales Treiben. Dies ist konsistent mit analytischen Modellen.

Abstract

The goal of this work is to improve our understanding of the role of interstellar turbulence in star formation. In particular, the mechanism of turbulence energy injection, the turbulence forcing, is investigated with hydrodynamical simulations. In a systematic comparison, I study the two limiting cases of turbulence forcing: solenoidal (divergence-free) forcing and compressive (curl-free) forcing. I show that these two cases yield significantly different gas density and velocity statistics. The fractal structure of the gas and the turbulent density probability distribution function (PDF) are explored in detail. I find that compressive forcing yields a three times higher standard deviation of the roughly Gaussian density PDF. I discuss the impact of this result on analytic models of star formation. A detailed comparison with observational data reveals that different observed regions show evidence of different mixtures of compressive and solenoidal forcing, with more compressive forcing occurring primarily in swept-up shells. To follow the gravitational collapse of dense gas in numerical simulations, I implemented accreting sink particles in the adaptive mesh refinement code FLASH. Using sink particles, I show that compressive forcing yields star formation rates more than one order of magnitude higher than solenoidal forcing, consistent with analytic models.

List of publications (*=results of which are presented in part or in full in this thesis)

1. **Federrath, C.*, Klessen, R. S., Schmidt, W., (2008), 'The Density Probability Distribution in Compressible Isothermal Turbulence: Solenoidal versus Compressive Forcing', *The Astrophysical Journal*, **688**, L79 (arXiv:0808.0605)
2. **Federrath, C.*, Klessen, R. S., Schmidt, W., (2009), 'The Fractal Density Structure in Supersonic Isothermal Turbulence: Solenoidal Versus Compressive Energy Injection', *The Astrophysical Journal*, **692**, 364 (arXiv:0710.1359)
3. **Federrath, C.*, Roman-Duval, J., Klessen, R. S., Schmidt, W., Mac Low, M.-M., (2010), 'Comparing the statistics of interstellar turbulence in simulations and observations: Solenoidal versus compressive turbulence forcing', *Astronomy & Astrophysics*, **512**, A81 (arXiv:0905.1060)
4. **Federrath, C.*, Banerjee, R., Clark, P. C., Klessen, R. S., (2010), 'Modeling Accretion in Turbulent Gas Clouds: Implementation and Comparison of Sink Particles in AMR and SPH', *The Astrophysical Journal*, **713**, 269 (arXiv:1001.4456)
5. *Glover, S. C. O., *Federrath, C.*, Mac Low, M.-M., Klessen, R. S., (2010), 'Modelling CO formation in the turbulent interstellar medium', *Monthly Notices of the Royal Astronomical Society*, in press (arXiv:0907.4081)
6. *Schneider, N., Bontemps, S., Simon, R., Ossenkopf, V., *Federrath, C.*, Klessen, R. S., Motte, F., Brunt, C. M., (2010), 'The link between molecular cloud structure and turbulence', *Astronomy & Astrophysics*, submitted (arXiv:1001.2453)
7. Brunt, C. M., *Federrath, C.*, Price, D. J., (2010), 'A method for reconstructing the variance of a 3D physical field from 2D observations: application to turbulence in the interstellar medium', *Monthly Notices of the Royal Astronomical Society*, **403**, 1507 (arXiv:1001.1046)
8. Brunt, C. M., *Federrath, C.*, Price, D. J., (2010), 'A method for reconstructing the PDF of a 3D turbulent density field from 2D observations', *Monthly Notices of the Royal Astronomical Society*, in press (arXiv:1003.4151)
9. *Federrath, C.*, Glover, S. C. O., Klessen, R. S., Schmidt, W., (2008), 'Turbulent mixing in the interstellar medium: an application for Lagrangian tracer particles', *Physica Scripta T*, **132**, 014025 (arXiv:0805.0196)
10. Kitsionas, S., *Federrath, C.*, Klessen, R. S., Schmidt, W., Price, D. J., Dursi, L. J., Gritschneder, M., Walch, S., Piontek, R., Kim, J., Jappsen, A.-K., Ciecielag, P., Mac Low, M.-M., (2009), 'Algorithmic comparisons of decaying, isothermal, supersonic turbulence', *Astronomy & Astrophysics*, **508**, 541 (arXiv:0810.4599)
11. Price, D. J. & *Federrath, C.* (2010), 'A comparison between grid and particle methods on the statistics of driven, supersonic, isothermal turbulence', *Monthly Notices of the Royal Astronomical Society*, accepted (arXiv:1004.1446)
12. Schmidt, W., *Federrath, C.*, Klessen, R. S., (2008), 'Is the Scaling of Supersonic Turbulence Universal?', *Physical Review Letters*, **101**, 194505 (arXiv:0810.1397)
13. Schmidt, W., *Federrath, C.*, Hupp, M., Kern, S., Niemeyer, J. C., (2009), 'Numerical simulations of compressively driven interstellar turbulence. I. Isothermal gas', *Astronomy & Astrophysics*, **494**, 127 (arXiv:0809.1321)
14. Schmidt, W.; Kern, S. A. W.; *Federrath, C.*; Klessen, R. S., (2010), 'Numerical and semi-analytic core mass distributions in supersonic isothermal turbulence', *Astronomy & Astrophysics*, submitted (arXiv:1002.2359)
15. Schneider, N., Csengeri, T., Bontemps, S., Motte, F., Simon, R., Hennebelle, P., *Federrath, C.*, Klessen, R. S., (2010), 'Dynamic star formation in the massive DR21 filament', *Astronomy & Astrophysics*, submitted (arXiv:1003.4198)

Contents

Chapter 1

Introduction

This thesis is concerned with the statistics of turbulence in molecular clouds and the role of turbulence in star formation. The results presented here are based mainly on numerical experiments with turbulent gas flows, the basic principles of which are described in section 1.4 below. I also discuss analytic and semi-analytic models of star formation, for which turbulence is a key-ingredient in section 1.2. Before turning to the numerical and analytic models, however, I start by given some of the observational evidence, from which I conclude that turbulence is essential for star formation. Understanding the nature and origin of supersonic turbulence is a key – perhaps *the* key – to understanding star formation (Mac Low & Klessen, 2004; Elmegreen & Scalo, 2004; Scalo & Elmegreen, 2004; McKee & Ostriker, 2007).

1.1 General properties of turbulent molecular clouds

The gas from which stars form is turbulent. This is known from observations of molecular line emission in molecular clouds. Molecular clouds provide the 'raw' material from which stars form. They consist mainly of molecular hydrogen, H_2. The second most abundant molecule is carbon monoxide, CO. CO is typically used to measure the turbulent velocities in molecular clouds, because at the low temperatures of about 10–50 K, H_2 is unobservable due to its missing permanent dipole moment. An observational example is given in Figure 1.1, the Polaris Flare, observed in the rotational molecular transitions, $J = 1 \rightarrow 0$ and $J = 2 \rightarrow 1$ of the two different isotopologues, ^{12}CO and ^{13}CO. Using different transitions and different molecular tracers allows us to probe very different density environments in molecular clouds. The mean number densities of molecular species range from $\langle n_{\rm tot} \rangle \approx 100\,{\rm cm}^{-3}$ for Giant Molecular Clouds (GMCs) up to $10^4\,{\rm cm}^{-3}$ for dense cores and Bok globules (see, e.g., Stahler & Palla, 2004, for fundamental properties of molecular clouds). The total masses of these highly filamentary objects range from $M = 10^5\,{\rm M}_\odot$ down to $10\,{\rm M}_\odot$, and their linear sizes are roughly $L = 50\,{\rm pc}$ down to about 0.1 pc for GMCs and Bok globules, respectively. Figure 1.1 shows that the Polaris Flare, which has a linear size of about 50 pc on the largest scale, contains substructure on virtually all scales observed with higher density tracers.

This hierarchical structure seen in the Polaris Flare is shared among all molecular clouds. The complex interplay of turbulence and gravity can produce such hierarchical, fractal patterns (e.g., Elmegreen & Falgarone, 1996), which is discussed in more detail in Chapter 3. Indeed, measurements of the Doppler shift of molecular emission lines show that the internal motions of the clouds are random, with typical root-mean-squared (RMS) velocity fluctuations ranging from about $\sigma_v(L) \approx 20\,{\rm km\,s}^{-1}$ down to about $1\,{\rm km\,s}^{-1}$ over the entire projected cloud (Zuckerman & Evans, 1974). Given the typical temperatures of the clouds, which imply sound speeds of the order of $c_{\rm s} \approx 0.2$–$0.3\,{\rm km\,s}^{-1}$, leads to typical large-scale RMS Mach numbers, $\mathcal{M} = \sigma_V / c_{\rm s} \approx 3$–

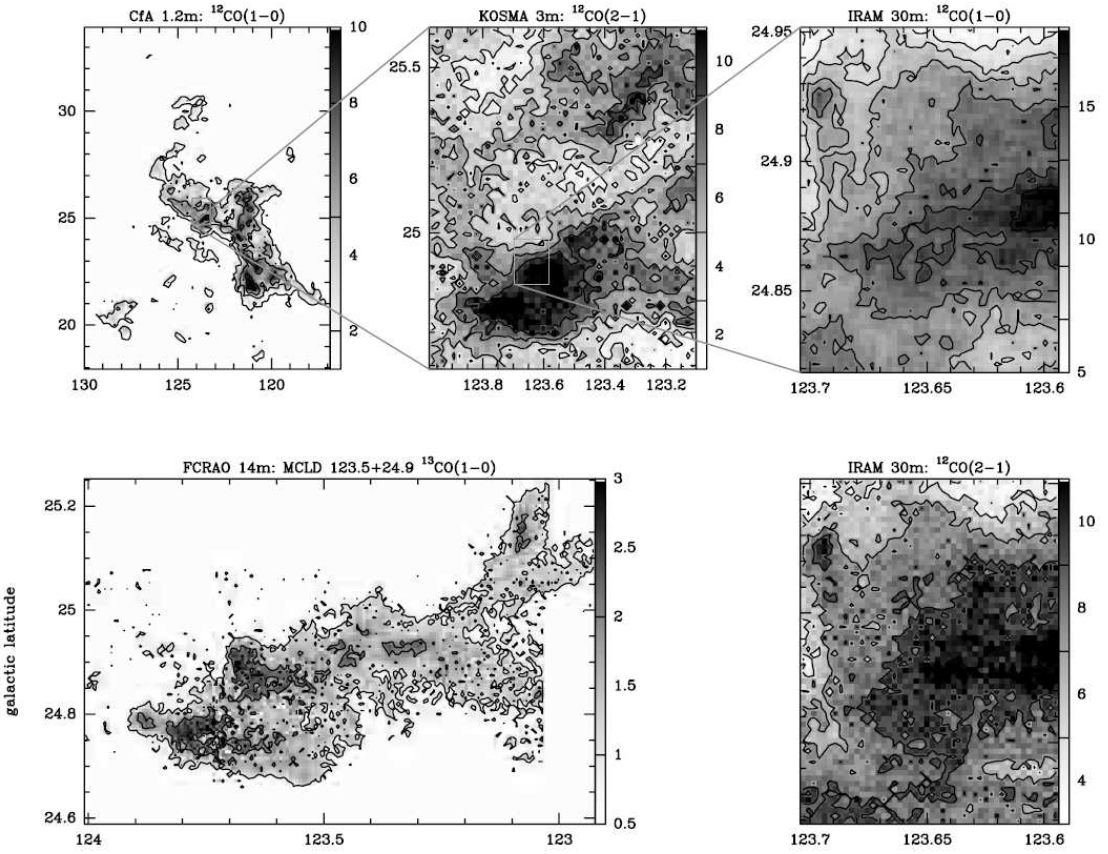

Figure 1.1: Velocity integrated spectral line maps of the rotational transition ^{12}CO $J = 1 \rightarrow 0$, ^{12}CO $J = 2 \rightarrow 1$ and ^{13}CO $J = 1 \rightarrow 0$, observed toward the Polaris Flare, and one of its cores, MCLD 123.5+24.9. The transition and the telescope are indicated at the top of each panel. The line intensity is given in main beam brightness temperature. Iso-intensity levels are shown from 2 to 8 in steps of 2 (CfA map), 1 to 11 by 2 (KOSMA), 1 to 4 by 1 (FCRAO), 5 to 17 by 2 (IRAM, ^{12}CO $J = 1 \rightarrow 0$), 3 to 11 by 2 (IRAM, ^{12}CO $J = 2 \rightarrow 1$), in units of $\mathrm{K\,km\,s^{-1}}$. Image credit: Bensch et al. (2001), Copyright Astronomy & Astrophysics 2001.

100. This means that molecular clouds are supersonically turbulent, i.e., $\mathcal{M} > 1$. When averaged over smaller and smaller scales, however, the velocity dispersion drops, and exhibits a power-law behavior as a function of scale, ℓ,

$$\sigma_v(\ell) = \sigma_v(L) \left(\frac{\ell}{L}\right)^p \tag{1.1}$$

$$\approx 1\,\mathrm{km\,s^{-1}} \left(\frac{\ell}{1\,\mathrm{pc}}\right)^p . \tag{1.2}$$

The approximate equality in the second line of this equation comes from the combined evidence obtained in various measurements of the normalization and the power-law index, $p \approx 0.4$–0.5 over the last years (e.g., Solomon et al., 1987; Heyer & Brunt, 2004; Heyer et al., 2009), since the early observations by Larson (1981). This power-law form is indeed similar to the power law obtained in the famous Kolmogorov model of turbulence, however, there $p = 1/3$ (Kolmogorov, 1941; Frisch, 1995). Although often referred to in the astrophysical context of molecular cloud

turbulence, the phenomenological model of turbulence provided by Kolmogorov (1941), strictly speaking, only applies to incompressible gas. Early attemps to understand interstellar turbulence (von Weizsäcker, 1943, 1951; Chandrasekhar, 1949, 1951a,b) were based on insigths drawn from incompressible turbulence. However, in the case of molecular clouds, we are dealing with highly supersonic, compressible gas flows. Such flows develop shocks, which may be better described in the framework of shock-dominated turbulence presented by Burgers (1948), for which $p = 0.5$. Independent numerical simulations of supersonic turbulence over the last 30 years basically agree with the observed value of $p \approx 0.4$–0.5, i.e., a slightly steeper power law than the Kolmogorov index, which is discussed in more detail in Chapter 4.

The power law of equation (1.1) means that the velocity fluctuations will decrease on smaller and smaller scales, and will eventually become subsonic, i.e., the local Mach number will drop below unity. The scale at which this transition occurs is the sonic scale, λ_s, above which turbulence is supersonic, and below which turbulence is subsonic. This scale is of paramount importance, because it provides a natural definition of the size of dense cores from which stars form. Figure 1.2 provides a striking example of the transition from the fractal, filamentary, hierarchical structure of molecular clouds on scales larger than λ_s to the more regular, sometimes even elliptic or round distribution of emission seen in the most highly resolved images in Figure 1.2 (c–h) on scales of about 0.1 pc. It is these dense cores that are the progenitors of stars. In this sense, the sonic scale sets the characteristic scale of star formation, below which the turbulent support is at most as big as the thermal support in an otherwise supersonic, turbulent medium, in which the whole cloud is stabilized against global gravitational collapse. Turbulence thus plays a dual role: on the one hand, it provides support against the global collapse of molecular clouds, and the other, it compresses gas locally in shocks, some of which are dense enough to go into free fall collapse on roughly the sonic scale (Mac Low & Klessen, 2004; McKee & Ostriker, 2007). The role of the sonic scale is discussed in more detail in section 4.9 of Chapter 4.

1.2 Turbulent star formation theories

In this section, I motivate the fundamental role of turbulence statistics for analytic theories of star formation. In particular, I show that the most recent models of star formation that are used to explain the core mass function and the stellar initial mass function, the star formation efficiency and the star formation rate all rely on the turbulent density probability distribution function (PDF). It is the dependence of the density PDF on the forcing of the turbulence that is investigated in detail in this thesis, in particular in Chapters 2 and 4.

I begin by making a useful transformation of the gas density variable, ρ. The density is divided by the mean density, $\langle\rho\rangle$, and we take the natural logarithm, which gives the definition of the new independent variable,

$$s = \ln \frac{\rho}{\langle\rho\rangle} \, . \tag{1.3}$$

It is useful to make this conversion, because in turbulent, isothermal, supersonic gas flows, it is the random variable s that seems to follow a Gaussian distribution,

$$p(s) = \frac{1}{\sqrt{2\pi\sigma_s^2}} \exp\left[-\frac{(s - \langle s\rangle)^2}{2\sigma_s^2}\right] , \tag{1.4}$$

i.e., the density, ρ follows a log-normal distribution (e.g., Vázquez-Semadeni, 1994; Passot & Vázquez-Semadeni, 1998). The assumption of this log-normal density PDF is explored in more detail in Chapters 2 and 4. It turns out that equation (1.4) is usually a good approximation, though a detailed analysis shows that non-Gaussian, higher-order moments are present in real density distributions obtained both from observations and numerical simulations, as discussed in

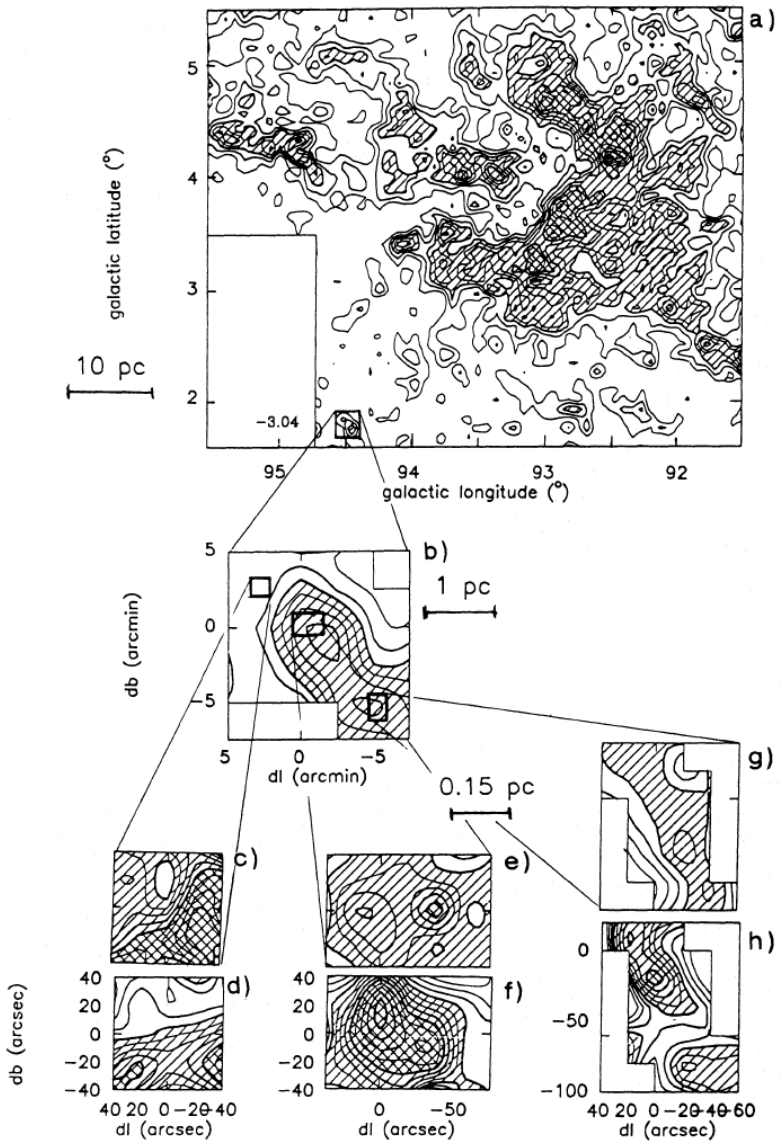

Figure 1.2: Maps of the Cyg OB7 field. *a)* Large scale map of the ^{13}CO $J = 1 \rightarrow 0$ emission integrated over $\Delta v = 1\,\mathrm{km\,s^{-1}}$ and centered at $v_{\mathrm{lsr}} = -3.04\,\mathrm{km\,s^{-1}}$ (Bordeaux telescope, HPBW 4.4', sampling 5'). First level and contour spacing 0.25 K. *b)* Map of the integrated intensity of the same transition over the small field shown in the offset with a sampling of 2.5' and the same telescope. The first level and contour spacing are $0.3\,\mathrm{K\,km\,s^{-1}}$. The three fields observed at higher angular resolution were mapped with the IRAM 30 m telescope. *c)* ^{12}CO $J = 1 \rightarrow 0$ first level and step $1\,\mathrm{K\,km\,s^{-1}}$. *d)* ^{13}CO $J = 1 \rightarrow 0$ first level and step $0.3\,\mathrm{K\,km\,s^{-1}}$. *e)* ^{13}CO $J = 1 \rightarrow 0$ first level and step $1\,\mathrm{K\,km\,s^{-1}}$. *f)* C^{18}O $J = 1 \rightarrow 0$ first level and step $0.1\,\mathrm{K\,km\,s^{-1}}$. *g)* ^{13}CO $J = 1 \rightarrow 0$ first level and step $1\,\mathrm{K\,km\,s^{-1}}$. *h)* C^{18}O $J = 1 \rightarrow 0$ first level and step $0.1\,\mathrm{K\,km\,s^{-1}}$. The linear sizes indicated are given for a distance of 750 pc. Image credit: Falgarone et al. (1992), Copyright Astronomy & Astrophysics 1992.

Chapter 4.

The variance of the logarithmic density fluctuations, σ_s^2 in equation (1.4) is a key quantity for the star formation models discussed in the following sections. I will show in Chapters 2 and 4 that the variance is given by

$$\sigma_s^2 = \ln\left(1 + b^2\mathcal{M}^2\right) . \tag{1.5}$$

It has two important dependencies. First, σ_s^2 increases with the root-mean-squared (RMS) Mach number $\mathcal{M}$ in a non-linear way. This dependence was first investigated in detail by Padoan et al. (1997) and Passot & Vázquez-Semadeni (1998). The second dependence is on the forcing parameter, which I call b in the following. This parameter has not been investigated systematically before. For instance, Padoan et al. (1997) found $b \approx 0.5$ from three-dimensional magnetohydrodynamical turbulence simulations. On the other hand, Passot & Vázquez-Semadeni (1998) found $b \approx 1$ in one-dimensional simulations. Up to now, this discrepancy has not been addressed and remained unresolved. With the systematic numerical comparisons presented in Chapters 2–4, I show that the parameter b is function of the turbulence forcing, i.e., a function of the mechanism by which turbulence is excited. In Chapters 2 and 4, I show that the disagreement of the results by Padoan et al. (1997) and Passot & Vázquez-Semadeni (1998) can be reconciled, if a mixture of compressible and rotational modes is considered. In essence, the ratio of compressible to rotational modes of the turbulence depends strongly on the nature of the turbulence forcing, which makes the parameter b in equation (1.5) dependent on the forcing. The main result is that for the two limiting cases of turbulence forcing, i.e., first, fully solenoidal (divergence-free) forcing, and second, fully compressive (curl-free) forcing, I find $b \approx 1/3$, and $b \approx 1$, respectively. A graphical representation of these two limiting cases of turbulence forcing is given in section 1.4 below, however, for the time being I just mention that b can vary between 1/3 and 1 for the same RMS Mach number. I will show the consequences of this result for analytic solutions of star formation models that are based on the turbulent density PDF, equation (1.4), and on the density variance–Mach number relation, equation (1.5) in the following three subsections.

1.2.1 The core and stellar initial mass function

One of the most important observational piece of evidence in star formation is the initial core mass function (CMF) and the stellar initial mass function (IMF). The CMF and the IMF are the number, $\mathcal{N}(M)$, of dense cores and stars, respectively, as a function of their mass. Since the early measurement by Salpeter (1955), more and more elaborate and complete measurements have provided us with high-quality data of the IMF. These data point toward a universal form of the IMF, exhibiting a peak between 0.1–0.6 $\mathrm{M}_\odot$ (see, e.g., Elmegreen, Klessen, & Wilson, 2008, for a theoretical discussion of this characteristic mass scale), and a steeply decreasing tail for masses, $M \gtrsim 1\,\mathrm{M}_\odot$ (see, e.g., Kroupa, 2001; Muench et al., 2002; Chabrier, 2003). This high-mass tail can be approximated with a power law of the form

$$\mathrm{d}\mathcal{N}(M) \propto M^{-1.35}\mathrm{d}\log M\,. \tag{1.6}$$

Moreover, there is evidence that the CMF exhibits a very similar power-law tail, but shifted to higher masses by a factor of a few. This observation may be interpreted as the IMF being a more or less linear conversion of the CMF into stars (e.g., Alves et al., 2007). This is an attractive idea, because it would be the simplest possible explanation for the similarity of the CMF and the IMF. However, many different physical processes can lead to the same power-law IMF (e.g., Clark et al., 2009; Goodwin & Kouwenhoven, 2009; Smith et al., 2009). In any case, explaining the universal form of the IMF in different environments has been, and will stay among the most challenging tasks of observational, theoretical and numerical astrophysics.

What can we say about the dependence of the CMF and the IMF on the statistics of interstellar

turbulence? Mac Low & Klessen (2004), Elmegreen & Scalo (2004) and Scalo & Elmegreen (2004) reviewed the role of turbulence for the IMF. Taken together, turbulence and gravity are the two main physical processes determining the CMF and the IMF. It is likely that the statistics of the turbulence translate –through gravity– to the statistics of the CMF and the IMF, only the exact form of this translation is unknown. However, turbulent compression of the gas is expected to play a key role in creating the dense seeds for local gravitational collapse into cores and stars.

On the theoretical side, Padoan & Nordlund (2002) and Hennebelle & Chabrier (2008) have provided analytic models of the CMF and the IMF, based on the statistics of supersonic turbulence. Both theories reproduce the basic features of the CMF and the IMF, namely the high-mass power-law tail and the turnover at lower masses. Since the log-normal density PDF, equation (1.4) and the density variance–Mach number relation, equation (1.5) are crucial ingredients for the theories, we expect some dependence of the CMF/ and the IMF on the turbulence forcing mechanism, which enters through the forcing parameter b in equation (1.5). As discussed by Hennebelle & Chabrier (2009) and Schmidt et al. (2010), the theoretically predicted characteristic mass shifts to lower masses for increasing b, while the power-law tail is almost independent of the forcing. The Hennebelle & Chabrier (2008) theory predicts a shift of the characteristic mass of about a factor of 4.6 between solenoidal ($b = 1/3$) and compressive turbulence forcing ($b = 1$). The dependence of this shift on b is the same dependence of the shift on the Mach number $\mathcal{M}$, because both the Mach number and the forcing parameter enter the theory only through equation (1.5), for which b and $\mathcal{M}$ enter in the same way. Given the fact that the turbulent Mach numbers vary over at least an order of magnitude in different molecular clouds, depending on their size, means that the theory predicts a variation of the characteristic mass of about 2 orders of magnitude (see, Hennebelle & Chabrier, 2008, Fig. 2). A similarly strong variation of the characteristic mass with Mach number is predicted in the IMF theory by Padoan & Nordlund (2002, Fig. 1). This is however hard to accommodate with the observation of an almost fixed characteristic mass as discussed above, and thus needs further investigation. A way to test the theories of the CMF and the IMF is through numerical simulations in which the mass distribution of fragments can be measured directly. The best available method to do this is to use sink particles, which are described in Chapter 5. A preliminary comparison of the mass distributions obtained for solenoidal and compressive forcing is presented in Chapter 6, indicating that the characteristic mass is rather unaffected by the forcing parameter, b.

1.2.2 The star formation rate

The total star formation rate in the galaxy is about 3–5 $\mathrm{M}_\odot\,\mathrm{yr}^{-1}$. However, the star formation rate is much higher in the galactic center and in the spiral arms than in the interarm regions. Clearly, the star formation rate depends on environmental conditions, the most important of which are the gas surface density, and the density enhancements produced by supersonic turbulence. The star formation rate is thus expected to depend on the statistical properties of the turbulence in the galaxy.

Krumholz & McKee (2005) came up with a theory of the star formation rate based on the density probability distribution function, equation (1.4). Their model was developed further by Krumholz et al. (2009) and Padoan & Nordlund (2009). However, the basic derivation of the star formation rate remains the same in all those models. Equivalent to the CMF and IMF models discussed in the previous section, Krumholz & McKee (2005) estimate the amount of mass above a certain density threshold,

$$s_{\mathrm{crit}} = \ln\left(\frac{\rho_{\mathrm{crit}}}{\langle\rho\rangle}\right) , \tag{1.7}$$

by evaluating the following integral,

$$\mathrm{SFR}_{\mathrm{ff}} = \epsilon_{\mathrm{core}} \int_{s_{\mathrm{crit}}}^{\infty} \exp(s)\, p(s)\, \mathrm{d}s \,, \tag{1.8}$$

which they call the star formation rate per free fall time. Strictly speaking, this integral is nothing but the mass fraction of gas above the density threshold, s_{crit}. The factor ϵ_{core} is used to account for the mass loss during star formation. For instance, if the dense, star-forming cores lost half of the collapsing mass due to feedback processes (e.g., protostellar winds and outflows), then $\epsilon_{\mathrm{core}} = 0.5$. The true value of ϵ_{core} is uncertain, as it depends on environmental conditions, but it is reasonable to expect that ϵ_{core} varies between 0.25 and 1.0, such that at most 75% of the mass could be reinjected into the cloud from which the core formed (e.g., Matzner & McKee, 2000). Alternately, ϵ_{core} may be interpreted as a star formation efficiency. Alves et al. (2007) conclude that the star formation efficiency should be about 30% to account for the shift of the core mass function to the stellar initial mass function, so one might take $\epsilon_{\mathrm{core}} \approx 0.3$. In the following, I will take $\epsilon_{\mathrm{core}} = 1$, which corresponds to the situation of negligible mass loss, such that equation (1.8) gives the core formation rate prior to any feedback activity. The $\mathrm{SFR}_{\mathrm{ff}}$ is a dimensionless quantity that can be turned into a real star formation rate,

$$\dot{M}_{\mathrm{cloud}} = \mathrm{SFR}_{\mathrm{ff}} \, \frac{M_{\mathrm{cloud}}}{\phi_t \, t_{\mathrm{ff,\,cloud}}} \,, \tag{1.9}$$

where the numerical factor ϕ_t may be used to compensate for differences in the actual time for star formation from the free fall time of the cloud. ϕ_t is expected to be of order unity. Krumholz & McKee (2005) actually find that the best-fit value is $\phi_t \approx 1.9$ for the simulations discussed by Vázquez-Semadeni, Ballesteros-Paredes, & Klessen (2003). The lower bound of the integral in equation (1.8) is the critical logarithmic density, s_{crit}, above which the gas goes into free fall collapse and forms stars. Krumholz & McKee (2005) define this critical overdensity by comparing the Jeans length at the mean density, $\lambda_{\mathrm{J},0}$ with the sonic scale, λ_{s}:

$$s_{\mathrm{crit}} = 2 \, \ln\left(\phi_x \frac{\lambda_{\mathrm{J},0}}{\lambda_{\mathrm{s}}}\right) \,. \tag{1.10}$$

This choice is motivated by the expectation that the collapse sets in roughly at the sonic scale, where the turbulent fluctuations are of the order of the thermal sound speed, i.e., the local Mach number has dropped to about unity at the sonic scale. The global turbulent supersonic support is expected to become insignificant at the sonic scale, such that collapse can proceed below that scale (e.g., Mac Low & Klessen, 2004). The leading factor 2 in equation (1.10) stems from the density dependence of the Jeans length, $\lambda_{\mathrm{J}}(\rho) \propto \sqrt{\rho}$, and the numerical factor ϕ_x allows for slight variations in the actual scale on which the collapse sets in. Krumholz & McKee (2005) find $\phi_x \approx 1.1$ for the simulations by Vázquez-Semadeni et al. (2003). In real molecular clouds the sonic scale is expected to be of order 0.1 pc (e.g., Stahler & Palla, 2004). The role of the sonic scale is discussed further in Chapter 4.

Solving the integral in equation (1.8) gives the star formation rate per free fall time as a function of the critical density, s_{crit},

$$\mathrm{SFR}_{\mathrm{ff}} = \frac{\epsilon_{\mathrm{core}}}{2} \left[1 + \mathrm{erf}\left(\frac{-2\, s_{\mathrm{crit}} + \sigma_s^2}{2\sqrt{2}\, \sigma_s}\right)\right] \,. \tag{1.11}$$

In fact, $\mathrm{SFR}_{\mathrm{ff}}$ is also a function of the RMS Mach number, $\mathcal{M}$, and a function of the forcing parameter, b, because the logarithmic density variance, σ_s^2, is a function of both, as discussed

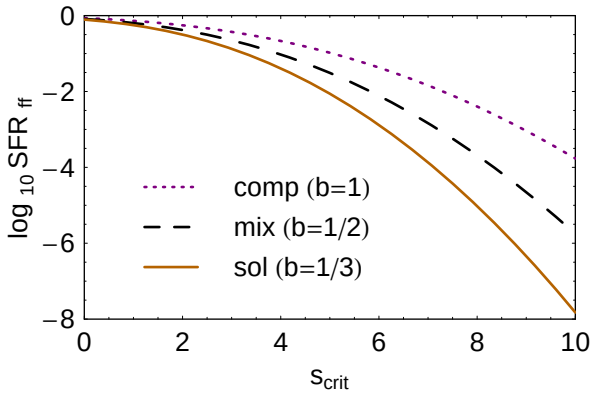

Figure 1.3: The star formation rate per free fall time, $\mathrm{SFR_{ff}}$ as a function of the logarithmic critical density, above which star formation is assumed to occur in the model by Krumholz & McKee (2005). The theoretical value of $\mathrm{SFR_{ff}}$ (equation 1.11) is shown as a function of the forcing parameter b for a fixed RMS Mach number, $\mathcal{M} = 10$.

above and shown in equation (1.5). Indeed, Krumholz & McKee (2005) give credit to the dependence of their star formation rate on the RMS Mach number by plotting $\mathrm{SFR_{ff}}$ as a function of the critical density in their Figure 1. However, they assumed a forcing parameter $b = 0.5$, without discussing the dependence of their star formation rate on this assumption. Although $b \approx 0.5$ is the result for a typical mixture of turbulence forcing, it is interesting to investigate the limiting cases $b = 1/3$ and $b = 1$ that I find for solenoidal and compressive forcing, respectively. As shown in Chapter 4, real molecular clouds show evidence of different forcing functions, and thus different values of b are expected to apply in different molecular cloud regions.

The results for $\mathrm{SFR_{ff}}$ from equation (1.11) are plotted in Figure 1.3 as a function of s_{crit} for a fixed Mach number, $\mathcal{M} = 10$, but for solenoidal forcing ($b = 1/3$), mixed forcing ($b = 1/2$) and compressive forcing ($b = 1$), respectively. Compressive forcing yields higher star formation rates than solenoidal forcing for all critical densities. The mixed forcing rates are bracketed by the two limiting cases. What is a reasonable critical density, s_{crit} for real clouds? Taking a mean number density of $100\,\mathrm{cm^{-3}}$ to be representative of a typical giant molecular cloud complex (e.g., Stahler & Palla, 2004) and a temperature of about 10 K, we find a mean Jeans length of about 2 pc. Furthermore assuming a sonic scale of about 0.1 pc, and taking $\phi_x = 1$ for simplicity, we find $s_{\mathrm{crit}} \approx 6$ from equation (1.10). Figure 1.3 shows that for this critical density, compressive forcing yields a star formation rate about 30 times higher than solenoidal forcing at the same RMS Mach number. This numerical example shows that the forcing dependence must be taken into account in models of the star formation rate, as the ones by Krumholz & McKee (2005), Krumholz et al. (2009) and Padoan & Nordlund (2009).

1.2.3 The star formation rate in virialized objects

Figure 1.3 suggests that the star formation rate per free fall time should increase with increasing Mach number in the same way as it increases with the forcing parameter, b. This is because σ_s, equation (1.5) depends on $\mathcal{M}$ and on b in the same way. From numerical simulations, however, Klessen, Heitsch, & Mac Low (2000) find that the star formation rate *decreases* with increasing Mach number. Intuitively, one would expect that the star formation rate becomes smaller as the Mach number increases, because increasing the Mach number means increasing the kinetic energy, which can provide support against gravitational collapse. On the other hand, higher Mach numbers lead to stronger shocks and thus to stronger local density enhancements, which

are the seeds for gravitational collapse. In summary, the dependence of the star formation rate on the turbulent Mach number is non-trivial, because of the two competing effects of interstellar turbulence: providing global support on the one hand, and creating local compressions on the other (see, Mac Low & Klessen, 2004). In contrast to this expected competition, Figure 1.3 shows that the star formation rate always increases with increasing Mach number and/or increasing forcing parameter b. A possible solution to this contradiction is that the true star formation rate depends on Mach number not only through σ_s, equation (1.5), but also through the critical density, $s_{\rm crit}$.

If we go back to the definition of the critical density, $s_{\rm crit}$, above which the gas goes into free fall collapse, equation (1.10), we see that it depends on the Jeans length of the cloud and on the sonic scale. The Jeans length can be rewritten as

$$\lambda_{\rm J,0} = \left(\frac{\pi c_{\rm s}^2}{G\rho_0}\right)^{1/2} = \pi c_{\rm s} \left(\frac{L^3}{6GM}\right)^{1/2} , \tag{1.12}$$

where we have assumed a spherical cloud with diameter L, mass M, and isothermal sound speed $c_{\rm s}$. Since the velocity fluctuations in a turbulent medium depend on the length scale, ℓ as $\sigma_v = \sigma_V \, (\ell/L)^p$, equation (1.1), where σ_V is the velocity dispersion on the scale L, and $p \approx 0.5$ from both observations and numerical simulations (see Chapter 4), the sonic scale can be written as

$$\lambda_{\rm s} = L \left(\frac{c_{\rm s}}{\sigma_V}\right)^{1/p} . \tag{1.13}$$

Substituting equations (1.12) and (1.13) into equation (1.10), we find

$$s_{\rm crit} = \ln\left[\frac{\phi_x^2\pi^2}{5}\,\frac{5\sigma_V^2 L}{6GM}\,\left(\frac{\sigma_V}{c_{\rm s}}\right)^{2(1-p)/p}\right] \tag{1.14}$$

$$= \ln\left[\frac{\phi_x^2\pi^2}{5}\,\alpha_{\rm vir}\,\mathcal{M}^{2/p-2}\right] , \tag{1.15}$$

where I have identified the virial parameter, $\alpha_{\rm vir} = 5\sigma_V^2 L/(6GM)$, and the RMS Mach number, $\mathcal{M} = \sigma_V/c_{\rm s}$ in the second step. This derivation is essentially identical to the one presented in Krumholz & McKee (2005), with the exception that I have defined the virial parameter, $\alpha_{\rm vir} = 2E_{\rm kin}/\left|E_{\rm pot}\right|$ with $E_{\rm kin} = M\sigma_V^2/2$ and $E_{\rm pot} = -3GM^2/(5R)$. This definition means that $\alpha_{\rm vir} = 1$ for a spherical cloud in virial equilibrium, where I have assumed that the thermal and magnetic energies of the cloud are negligible compared to the kinetic energy. While the assumption a negligible thermal energy is safely fulfilled in molecular clouds (see, e.g., Stahler & Palla, 2004), the assumption of a negligible magnetic energy needs to be relaxed in future work. Some attempts to do this are presented in Padoan & Nordlund (2009).

Equation (1.14) shows that the critical density, $s_{\rm crit}$ depends on the RMS Mach number, and thus the actual star formation rate calculated with equation (1.11) depends on Mach number, not only through σ_s, but also through $\rm s_{crit}$. Taken together, we can now investigate the theoretical prediction for the star formation rate, $\rm SFR_{ff}$ as a function of the Mach number, $\mathcal{M}$, and the forcing parameter, b. For this purpose, I assume a virial parameter of $\alpha_{\rm vir} = 1$, although one must keep in mind that this is not necessarily the correct value for molecular clouds (see, e.g., the discussion of surface terms in the virial equation by Dib et al., 2007). In any case, variations in the virial parameter are not expected to have a strong influence on the derived $\rm SFR_{ff}$ compared to the Mach number, which enters quadratically in equation (1.14), while $\alpha_{\rm vir}$ enters only linearly. For simplicity, I use $\phi_x = 1$, and combine equations (1.14) and (1.11) to obtain the star formation rate per free fall time as a function of $\mathcal{M}$ and b. The results are plotted in Figure 1.4 for $b = 1/3$, $1/2$, and 1 as a function of $\mathcal{M} = [1, 100]$. We see an immediate conspicuous features here: the star

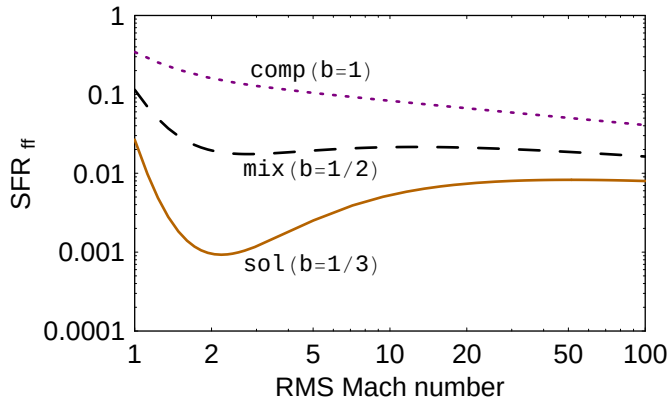

Figure 1.4: The star formation rate per free fall time, $\mathrm{SFR_{ff}}$ as a function of the RMS Mach number, $\mathcal{M}$. Three different forcing parameters are shown: the two limiting cases of solenoidal ($b = 1/3$) and compressive forcing ($b = 1$), and an intermediate, mixed forcing case ($b = 1/2$).

formation rate decreases monotonically with increasing $\mathcal{M}$ only for compressive forcing, while it is almost insensitive to $\mathcal{M}$ for the mixed forcing case for $\mathcal{M} \gtrsim 2$, and exhibits a minimum at around $\mathcal{M} \approx 2$ for solenoidal forcing, followed by a rise in $\mathrm{SFR_{ff}}$ up to $\mathcal{M} \approx 30$. For typical molecular cloud Mach numbers, $\mathcal{M} \approx 10$, compressive forcing would thus yield a roughly 16 times higher star formation rate than solenoidal forcing. Moreover, for all Mach numbers up to $\mathcal{M} = 100$ the predicted star formation rate is more than a factor of 5 higher for compressive forcing than for solenoidal forcing. For $\mathcal{M} \approx 2$ the difference between solenoidal and compressive forcing is even a factor of 168. This theoretical prediction needs to be tested with numerical simulations. I provide some preliminary results of such a numerical test in Chapter 6. Indeed, compressive forcing yields star formation rates about an order of magnitude higher than solenoidal forcing. Figure 1.4 shows that the forcing dependence of the star formation rate is typically stronger than the Mach number dependence, suggesting that the nature of the turbulence forcing must be taken into consideration.

1.3 Turbulent driving agents and triggering

Supersonic turbulence is the key-mechanism to locally compress interstellar gas in the galaxy, consequently triggering star formation (e.g., Elmegreen, 2009). What physical drivers of interstellar turbulence can we identify and what is their relative contribution to the overall kinetic energy budget of the interstellar medium? On which scales do these drivers act and how much compression is induced by them? Providing answers to these questions is at the heart of understanding interstellar turbulence, and thus of understanding star formation. However, these questions still remain open and an active field of research.

Mac Low & Klessen (2004) discuss potential energy sources of turbulence and provide estimates of the energy injection rates. Using results of numerical experiments of decaying turbulence by Mac Low et al. (1998), they estimate the galactic decay rate of the kinetic energy density,

$$\dot{e} \simeq -\frac{1}{2}\langle\rho\rangle \frac{\sigma_V^3}{L_{\mathrm{inj}}} \approx -3 \times 10^{-27}\,\mathrm{erg\,cm^{-3}\,s^{-1}} \tag{1.16}$$

for a mean number density of $\langle n\rangle \approx 1\mathrm{cm}^{-3}$, a velocity dispersion of $10\,\mathrm{km\,s^{-1}}$, and an injection scale, $L_{\mathrm{inj}} \approx 100\,\mathrm{pc}$. Different physical drivers may contribute to inject turbulent energy, balanc-

Driving mechanism	$\dot{e}$ in erg cm^{-3} s^{-1}	injection scale
Magnetorotational instabilities	3×10^{-29}	large
Gravitational instabilities	4×10^{-29}	large
Protostellar outflows	4×10^{-28}	small–intermediate
Thermal instabilities	5×10^{-29}	intermediate
Ionization fronts (H II regions)	3×10^{-30}	intermediate–large
Supernova explosions	3×10^{-26}	intermediate–large

Table 1.1: Possible drivers of interstellar turbulence and their energy injection rates per unit volume as estimated by Mac Low & Klessen (2004). Note that I have assumed a disk scale height of $H = 100$ pc for all processes in this table, while Mac Low & Klessen (2004) use $H = 200$ pc to estimate $\dot{e}$ from protostellar outflows.

ing this decay rate. Table 1.1 summarizes the possible drivers of turbulence and their individual energy injection rates as discussed by Mac Low & Klessen (2004). Mac Low & Klessen (2004) conclude that supernova explosions contribute most. Their energy injection rate is about one order of magnitude higher than the average galactic decay rate. The second most powerful mechanism to maintain turbulence seems to be driving from protostellar outflows, which is, however, two orders of magnitude less efficient than supernova driving, and thus only capable of balancing about 10% of the global decay rate. Supernovae are also particularly attractive as turbulent drivers, because they likely inject energy on rather large scales, in form of superbubbles. Observations show that turbulence is mainly driven on large scales (e.g., Ossenkopf & Mac Low, 2002; Tamburro et al., 2009; Brunt et al., 2009). It is thus hard to see how protostellar outflows could be the main drivers of large-scale interstellar turbulence, however, they may contribute significantly on local, smaller scales (see the discussion in section 6.2.5 of Chapter 6).

It is important to emphasize that most of the potential drivers of turbulence will excite a considerable amount of compressible modes. Supernova explosions, in particular, are known to create gigantic superbubbles. While expanding, these shells compress gas, a process that drives turbulence inside the shell, and triggers new star formation. A fascinating example of possible triggering of star formation in expanding shells is the Cygnus X complex (Reipurth & Schneider, 2008), shown in Figure 1.5. This region is strongly affected by radiation from the Cygnus OB2/OB9 clusters, expanding H II regions, and a large number of outflow sources, which may all contribute to driving the turbulence in this region.

1.4 Systematic numerical approach

Given that a full theory of turbulence is elusive even in the incompressible regime apart from the phenomenology provided by Kolmogorov (1941), one inevitably turns to numerical simulations to glean insight. The basic numerical approach followed to investigate the forcing dependence of interstellar turbulence is described here. As with all numerical models, the applicability of these simulations to real molecular clouds is limited (see section 4.10 of Chapter 4), and this needs to be kept in mind. The basic numerical approach is to set up a cubic box of linear size L, initially filled with gas of uniform density, $\langle\rho\rangle$. For simplicity, this box has periodic boundaries. This means that we only consider a small sub-part of a much more extended cloud. We can imagine, however, that the structures surrounding this small cubic domain are similar on all sides viewed from the center, so long as we are not close to the boundary of the whole cloud (see, e.g., the inner parts of the Polaris Flare shown in Figure 1.1). The initially uniform and static gas distribution is then accelerated by a random force. This setup is often called "turbulence-in-a-box", because of

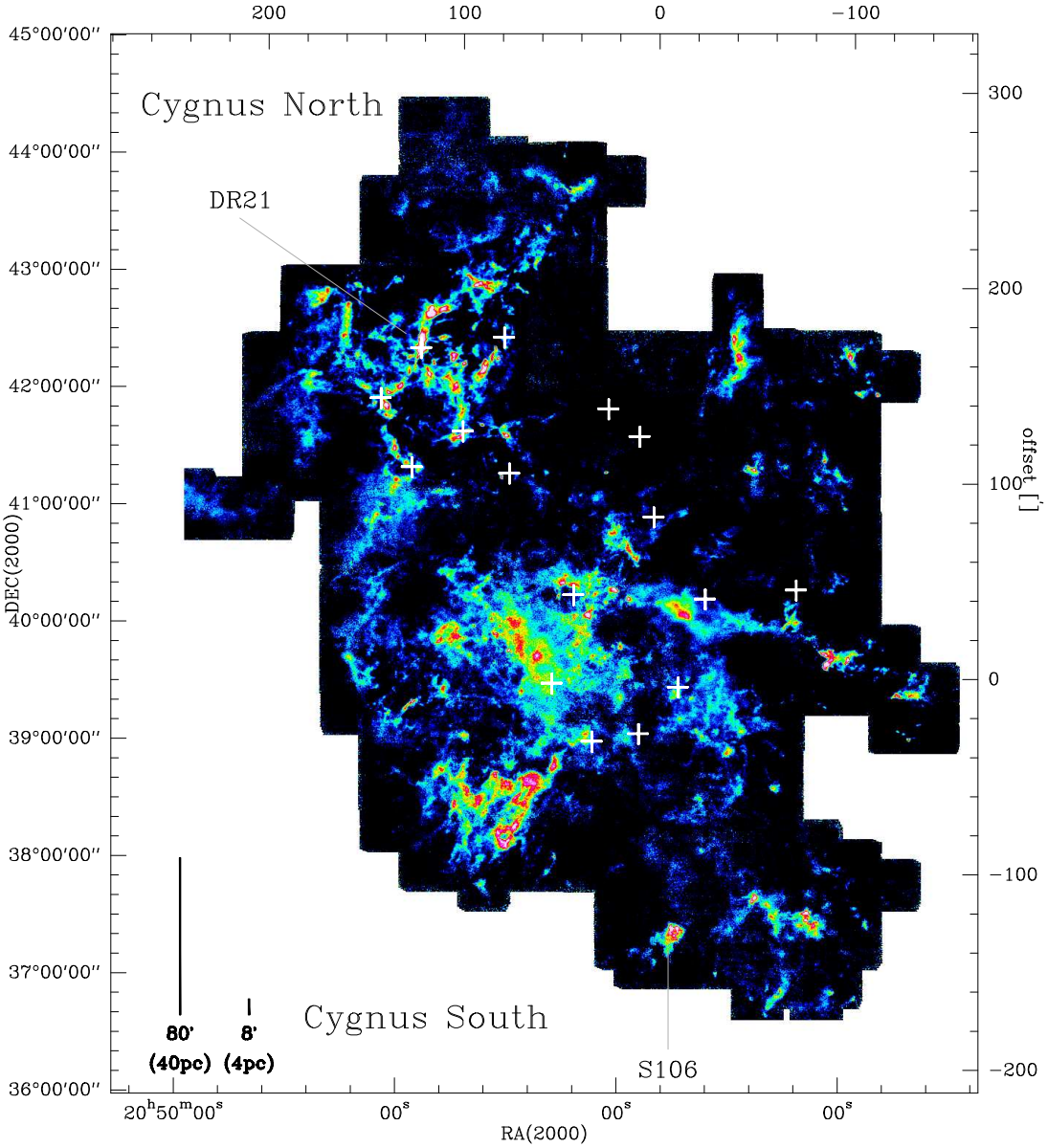

Figure 1.5: Line integrated map of Cygnus X in ^{13}CO 1 → 0 emission with the intensity (−1 to 16 K km s^{-1}) coded in color. Crosses indicate the location of thermal H II regions and the massive star-forming regions DR21 and S106 are labeled. The distance to Cygnus X is about 1.7 kpc. Image credit: Schneider et al. (2010).

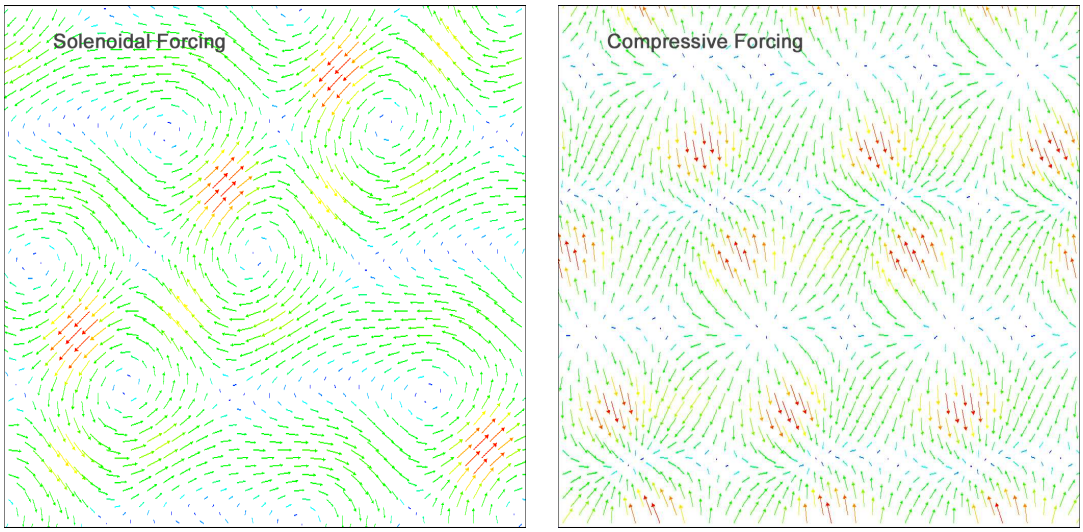

Figure 1.6: A two-dimensional representation of a solenoidal (divergence-free) forcing field (left), and a compressive (curl-free) forcing field (right) at a randomly chosen time. The length and color of the vectors are proportional to the local amplitude of the field.

its simplicity, but has provided indispensable insight into the statistics of interstellar turbulence and star formation (e.g., Porter et al., 1992b; Vázquez-Semadeni, 1994; Padoan et al., 1997; Klessen et al., 1998; Mac Low et al., 1998; Passot & Vázquez-Semadeni, 1998; Stone et al., 1998; Mac Low, 1999; Klessen, 2000; Heitsch et al., 2001; Boldyrev et al., 2002; Cho et al., 2002; Li et al., 2003; Padoan et al., 2004a; Jappsen et al., 2005; Ballesteros-Paredes et al., 2006; Glover & Mac Low, 2007a,b; Kritsuk et al., 2007; Kowal et al., 2007; Beetz et al., 2008; Dib et al., 2008; Offner et al., 2008; Lemaster & Stone, 2009; Schmidt et al., 2009).

Most turbulence-in-a-box studies have in common that a random driving force, $\mathbf{f}$, is used to accelerate the gas, until the gas reaches a state of fully developed turbulence. The properties of the forcing, $\mathbf{f}$, however, can be varied. A detailed discussion of the turbulence forcing used in this study and in previous studies is provided in section 4.2.1, however, the essential numerical approach followed in this thesis is summarized here. Since $\mathbf{f}$ is a random vector field, we are free to vary the ratio of rotational to compressible modes of the vector field. Any one-, two-, or three-dimensional vector field can be decomposed into two parts, a solenoidal (divergence-free) part, $\nabla \cdot \mathbf{f} = 0$ and a compressible (curl-free) part, $\nabla \times \mathbf{f} = 0$. This allows us to construct a new random vector field with any desired ratio of solenoidal and compressible modes by taking scaled versions of the original parts and mixing them together. We can thus also construct the two extreme cases of such a field: first, a completely solenoidal (divergence-free) field, and second, a completely compressible (curl-free) field. I call these two limiting cases *solenoidal forcing* and *compressive forcing*, respectively [1].

A spatial representation of the two limiting forcing cases is shown in Figure 1.6. For clarity, I show a two-dimensional forcing field in this figure. However, the generalization to three dimensions is straight forward, such that the fields preserve the properties that $\nabla \cdot \mathbf{f} = 0$ for solenoidal forcing, and $\nabla \times \mathbf{f} = 0$ for compressive forcing. To drive turbulence, a new random forcing pattern is constructed every timestep. The forcing is implemented such that it maintains the given ratio of solenoidal to compressible modes at any time, and that the field varies smoothly

[1] Note that I use the term 'compressive forcing' instead of 'compressible forcing' to emphasize the action of this new kind of forcing, namely to *compress* the gas.

in space and time, following the procedure described in section 4.2.1.

All turbulence-in-a-box studies have so far considered only solenoidal or mixed forcing, but no study existed with purely compressive forcing. This is very surprising, given that most of the proposed physical mechanisms for driving interstellar turbulence are expected to excite compressible modes rather than solenoidal modes (see section 1.3). The main work presented in this thesis, fills this empty gap, and provides a systematic comparison of turbulence forcing. The main conclusion is that the turbulence forcing mechanism determines the statistics of the turbulence, and thus controls key-properties of star formation, for instance, the star formation rate (see sections 1.2.2 and 6.2.1).

Chapter 2

The density probability distribution in compressible isothermal turbulence: solenoidal vs compressive forcing

The probability density function (PDF) of the gas density in turbulent supersonic flows is investigated with high-resolution numerical simulations in this Chapter. In a systematic study, I compare the density statistics of compressible turbulence driven by the usually adopted solenoidal forcing (divergence-free) and by compressive forcing (curl-free). Our results are in agreement with studies using solenoidal forcing. However, compressive forcing yields a significantly broader density distribution with standard deviation $\sim$3 times larger at the same RMS Mach number. The standard deviation-Mach number relation used in analytical models of star formation is reviewed and a modification of the existing expression is proposed, which takes into account the ratio of solenoidal and compressive modes of the turbulence forcing. The results presented in this Chapter are published in Federrath et al. (2008b).

2.1 Introduction

The pioneering works by Padoan et al. (1997, PNJ97 below) and Passot & Vázquez-Semadeni (1998, PV98 below) have shown that the standard deviation (stddev) σ_ρ, i.e., the width or dispersion of the linear density PDF p_ρ grows proportional to the RMS Mach number $\mathcal{M}$ of the turbulent flow, however, with proportionality constants in disagreement by a factor of 2. The exact dependence of the PDF's stddev on the RMS Mach number is a key ingredient for analytical models of star formation. For instance, Padoan & Nordlund (2002) and Hennebelle & Chabrier (2008) relate the density PDF to the core mass function (CMF) and stellar initial mass function (IMF). Tassis (2007) uses the density PDF on galactic scales to reproduce the Kennicutt-Schmidt relation. Elmegreen (2008) suggests that the star formation efficiency is a function of the density PDF.

In the present work, we solve the discrepancy between PNJ97 and PV98 by showing that the stddev of the PDF is not only a function of the RMS Mach number, but is also very sensitive to the relative importance of solenoidal (divergence-free) and compressive (curl-free) modes of the turbulence forcing, leading to variations in the stddev up to factors of ~ 3 for the same RMS Mach number. The main result of the present work is that the conclusions of PNJ97 and PV98 can be harmonized, if we take into account that PNJ97 have analyzed purely solenoidal forcing, whereas PV98 have studied purely compressive forcing. This apparent difference has not been considered analytically or numerically before.

We begin by explaining our numerical method in section 2.2. Section 2.3 shows that our results

are consistent with previous studies using solenoidal forcing, whereas compressive forcing yields a PDF with stddev ~ 3 times larger in 3-dimensional turbulent flows. We present a heuristic model explaining this difference, which is based on the ratio of solenoidal to compressive modes of the forcing to estimate the proportionality constant in the stddev-Mach relation. Section 2.4 summarizes our conclusions.

2.2 Numerical methods

The piecewise parabolic method (Colella & Woodward, 1984) implementation of FLASH v3 (Fryxell et al., 2000; Dubey et al., 2008) was used to solve the hydrodynamic equations on periodic uniform grids with 16384^1, 4096^2, and 1024^3 grid points in 1, 2 and 3 dimension(s) (1D, 2D, 3D). Since we model isothermal gas, it is convenient to define $s \equiv \ln(\rho/\rho_0)$ as the natural logarithm of the density divided by the mean density ρ_0. Isothermal gas has been modeled several times in the context of molecular cloud dynamics taking periodic boundaries and studying compressible turbulence with solenoidal or weakly compressive forcing (e.g., Stone et al., 1998; Mac Low et al., 1998; Mac Low, 1999; Klessen et al., 2000; Heitsch et al., 2001; Boldyrev et al., 2002; Li et al., 2003; Padoan et al., 2004b; Jappsen et al., 2005; Ballesteros-Paredes et al., 2006; Kritsuk et al., 2007; Dib et al., 2008; Offner et al., 2008). Most of these studies have purely solenoidal forcing motivated by incompressible turbulence studies, some have weakly compressive forcing. The latter is a result of the natural ratio of solenoidal to compressible modes of a Gaussian field prepared in Fourier space without subsequent projection. This natural ratio is 2:1 in 3D and 1:1 in 2D. Accordingly, the ratio of compressive to the sum of compressive plus solenoidal modes is 1:3 in 3D and 1:2 in 2D. Only PV98 have purely compressive forcing, because they analyze 1D simulations where no solenoidal component exists and the ratio of compressive to total modes is 1:1.

The forcing is typically either modeled as a static pattern following the recipes by Mac Low et al. (1998) and Stone et al. (1998), or by an Ornstein-Uhlenbeck (OU) process with finite autocorrelation timescale T (e.g., Eswaran & Pope, 1988; Schmidt et al., 2006). Note that driving with a static pattern is the limiting case of an OU process with infinite autocorrelation timescale. We use the OU process and follow the usual approach, setting T equal to the dynamical timescale, $T = L/(2V)$. In code units, $L = 1$ is the size of the computational domain, $V = c_s\mathcal{M}$ is the RMS velocity, $\mathcal{M} \approx 5.5$ is the RMS Mach number, and $c_\mathrm{s} = 1$ is the sound speed. The dynamical time, T, was set equal to the decay time constant of the turbulence (Stone et al., 1998; Mac Low, 1999) at the scales of energy injection $1 < k < 3$. This guarantees a well-defined stochastic driving field, which varies smoothly in space and time. We checked that modeling of the forcing as an almost static pattern (increasing T by one order of magnitude) did not significantly affect our results.

The absence of a physical scale in the equations of hydrodynamics solved here (discussed in Chapters 3 and 4) means that the results can be arbitrarily scaled to the interstellar medium by defining length, mass and time scales. For example, adopting a length scale of 1 pc and a sound speed of $0.2\,\mathrm{km\,s^{-1}}$, gives the physical time from the code units according to

$$\frac{T_\mathrm{physical}}{T} = 0.49\,\mathrm{Myr}\left(\frac{L}{1\,\mathrm{pc}}\right)\left(\frac{\mathcal{M}}{5}\right)^{-1}\left(\frac{c_\mathrm{s}}{0.2\,\mathrm{km\,s^{-1}}}\right)^{-1}. \tag{2.1}$$

One can similarly set a mass scale by defining the initial (mean) density to be $n_0 = 1000\,\mathrm{cm^{-3}}$,

$$\rho_\mathrm{physical} = 3.85\times10^{-21}\,\mathrm{g\,cm^{-3}}\left(\frac{n_0}{1000\,\mathrm{cm^{-3}}}\right)\left(\frac{\mu}{2.3}\right)\exp(s) \tag{2.2}$$

assuming fully molecular hydrogen gas with a mean molecular weight of 2.3, giving a total mass

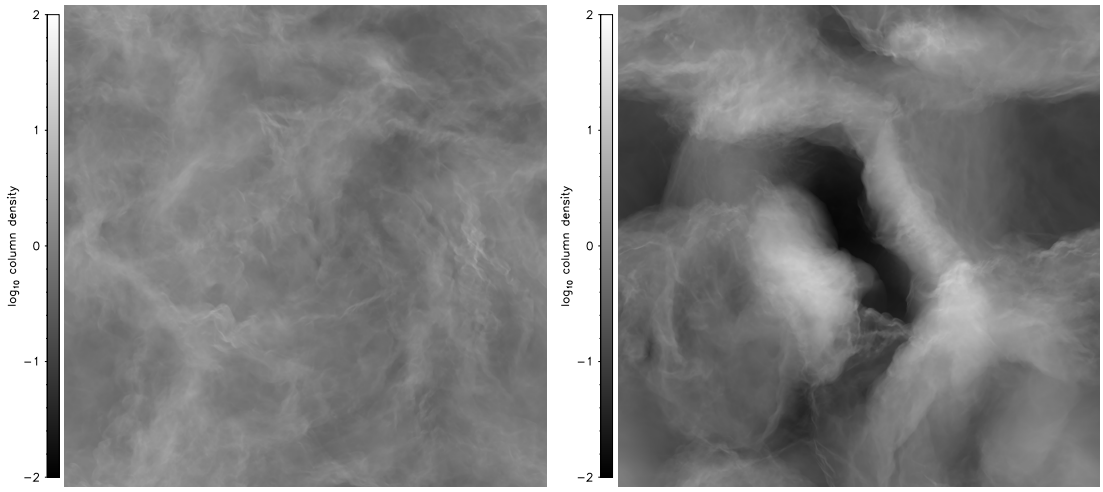

Figure 2.1: Column density field in units of the mean column density for solenoidal forcing (*left*), and compressive forcing (*right*) at a randomly picked time in the regime of statistically stationary turbulence. Both maps show 4 orders of magnitude in column density with the same scaling for direct comparison of solenoidal and compressive forcing at RMS Mach number ~ 5.5.

in the box of about $57\,\mathrm{M}_\odot$. The physical values of the length, mass and time scales used in these two expressions is consistent with the observations presented by Falgarone et al. (1992).

In order to obtain a purely solenoidal, or a purely compressive forcing (or any combination), a Helmholtz decomposition can be made by applying the projection operator in Fourier space (k-space)

$$\mathcal{P}_{ij}^{\zeta} = \zeta \mathcal{P}_{ij}^{\perp} + (1-\zeta)\mathcal{P}_{ij}^{\parallel} = \zeta\delta_{ij} + (1-2\zeta)\frac{k_i k_j}{|k|^2}\,, \tag{2.3}$$

to the random vector field returned by the OU process or generated by the usual recipes. The parameter $\zeta \in [0,1]$ controls the relative importance of solenoidal and compressive modes. If we set $\zeta = 1$, $\mathcal{P}_{ij}^{\zeta}$ projects only the solenoidal component, whereas only the compressive component is obtained by setting $\zeta = 0$.

2.3 Results and discussion

Figure 2.1 compares column density maps for solenoidal vs. compressive forcing of our 3D models (1024^3) from a randomly picked snapshot in the regime of statistically stationary turbulence. Obviously, compressive forcing yields much larger density contrasts, despite the fact that the RMS Mach number $\mathcal{M} \sim 5.5$ is about the same in both cases. This is quantitatively shown in Fig. 2.2, which presents the comparison of the time averaged volume-weighted density PDFs in the solenoidally and compressively driven cases. Most importantly, although the RMS Mach numbers are almost the same, the stddev σ_ρ of the PDF obtained in compressive forcing is ~ 3 times larger than for solenoidal forcing (Tab. 2.1). This is the main result of the present study and has important consequences: The stddev of the density PDF is not only a function of the RMS Mach number as found by PNJ97 and PV98, but also a function of the relative strength of solenoidal to compressive modes of the turbulence forcing, i.e., a function of the projection parameter ζ in eq. (2.3). In the following, we review the stddev-Mach number relation and present a heuristic model for the proportionality constant in this relation.

It has been pointed out by PNJ97 and measured by PV98 that the stddev σ_ρ of the PDF of

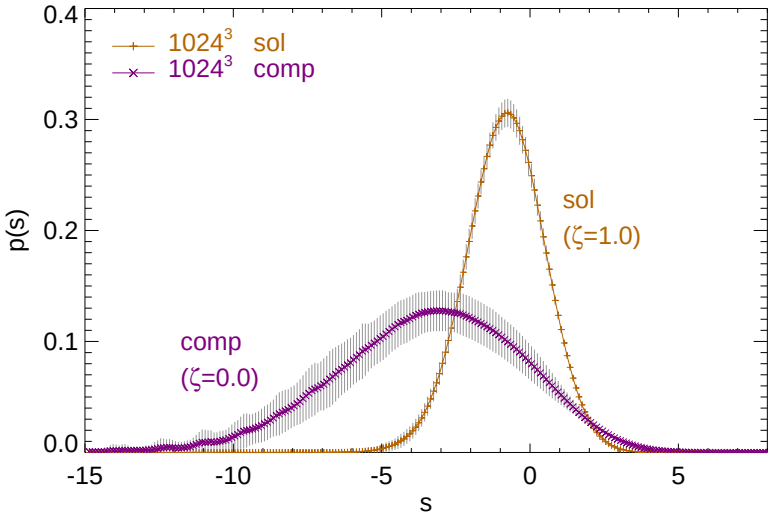

Figure 2.2: Volume-weighted density PDFs $p(s)$ in linear scaling where $s = \ln(\rho/\rho_0)$. The PDF obtained by compressive forcing (comp, $\zeta = 0.0$) is much broader compared to the solenoidal one (sol, $\zeta = 1.0$) at the same RMS Mach number. The peak is shifted due to mass conservation (Vázquez-Semadeni, 1994). Gray error bars indicate 1-sigma temporal fluctuations of the PDF. A sample of $\sim 10^{11}$ datapoints contribute to each PDF.

the linear density p_ρ grows linear with the RMS Mach number $\mathcal{M}$ like

$$\sigma_\rho/\rho_0 = b\mathcal{M} \tag{2.4}$$

with the proportionality constant b. PV98 find $b \sim 1$ in 1D simulations with $\mathcal{M}$ ranging from subsonic to supersonic flows. PNJ97 motivate and explain eq. (2.4) with the isothermal hydrodynamic shock jump conditions. They assume the PDF follows a lognormal analytical form

$$p_s(s) = \frac{1}{\sqrt{2\pi\sigma_s^2}} \exp\left[-\frac{(s-s_0)^2}{2\sigma_s^2}\right] \tag{2.5}$$

to get an expression for the stddev in the logarithmic density

$$\sigma_s = \left[\ln\left(1 + b^2\mathcal{M}^2\right)\right]^{1/2} . \tag{2.6}$$

Using $p_s ds = p_\rho d\rho$, it is easy to show that for any density PDF, whether lognormal or not, $\sigma_\rho^2 = \rho_0^2 \int_{-\infty}^{\infty} [\exp(s) - 1]^2 \, p_s ds$. From the assumption (2.5) it follows that eq. (2.6) and (2.4) are equivalent and that both expressions have the same b. This means that eq. (2.4) is the basic stddev-Mach number relation from which eq. (2.6) follows, if a lognormal PDF is assumed.

PNJ97 applied eq. (2.6) to magnetohydrodynamical (MHD) simulations and obtained $b \sim 0.5$. Consequently, their stddev is only half as large as that found by PV98. Padoan et al. (2007) argue that eq. (2.6) may hold for MHD turbulence as well, if $\mathcal{M}$ is replaced by the Alfvénic Mach number, although the shock jump conditions motivating eq. (2.4) are different for shocks perpendicular to the magnetic field. In MHD simulations, Li et al. (2004) and Li et al. (2008) find $b \sim 0.38$ and $b \sim 0.41$ for ideal MHD and $b \sim 0.58$ by including ambipolar diffusion (AD). The latter means that including AD broadens the PDF over ideal MHD, because of the reduced magnetic pressure compared to ideal MHD. Therefore, the parameter b in eq. (2.4) and (2.6) is not expected to be universal, but depends on the magnetic field (see also, Vázquez-Semadeni

D	resolution	ζ	$\mathcal{M}$	σ_ρ/ρ_0	b
3	1024^3	1.0 (sol)	$5.3^{\pm 0.2}$	$1.9^{\pm 0.1}$	$0.36^{\pm 0.03}$
3	1024^3	0.0 (comp)	$5.6^{\pm 0.3}$	$5.9^{\pm 1.0}$	$1.05^{\pm 0.19}$
2	4096^2	1.0 (sol)	$5.6^{\pm 0.5}$	$2.4^{\pm 0.5}$	$0.43^{\pm 0.10}$
2	4096^2	0.0 (comp)	$5.7^{\pm 0.6}$	$5.0^{\pm 1.5}$	$0.88^{\pm 0.28}$
1	16384^1	0.0 (comp)	$5.0^{\pm 1.0}$	$4.5^{\pm 2.0}$	$0.90^{\pm 0.44}$

Table 2.1: Parameters in solenoidal and compressive forcing

et al., 2005a). On the other hand, Lemaster & Stone (2008) find that even strong magnetic fields do not alter the stddev-Mach number relation significantly. In the following discussion, we will concentrate on purely hydrodynamical estimates showing that b is much more sensitive to the way of forcing compared to the reported MHD effects. In order to show this, we use the more fundamental stddev-Mach number relation given by eq. (2.4), which does not rest on the additional assumption of a lognormal density PDF.

From purely hydrodynamic studies utilizing different numerical methods and resolutions, typically smaller but roughly consistent values of b are found compared to $b\sim 1$ by PV98, e.g., $b\sim 0.35$ using 200,000 SPH particles (Li et al., 2003), $b\sim 0.26$ using ENZO with 1024^3 cells (Kritsuk et al., 2007)[1], $b\sim 0.37$ using another grid-based method with 512^3 cells (Beetz et al., 2008). It is important to note that all the aforementioned studies (including the MHD studies) use solenoidal or weakly compressive forcing, except for PV98, who naturally have purely compressive forcing because they analyze 1D simulations. Similar to PV98, we find $b\sim 1.05$ for purely compressive forcing (Tab. 2.1). For purely solenoidal forcing, we get $b\sim 0.36$ in agreement with the estimates by Li et al. (2003), Kritsuk et al. (2007) and Beetz et al. (2008). This shows that the width of the PDF does not only depend on the RMS Mach number given by eq. (2.4), but also on the mixture of solenoidal and compressive modes ζ of the forcing. This dependence was qualitatively mentioned by Nordlund & Padoan (1999), although up to now, no quantitative estimate existed.

Based on the diversity of b in eq. (2.4) and (2.6) obtained in the studies mentioned above and based on our direct comparison of solenoidal and compressive forcing, we suggest that a plausible estimate for the proportionality constant b is obtained by taking into account the compressibility induced by the forcing,

$$b = 1 + \left[\frac{1}{D} - 1\right]\zeta = \begin{cases} 1 - \frac{2}{3}\zeta, & \text{for } D = 3 \\ 1 - \frac{1}{2}\zeta, & \text{for } D = 2 \\ 1, & \text{for } D = 1\ . \end{cases} \tag{2.7}$$

The relative strength of solenoidal to compressive modes ζ is defined in the projection operator, eq. (2.3).

For solenoidal forcing ($\zeta = 1$), by construction no compression is directly induced by the forcing. Rather, density fluctuations are solely a result of compressions naturally building up in a supersonic turbulent flow. This is a consequence of the ratio of compressible modes to the sum of compressible plus solenoidal modes in the velocity field, that the turbulent gas adjusts itself to (see, e.g., Elmegreen & Scalo, 2004). This ratio is related to the number of degrees of freedom D (spatial directions) available for compressible modes and is simply given by $1/D$ showing up in eq. (2.7). Consequently, eq. (2.7) leads to $b\sim 1/3$ for the 3D case with solenoidal forcing. This is in reasonable agreement with the results by Li et al. (2003), Kritsuk et al. (2007), Beetz et al. (2008) and ours.

[1] In their recent 2048^3 study with solenoidal forcing, they find a slightly larger $b\sim 0.32$ (Kritsuk 2008, private communication).

The 1D case as analyzed by PV98 is a special case of compressive forcing in arbitrary dimensions. Note that for compressive forcing, eq. (2.7) always suggests $b \sim 1$ independent of D. This can be understood as a consequence of the *direct* compression induced by the compressive force field, contrary to solenoidal forcing for which the natural ratio of modes in the velocity field determines b. Compressive forcing by construction immediately induces compressions along all available spatial directions D directly, and $b \sim D/D = 1$. The 1D calculations ($\zeta = 0$) by PV98 therefore exhibit $b \sim 1$. Similar, in our high-resolution 3D case of purely compressive forcing ($\zeta = 0$), compression is induced along all the 3 available spatial directions resulting in $b \sim 3/3 = 1$.

Besides testing eq. (2.7) for the extreme cases of solenoidal and compressive forcing at different dimensionality, we also aim at testing it for intermediate values of ζ (mixtures of solenoidal and compressive forcing) using reported results in the literature and additional numerical simulations.

Vázquez-Semadeni (1994) have analyzed 2D simulations with a 1:1 mixture of solenoidal and compressive forcing ($\zeta = 0.5$). Thus, the expected value is $b \sim 0.75$, and they find $b \sim 0.7$ close to the expectation. Schmidt et al. (2009) use a mainly compressive forcing ($\zeta = 0.1$) obtaining $b \sim 0.94$ from their data, while eq. (2.7) suggests $b \sim 0.93$.

We ran additional 2D and 1D simulations with solenoidal and compressive forcing to support our heuristic model, eq. (2.7). In order to get a statistically significant sample, the numerical resolution along the spatial directions was increased from 1024 in 3D to 4096 in 2D and 16384 in 1D, as well as the integration times were increased yielding at least twice as many sampling points as PV98 have. Table 2.1 summarizes the parameters of all simulations and numerical estimates for b. As expected from eq. (2.7), the compressive cases in 1D, 2D and 3D, all exhibit nearly the same $b \sim 1$. Moreover, the PDFs are very similar in all of the compressively driven cases, which is shown in Fig. 2.3. The 3D case with solenoidal forcing is also included for comparison ($b \sim 1/3$), as well as the 2D case with solenoidal forcing, for which we estimate $b \sim 0.43$ close to the prediction $b \sim 1/2$.

2.4 Summary and conclusions

Performing high-resolution hydrodynamical simulations of driven isothermal compressible turbulence, we have found that the way of forcing the turbulence has a strong effect on density statistics. We have compared the usually adopted solenoidal forcing (divergence-free) and compressive forcing (curl-free). The most important result is that in 3D, compressive forcing yields a density PDF with stddev ~ 3 times larger compared to solenoidal forcing for the same RMS Mach number.

As found by PNJ97 and PV98, the stddev σ_ρ is increasing directly proportional to the RMS Mach number, however, they find different proportionality constants. Taking into account the ratio of solenoidal to compressive modes ζ of the forcing resolves the disagreement between PNJ97 and PV98. We suggest that the proportionality constant b in the stddev-Mach number relations (2.4) and (2.6) can be determined by a heuristic model summarized in eq. (2.7). In the case of compressive forcing ($\zeta = 0$), the proportionality constant $b \sim 1$ irrespective of the dimensionality of the simulation. Solenoidal forcing on the other hand yields $b \sim 1/3$ in 3D and $b \sim 1/2$ in 2D.

We mention the impact of our results on analytical models linking the statistics of supersonic turbulence to the CMF/IMF. Padoan & Nordlund (2002) and Hennebelle & Chabrier (2008) rely on integrals over the density PDF to get a handle on the mass of objects above a certain density threshold. Since the width of the PDF is so sensitive to the mixture of solenoidal and compressive modes ζ, we also expect a strong influence on the derived CMF/IMF. Indeed, the larger dispersion obtained from compressive forcing leads to better agreement (Hennebelle 2008, private communication) of the analytic expression with the observed IMF in Hennebelle &

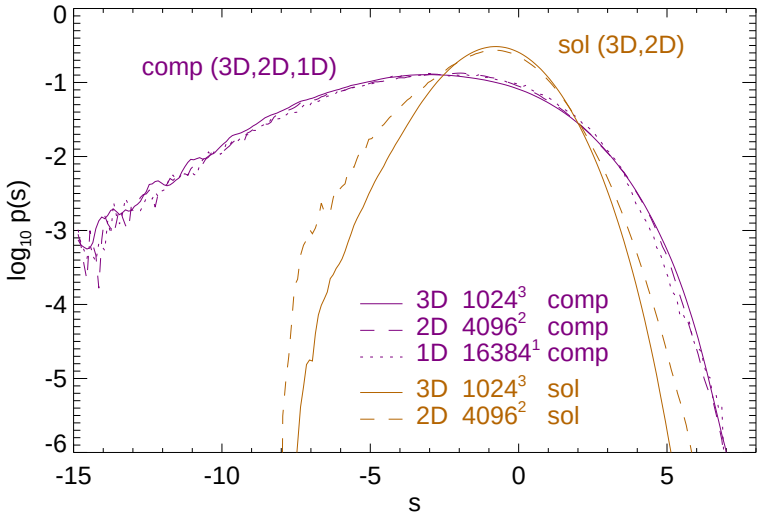

Figure 2.3: Density PDFs $p(s)$ obtained from 3D, 2D and 1D simulations with compressive forcing and from 3D and 2D simulations using solenoidal forcing in logarithmic scaling. Note that in 1D, only compressive forcing is possible as in the study by PV98. As suggested by eq. (2.7), compressive forcing yields almost identical density PDFs in 1D, 2D and 3D with $b\sim1$ because compressive forcing induces gas compression along all available spatial directions. Solenoidal forcing on the other hand leads to a density PDF with $b\sim1/2$ in 2D and with $b\sim1/3$ in 3D as a consequence of the natural ratio of compressible to compressible plus solenoidal modes building up in the velocity field, which is 1:2 in 2D and 1:3 in 3D for solenoidally driven supersonic turbulent flows.

Chabrier (2008).

Given that many proposed sources of interstellar turbulence (e.g., Elmegreen & Scalo, 2004; Mac Low & Klessen, 2004) are likely to directly excite compressive modes (e.g., galactic spiral density shocks, large scale gravitational contraction, supernova explosions, protostellar jets, winds and outflows), it is reasonable to expect that turbulence in the ISM is driven by a mixture of solenoidal and compressive modes, possibly with compressive modes being more important than solenoidal modes.

Chapter 3

The fractal density structure in supersonic isothermal turbulence: solenoidal vs compressive energy injection

Here, I compare the density statistics in high resolution numerical experiments of supersonic isothermal turbulence, driven by the usually adopted solenoidal (divergence-free) forcing and by compressive (curl-free) forcing. We find that for the same RMS Mach number, compressive forcing produces much stronger density enhancements and larger voids compared to solenoidal forcing. Consequently, the Fourier spectra of density fluctuations are significantly steeper. This result is confirmed using the Δ-variance analysis, which yields power law exponents $\beta \sim 3.4$ for compressive forcing and $\beta \sim 2.8$ for solenoidal forcing. We obtain fractal dimension estimates from the density spectra and Δ-variance scaling, and by using the box counting, mass size and perimeter area methods applied to the volumetric data, projections and slices of our turbulent density fields. Our results suggest that compressive forcing yields fractal dimensions significantly smaller compared to solenoidal forcing. However, the actual values depend sensitively on the adopted method, with the most reliable estimates based on the Δ-variance, or equivalently, on Fourier spectra. Using these methods, we obtain $D \sim 2.3$ for compressive and $D \sim 2.6$ for solenoidal forcing, which is within the range of fractal dimension estimates inferred from observations ($D \sim 2.0 \ldots 2.7$). The velocity dispersion to size relations for both solenoidal and compressive forcing obtained from velocity spectra follow a power law with exponents in the range $0.4 \ldots 0.5$, in good agreement with previous studies. The results presented in this Chapter are published in Federrath et al. (2009).

3.1 Introduction

Observations provide velocity dispersion to size relations for various molecular clouds (MCs), which document the existence of supersonic random motions on scales larger than ~ 0.1 pc (e.g., Larson, 1981; Myers, 1983; Perault et al., 1986; Solomon et al., 1987; Falgarone et al., 1992; Heyer & Brunt, 2004). These motions are associated with compressible turbulence (e.g., Elmegreen & Scalo, 2004; Scalo & Elmegreen, 2004; Mac Low & Klessen, 2004) in the interstellar medium (Ferrière, 2001) and exhibit a single turbulent cascade or spatially separated coexisting inertial ranges (Passot et al., 1988) similar to the kinetic energy cascade of incompressible Kolmogorov (1941) turbulence. However, there are various physical processes (e.g., self-gravity, magnetic fields, non-equilibrium chemistry) and especially the compressibility of the gas alter the scaling laws (e.g., Fleck, 1996) and statistics (e.g., intermittency corrections measured by Hily-Blant et al., 2008) established for incompressible turbulence.

The physical origin and characteristics of the turbulent fluctuations are still a matter of debate. To advance on the question of 'how is turbulence driven in the interstellar medium', we present results of high resolution numerical experiments of supersonic isothermal turbulence comparing two distinct and extreme ways of driving the turbulence in a systematic study: 1) solenoidal forcing (divergence-free or rotational forcing), and 2) compressive forcing (curl-free or dilatational forcing).

Various numerical and analytical studies have provided important insight into the statistics of supersonic isothermal turbulence (e.g., Porter et al., 1992b; Vázquez-Semadeni, 1994; Padoan et al., 1997; Passot & Vázquez-Semadeni, 1998; Stone et al., 1998; Mac Low, 1999; Klessen, 2000; Ostriker et al., 2001; Boldyrev et al., 2002; Li et al., 2003; Padoan et al., 2004b; Jappsen et al., 2005; Ballesteros-Paredes et al., 2006; Kritsuk et al., 2007; Lemaster & Stone, 2008). Most of these studies use purely solenoidal or weakly compressive kinetic energy injection mechanisms (forcing) to excite turbulent motions. In the present study, we aim at comparing the usual case of solenoidal (divergence-free) forcing with the case of fully compressive (curl-free) forcing. The actual way of turbulence production in real MCs is expected to be far more complex compared to what we can model with the present simulations, probably consisting of a convolution of various agents producing turbulence, and mixtures of solenoidal and compressive modes (e.g., Elmegreen & Scalo, 2004; Mac Low & Klessen, 2004). Here, we systematically investigate the extreme cases of purely solenoidal vs. purely compressive energy injection.

Analyzing the density correlation statistics and fractal structure obtained in our hydrodynamic simulations, we show that compressive forcing leads to significantly steeper density fluctuation spectra and consequently to fractal dimensions of the turbulent gas structures, that are significantly smaller compared to the usually adopted solenoidal forcing. We use Fourier analysis, Δ-variance analysis, structure functions, the fractal mass size, box counting, and perimeter area methods to obtain fractal dimension estimates. We apply the Δ-variance analysis to both our 3-dimensional data and to 2-dimensional projections, and the perimeter area method to projections and slices through the turbulent density structures supporting the result of a significantly smaller fractal dimension for compressive forcing compared to solenoidal forcing. Although compressive forcing yields significantly smaller fractal dimensions than solenoidal forcing, the estimated fractal dimensions are in the range $2.0 \ldots 2.7$ consistent with observational estimates (e.g., Elmegreen & Falgarone, 1996; Sánchez et al., 2007)

We explain our numerical method, construction of solenoidal and compressive forcing fields and fractal analysis techniques in Section 3.2. In Section 3.3, we show that our results are consistent with previous studies using solenoidal forcing, whereas compressive forcing yields much stronger density contrasts and consequently leads to significantly smaller fractal dimensions. In Section 3.4, we summarize our conclusions.

3.2 Simulations and methods

The piecewise parabolic method (Colella & Woodward, 1984) implementation of the astrophysical code FLASH v3 (Fryxell et al., 2000; Dubey et al., 2008) was used to integrate the hydrodynamic equations on periodic uniform grids with 256^3, 512^3 and 1024^3 grid points. Density ρ, velocity $\mathbf{v}$ and pressure P are related through the equations

$$\frac{\partial \rho}{\partial t} + \nabla \cdot (\rho \mathbf{v}) = 0 \tag{3.1}$$

$$\frac{\partial \mathbf{v}}{\partial t} + (\mathbf{v} \cdot \nabla)\mathbf{v} = -\frac{1}{\rho}\nabla P + \mathbf{f} \, . \tag{3.2}$$

Note that an energy equation is not needed, because we model isothermal gas. The pressure is simply given by $P = c_s^2 \rho$ with the constant sound speed c_s. Isothermality is a very crude, but reasonable first approximation for modeling the thermodynamic behavior of MCs (Wolfire et al., 1995; Pavlovski et al., 2006). Due to the isothermal approximation, the hydrodynamic equations are scale free, and we can solve them for a chosen density scale $\rho_0 = 1$ (mean density), sound speed $c_s = 1$ and domain size $L = 1$. The only remaining free parameter therefore is the dimensionless RMS Mach number $\mathcal{M}$, which can be varied. It is important to note that the forcing term $\mathbf{f}$ used to drive turbulent motions appearing as source term in equation (3.2) can also be varied. In the present study, we vary the forcing term, investigating the difference between purely solenoidal and purely compressive kinetic energy injection, while keeping the RMS Mach number fixed.

Equations (3.1) and (3.2) have been solved numerically with periodic boundary conditions using an isothermal equation of state in the context of MC dynamics in various studies (e.g., Padoan et al., 1997; Passot & Vázquez-Semadeni, 1998; Stone et al., 1998; Mac Low et al., 1998; Mac Low, 1999; Klessen et al., 2000; Heitsch et al., 2001; Boldyrev et al., 2002; Li et al., 2003; Padoan et al., 2004b; Jappsen et al., 2005; Ballesteros-Paredes et al., 2006; Kritsuk et al., 2007; Dib et al., 2008; Offner et al., 2008). We aim at comparing turbulence statistics obtained in our study with the results of these studies. In particular, we want to check the influence of different forcing. Therefore, we concentrate on two extreme cases: 1) the usually adopted solenoidal forcing (divergence-free forcing) and 2) fully compressive forcing (curl-free forcing).

3.2.1 Forcing module

Turbulent fluctuations have to be excited and maintained in order to study stationary turbulence statistics in detail. If not constantly driven by a random force field, turbulent motions damp due to dissipation. In most studies, the force field is constructed in Fourier space by a 3-dimensional stochastic procedure (e.g., Dubinski et al., 1995; Mac Low et al., 1998; Stone et al., 1998), which generates a random vector field $\mathbf{f}$ after Fourier transformation back into physical space. This field will on average contain 2/3 of its energy in solenoidal modes (transversal modes) and 1/3 in compressive modes (longitudinal modes), because in 3-dimensional space, waves have two spatial directions for the transversal part, whereas the longitudinal part has only one (see, e.g., Elmegreen & Scalo, 2004). In order to obtain a purely solenoidal, or a purely compressive forcing field $\mathbf{f}$, a Helmholtz decomposition can be made by applying the projection operator $\mathcal{P}_{ij}^{\zeta}$ in Fourier space (k-space)

$$\mathcal{P}_{ij}^{\zeta} = \zeta \mathcal{P}_{ij}^{\perp} + (1-\zeta)\mathcal{P}_{ij}^{\parallel} = \zeta \delta_{ij} + (1-2\zeta)\frac{k_i k_j}{|k|^2} \tag{3.3}$$

prior to the inverse Fourier transformation into real space. By setting the parameter $\zeta \in [0,1]$ one can adjust the mixture of solenoidal and compressive modes. If we set $\zeta = 1$, $\mathcal{P}_{ij}^{\zeta}$ projects only the solenoidal component, whereas only the compressive component is obtained by setting $\zeta = 0$.

The forcing term $\mathbf{f}$ is typically either modeled as a spatially static pattern with time-dependent amplitude (following the recipes, e.g., by Mac Low et al., 1998; Stone et al., 1998) or by using an Ornstein-Uhlenbeck (OU) process (e.g., Eswaran & Pope, 1988; Schmidt et al., 2006), which modulates the pattern smoothly in space and time on a well-defined autocorrelation timescale T resulting in a constant energy input rate. We follow the usual approach and set the autocorrelation timescale equal to the dynamical timescale $T = L/(2V)$, where L is the size of the computational domain, $V = c_s\mathcal{M}$ and $\mathcal{M} \approx 5.5$ is the RMS Mach number in all runs. Therefore, T is the time for the most energetic fluctuations (at $k = 2$ in Fourier space, which corresponds to $L/2$) to cross half of the box. It is furthermore equal to the decay time constant of the turbulence (Stone et al., 1998; Mac Low, 1999). The forcing amplitude follows a parabolic power spectrum

only containing power on the largest scales in a small interval of wave numbers $1 < k < 3$ peaking at $k = 2$. The influence of varying the scale of energy input has been investigated for instance by Mac Low (1999), Klessen et al. (2000), Heitsch et al. (2001) and Vázquez-Semadeni et al. (2003). Here, we only consider the usually applied large scale stochastic forcing. This way of forcing models the kinetic energy input from larger scale turbulent fluctuations breaking up into smaller structures and feeding kinetic energy to smaller scales.

We checked that our results are not sensitive to the particular method for generating turbulent motions, i.e., by using an almost static pattern (using a very large autocorrelation time in the OU process), and by using a band spectrum instead of a parabolic Fourier spectrum for forcing. Variations in the spectral form of the large scale forcing did not significantly change the results obtained in the present study. However, changing the mixture of modes from a purely solenoidal to a purely compressive forcing always yielded significant differences.

3.2.2 Initial conditions and post processing

Starting from a uniform density distribution and zero velocity, the forcing excites turbulent motions. The forcing amplitude is adjusted to excite turbulence with RMS Mach number $\mathcal{M} \sim 5.5$. We use $\mathcal{M}$ as the control parameter, because this dimensionless number is often expected to solely determine physical properties of scale-invariant turbulent flows. The purpose of the present study was to determine the effect of varying the forcing from purely solenoidal to purely compressive, so we keep the RMS Mach number fixed besides all other parameters and varied only the forcing between solenoidal and compressive.

Equations (3.1) and (3.2) were evolved for 10 dynamical timescales T, which allows us to study a large sample of statistically stationary realizations of the turbulent flow. We wait for two dynamical timescales before averaging all statistical measures in the time interval $2 \leq t/T \leq 10$. Since we have produced snapshots every $0.1\,T$, the resulting statistical sample consists of 81 realizations of the turbulent field. The averaging procedure is important to derive meaningful statistics, because all quantities are subject to statistical fluctuations (e.g., Kritsuk et al., 2007). The averaging procedure furthermore provides a handle on the 1-sigma temporal fluctuations between different realizations. Unless otherwise stated, the 1-sigma temporal fluctuations are indicated as error bars in the results section.

3.2.3 Box counting method

We analyzed fractal structures in our simulation data using the box counting method. In the first step, the fractal structure is defined by marking all cells belonging to the fractal set, if they are above a certain density threshold, whereas all cells below that threshold are marked as not belonging to the fractal structure. In the second step, the structure as defined above was scanned by applying a box (mask) of size l and counting how often the structure is covered by that box. This procedure was repeated varying the size of the box resulting in a set of counts N_i and box sizes l_i. A plot of $\log(N_i)$ against $\log(l_i)$ often reveals a scaling range over which the points fall close to a straight line with the box counting dimension D_b as the negative slope of that line (e.g., Mandelbrot & Frame, 2002; Peitgen et al., 2004). This implies a power law scaling $N(l) \propto l^{-D_b}$ in the scaling range.

Setting the density threshold $\rho_{\rm th}$ for defining the fractal structure is obviously a critical choice. Using $\rho_{\rm th} = 0$ naturally results in $D_b = 3$, whereas setting $\rho_{\rm th} = \rho_{\rm max}$ leads to $D_b = 0$. We computed the box counting dimension for different density thresholds and discuss its influence on the results.

3.2.4 Mass size method

The fractal mass size dimension was obtained by computing the mass contained inside concentric boxes with increasing box size l centered on the densest cells of the dataset and averaging over cells with $\rho > \rho_{\max}/2$, following the method described by Kritsuk et al. (2007). This yields a set of masses M_i and box sizes l_i. A plot of $\log(M_i)$ against $\log(l_i)$ often reveals a scaling range over which the points fall close to a straight line with the mass size dimension D_m as the slope of that line (e.g., Mandelbrot & Frame, 2002; Peitgen et al., 2004). This implies a power law scaling $M(l) \propto l^{D_m}$ in the scaling range.

Power law relations of the form $M(l) \propto l^a$ should be considered with caution in the context of fractals, because such relations often occur in physics and do not necessarily imply that a is a fractal dimension, i.e., for a 3-dimensional density distribution, $a > 3$ can occur (see Mandelbrot, 1983; Elmegreen & Falgarone, 1996).

3.2.5 Perimeter area method

We also applied the perimeter area method, which is frequently applied for measuring the fractal dimension of interstellar gas clouds. The boundary curves and areas of coherent structures with equal density were identified in both, 2-dimensional projections and 2-dimensional slices through the computational domain. Varying the density threshold yields a set of structures with perimeters $\mathcal{P}_i$ and areas $\mathcal{A}_i$. Fitting a power law of the form $\mathcal{P} \propto \mathcal{A}^{D_p/2}$ (log-log plot as for the box counting and mass size dimensions) yields the perimeter area dimension D_p. Structures with very smooth boundary curves exhibit $D_p = 1$, whereas for structures with totally convoluted perimeters, $\mathcal{P}$ grows linearly with the area occupied by the structure resulting in $D_p = 2$.

3.3 Results and discussion

3.3.1 Time evolution

Figure 3.1 compares projections (top panels) and slices (bottom panels) of the density field in the x-y-plane from a randomly picked snapshot ($t = 5\,T$) for solenoidal vs. compressive forcing as an example of the typical density structure in the state of statistically stationary supersonic turbulent flow. This regime was safely reached after 2 dynamical times T, which is demonstrated in Figure 3.2. The RMS Mach number has settled to $\mathcal{M} \sim 5.5$ for both solenoidal and compressive forcing, and for numerical resolutions of 256^3, 512^3 and 1024^3 grid points after 2 dynamical times. Not only the velocity statistics has converged to a stationary state, but also the density statistics, which is shown in terms of minimum and maximum density in the top panel of Figure 3.2. Obviously, compressive forcing produces larger density contrasts, which results in higher density peaks and larger voids. Although both cases exhibit the same RMS Mach number, the solenoidally driven case gives a much smoother density distribution with smaller dispersion. In both cases, the maximum density is subject to strong intermittent fluctuations (e.g., Falgarone et al., 1994; Kritsuk et al., 2007) leading to temporal variations in the maximum density of order one magnitude.

3.3.2 Fourier spectrum functions

We begin the analysis of spatial correlations by showing 1-dimensional Fourier spectra derived for solenoidal and compressive forcing. Figure 3.3 presents a comparison of velocity Fourier spectra

$$E(k)\,dk = \frac{1}{2}\int \widehat{\mathbf{v}} \cdot \widehat{\mathbf{v}}^*\, 4\pi k^2 dk \tag{3.4}$$

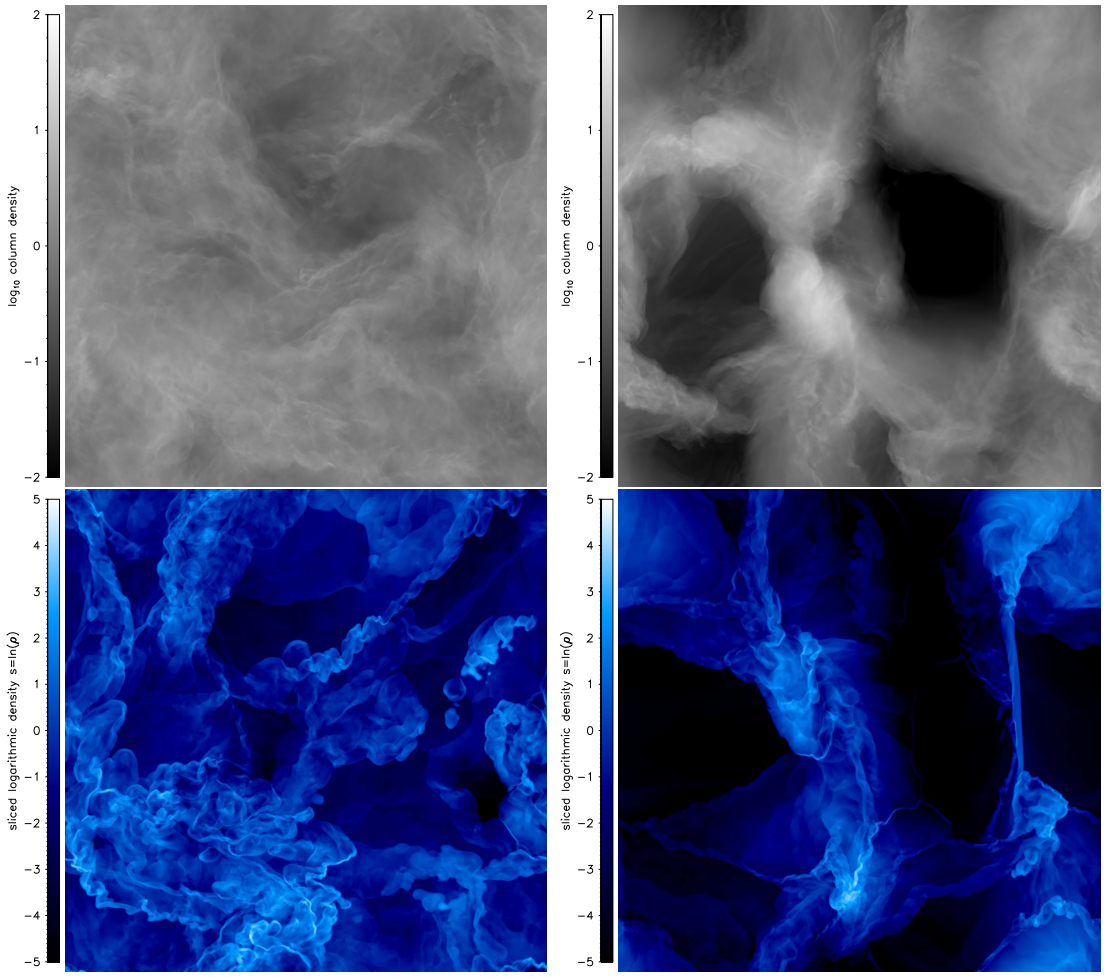

Figure 3.1: *Top panels:* Column density computed along the z-axis in units of the mean column density for solenoidal forcing (*left*), and compressive forcing (*right*) at a randomly picked time $t = 5\,T$ in the regime of statistically stationary compressible turbulence. Both maps show 4 orders of magnitude in column density with the same scaling for direct comparison of solenoidal and compressive forcing at RMS Mach number ~ 5.5. *Bottom panels:* Same as top panels, but slices through the density field at $z = 0$. Compressive forcing yields stronger density enhancements and larger voids compared to solenoidal forcing.

and density fluctuation Fourier spectra

$$P(k)\,dk = \int (\widehat{\rho - \rho_0})(\widehat{\rho - \rho_0})^* \, 4\pi k^2 dk\,. \tag{3.5}$$

These were computed with the standard method (e.g., Frisch, 1995), i.e., by integration over spherical shells in Fourier space using the Fourier transformed velocity components $\widehat{v_i}(k)$ and the Fourier transformed density fluctuations $\widehat{\rho - \rho_0}(k)$, where ρ_0 denotes the mean density. Velocity Fourier spectra $E(k)$ are typically used to distinguish between Kolmogorov (1941) turbulence, $E(k) \propto k^{-5/3}$ and Burgers turbulence, $E(k) \propto k^{-2}$ in the inertial range. For highly compressible isothermal supersonic turbulent flow, it has been shown that the inertial range scaling is closer to Burgers turbulence. For instance, Kritsuk et al. (2007) find $E(k) \propto k^{-1.95}$ and Schmidt

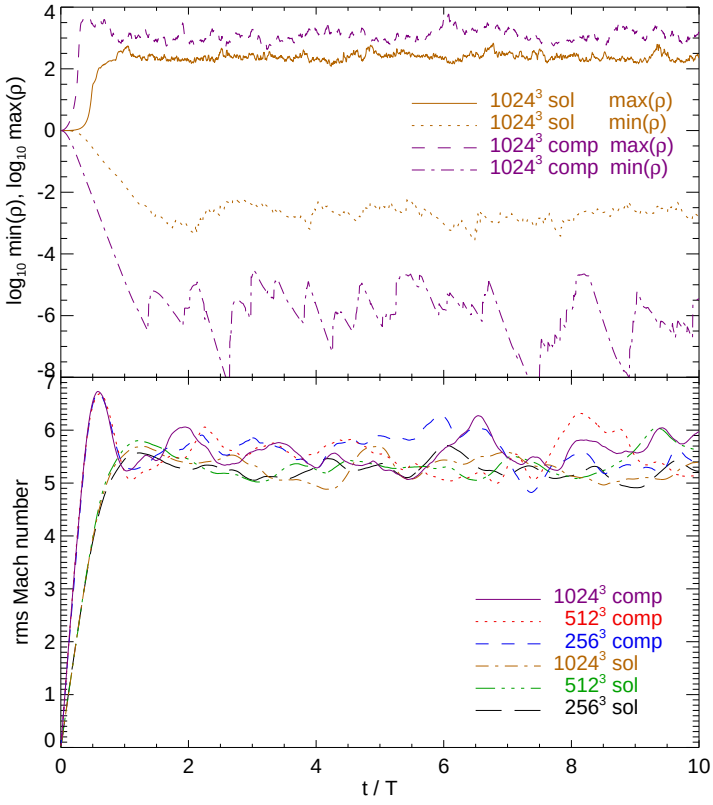

Figure 3.2: *Bottom*: RMS Mach number $\mathcal{M}$ as function of the dynamical time T for 256^3, 512^3 and 1024^3 numerical grid resolution. *Top*: Minimum and maximum density as function of the dynamical time T. At $\sim 2\,T$, a statistically stationary state was reached for both solenoidal (sol) and compressive (comp) forcing. Consequently, we can use all the available 81 snapshots within $2 \leq t/T \leq 10$ for averaging statistical measures (e.g., Fourier spectra, structure functions, Δ-variance, fractal perimeter area, box counting and mass size analysis) to improve statistical significance and to compute corresponding 1-sigma temporal fluctuations. Note that on average, the maximum density is almost ~ 10 times larger for compressive forcing compared to solenoidal forcing, although the RMS Mach number is roughly the same in both cases. The maximum density is subject to strongly intermittent fluctuations (e.g., Kritsuk et al., 2007) for both solenoidal and compressive forcing.

et al. (2009) measured $E(k) \propto k^{-1.87}$. In the present study, we obtain $E(k) \propto k^{-1.94}$ for compressive forcing, slightly steeper than $E(k) \propto k^{-1.86}$ for solenoidal forcing. Taking the error bars (temporal variations) into account, this represents just marginal difference between both forcing schemes, and our estimates within the inertial range are consistent with Kritsuk et al. (2007) and Schmidt et al. (2009). Table 3.1 summarizes all results obtained for solenoidal and compressive forcing providing the formal least-squares fitting errors, which were obtained by taking into account the 1-sigma temporal fluctuations. Table 3.1 furthermore provides a summary of defining relations for the following fractal dimension estimates.

Note that similar to Kritsuk et al. (2007) and Schmidt et al. (2009), we define our inertial range in a very small range of wavenumbers $5 \lesssim k \lesssim 15$ because even at numerical resolutions of 1024^3 grid points, the inertial range is very small (see, e.g., Klein et al., 2007) due to the bottleneck effect (e.g., Dobler et al., 2003; Haugen & Brandenburg, 2004; Schmidt et al., 2006; Kritsuk et al., 2007), which affects the Fourier spectrum in the dissipation range. For our simulations, we

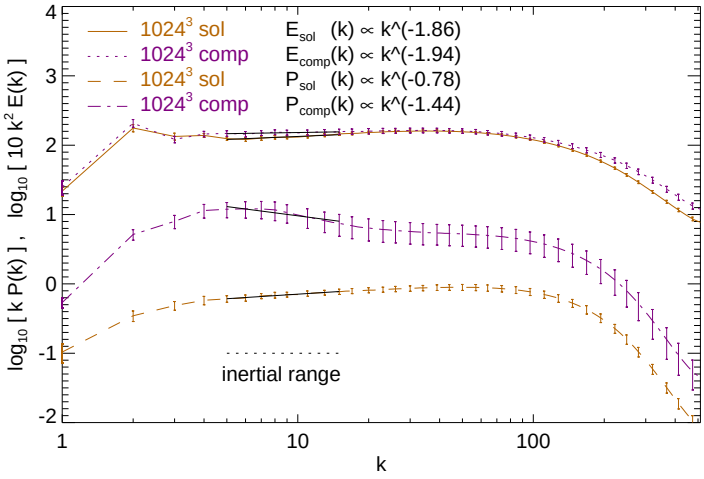

Figure 3.3: Kinetic energy Fourier spectra $E(k)$ compensated by k^2 corresponding to Burgers turbulence (upper curves), and density fluctuation Fourier spectra compensated by k (lower curves) for solenoidal and compressive forcing respectively. Power law fits in the inertial range $5 \lesssim k \lesssim 15$ are shown as thin solid lines. The velocity power spectra exhibit only marginal differences between solenoidal and compressive forcing. The scaling of the density power spectra on the other hand differs significantly comparing both forcings. Accordingly, the stepper density power spectrum for compressive forcing leads to a smaller fractal box coverage dimension $D_b \sim 2.28$ compared to $D_b \sim 2.61$ for solenoidal forcing.

estimate that wavenumbers $k \gtrsim 20$ are affected by the bottleneck. The influence of the bottleneck effect is less pronounced in physical space, which allows for a somewhat larger fitting range for scaling estimates obtained in physical space (similar to, e.g., Kowal & Lazarian, 2007; Kritsuk et al., 2007; Schmidt et al., 2009) for the Δ-variance analysis in Section 3.3.3.

The density fluctuation spectra in Figure 3.3 show considerable differences in their amplitude and inertial range scaling for solenoidal and compressive forcing. First, we discuss the difference in the amplitudes. As discussed in Federrath et al. (2008b), the standard deviation of the density probability distribution function (PDF) is ~ 3 times larger for compressive forcing compared to solenoidal forcing. This result is recovered in the present analysis by integrating the density fluctuation spectra

$$\sigma_\rho^2 = \sum_{i=1}^{n} (\rho_i - \rho_0)^2 = \int P(k)\, dk\,, \tag{3.6}$$

where $n = 1024^3$ is the number of grid points, which yields the standard deviation σ_ρ. For solenoidal forcing, we compute $\int P(k) dk \sim 1.89$, whereas for compressive forcing, $\int P(k) dk \sim 5.93$, in very good agreement with the standard deviations $\sigma_\rho \sim 1.89$ and $\sigma_\rho \sim 5.86$ obtained from the PDFs in Federrath et al. (2008b).

Second, the inertial range scaling differs significantly for the two cases. For solenoidal forcing, $P(k) \propto k^{-0.78}$ and for compressive forcing, $P(k) \propto k^{-1.44}$. Our inertial range scaling inferred for solenoidal forcing is consistent with the weakly magnetized super-Alfvénic supersonic MHD models from Kowal et al. (2007, Tab. 2) using solenoidal forcing. Kowal et al. (2007) find $P(k) \propto k^{-0.6\pm0.2}$ for their model B.1P.01 with very weak magnetic field, slightly larger RMS Mach number ($\mathcal{M} \sim 7.1$), and resolution[1] of 256^3 explaining the small differences comparing their result with ours. It is furthermore in agreement with the purely hydrodynamic estimates

[1]The resolution dependence for our simulations is discussed in Section 3.3.3.

	symbol	relation	solenoidal	compressive
1D power law index for velocity Fourier spectra	ϵ	$E_{1\mathrm{D}}(k) \propto k^{-\epsilon}$	$1.86^{\pm 0.05}$	$1.94^{\pm 0.05}$
1D power law index for density fluctuation Fourier spectra	α	$P_{1\mathrm{D}}(k) \propto k^{-\alpha}$	$0.78^{\pm 0.06}$	$1.44^{\pm 0.23}$
3D power law index for density fluctuation Fourier spectra	β	$P_{3\mathrm{D}}(k) \propto k^{-\beta} \propto k^{-(\alpha+2)}$	$2.78^{\pm 0.06}$	$3.44^{\pm 0.23}$
derived Hurst exponent	H	$H = (\beta - 2)/2$	$0.39^{\pm 0.03}$	$0.72^{\pm 0.12}$
box counting dimension	D_b	$D_b = 3 - H$	$2.61^{\pm 0.03}$	$2.28^{\pm 0.12}$
perimeter area dimension	D_p	$D_p = 2 - H$	$1.61^{\pm 0.03}$	$1.28^{\pm 0.12}$
power law index for Δ-variance applied to 3D data	$\tilde{\beta}$	$\sigma^2_\Delta(l) \propto l^{\tilde{\beta}-2}$, $\tilde{\beta} \approx \beta$	$2.89^{\pm 0.05}$	$3.44^{\pm 0.19}$
derived Hurst exponent	H	$H = (\tilde{\beta} - 2)/2$	$0.45^{\pm 0.03}$	$0.72^{\pm 0.10}$
box counting dimension	D_b	$D_b = 3 - H$	$2.55^{\pm 0.03}$	$2.28^{\pm 0.10}$
perimeter area dimension	D_p	$D_p = 2 - H$	$1.55^{\pm 0.03}$	$1.28^{\pm 0.10}$
power law index for Δ-variance applied to 2D projections	$\hat{\beta}$	$\sigma^2_\Delta(l) \propto l^{\hat{\beta}-2}$, $\hat{\beta} \approx \beta$	$2.81^{\pm 0.07}$	$3.37^{\pm 0.21}$
derived Hurst exponent	H	$H = (\hat{\beta} - 2)/2$	$0.41^{\pm 0.04}$	$0.69^{\pm 0.11}$
box counting dimension	D_b	$D_b = 3 - H$	$2.59^{\pm 0.04}$	$2.31^{\pm 0.11}$
perimeter area dimension	D_p	$D_p = 2 - H$	$1.59^{\pm 0.04}$	$1.31^{\pm 0.11}$
power law index of 2nd order density structure function	η	$\mathrm{SF}_2(l) \propto l^\eta \propto l^{\alpha-1}$; $1 < \alpha < 3$	$0.24^{\pm 0.03}$	$0.47^{\pm 0.09}$
mass size method averaged over density peaks with $\rho > \rho_{\max}/2$	D_m	$M(l) \propto l^{D_m}$	$2.11^{\pm 0.16}$	$2.03^{\pm 0.26}$
box counting dimension with ρ_0 as defining threshold	D_b	$N(l) \propto l^{-D_b}$	$2.68^{\pm 0.04}$	$2.51^{\pm 0.08}$
box counting dimension with σ_ρ as defining threshold	$\tilde{D}_b$	$N(l) \propto l^{-\tilde{D}_b}$	$2.51^{\pm 0.05}$	$2.32^{\pm 0.10}$
perimeter area dimension for 2D projections	D_p	$\mathcal{P}(\mathcal{A}) \propto \mathcal{A}^{D_p/2}$	$1.36^{\pm 0.09}$	$1.18^{\pm 0.10}$
perimeter area dimension for 2D slices	$\tilde{D}_p$	$\mathcal{P}(\mathcal{A}) \propto \mathcal{A}^{\tilde{D}_p/2}$	$1.43^{\pm 0.09}$	$1.28^{\pm 0.11}$

Table 3.1: Power law exponents and fractal dimension estimates comparing solenoidal and compressive forcing

by Kritsuk et al. (2006) with resolutions up to 2048^3 using adaptive mesh refinement, who obtain $P(k) \propto k^{-0.8...0.9}$.

Note that in general, the power law exponents α of 1-dimensional Fourier spectra are related to the power law exponents β of the corresponding 3-dimensional Fourier power spectra through $\beta = \alpha + 2$. As discussed by Stutzki et al. (1998), the power law scaling of the density spectrum is furthermore related to the fractal drift exponent H (Hurst exponent). Considering a 1-dimensional density power spectrum $P(k) \propto k^{-\alpha}$ leads to a Hurst exponent of $H = \alpha/2 = (\beta - 2)/2$. The Hurst exponent is related to the fractal box coverage dimension $D_b = E + 1 - H$ with the dimensionality $E = 2$ for the box coverage of a fractal surface embedded in 3-dimensional space (Stutzki et al., 1998). Consequently, we obtain $H \sim 0.39$ and $D_b \sim 2.61$ for solenoidal forcing, and $H \sim 0.72$ and $D_b \sim 2.28$ for compressive forcing. Thus, the fractal Hurst exponent is significantly smaller for compressive forcing. The estimates for the Hurst exponents and the corresponding relations with box counting and perimeter area dimensions are summarized in Table 3.1.

3.3.3 Δ-variance analysis

In this section, we present results of the Δ-variance method, which provides an independent measure of the scaling of the density Fourier spectra. Stutzki et al. (1998) introduced a wavelet transformation called Δ-variance for measuring the exponent of the Fourier spectrum. As complementary analysis, we performed the Δ-variance with the tool developed and provided by Ossenkopf et al. (2008a). It is an improved version of the original Δ-variance (Stutzki et al., 1998; Bensch et al., 2001). The Δ-variance measures the amount of structure on a given length scale l, filtering the dataset $\Phi(\mathbf{x})$ by applying an up-down-function $\bigodot_l$ (typically a French-hat or Mexican-hat filter) of size l and computing the variance of the filtered dataset. The Δ-variance is defined as

$$\sigma^2_\Delta(l) = \left\langle \left(\Phi(\mathbf{x}) * \bigodot_l (\mathbf{x}) \right)^2 \right\rangle_{\mathbf{x}} , \tag{3.7}$$

where the average is computed over all valid datapoints at positions $\mathbf{x}$, and the operator $*$ stands for the convolution. The dataset can have arbitrary dimensionality. In the present study, we apply the Δ-variance to both, 2-dimensional (projections) and 3-dimensional datasets. We checked the influence of varying the filter function from French-hat to Mexican-hat, as well as varying the diameter ratio of the filter, which yielded no significant differences. The choice of the filter function and the best choice for its diameter ratio is discussed by Ossenkopf et al. (2008a). Here, we use the original French-hat filter with a diameter ratio of 3.0 as it has been used before (e.g., Stutzki et al., 1998; Mac Low & Ossenkopf, 2000; Ossenkopf et al., 2001; Ossenkopf & Mac Low, 2002; Ossenkopf et al., 2006). Note that originally, Stutzki et al. (1998) applied the Δ-variance to 2-dimensional integrated maps for comparison with observations. Although we have access to the 3-dimensional data from our simulations, we nevertheless computed column density maps and applied the Δ-variance to both the 2-dimensional and 3-dimensional data to determine the effect of projection for applying the Δ-variance. Prior to the 3-dimensional analysis, we resampled the density datacubes with 1024^3 grid points to a resolution of 256^3 due to performance issues of the Δ-variance, which is not (yet) a parallelized tool. The resampling to lower resolution is not expected to cause deviations in the inertial range scaling. As long as the simulation itself had enough spatial resolution to resolve the inertial range scaling, the resampling to lower resolution only affects the dissipation range leaving density spectra almost up to the new Nyquist frequency (e.g., Padoan et al., 2006). We explicitly show in the bottom panel of Figure 3.4 that the resampling indeed did not affect the inertial range. Only the compressive forcing case is shown but the resampling for the solenoidal case exhibits similar behavior.

The upper panel of Figure 3.4 shows the influence of varying the numerical resolution of the simulation. The inertial range scaling depends on the numerical resolution. A resolution of 256^3 grid points seems insufficient to resolve the *exact* inertial range scaling, although the 15% difference compared to the 1024^3 simulation is of the order of the temporal fluctuations, whereas the difference between solenoidal and compressive forcing (Fig. 3.3) is significant. At resolutions of 512^3 and 1024^3 grid points, the best fit power law scaling agrees quite well, indicating almost numerical convergence. A similar conclusion can be drawn from the density Fourier spectra presented by Kritsuk et al. (2006, Fig. 4) computed for solenoidal forcing.

The results of the Δ-variance are presented in Figure 3.5. In the top panel, we show the Δ-variance applied to the 3-dimensional data resampled to 256^3 grid cells, whereas the bottom panel presents the Δ-variance applied to projections averaged along all three spatial axis. The variation for different projections is almost negligible compared to the temporal fluctuations. We nevertheless added the variation due to projection along the three different axis to the 1-sigma error bars due to temporal fluctuations. Following Stutzki et al. (1998), the values of the best fit power law exponents β are shown corresponding to the 3-dimensional Fourier spectra. Note that the slope α fitted to the Δ-variance is related to the slope of the 3-dimensional Fourier spectrum by $\beta = \alpha + E$, where $E = 2$ for the projected data and $E = 3$ for the 3-dimensional

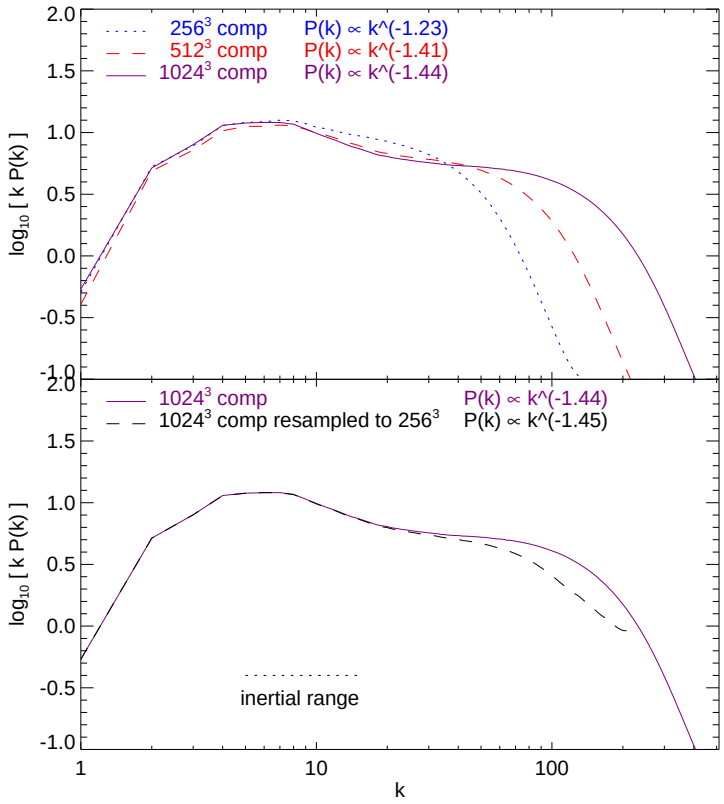

Figure 3.4: *Top panel:* Numerical resolution comparison of density fluctuation Fourier spectra for compressive forcing. At 512^3 and 1024^3, the spectra are almost converged with resolution, whereas the 256^3 run deviates by $\sim$15%. *Bottom panel*: Density fluctuation Fourier spectra at 1024^3 in comparison with its resampled version to 256^3 cells. The resampling had virtually no influence on our results within the inertial range.

data resulting in the same power law exponent β. As shown by Stutzki et al. (1998), the power law scaling of the Fourier spectrum should be preserved at projection to lower dimensions. In agreement with the results by Mac Low & Ossenkopf (2000), we find that the slopes $\beta \sim 2.89$ (3D) and $\beta \sim 2.81$ (2D projection) for solenoidal forcing, and $\beta \sim 3.44$ (3D) and $\beta \sim 3.37$ (2D projection) for compressive forcing are almost preserved during projection (see Table 3.1).

We can furthermore check whether the Δ-variance results agree with the Fourier power spectra, since the Δ-variance is supposed to measure the power law exponent of the Fourier spectrum. As shown in Figure 3.3, the density spectra exhibit power laws in the inertial range corresponding to 3-dimensional Fourier power law exponents $\beta = \alpha + 2 = 2.78$ for solenoidal and $\beta = 3.44$ for compressive forcing in consistency with the Δ-variance. Therefore, the Δ-variance confirms the results obtained by the density Fourier spectra, showing that compressive forcing yields a systematically steeper density spectrum compared to solenoidal forcing.

3.3.4 Structure functions

Besides the Fourier spectra and the Δ-variance analyzed in the previous sections, structure functions are often used to measure spatial correlations in turbulent velocity and density fields

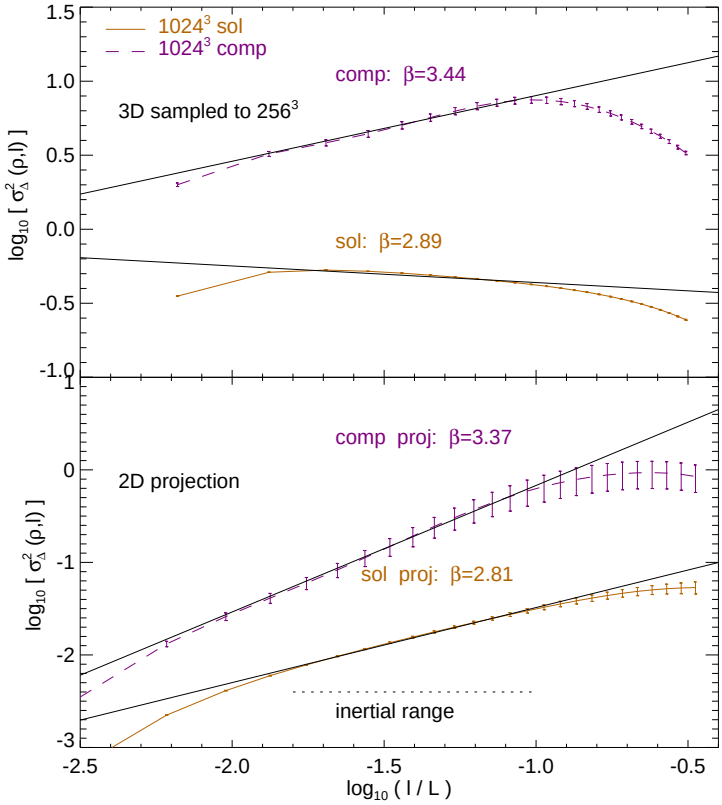

Figure 3.5: *Top panel:* Δ-variance analysis for the 3-dimensional dataset resampled to a resolution of 256^3 grid cells. *Bottom panel:* Δ-variance applied to the 2-dimensional projections of the 1024^3 dataset. As shown by Stutzki et al. (1998), the power law scaling within the inertial range is preserved upon projection and agrees with the scaling of the Fourier power spectra of Figure 3.3 within the uncertainties from temporal fluctuations (see Tab. 3.1).

(e.g., Boldyrev et al., 2002; Padoan et al., 2003; Esquivel & Lazarian, 2005; Kritsuk et al., 2007; Schmidt et al., 2009; Hily-Blant et al., 2008). Here, we restrict our analysis to the 2nd order structure functions of the density field for comparison with the Fourier spectra and Δ-variances. The 2nd order structure function of the density is defined as

$$\mathrm{SF}_2(l) = \left\langle \left|\rho(\mathbf{x}) - \rho(\mathbf{x}+\mathbf{l})\right|^2 \right\rangle_{\mathbf{x}} . \tag{3.8}$$

Figure 3.6 presents the 2nd order density structure functions for compressive and solenoidal forcing respectively. In the following, we draw the connection of these structure functions to the power spectra and Δ-variance. One feature of the structure function is its relation to the autocorrelation function $A(l)$ (Stutzki et al., 1998):

$$\mathrm{SF}_2(l) = 2\left[A(0) - A(l)\right] = 2\left[\sigma^2 - A(l)\right] . \tag{3.9}$$

Since the autocorrelation function vanishes on large scales close to our periodic box size ($l \to L$), the 2nd order structure function of a variable can be used to measure the standard deviation σ of this variable because $\mathrm{SF}_2(l \to L) = 2\sigma^2$. In our case, we obtained the standard deviations of the density $\sigma_\rho \sim 1.88$ for solenoidal and $\sigma_\rho \sim 5.95$ for compressive forcing simply by evaluating

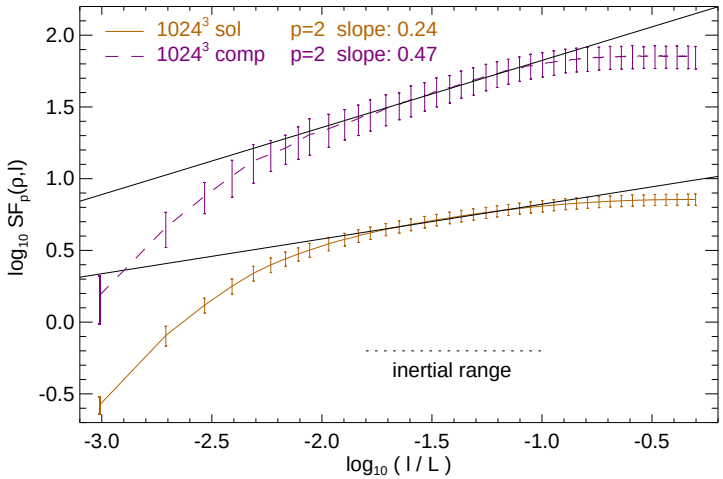

Figure 3.6: Second order structure functions of the density ρ for solenoidal and compressive forcing. The absolute values of the structure functions are in agreement with the measures of the power spectra and PDFs. The inertial range scaling, however, agrees with the Fourier spectra for compressive forcing only. Solenoidal forcing exhibits a density Fourier spectrum with power law exponent $\alpha < 1$ (Fig. 3.3), which precludes the determination of the power law exponent via structure function analysis (Stutzki et al., 1998, Appendix B).

$\sigma_\rho = [0.5\,\mathrm{SF}_2(l = 0.5\,L)]^{1/2}$ from Figure 3.6. Note that for periodic boxes, the maximum length scale for measuring spatial correlations is half of the box size L. As for the power spectra, this is in good agreement with the independent analysis of the density PDFs (Federrath et al., 2008b).

The best fit values of power law exponents $\mathrm{SF}_2(l) \propto l^\eta$ of the structure functions in the inertial range are indicated in Figure 3.6 as well. Since $\mathrm{SF}_2(l) \propto l^\eta$ is the Fourier transform of the 1-dimensional Fourier spectrum $P(k) \propto k^{-\alpha}$, it follows that $\alpha = \eta + 1$. For compressive forcing, the power law scaling is in agreement with the Δ-variance and Fourier spectra estimates. The corresponding value for the 3-dimensional density power spectrum derived from the structure function is $\beta = \alpha + 2 = \eta + 3 \sim 3.47$ (see Table 3.1). For solenoidal forcing on the other hand, the best fit value derived from the structure functions is ~ 3.24 is in significant disagreement with the estimates from the Fourier spectra and Δ-variance ($\beta \sim 2.8$). Stutzki et al. (1998) provide the mathematical explanation for this. For a power law scaling of Fourier spectrum functions with power law exponent $\beta < E$ (here $E = 3$), i.e. $\alpha < 1$, the E-dimensional two-point correlation function (structure function) does not necessarily increase in a power law fashion (Stutzki et al., 1998, Appendix B). This limits the applicability of structure functions for estimating the inertial range scaling to density Fourier power law exponents $E < \beta < E + 2$.

3.3.5 Mass size method

Figure 3.7 shows the results obtained by applying the mass size method as described in Section 3.2.4. In rough agreement with the results of the methods discussed so far, compressive forcing yields a smaller mass size exponent $D_m \sim 2.03$ compared to solenoidal forcing with $D_m \sim 2.11$ in the inertial range (Table 3.1). Unlike the other methods, however, this difference is not significant. The large 1-sigma error is a direct consequence of the strong temporal fluctuations of the maximum density seen in Figure 3.2. Since the mass size relation $M(l)$ is computed by growing concentric boxes centered on density peaks with $\rho > \rho_{\max}/2$, the mass is expected to fluctuate strongly, following the temporal fluctuations of the density peaks. Our results are

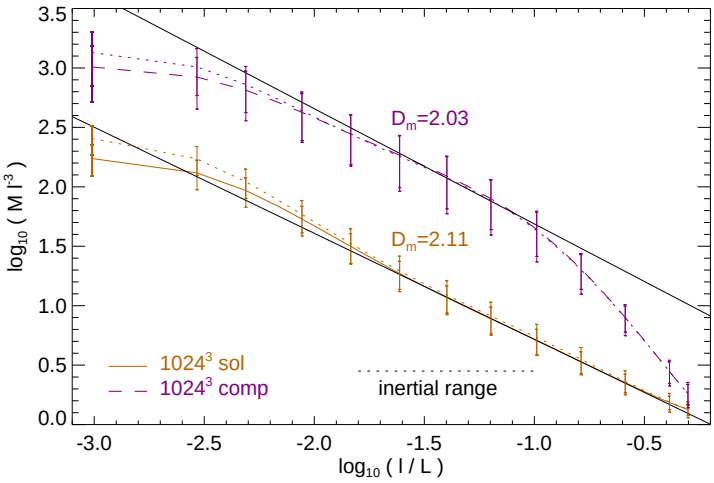

Figure 3.7: Log-log plot of the mass $M(l)$ compensated by l^{-3} obtained by the mass size method described in Section 3.2.4 for solenoidal and compressive forcing. As in Kowal & Lazarian (2007), a horizontal strait line therefore corresponds to a fractal mass dimension $D_m = 3$. Power law fits in the inertial range yield a fractal mass dimension $D_m \sim 2.11$ for solenoidal forcing and $D_m \sim 2.03$ for compressive forcing. However, the difference between solenoidal and compressive forcing inferred from the mass size method is not significant due to the large uncertainties (error bars). These large uncertainties are a result of the strong temporal fluctuations of the maximum density (Fig. 3.2), since the mass size method relies on the density peaks, i.e., all cells with density $\rho > \rho_{\max}/2$ are used as a basis for computing the mass size relation $M(l)$. The dotted lines show $M\,l^{-3}$ using $\rho_{\max}$ only, i.e., without averaging over cells with $\rho > \rho_{\max}/2$. There is a systematic decrease of $M(l)$ with decreasing averaging threshold, which does not affect the inertial range scaling as long as the averaging is performed over all cells with $\rho > \rho_{\max}/2$.

therefore roughly consistent with the mass size analysis by Kowal & Lazarian (2007) and Kritsuk et al. (2007).

3.3.6 Box counting method

The results of the analysis using the box counting method as explained in Section 3.2.3 are presented in Figure 3.8. In this case, the fractal structure was defined by the mean density $\rho_0 = 1$ as threshold density for both solenoidal and compressive forcing. The analyzed structure as defined by ρ_0 is shown in Figure 3.9. We obtain the box counting dimensions $D_b \sim 2.68$ for solenoidal, and $D_b \sim 2.51$ for compressive forcing in the inertial range (Table 3.1). As discussed in Section 3.2.3, the box counting dimension depends on the threshold for defining the fractal structure. We have checked its dependence on the threshold $\rho_{\rm th}$ by varying $\tau \equiv \log_{10}(\rho_{\rm th}/\rho_0)$. The results obtained by computing the box counting dimension for $\tau = -1, 0, 1, 2$ are shown in Figure 3.10 for solenoidal forcing (left panel) and compressive forcing (right panel). Note that $\tau = 0$ corresponds to the mean density as defining threshold. As expected, the box dimension strongly depends on $\rho_{\rm th}$. Significant differences between solenoidal and compressive forcing are obtained for different threshold densities. For thresholds $\tau \gtrsim 0$, the box dimension is smaller for solenoidal forcing than for compressive forcing in contrast to $\tau \lesssim 0$. This is as a consequence of the much more space filling density structure for the solenoidal case (see Fig. 3.1). For instance, at $\tau = 2$ the solenoidal case yields point like structure with small fractal box dimension ($D_b \sim 0.72$), while the structures in the compressive case are still coherent presumably elongated structures

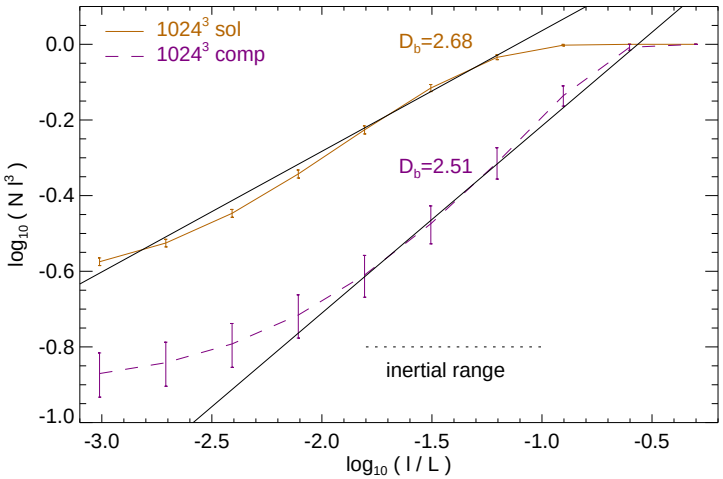

Figure 3.8: Log-log plot of $N(l)$ compensated with l^3 obtained by the box counting analysis described in Section 3.2.3 for solenoidal and compressive forcing respectively. A horizontal strait line would correspond to a box dimension of $D_b = 3$. The power law exponents D_b obtained from fits within the inertial range are drawn as strait lines. Compressive forcing yields a significantly smaller box dimension $D_b \sim 2.51$ compared to solenoidal forcing ($D_b \sim 2.68$).

with larger fractal dimension ($D_b \sim 1.63$). Obtaining absolute estimates for the fractal dimension using the box counting method in the present context is consequently impossible. However, differences among different datasets, e.g., solenoidal vs. compressive forcing can be measured with the box counting method, if the same defining density threshold is used.

3.3.7 Perimeter area method

In this section, we show results of the perimeter area method described in Section 3.2.5. This method is often applied to observational datasets to infer the fractal dimension of interstellar clouds. Although we are aware of the fact that our simulations can only provide a very limited approximation to real interstellar gas, we nevertheless are convinced that comparison with observational data will provide physical insight. The perimeters of interstellar gas clouds exhibit fractal dimensions in the range $D_p \sim 1.2 \ldots 1.6$ (e.g., Beech, 1987; Bazell & Desert, 1988; Dickman et al., 1990; Falgarone et al., 1991; Vogelaar et al., 1991; Hetem & Lepine, 1993; Vogelaar & Wakker, 1994; Westpfahl et al., 1999; Kim et al., 2003; Lee, 2004; Sánchez et al., 2007) with most of the studies finding $D_p \sim 1.3 \ldots 1.4$. These results are always obtained from projected images. A plausible conversion to the 3-dimensional fractal dimension, $D \sim D_p + 1$ is discussed by Beech (1992). However, this relation holds rigorously only for the analysis of slices through an isotropic 3-dimensional monofractal, while interstellar clouds could be multifractals (e.g., Chappell & Scalo, 2001). As discussed by Stutzki et al. (1998) and shown by Sánchez et al. (2005), $D_p + 1$ can be different from the 3-dimensional fractal dimension for projected images.

We applied the perimeter area method to projections along the x-, y- and z-axis, as well as to slices at $x = 0$, $y = 0$ and $z = 0$ of our simulation data cubes. The results are presented in Figure 3.11 for the projections (top panel) and the slices (bottom panel). Best fit power laws to the projected data yield $D_p \sim 1.36$ for solenoidal forcing and $D_p \sim 1.18$ for compressive forcing, whereas for the slices we find $D_p \sim 1.43$ and $D_p \sim 1.28$, respectively. Thus, we find that the projections yield perimeter area dimensions systematically smaller than the slices for both

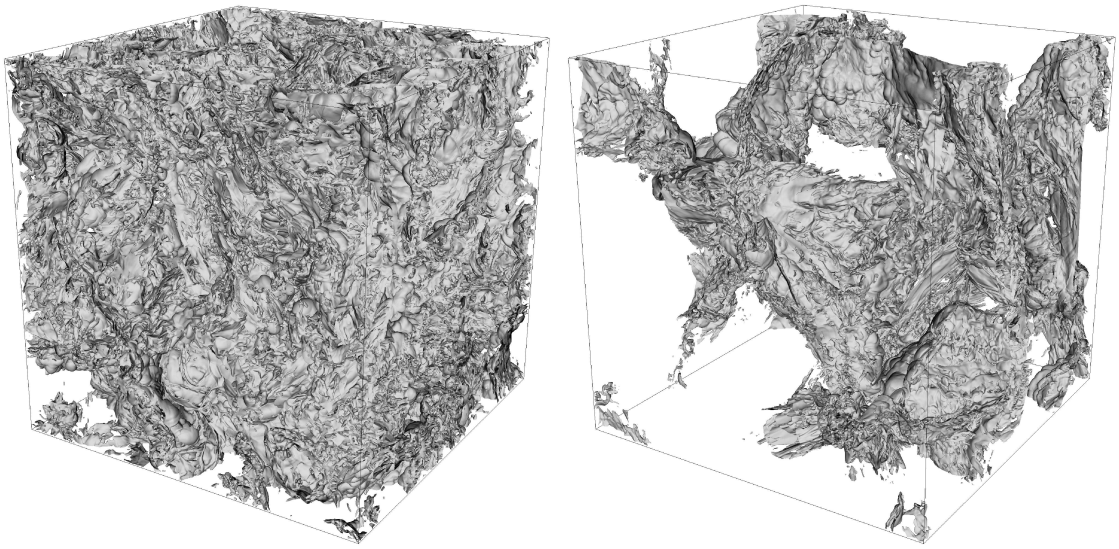

Figure 3.9: Isosurface plots of the fractal structure defined by the mean density for solenoidal (*left*) and compressive forcing (*right*). The presence of hierarchical visual complexity indicates a fractal structure that can be analyzed with the box counting method (Mandelbrot & Frame, 2002).

forcings (Table 3.1). In agreement with the results obtained from the density Fourier spectra and the Δ-variance analysis, the perimeter area method yields a significantly smaller perimeter area dimension for compressive forcing compared to solenoidal forcing.

3.4 Conclusions

We have presented results of two high resolution (1024^3 grid cells) hydrodynamic simulations of supersonic isothermal turbulence driven to RMS Mach numbers $\mathcal{M} \sim 5.5$. The first simulation uses the typically adopted solenoidal (divergence-free) forcing to excite turbulent motions, whereas the second one uses compressive (curl-free) forcing. We have shown that compressive forcing yields much stronger density contrasts compared to solenoidal forcing for the same RMS Mach number. This implies that the turbulence production mechanism leaves a strong imprint on compressible turbulence statistics, especially altering the density statistics. Our results particularly suggests that the mixture of solenoidal and compressive modes of the turbulence forcing must be taken into account. We summarize our results as follows:

- The velocity Fourier spectra exhibit power laws in the inertial range for solenoidal and compressive forcing. The slopes obtained for both forcings are significantly steeper ($\sim$1.9) compared to the Kolmogorov slope (5/3), in agreement with previous studies (e.g., Kritsuk et al., 2007; Schmidt et al., 2009) and in agreement with velocity dispersion to size relations inferred from observations (e.g., Larson, 1981; Falgarone et al., 1992; Heyer & Brunt, 2004; Padoan et al., 2006).

- From the integral of the density fluctuation Fourier spectra and from the asymptotic behavior of the 2nd order density structure function, we obtained the standard deviation of the density distribution σ_ρ. Compressive forcing yields a standard deviation ~ 3 times larger compared to solenoidal forcing, in agreement with the results found in our previous study analyzing density probability distribution functions (Federrath et al., 2008b) and in

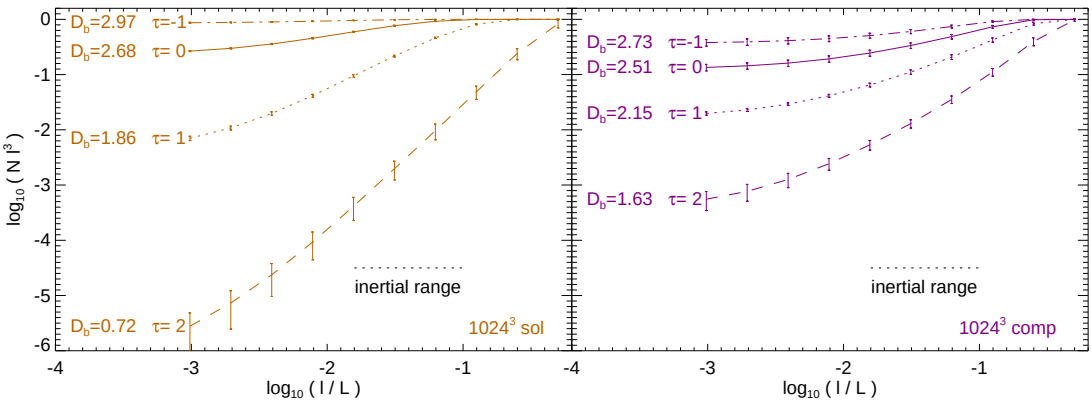

Figure 3.10: Shows the dependence of the box counting dimension on the threshold density $\rho_{\rm th}$ defining the fractal structure. Computing the fractal box counting dimension for $\tau \equiv \log_{10}(\rho_{\rm th}/\rho_0) = -1,\, 0,\, 1,\, 2$ reveals the strong dependence of the inferred fractal dimension on the defining density threshold. *Left panel:* solenoidal forcing; *Right panel:* compressive forcing.

agreement with the studies by Passot & Vázquez-Semadeni (1998), Kritsuk et al. (2007), Beetz et al. (2008) and Schmidt et al. (2009).

- The density fluctuation Fourier spectra are significantly steeper for compressive forcing in the inertial range compared to solenoidal forcing. Consistent results were obtained using complementary analysis methods, i.e., by comparing the Δ-variances (Ossenkopf et al., 2008a) and the 2nd order structure functions of the density field. Our estimates of density spectra for solenoidal forcing are in agreement with previous studies, e.g., the weakly magnetized super-Alfvénic supersonic MHD models by Padoan et al. (2004a) and Kowal et al. (2007), and consistent with the hydrodynamic estimates by Kritsuk et al. (2006). Although a comparison with observational results must be regarded with caution due to systematic uncertainties, our results for solenoidal and compressive forcing are in the range of inferred scaling exponents by observations (e.g., Bensch et al., 2001).

- From the scaling of the density fluctuation Fourier spectra and the Δ-variance applied to the 3-dimensional data and applied to 2-dimensional projections, we obtained fractal Hurst exponents following the analysis by Stutzki et al. (1998). This implies fractal box counting and fractal perimeter area dimensions significantly smaller for compressive forcing compared to solenoidal forcing (see Table 3.1).

- We analyzed the density structure using the fractal mass size method as introduced by Kritsuk et al. (2007). Compressive forcing yields a smaller fractal mass dimension compared to solenoidal forcing. The mass size method is, however, particularly sensitive to the temporal fluctuations of density peaks. Given the large uncertainties, our results using this method are roughly consistent with the estimates by Kritsuk et al. (2007) and Kowal & Lazarian (2007).

- We analyzed the fractal density structure using the box counting method described in Section 3.2.3 and the perimeter area method (Section 3.2.5) applied to projections and slices. We recover the significant differences between solenoidal and compressive forcing inferred from the density spectra and Δ-variance analysis. However, the box counting dimension varies strongly with the defining density threshold. The perimeter area dimensions obtained

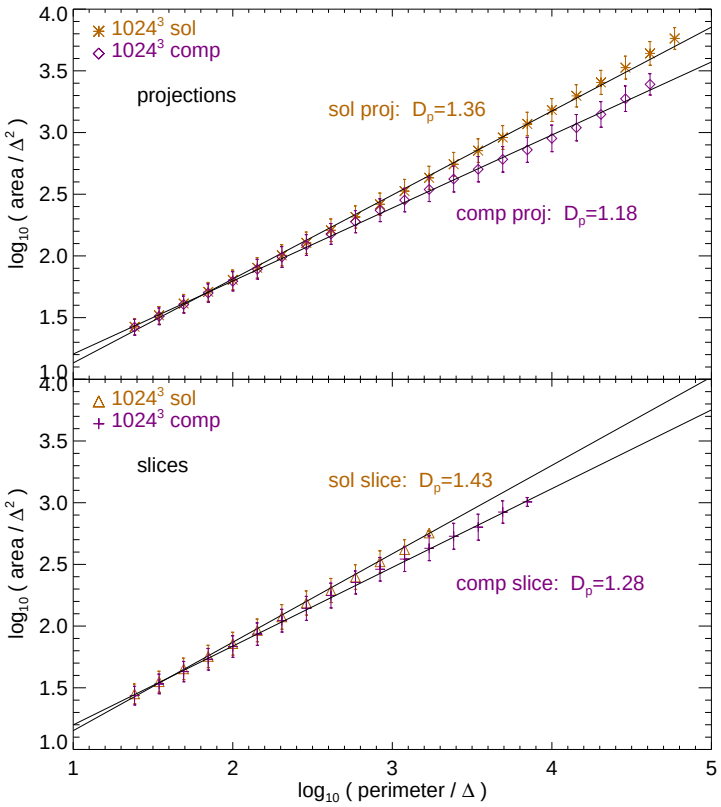

Figure 3.11: *Top panel:* Perimeter area method applied to projections along x, y and z for solenoidal and compressive forcing respectively. *Bottom panel:* Same as top panel but for slices at $x = 0$, $y = 0$ and $z = 0$. The perimeter is given in units of the numerical cell size $\Delta = L/1024$.

from slices are roughly consistent with the computed perimeter area dimensions from the Δ-variance given the systematic uncertainties (probably of order ~ 0.1 for fractal dimension estimates) comparing different methods. The range of fractal dimensions obtained is consistent with the observations analyzed by Elmegreen & Falgarone (1996) suggesting an overall fractal dimension of interstellar clouds in the range $D \sim 2.3 \pm 0.3$.

Chapter 4

Comparing the statistics of interstellar turbulence in simulations and observations: solenoidal vs compressive turbulence forcing

In addition to the high-resolution comparison of solenoidal and compressive forcing presented in the two previous Chapters, I here analyze eleven lower-resolution models with different forcing mixtures. Using Fourier spectra and Δ-variance, we find velocity dispersion–size relations consistent with observations and independent numerical simulations, irrespective of the type of forcing. However, compressive forcing yields stronger compression at the same RMS Mach number than solenoidal forcing, resulting in a three times larger standard deviation of volumetric and column density probability distributions (PDFs). We compare our results to different characterizations of several observed regions, and find evidence of different forcing functions. Column density PDFs in the Perseus MC suggest the presence of a mainly compressive forcing agent within a shell, driven by a massive star. Although the PDFs are close to log-normal, they have non-Gaussian skewness and kurtosis caused by intermittency. Centroid velocity increments measured in the Polaris Flare on intermediate scales agree with solenoidal forcing on that scale. However, Δ-variance analysis of the column density in the Polaris Flare suggests that turbulence is driven on large scales, with a significant compressive component on the forcing scale. This indicates that, although likely driven with mostly compressive modes on large scales, turbulence can behave like solenoidal turbulence on smaller scales. Principal component analysis of G216-2.5 and most of the Rosette MC agree with solenoidal forcing, but the interior of an ionized shell within the Rosette MC displays clear signatures of compressive forcing. The strong dependence of the density PDF on the type of forcing must be taken into account in any theory using the PDF to predict properties of star formation. We supply a quantitative description of this dependence. We find that different observed regions show evidence of different mixtures of compressive and solenoidal forcing, with more compressive forcing occurring primarily in swept-up shells. Finally, we emphasize the role of the sonic scale for protostellar core formation, because core formation close to the sonic scale would naturally explain the observed subsonic velocity dispersions of protostellar cores. The results presented in this Chapter are published in Federrath et al. (2010b).

4.1 Introduction

Studying the density and velocity distributions of interstellar gas provides essential information about virtually all physical processes relevant to the dynamical evolution of the interstellar medium (ISM). Along with gravity, magnetic fields and the thermodynamics of the gas, super-

sonic turbulence plays a fundamental role in determining the density and velocity statistics of the ISM (e.g., Scalo et al., 1998). Thus, supersonic turbulence is considered a key process for star formation (Mac Low & Klessen, 2004; Elmegreen & Scalo, 2004; Scalo & Elmegreen, 2004; McKee & Ostriker, 2007).

In this Chapter, we continue our analysis of the density probability distribution function (PDF) obtained in numerical experiments of driven supersonic isothermal turbulence. Understanding the density PDF and its turbulent origin is essential, because it is a key ingredient for analytical models of star formation: The turbulent density PDF is used to explain the stellar initial mass function (Padoan & Nordlund, 2002; Hennebelle & Chabrier, 2008, 2009), the star formation rate (Krumholz & McKee, 2005; Krumholz et al., 2009; Padoan & Nordlund, 2009), the star formation efficiency (Elmegreen, 2008), and the Kennicutt-Schmidt relation on galactic scales (Elmegreen, 2002; Kravtsov, 2003; Tassis, 2007). In Federrath et al. (2008b), we found that supersonic turbulence driven by a purely compressive (curl-free) force field yields a density PDF with roughly three times larger standard deviation compared to solenoidal (divergence-free) turbulence forcing, which strongly affects the results obtained in these analytical models. Here, we want to compare our results for the density PDF to observations of column density PDFs (e.g., Goodman et al., 2009).

Moreover, in Federrath et al. (2009) we investigated the fractal density distribution of our two models with solenoidal and compressive turbulence forcing, which showed that compressive forcing yields a significantly lower fractal dimension ($D_\mathrm{f} \approx 2.3$) compared to solenoidal forcing ($D_\mathrm{f} \approx 2.6$). In the present contribution, we consider the scaling of centroid velocity increments computed for these models, and we compare them to observations of the Polaris Flare by Hily-Blant et al. (2008). We additionally used principal component analysis and compared our results to observations of the G216-2.5 (Maddalena's Cloud) and the Rosette MC by Heyer et al. (2006).

Our results indicate that interstellar turbulence is driven by mixtures of solenoidal and compressive forcing. The ratio between solenoidal and compressive modes of the turbulence forcing may vary strongly across different regions of the ISM. This provides an explanation for the apparent lack of correlation between turbulent density and velocity dispersions found in observations (e.g., Goodman et al., 2009; Pineda et al., 2008). We conclude that solenoidal forcing is more likely to be realized in quiescent regions with low star formation activity as in the Polaris Flare and in Maddalena's Cloud. On the other hand, in regions of enhanced stellar feedback, compressive forcing leads to larger standard deviations of the density PDFs, as seen in one of the subregions of the Perseus MC surrounding a central B star. Moreover, compressive forcing exhibits a higher scaling exponent of principal component analysis than solenoidal forcing. This higher scaling exponent is consistent with the measured scaling exponent for the interior of an ionizing shell in the Rosette MC.

In section 4.2, we explain the numerical setup and turbulence forcing used for the present study. We discuss our results obtained using PDFs, centroid velocity increments, principal component analysis, Fourier spectrum functions, and Δ-variance analyses in section 4.3, 4.4, 4.5, 4.6, and 4.7, respectively. In each of these sections, we compare the turbulence statistics obtained for solenoidal and compressive forcing with observational data available in the literature. In section 4.9, we discuss the possibility that transonic pre-stellar cores typically form close to the sonic scale in a globally supersonic, turbulent medium. Section 4.10 provides a list of the limitations in our comparison of numerical simulations with observations. A summary of our results and conclusions is given in section 4.11.

4.2 Simulations and methods

The piecewise parabolic method (Colella & Woodward, 1984), implemented in the astrophysical code FLASH v3 (Fryxell et al., 2000; Dubey et al., 2008) was used to integrate the equations

of hydrodynamics on three-dimensional (3D) periodic uniform grids with 256^3, 512^3, and 1024^3 grid points. Since isothermal gas is assumed throughout this study, it is convenient to define

$$s \equiv \ln \frac{\rho}{\langle\rho\rangle} \tag{4.1}$$

as the natural logarithm of the density divided by the mean density $\langle\rho\rangle$ in the system. For isothermal gas, the pressure, $P = \rho c_\mathrm{s}^2$, is proportional to the density ρ with the constant sound speed c_s. The equations of hydrodynamics solved here are consequently given by

$$\frac{\partial s}{\partial t} + (\mathbf{v}\cdot\nabla)s = -\nabla\cdot\mathbf{v} \tag{4.2}$$

$$\frac{\partial \mathbf{v}}{\partial t} + (\mathbf{v}\cdot\nabla)\mathbf{v} = -c_\mathrm{s}^2\,\nabla s + \mathbf{f}\,, \tag{4.3}$$

where $\mathbf{v}$ denotes the velocity of the gas. An energy equation is not needed, because the gas is isothermal. The assumption of isothermal gas is very crude, but may still provide an adequate physical approximation to the real thermodynamics in dense molecular gas (Wolfire et al., 1995; Pavlovski et al., 2006). We discuss further limitations of our simulations in section 4.10. The stochastic forcing term $\mathbf{f}$ is used to drive turbulent motions.

4.2.1 Forcing module

Equations (4.2) and (4.3) have been solved before in the context of molecular cloud dynamics, studying compressible turbulence with either solenoidal (divergence-free) forcing or with a 2:1 mixture of solenoidal to compressive modes in the turbulence forcing (e.g., Padoan et al., 1997; Stone et al., 1998; Mac Low et al., 1998; Mac Low, 1999; Klessen et al., 2000; Heitsch et al., 2001; Klessen, 2001; Boldyrev et al., 2002; Li et al., 2003; Padoan et al., 2004b; Jappsen et al., 2005; Ballesteros-Paredes et al., 2006; Kritsuk et al., 2007; Dib et al., 2008; Kissmann et al., 2008; Offner et al., 2008; Schmidt et al., 2009). The case of a 2:1 mixture of solenoidal to compressive modes is the natural result obtained for 3D forcing, if no Helmholtz decomposition (see below) is performed. Then, the solenoidal modes occupy two of the three available spatial dimensions on average, while the compressive modes only occupy one (Elmegreen & Scalo, 2004; Federrath et al., 2008b). In the present study, the solenoidal forcing case is thus also used as a control run for comparison with previous studies using solenoidal forcing. However, we additionally applied purely compressive (curl-free) forcing and analyzed the resulting turbulence statistics in detail. Each simulation at a resolution of 1024^3 grid cells consumed roughly 100 000 CPU hours. Therefore, we concentrated on two extreme cases of turbulence forcing with high resolution: (1) the widely adopted purely solenoidal forcing ($\nabla\cdot\mathbf{f} = 0$), and (2) purely compressive forcing ($\nabla\times\mathbf{f} = 0$). However, we also studied eleven simulations at numerical resolution of 256^3 in which we smoothly varied the forcing from purely solenoidal to purely compressive by producing eleven different forcing mixtures.

The forcing term $\mathbf{f}$ is often modeled with a spatially static pattern, for which the amplitude is adjusted in time following the methods introduced by Mac Low et al. (1998) and Stone et al. (1998). This results in a roughly constant energy input on large scales. Other studies model the random forcing term $\mathbf{f}$ such that it can vary in time *and* space (e.g., Padoan et al., 2004b; Kritsuk et al., 2007; Federrath et al., 2008b; Schmidt et al., 2009). Here, we used the Ornstein-Uhlenbeck (OU) process to model $\mathbf{f}$, which belongs to the latter type. The OU process is a well-defined stochastic process with a finite autocorrelation timescale. It can be used to excite turbulent motions in 3D, 2D, and 1D simulations as explained in Eswaran & Pope (1988) and Schmidt et al. (2006). Using an OU process enables us to control the autocorrelation timescale T of the forcing. The concept of using the OU process to excite turbulence and the projections in Fourier

space necessary to get solenoidal and compressive force fields are described below.

The OU process is a stochastic differential equation describing the evolution of the forcing term $\widehat{\mathbf{f}}$ in Fourier space (k-space):

$$\mathrm{d}\widehat{\mathbf{f}}\,(\mathbf{k},t) = f_0\,(\mathbf{k})\;\underline{\mathcal{P}}^{\zeta}(\mathbf{k})\;\mathrm{d}\mathbf{W}(t)\;-\;\widehat{\mathbf{f}}\,(\mathbf{k},t)\,\frac{\mathrm{d}t}{T}\;. \tag{4.4}$$

The first term on the right hand side is a diffusion term. This term is modeled using a Wiener process $\mathbf{W}(t)$, which adds a Gaussian random increment to the vector field given in the previous time step $\mathrm{d}t$. Wiener processes are random processes, such that

$$\mathbf{W}(t) - \mathbf{W}(t-\mathrm{d}t) = \mathbf{N}(0,\mathrm{d}t)\;, \tag{4.5}$$

where $\mathbf{N}(0,\mathrm{d}t)$ denotes the 3D, 2D, or 1D version of a Gaussian distribution with zero mean and standard deviation $\mathrm{d}t$. This is followed by a projection with the projection tensor $\underline{\mathcal{P}}^{\zeta}(\mathbf{k})$ in Fourier space. In index notation, the projection operator reads

$$\mathcal{P}^{\zeta}_{ij}\,(\mathbf{k}) = \zeta\,\mathcal{P}^{\perp}_{ij}\,(\mathbf{k}) + (1-\zeta)\,\mathcal{P}^{\parallel}_{ij}\,(\mathbf{k}) = \zeta\,\delta_{ij} + (1-2\zeta)\,\frac{k_i k_j}{|k|^2}\;, \tag{4.6}$$

where δ_{ij} is the Kronecker symbol, and $\mathcal{P}^{\perp}_{ij} = \delta_{ij} - k_i k_j/k^2$ and $\mathcal{P}^{\parallel}_{ij} = k_i k_j/k^2$ are the fully solenoidal and the fully compressive projection operators, respectively. The projection operator serves to construct a purely solenoidal force field by setting $\zeta = 1$. For $\zeta = 0$, a purely compressive force field is obtained. Any combination of solenoidal and compressive modes can be constructed by choosing $\zeta \in [0,1]$. By changing the parameter ζ, we can thus set the power of compressive modes with respect to the total power of the forcing. The analytical ratio of compressive power to total power can be derived from equation (4.6) by evaluating the norm of the compressive component of the projection tensor,

$$\left|(1-\zeta)\,\mathcal{P}^{\parallel}_{ij}\right|^2 = (1-\zeta)^2\;, \tag{4.7}$$

and by evaluating the norm of the full projection tensor

$$\left|\mathcal{P}^{\zeta}_{ij}\right|^2 = 1 - 2\zeta + D\zeta^2\;. \tag{4.8}$$

The result of the last equation depends on the dimensionality $D = 1, 2, 3$ of the forcing, because the norm of the Kronecker symbol $|\delta_{ij}| = 1$, 2 and 3 in one, two and three dimensions, respectively. The ratio of equations (4.7) and (4.8) gives the ratio of compressive forcing power F_{long} to the total forcing power F_{tot} as a function of the parameter ζ:

$$\frac{F_{\mathrm{long}}}{F_{\mathrm{tot}}} = \frac{(1-\zeta)^2}{1-2\zeta+D\zeta^2}\;. \tag{4.9}$$

Figure 4.1 provides a graphical representation of this ratio for the 1D, 2D, and 3D case. For comparison, we plot numerical values of the forcing ratio obtained in eleven 3D and 2D hydrodynamical runs with resolutions of 256^3 and 1024^2 grid points, in which we have varied the forcing parameter ζ from purely compressive forcing ($\zeta = 0$) to purely solenoidal forcing ($\zeta = 1$) in the range $\zeta = [0,1]$, separated by $\Delta\zeta = 0.1$. Note that a natural mixture of forcing modes is obtained for $\zeta = 0.5$, which leads to $F_{\mathrm{long}}/F_{\mathrm{tot}} = 1/3$ for 3D turbulence, and $F_{\mathrm{long}}/F_{\mathrm{tot}} = 1/2$ for 2D turbulence. A simple way to understand this natural ratio is to consider longitudinal and transverse waves. In 3D, the longitudinal waves occupy one of the three spatial dimensions, while the transverse waves occupy two of the three on average. Thus, the longitudinal (compressive)

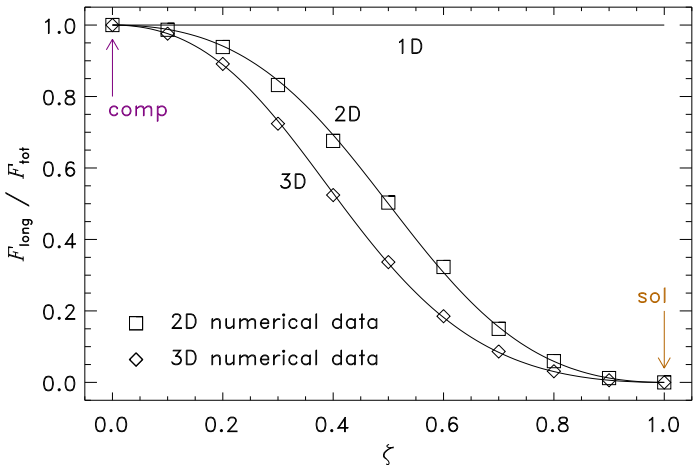

Figure 4.1: Ratio of compressive power to the total power in the turbulence force field. The solid lines labeled with 1D, 2D, and 3D show the analytical expectation for this ratio, equation (4.9), as a function of the forcing parameter ζ for one-, two- and three-dimensional forcing, respectively. The diamonds and squares show results of numerical simulations in 3D and 2D with $\zeta = [0, 1]$, separated by $\Delta\zeta = 0.1$. Those models were run at a numerical resolution of 256^3 and 1024^2 grid points in 3D and 2D, respectively. The two extreme forcing cases of purely solenoidal forcing ($\zeta = 1$) and purely compressive forcing ($\zeta = 0$) are indicated as "sol" and "comp", respectively. Note that in any 1D model, all power is in the compressive component, and thus $F_{\rm long}/F_{\rm tot} = 1$, independent of ζ.

part has a power of 1/3, while the transverse (solenoidal) part has a power of 2/3 in 3D. In 2D, the natural ratio is 1/2, because longitudinal and transverse waves are evenly distributed in two dimensions.

The second term on the right hand side of equation (4.4) is a drift term, which models the exponentially decaying correlation of the force field with itself. Thus, the autocorrelation timescale of the forcing is denoted by T. We set the autocorrelation timescale equal to the dynamical timescale $T = L/(2V)$ on the scale of energy injection, where L is the size of the computational domain, $V = c_{\rm s}\mathcal{M}$ and $\mathcal{M} \approx 5.5$ is the RMS Mach number in all runs. The autocorrelation timescale is therefore equal to the decay time constant in supersonic hydrodynamic and magnetohydrodynamic turbulence driven on large scales (Stone et al., 1998; Mac Low, 1999). The forcing amplitude $f_0(\mathbf{k})$ is a paraboloid in 3D Fourier space, only containing power on the largest scales in a small interval of wavenumbers $1 < |\mathbf{k}| < 3$ peaking at $k = 2$, which corresponds to half of the box size $L/2$. The effects of varying the scale of energy input were investigated by Mac Low (1999), Klessen et al. (2000), Heitsch et al. (2001) and Vázquez-Semadeni et al. (2003). Here, we consider large-scale stochastic forcing, which is closer to the observational data (e.g., Ossenkopf & Mac Low, 2002; Brunt et al., 2009). This type of forcing models the kinetic energy input from large-scale turbulent fluctuations, breaking up into smaller structures. Kinetic energy cascades down to smaller and smaller scales, and thereby effectively drives turbulent fluctuations on scales smaller than the turbulence injection scale.

We have verified that our results are not sensitive to the general approach of using an Ornstein-Uhlenbeck process for the turbulence forcing. For instance, we have used an almost static forcing pattern, which is obtained in the limit $T \to \infty$ in test simulations. We have furthermore checked that the particular choice of Fourier amplitudes did not affect our results by using a band spectrum instead of a parabolic forcing spectrum. Varying these parameters did not strongly affect our results. In contrast, changing ζ from $\zeta = 1$ (solenoidal forcing) to $\zeta = 0$ (compressive forcing)

always led to significant changes in the turbulence statistics.

4.2.2 Initial conditions and post-processing

Starting from a uniform density distribution and zero velocities, the forcing excites turbulent motions. Equations (4.2) and (4.3) have been evolved for ten dynamical times T, which allows us to study a large sample of realizations of the turbulent flow. Compressible turbulence reached a statistically invariant state within $2\,T$ (Federrath et al., 2009). This allows us to average all statistical measures over $8\,T$ separated by $0.1\,T$ in the fully developed regime. We are thus able to average over 81 different realizations of the turbulence to improve statistical significance. The 1-σ temporal fluctuations obtained from this averaging procedure are indicated as error bars for the PDFs, centroid velocity increments, principal component analysis, Fourier spectra and Δ-variance analyses in the following sections and in all figures showing error bars throughout this study. The forcing amplitude was adjusted to excite a turbulent flow with an RMS Mach number $\mathcal{M} \approx 5.5$ in all cases. We use the RMS Mach number as the control parameter, because this dimensionless number determines most of the physical properties of scale-invariant turbulent flows and is often used to derive important flow statistics such as the standard deviation of the density distribution. However, in the next section we show that the latter depends sensitively on the turbulence forcing parameter ζ as well.

Figure 4.2 (top panels) shows column density fields projected along the z-axis from a randomly selected snapshot at time $t = 2\,T$ in the regime of fully developed, statistically stationary turbulence for solenoidal (left) versus compressive forcing (right). This regime was reached after 2 dynamical times T, which is shown in Figure 4.3 for the minimum and maximum logarithmic densities s (top panel) and RMS curl and divergence of the velocity field (bottom panel) as a function of the dynamical time. It is evident that compressive forcing produces higher density contrasts, resulting in higher density peaks and bigger voids compared to solenoidal forcing.

4.3 The probability density function of the gas density

It is interesting to study the probability distribution of turbulent density fluctuations, because it is a key ingredient for many analytical models of star formation: it is used to explain the stellar initial mass function (Padoan & Nordlund, 2002; Hennebelle & Chabrier, 2008, 2009), the star formation rate (Krumholz & McKee, 2005; Krumholz et al., 2009; Padoan & Nordlund, 2009), the star formation efficiency (Elmegreen, 2008), and the Kennicutt-Schmidt relation on galactic scales (Elmegreen, 2002; Kravtsov, 2003; Tassis, 2007).

The probability to find a volume with gas density in the range $[\rho, \rho{+}\mathrm{d}\rho]$ is given by the integral over the volume-weighted probability density function (PDF) of the gas density: $\int_{\rho}^{\rho+\mathrm{d}\rho} p_\rho(\rho')\,\mathrm{d}\rho'$. Thus, the PDF p describes a *probability density*, which has dimensions of probability divided by gas density in the case of $p_\rho(\rho)$. By the same definition, $p_s(s)$ denotes the PDF of the logarithmic density $s = \ln(\rho/\langle\rho\rangle)$.

Figure 4.4 presents the comparison of the time-averaged volume-weighted density PDFs $p_s(s)$ obtained for solenoidal and compressive forcing. The linear plot of $p_s(s)$ (top panel) displays the peak best, whereas the logarithmic representation (bottom panel) reveals the low- and high-density wings of the distributions. Three different fits to analytic expressions (discussed below) are shown as well.

4.3.1 The density PDF for solenoidal forcing

In numerical experiments of driven supersonic isothermal turbulence with solenoidal and/or weakly compressive forcing (e.g., Vázquez-Semadeni, 1994; Padoan et al., 1997; Stone et al.,

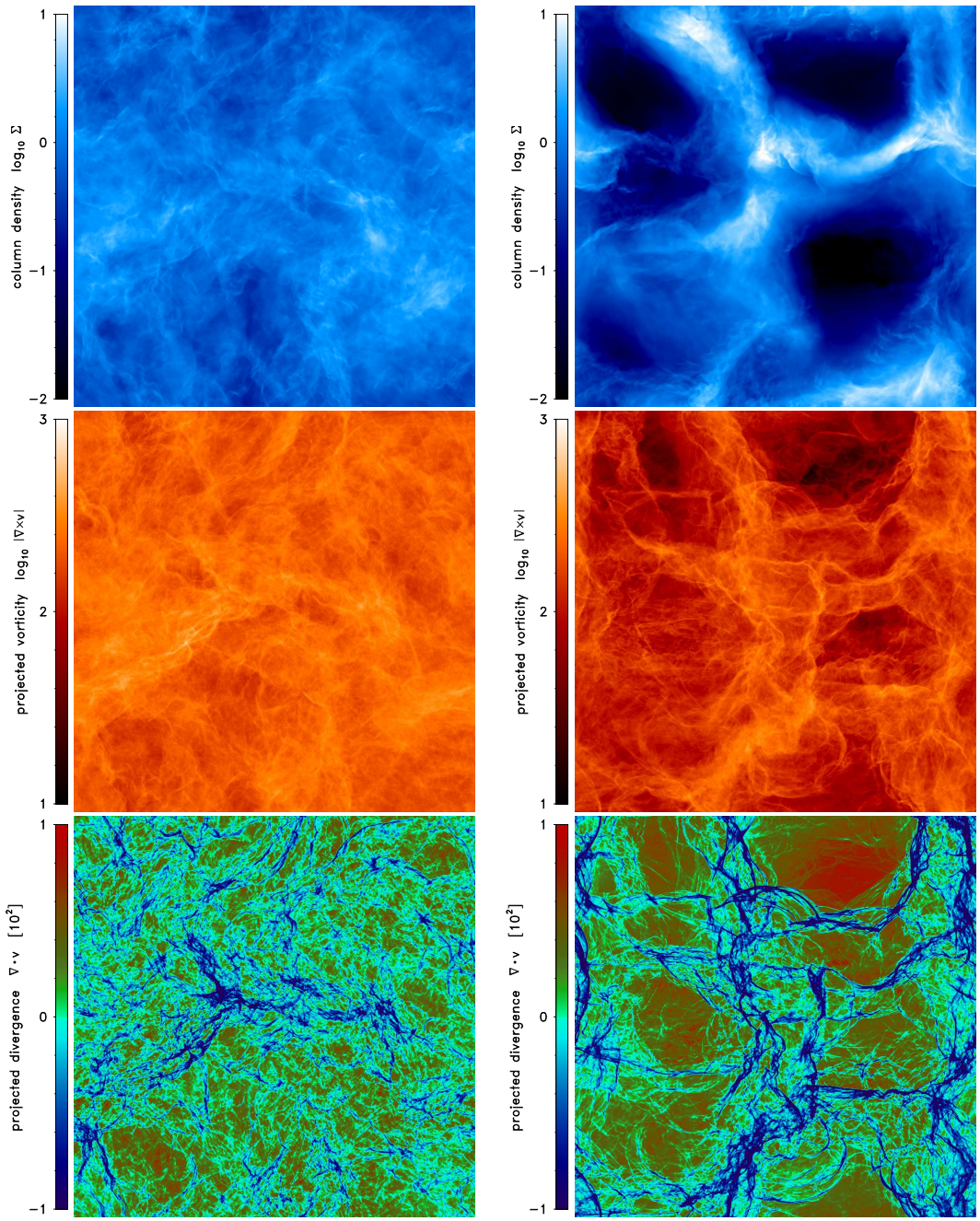

Figure 4.2: Maps showing density (*top*), vorticity (*middle*) and divergence (*bottom*) in projection along the z-axis at time $t = 2\,T$ as an example for the regime of statistically fully developed, compressible turbulence for solenoidal forcing (*left*) and compressive forcing (*right*). *Top panels:* Column density fields in units of the mean column density. Both maps show three orders of magnitude in column density with the same scaling and magnitudes for direct comparison. *Middle panels:* Projections of the modulus of the vorticity $|\nabla \times \mathbf{v}|$. Regions of intense vorticity appear to be elongated filamentary structures often coinciding with positions of intersecting shocks. *Bottom panels:* Projections of the divergence of the velocity field $\nabla \cdot \mathbf{v}$ showing the positions of shocks. Negative divergence corresponds to compression, while positive divergence corresponds to rarefaction.

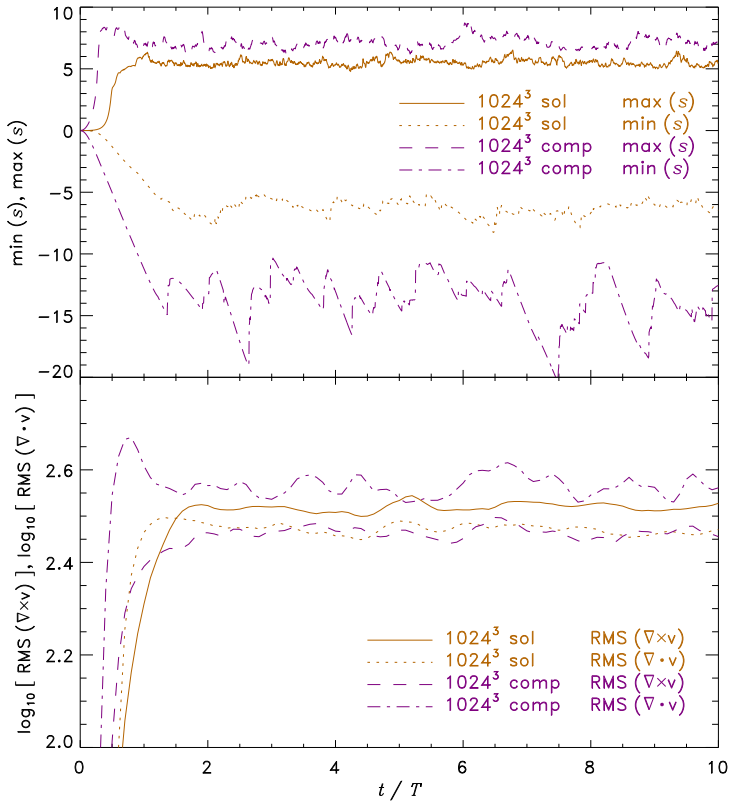

Figure 4.3: *Top panel*: Minimum and maximum logarithmic density $s = \ln(\rho/\langle\rho\rangle)$ as a function of the dynamical time T. Note that compressive forcing yields much stronger compression and rarefaction compared to solenoidal forcing, although the RMS Mach number is roughly the same in both cases (see Federrath et al., 2009, Fig. 2). *Bottom panel*: RMS vorticity $\langle(\nabla\times\mathbf{v})^2\rangle^{1/2}$ and RMS divergence $\langle(\nabla\cdot\mathbf{v})^2\rangle^{1/2}$ as a function of the dynamical time. Within the first $2\,T$, a statistically steady state was reached for both solenoidal (sol) and compressive (comp) forcing. This allows us to average statistical measures (probability density functions, centroid velocity increments, principal component analysis, Fourier spectra and Δ-variances) in the range $2 \leq t/T \leq 10$ to improve statistical significance of our results and to estimate the amplitude of temporal fluctuations (snapshot-to-snapshot variations) between different realizations of the turbulence.

1998; Mac Low, 1999; Nordlund & Padoan, 1999; Boldyrev et al., 2002; Li et al., 2003; Padoan et al., 2004b; Kritsuk et al., 2007; Beetz et al., 2008), but also in decaying turbulence (e.g., Ostriker et al., 1999; Klessen, 2000; Ostriker et al., 2001; Glover & Mac Low, 2007b) it was shown that the density PDF p_s is close to a log-normal distribution,

$$p_s\,\mathrm{d}s = \frac{1}{\sqrt{2\pi\sigma_s^2}}\,\exp\left[-\frac{(s-\langle s\rangle)^2}{2\sigma_s^2}\right]\mathrm{d}s\,, \tag{4.10}$$

where the mean $\langle s \rangle$ is related to the standard deviation σ_s by $\langle s \rangle = -\sigma_s^2/2$ due to the constraint of mass conservation (e.g., Vázquez-Semadeni, 1994):

$$\int_{-\infty}^{\infty} \exp(s)\, p_s \, \mathrm{d}s = \int_{0}^{\infty} \rho \, p_\rho \, \mathrm{d}\rho = \langle \rho \rangle \ . \tag{4.11}$$

Equation (4.11) simply states that the mean density has to be recovered. This constraint together with the PDF normalization,

$$\int_{-\infty}^{\infty} p_s \, \mathrm{d}s = \int_{0}^{\infty} p_\rho \, \mathrm{d}\rho = 1 \tag{4.12}$$

must always be fulfilled for any density PDF whether log-normal or non-Gaussian.

From our simulations, we obtain density PDFs in agreement with log-normal distributions for solenoidal forcing. The log-normal fit using equation (4.10) is shown in Figure 4.4 as dashed lines. However, the PDF is not perfectly log-normal, i.e., there are weak non-Gaussian contributions (see also, Dubinski et al., 1995), especially affecting the wings of the distribution. The strength of these non-Gaussian features is quantified by computing higher-order moments (skewness and kurtosis) of the distributions. The first four standardized central moments (see, e.g., Press et al., 1986) of a discrete dataset $\{q\}$ with N elements are defined as

$$\begin{aligned}
&\text{mean :} && \langle q \rangle &&= \frac{1}{N} \sum_{i=1}^{N} q_i \\
&\text{dispersion :} && \sigma_q &&= \sqrt{\left\langle \left(q - \langle q \rangle \right)^2 \right\rangle} \\
&\text{skewness :} && \mathcal{S}_q &&= \frac{\left\langle \left(q - \langle q \rangle \right)^3 \right\rangle}{\sigma^3} \\
&\text{kurtosis :} && \mathcal{K}_q &&= \frac{\left\langle \left(q - \langle q \rangle \right)^4 \right\rangle}{\sigma^4} \ .
\end{aligned} \tag{4.13}$$

Note that in our definition of the kurtosis (also called flatness), the Gaussian distribution has $\mathcal{K} = 3$. We have computed the first four statistical moments of the volumetric density PDFs shown in Figure 4.4. The results are summarized in Table 4.1. The 1-σ error given for each statistical moment was obtained by averaging over 81 realizations of the turbulence as described in section 4.2.2. Both solenoidal and compressive forcing yield density PDFs with deviations from the Gaussian 3rd order (skewness $\mathcal{S} = 0$) and 4th order (kurtosis $\mathcal{K} = 3$) moments.

4.3.2 The density PDF for compressive forcing

Contrary to the solenoidal case, the PDF obtained for compressive forcing is not at all well fitted with the perfect log-normal functional form (dashed line in Figure 4.4 for compressive forcing). Due to the constraints of mass conservation (eq. 4.11) and normalization (eq. 4.12), the peak position and its amplitude cannot be reproduced simultaneously. The skewness and kurtosis for the compressive forcing case are also listed in Table 4.1. Non-Gaussian values of skewness and kurtosis, i.e., higher-order moments require modifications to the analytic expression of the log-normal PDF given by equation (4.10). A first step of modification is to allow for a finite

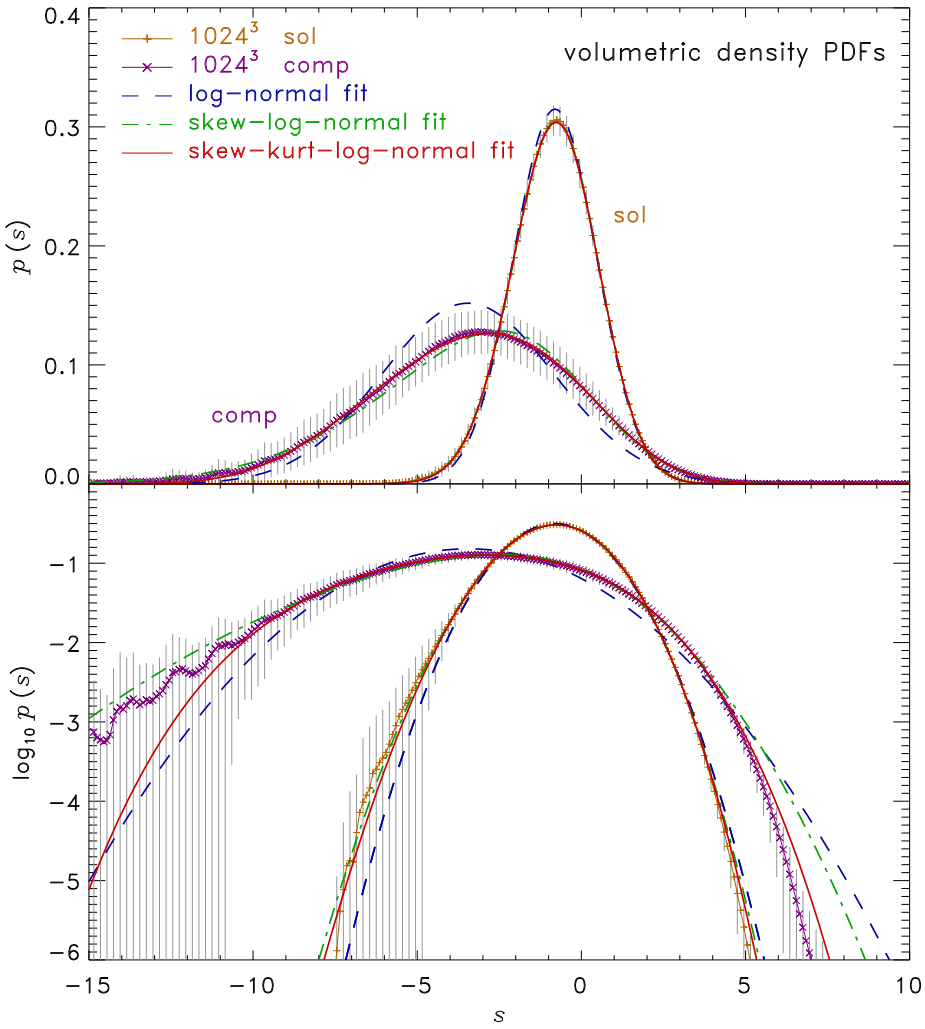

Figure 4.4: Volume-weighted density PDFs $p(s)$ of the logarithmic density $s = \ln(\rho/\langle\rho\rangle)$ in linear scaling (*top panel*), which displays the peak best, and in logarithmic scaling (*bottom panel*) to depict the low- and high-density wings. The PDF obtained from compressive forcing (1024^3 comp) is significantly wider than the solenoidal one (1024^3 sol). The peak is shifted to lower values of the logarithmic density s, because of mass conservation, defined in eq. (4.11). The density PDF from solenoidal forcing is compatible with a Gaussian distribution. However, there are also non-Gaussian features present, which are associated with intermittency effects. These are more prominent in the density PDF obtained from compressive forcing, exhibiting statistically significant deviations from a perfect log-normal (fit using eq. 4.10 shown as dashed lines). A skewed log-normal fit (dash-dotted lines) given by eq. (4.14) provides a better representation, but still does not fit the high-density tail of the PDF obtained for compressive forcing. Both the PDF data obtained from solenoidal and compressive forcing are best described as log-normal distributions with higher-order corrections defined in eq. (4.17), which take into account both the non-Gaussian skewness and kurtosis of the distributions. These fits are shown as solid lines (skew-kurt-log-normal fit). The first four standardized moments defined in equations (4.13) of the distributions in ρ and s are summarized in Table 4.1 together with the fit parameters. The gray shaded regions indicate 1-σ error bars due to temporal fluctuations of the distributions in the regime of fully developed, supersonic turbulence. A total number of $1024^3 \times 81 \approx 10^{11}$ data points contribute to each PDF.

		Solenoidal Forcing	Compressive Forcing
Standardized Moments of ρ	$\langle\rho\rangle$	1.00 ± 0.00	1.00 ± 0.00
	σ_ρ	1.89 ± 0.09	5.86 ± 0.96
	$\mathcal{S}_\rho$	9.03 ± 1.06	26.7 ± 10.1
	$\mathcal{K}_\rho$	$211. \pm 69.8$	1720 ± 2000
Standardized Moments of $s = \ln(\rho/\langle\rho\rangle)$	$\langle s\rangle$	-0.83 ± 0.05	-3.40 ± 0.43
	σ_s	1.32 ± 0.06	3.04 ± 0.24
	$\mathcal{S}_s$	-0.10 ± 0.11	-0.26 ± 0.20
	$\mathcal{K}_s$	3.03 ± 0.17	2.91 ± 0.43
Skewed Log-normal Approximation using equation (4.14)	ξ	0.010 ± 0.050	-0.048 ± 0.133
	ω	1.562 ± 0.035	4.712 ± 0.193
	α	-0.911 ± 0.064	-2.163 ± 0.173
4th Order Approximation (including skewness and kurtosis) using equation (4.17)	a_0	-1.3664 ± 0.0091	-2.5014 ± 0.0259
	a_1	-0.4592 ± 0.0064	-0.3437 ± 0.0132
	a_2	-0.3067 ± 0.0052	-0.0831 ± 0.0030
	a_3	-0.0073 ± 0.0011	-0.0065 ± 0.0011
	a_4	-0.0002 ± 0.0005	-0.0004 ± 0.0001

Table 4.1: Statistical moments and fit parameters of the PDFs of the volumetric density ρ for solenoidal and compressive forcing shown in Fig. 4.4.

skewness, which is possible with a skewed log-normal distribution (Azzalini, 1985)

$$p(s) = \frac{1}{\pi\,\omega}\,\exp\left[-\frac{(s-\xi)^2}{2\omega^2}\right] \int_{-\infty}^{(s-\xi)\alpha/\omega} \exp\left(-\frac{t^2}{2}\right) \mathrm{d}t\ , \tag{4.14}$$

where α, ξ and ω are fit parameters. Defining $\delta = \alpha/\sqrt{1+\alpha^2}$, the first four standardized central moments of the distribution are linked to the parameters α, ξ and ω, such that

$$\begin{aligned}
\text{mean :} \qquad \langle s\rangle &= \xi + \omega\,\delta\sqrt{2/\pi} \\
\text{dispersion :} \qquad \sigma_s &= \omega\left(1 - 2\delta^2/\pi\right)^{1/2} \\
\text{skewness :} \qquad \mathcal{S}_s &= \frac{4-\pi}{2}\frac{(\delta\sqrt{2/\pi})^3}{(1-2\delta^2/\pi)^{3/2}} \\
\text{kurtosis :} \qquad \mathcal{K}_s &= \frac{2(\pi-3)(\delta\sqrt{2/\pi})^4}{(1-2\delta^2/\pi)^2}\ .
\end{aligned} \tag{4.15}$$

Skewed log-normal fits are added to Figure 4.4 as dash-dotted lines and the corresponding fit parameters are given in Table 4.1. However, for a skewed log-normal distribution, the kurtosis is a function of the skewness, since the skewness and kurtosis in equations (4.15) both depend on the same parameter δ only.

Better agreement between an analytic functional form and the measured PDF can be obtained, if the actual kurtosis of the data is taken into account as an independent parameter in the analytical approach. The fundamental derivation of a standard Gaussian distribution is given by

$$\ln p(s) = a_0 + a_1 s + a_2 s^2\ , \tag{4.16}$$

where one parameter is constrained by the normalization and the two remaining ones are determined by the mean and the dispersion. We can extend this to a modified Gaussian-like distribution by including higher-order moments:

$$p(s) = \exp\left[a_0 + a_1 s + a_2 s^2 + a_3 s^3 + a_4 s^4 + \mathcal{O}(s^5)\right] \ . \tag{4.17}$$

Here, the expansion is stopped at the 4th moment. One parameter is again given by the normalization, and the remaining four parameters are related to the mean, dispersion, skewness and kurtosis. Fits obtained with this formula are included in Figure 4.4 as solid lines. The fit parameters are listed in Table 4.1. This new functional form is in good agreement with the data from solenoidal and compressive forcing, fitting both the peak and the wings very well. They follow the constraints of mass conservation and normalization given by equations (4.11) and (4.12). We have computed the first four moments of the fitted function and find very good agreement with the first four moments of the actual PDFs.

The fitted parameters a_3 and a_4, which represent the higher-order terms tend to zero compared to the standard Gaussian parameters a_0, a_1 and a_2 (see Table 4.1). This means that the higher-order corrections to the standard Gaussian are small. However, we point out that they are absolutely necessary to obtain a good analytic representation of the PDF data, given the fact that equations (4.11) and (4.12) must always be fulfilled and that the analytic PDF should return the correct values of the numerically computed moments of the measured distributions.

In the various independent numerical simulations mentioned above, the density PDFs were close to log-normal distributions as in our solenoidal and compressive forcing cases. However, most of these studies also report considerable deviations from Gaussian PDFs, which affected mainly the low- and high-density wings of their distributions. These deviations can be associated with rare events caused by strong intermittent fluctuations during head-on collisions of strong shocks and oscillations in very low-density rarefaction waves (e.g., Passot & Vázquez-Semadeni, 1998; Kritsuk et al., 2007). The pronounced deviations from the log-normal shape of the density PDF for compressively driven turbulence were also discussed by Schmidt et al. (2009). Even stronger deviations from log-normal PDFs were reported in strongly self-gravitating turbulent systems (e.g., Klessen, 2000; Federrath et al., 2008a; Kainulainen et al., 2009).

Intermittency is furthermore inferred from observations, affecting the wings of molecular line profiles (Falgarone & Phillips, 1990), and the statistics of centroid velocity increments (Hily-Blant et al., 2008). Goodman et al. (2009) measured column density PDFs using dust extinction and emission, as well as molecular lines of gas in the Perseus MC. Using dust extinction maps, Lombardi et al. (2006) obtained the column density PDF for the Pipe nebula. The PDFs found in these studies roughly follow log-normal distributions. However, deviations from perfect log-normal distributions are clearly present in the density PDFs obtained in these studies. They typically exhibit non-Gaussian features. For instance, Lombardi et al. (2006) had to apply combinations of multiple Gaussian distributions to obtain good agreement with the measured PDF data.

4.3.3 Density–Mach number correlation and signatures of intermittency in the density PDFs

As discussed by Passot & Vázquez-Semadeni (1998), a Gaussian distribution in the logarithm of the density, i.e., a log-normal distribution in ρ is expected for supersonic, isothermal turbulent flows. The fundamental assumption behind this model is that density fluctuations are built up by a hierarchical process. The local density $\rho(\mathbf{r}, t)$ at a given position $\mathbf{r}$ is determined by a Markov process, i.e., by the product $\rho(t_n) = \delta(t_{n-1})\rho(t_{n-1}) = \cdots = \delta(t_0)\rho(t_0)$ of a large number of *independent* random fluctuations $\delta(t_n) > 0$ in time (Vázquez-Semadeni, 1994). If these fluctuations were indeed independent, the quantity $s = \ln(\rho/\langle\rho\rangle)$ would be determined by the sum of

this large number of local fluctuations and the distribution in s becomes a Gaussian distribution according to the central limit theorem. Since the equations (4.2) and (4.3) are invariant under the transformation $s \rightarrow s + s_0$ for an arbitrary constant s_0, the random variable $s(t_n)$ should be independent of the local Mach number, and independent of the density at previous times $t_{n-1}, t_{n-2}, \ldots, t_0$. As pointed out by Vázquez-Semadeni (1994) and Passot & Vázquez-Semadeni (1998), this independence breaks down in strong shocks and density extrema, because s_0 cannot be arbitrarily high due to mass conservation, and an upper boundary s_+ exists. In consequence, if s_+ is reached locally, the density cannot increase anymore by a subsequent fluctuation, and the next density is *not* independent of the previous timestep, causing the fundamental assumption to break down. This also applies to strong rarefaction waves, because creating shocks always produces strongly rarefied regions outside the shock.

When the fundamental assumption breaks down, density and velocity statistics are expected to become correlated (Vázquez-Semadeni, 1994; Passot & Vázquez-Semadeni, 1998; Kritsuk et al., 2007). Since in isothermal gas, the sound speed is constant, this translates directly into Mach number–density correlations. The average local Mach number $M = v/c_\mathrm{s}$ may therefore exhibit some dependence on the average local density. For instance, it is intuitively clear that head-on collisions of strong shocks produce very high density peaks. In the stagnation point of the flow, the local velocity and consequently the local Mach number will almost drop to zero. The time evolution of the maximum and minimum density in Figure 4.3 shows these intermittent fluctuations (see also, Porter et al., 1992b; Kritsuk et al., 2007). The intermittent phenomenon corresponds to the situation explained above, for which s_+ might have been reached, and some dependence of the Mach number on density is expected.

In real molecular clouds, the maximum densities are similarly bounded, and cannot reach infinitely high values, either. This is–unlike the finite resolution constraints in simulations–because the gas becomes optically thick at a certain density ($\rho \gtrsim 10^{-14}\,\mathrm{g\,cm^{-3}}$), and cannot cool efficiently anymore (e.g., Larson, 1969; Penston, 1969; Larson, 2005; Jappsen et al., 2005, and references therein). The gas is not close to isothermal anymore in this regime, and adiabatic compression induced by turbulent motions remain finite in real molecular clouds. Thus, the reason for the breakdown of the density–Mach number independence is different in simulations and observations, but it might still be fundamental for the deviations from a log-normal PDF. Moreover, the existence of a characteristic scale may lead to a breakdown of the hierarchical model, and thus to a breakdown of the fundamental assumption. The scale at which supersonic turbulence becomes subsonic is such a scale. This scale is called the sonic scale, and is discussed later in section 4.9.

We have computed the probability distributions for Mach number–density correlations. Figure 4.5 shows the volume-weighted correlation PDFs of local Mach number M versus density ρ. Although the correlation between density and Mach number is weak as expected for isothermal turbulence (Vázquez-Semadeni, 1994; Passot & Vázquez-Semadeni, 1998), these two quantities are not entirely uncorrelated, which may explain the deviations from perfect log-normal distributions. There is a weak trend for high-density regions to exhibit lower Mach numbers on average. Power-law estimates for densities above the mean logarithmic density indicate Mach number–density correlations of the form $M(\rho) \propto \rho^{-0.06}$ for solenoidal and $M(\rho) \propto \rho^{-0.05}$ for compressive forcing. A similar power law exponent can be obtained from Kritsuk et al. (2007, Fig. 4).

4.3.4 Numerical resolution dependence of the density PDFs

The high-density tails of the PDFs in Figure 4.4 are not perfectly fit, even when the skewness and kurtosis are taken into account. This is partly due to non-zero 5th, 6th and higher-order moments in the distributions, and partly because our numerical resolution is insufficient to sample the high-density tail perfectly. Figure 4.6 shows that even at a numerical resolution of 1024^3 grid points, the high-density tails are not converged in both solenoidal and compressive forcing and tend to

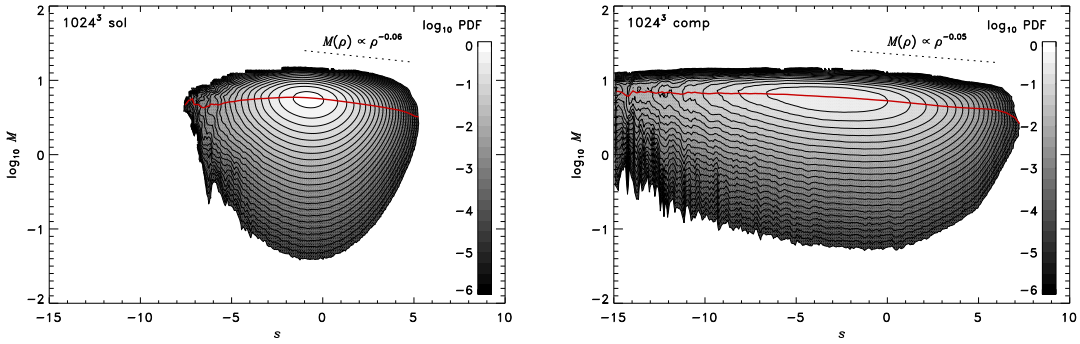

Figure 4.5: Volume-weighted correlation PDFs of local Mach number M versus logarithmic density s for solenoidal (*left*) and compressive forcing (*right*). Adjacent contour levels are spaced by 0.25 dex in probability density. Density and Mach number exhibit a very weak, but non-zero correlation in both forcing cases, which provides an explanation for the non-Gaussian features in the density PDFs of Fig. 4.4 (Vázquez-Semadeni, 1994; Passot & Vázquez-Semadeni, 1998; Kritsuk et al., 2007). The two solid lines, intersecting the maxima of both distributions show the mean Mach number as a function of the logarithmic density $s = \ln(\rho/\langle\rho\rangle)$. The tendency for high-density gas having lower Mach numbers on average is indicated as power laws in the high-density parts of the distributions. This suggests that the Mach number $M(\rho) \propto \rho^{-0.06}$ for solenoidal and $M(\rho) \propto \rho^{-0.05}$ for compressive forcing.

Grid Resolution	Solenoidal Forcing		Compressive Forcing	
	σ_ρ	σ_s	σ_ρ	σ_s
256^3	1.79 ± 0.08	1.36 ± 0.07	5.66 ± 0.79	3.09 ± 0.21
512^3	1.89 ± 0.10	1.35 ± 0.05	5.59 ± 0.67	3.15 ± 0.34
1024^3	1.89 ± 0.09	1.32 ± 0.06	5.86 ± 0.96	3.04 ± 0.24

Table 4.2: Standard deviations of the density PDFs as a function of numerical resolution for solenoidal and compressive forcing shown in Fig. 4.6.

underestimate high densities. This limitation is shared among all turbulence simulations (see, for instance, the turbulence comparison project by Kitsionas et al., 2009), since the strongest and most intermittent fluctuations building up in the tails will always be truncated due to limited numerical resolution (see also Hennebelle & Audit, 2007; Kowal et al., 2007; Price & Federrath, 2010). However, the peak and the standard deviation of the PDFs are reproduced quite accurately at a resolution of 256^3. Table 4.2 shows the values of the linear standard deviation σ_ρ and logarithmic standard deviation σ_s for numerical resolutions of 256^3, 512^3 and 1024^3. There appears to be no strong systematic dependence of the standard deviations on the numerical resolution for resolutions above 256^3. The statistical fluctuations are the dominant source of uncertainty in the derived values of the standard deviations. It should be noted however that we have tested only the case of an RMS Mach number of about 5-6 here. There might be a stronger resolution dependence for higher Mach numbers, due to the stronger shocks produced in higher Mach number turbulence, which should be tested in a separate study.

4.3.5 The column density PDFs and comparison with observations

The strong difference between the statistics of the solenoidal and compressive forcing cases seen in the PDFs of the volumetric density shown in Figure 4.4 is reflected by the corresponding column density PDFs. The time-averaged and projection-averaged column density PDFs are shown in

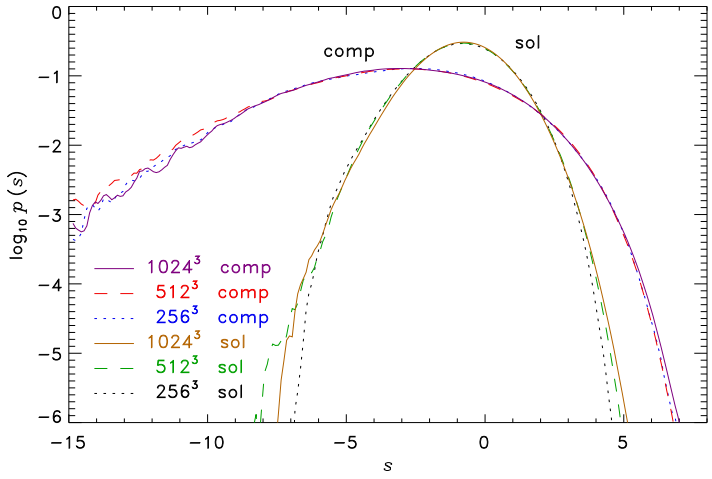

Figure 4.6: Density PDFs at numerical resolutions of 256^3, 512^3 and 1024^3 grid cells. The PDFs show very good overall convergence, especially around the peaks. Table 4.2 shows that the standard deviations are converged with numerical resolution. The high-density tails, however, are not converged even at a numerical resolution of 1024^3 grid points, indicating a systematic shift to higher densities with resolution. This limitation is shared among all turbulence simulations (see also, Hennebelle & Audit, 2007; Kitsionas et al., 2009; Price & Federrath, 2010). The low-density wings are subject to strong temporal fluctuations due to intermittent bursts caused by head-on collisions of shocks followed by strong rarefaction waves (e.g., Kritsuk et al., 2007). The intermittency causes deviations from a perfect Gaussian distribution and accounts for non-Gaussian higher-order moments (skewness and kurtosis) in the distributions.

Figure 4.7. Analogous to Table 4.1 for the volumetric density PDFs, we summarize the statistical quantities and fit parameters for the column density PDFs in Table 4.3. The main results and conclusions obtained for the volumetric density distributions also hold for the column density distributions. Compressive forcing yields a column density standard deviation roughly three times larger than solenoidal forcing. The relative difference between solenoidal and compressive forcing is thus roughly the same for the volumetric and the column density distributions. However, the absolute values are lower for the column density distributions compared to the volumetric density distributions. The reason for this is that by computing projections of the volumetric density fields, density fluctuations are effectively averaged out by integration along the line-of-sight, and as a consequence, the column density dispersions become smaller compared to the corresponding volumetric density dispersions.

The small inset in the upper right corner of Figure 4.7 additionally shows the column density PDFs computed along the z-axis at one single time $t = 2\,T$ corresponding to the map shown in Figure 4.2. This figure shows the effect of studying one realization only, without time- and/or projection-averaging. This is interesting to consider, because observations can only measure column density distributions at one single time. Improving the statistical significance would only be possible by studying multiple fields and averaging in space rather than in time invoking the ergodic theorem as suggested by Goodman et al. (2009). However, even by studying one turbulent realization only, the difference between solenoidal and compressive forcing is recovered from the dispersions of the distributions. We therefore expect that using observations of column density PDFs, one can distinguish purely solenoidal from purely compressive forcing by measuring the dispersion of the column density PDF.

Goodman et al. (2009) provided measurements of the column density PDFs in the Perseus MC obtained with three different methods: dust extinction, dust emission, and ^{13}CO gas emis-

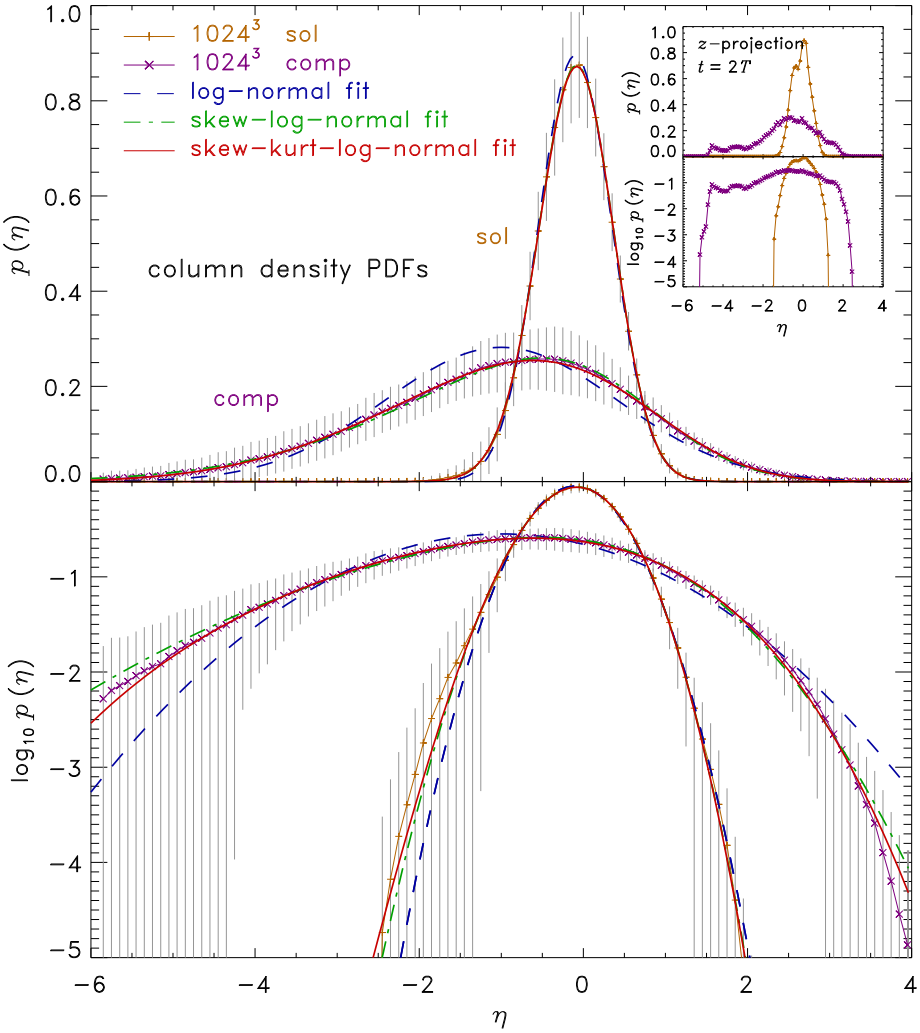

Figure 4.7: Same as Figure 4.4, but the time- and projection-averaged logarithmic *column* density PDFs of $\eta = \ln(\Sigma_i / \langle\Sigma_i\rangle)$ are shown. Σ_i and $\langle\Sigma_i\rangle$ denote the column density and the mean column density integrated along the $i = x, y, z$ principal axes respectively. As for the volumetric PDFs of Fig. 4.4, the standard deviation of the column density PDF obtained from compressive forcing is roughly three times larger than from solenoidal forcing (see Table 4.3). The inset in the upper right corner shows the PDFs of column density computed in z-projection at a fixed time $t = 2\,T$, corresponding to the snapshots shown in Figure 4.2. The density dispersions computed for these instantaneous PDFs are $\sigma_\Sigma = 0.49$ and $\sigma_\eta = 0.45$ for solenoidal forcing, and $\sigma_\Sigma = 1.34$ and $\sigma_\eta = 1.56$ for compressive forcing. Although these distributions are quite noisy, the influence of the forcing is still clearly discernible. Thus, by studying instantaneous column density PDFs, which are accessible to observations, one should be able to distinguish solenoidal from compressive forcing.

		Solenoidal Forcing	Compressive Forcing
Standardized Moments of Σ	$\langle\Sigma\rangle$	1.00 ± 0.00	1.00 ± 0.00
	σ_Σ	0.47 ± 0.05	1.74 ± 0.43
	$\mathcal{S}_\Sigma$	1.38 ± 0.38	4.57 ± 1.44
	$\mathcal{K}_\Sigma$	6.32 ± 2.20	36.8 ± 24.3
Standardized Moments of $\eta = \ln(\Sigma/\langle\Sigma\rangle)$	$\langle\eta\rangle$	-0.10 ± 0.02	-1.00 ± 0.33
	σ_η	0.46 ± 0.06	1.51 ± 0.28
	$\mathcal{S}_\eta$	-0.04 ± 0.30	-0.17 ± 0.29
	$\mathcal{K}_\eta$	2.97 ± 0.40	2.69 ± 0.45
Skewed Log-normal Approximation using equation (4.14)	ξ	0.180 ± 0.088	0.717 ± 0.102
	ω	0.539 ± 0.058	2.392 ± 0.160
	α	-0.878 ± 0.342	-2.371 ± 0.300
4th Order Approximation (including skewness and kurtosis) using equation (4.17)	a_0	-0.1524 ± 0.0451	-1.4547 ± 0.0532
	a_1	-0.3900 ± 0.1080	-0.2902 ± 0.0417
	a_2	-2.4643 ± 0.1994	-0.2669 ± 0.0259
	a_3	-0.1748 ± 0.1469	-0.0370 ± 0.0080
	a_4	0.0204 ± 0.1239	-0.0035 ± 0.0024

Table 4.3: Same as Table 4.1, but for the PDFs of the column density Σ shown in Fig. 4.7.

sion. Although systematic differences were found between the three methods, they conclude that in general, the measured column density PDFs are close to, but not perfect log-normal distributions, which is consistent with our results. They furthermore provided the column density PDFs and the column density dispersions for six subregions in the Perseus MC. The difference between the dispersions measured for these subregions is not as large as the difference between purely solenoidal and purely compressive forcing. The largest difference in the column density dispersions among the six subregions found by Goodman et al. (2009) is only about 50% relative to the average column density dispersion measured in the Perseus MC. This indicates that both purely solenoidal and purely compressive forcing are very unlikely to occur in nature. On the other hand, a varying mixture of solenoidal and compressive modes close to the natural mixture of 2:1 can easily explain the 50% difference in density dispersion measured among the different regions. In particular, the Shell region (Ridge et al., 2006), which surrounds the B star HD 278942 exhibits the largest density dispersion among all the subregions studied by Goodman et al. (2009), although its velocity dispersion is rather small compared to the others. This indicates that turbulent motions may be driven compressively rather than solenoidally within the Shell region. Goodman et al. (2009) indeed mentioned that the gas in the Shell is dominated by an "obvious driver", skewing the column density distribution towards lower values compared to the other regions. Due to the constraints of mass conservation (eq. 4.11) and normalization (eq. 4.12), both the peak position and the peak value of the PDF skew to lower values, if the density dispersion increases (see Figure 4.7). Taken together, this suggests that the Shell in the Perseus MC represents an example of strongly compressive turbulence forcing rather than purely solenoidal forcing.

4.3.6 The forcing dependence of the density dispersion–Mach number relation

In Federrath et al. (2008b), we investigated the density dispersion–Mach number relation (Padoan et al., 1997; Passot & Vázquez-Semadeni, 1998)[1],

$$\frac{\sigma_\rho}{\langle\rho\rangle} = b\mathcal{M} \; . \tag{4.18}$$

This relation was also investigated in Kowal et al. (2007, Fig. 11), indicating that the standard deviation of turbulent density fluctuations, σ_ρ is directly proportional to the sonic Mach number in the supersonic regime. It must be noted, however, that it was only directly tested for rather low RMS Mach numbers, $\mathcal{M} \lesssim 2.5$ (Kowal et al., 2007) and $\mathcal{M} \lesssim 3.5$ (Passot & Vázquez-Semadeni, 1998), compared to typical Mach numbers in molecular clouds. If additionally a log-normal PDF, equation (4.10) is assumed, then equation (4.18) can be expressed as

$$\sigma_s^2 = \ln\left(1 + b^2\mathcal{M}^2\right) \; , \tag{4.19}$$

with the *same* parameter b (Padoan et al., 1997; Federrath et al., 2008b).

We begin our discussion of the forcing dependence of the density dispersion–Mach number relation with a problem raised by Mac Low et al. (2005) and Glover & Mac Low (2007b). Mac Low et al. (2005) and Glover & Mac Low (2007b) claimed that the density dispersion–Mach number relation found by Passot & Vázquez-Semadeni (1998), $\sigma_s = b\mathcal{M}$ (which is a Taylor expansion of eq. 4.19 for small RMS Mach numbers), with $b \approx 1$ did not at all fit their results for pressure and density PDFs, while equation (4.19) with $b \approx 0.5$ (Padoan et al., 1997) provided a much better representation of their data. The main difference in the density dispersion–Mach number relations by Padoan et al. (1997) and Passot & Vázquez-Semadeni (1998) is the proportionality constant b. It is $b \approx 0.5$ and $b \approx 1$ in Padoan et al. (1997) and Passot & Vázquez-Semadeni (1998), respectively. Our forcing analysis provides the solution to this apparent difference, which lies at the heart of the disagreement of the PDF data analyzed in Mac Low et al. (2005) and Glover & Mac Low (2007b) with the model by Passot & Vázquez-Semadeni (1998). Passot & Vázquez-Semadeni (1998) used 1D models. In 1D, only compressive forcing is possible, because no transverse waves can exist. In contrast, Mac Low et al. (2005) and Glover & Mac Low (2007b) used a mixture of solenoidal and compressive forcing in 3D. In this section, we show that the parameter b in both equations (4.18) and (4.19) is a function of the forcing parameter ζ. Indeed, using the relation $\sigma_s = b\mathcal{M}$ analyzed in Passot & Vázquez-Semadeni (1998), but with a lower proportionality constant ($b = 0.5$ in contrast to $b = 1$) gives a very good representation of the PDF data in Mac Low et al. (2005, Fig. 8). Thus, an investigation of the parameters that control b seems necessary and important.

Moreover, relations (4.18) and (4.19) are key ingredients for the analytical models of the stellar initial mass function by Padoan & Nordlund (2002) and Hennebelle & Chabrier (2008), as well as for the star formation rate model by Krumholz & McKee (2005) and Krumholz et al. (2009) and for the star formation efficiency model by Elmegreen (2008). In all these models, b is assumed to be 0.5, which is an empirical result from magnetohydrodynamical simulations by Padoan et al. (1997). On the other hand, Passot & Vázquez-Semadeni (1998) found $b \approx 1$ from 1D hydrodynamical simulations. Federrath et al. (2008b) resolved this disagreement between Padoan et al. (1997) and Passot & Vázquez-Semadeni (1998) by showing that b is a function of the ratio $\zeta \in [0, 1]$ of compressive to solenoidal modes of the turbulence forcing. However, Federrath et al. (2008b) only tested the two limiting cases of purely solenoidal forcing ($\zeta = 1$) and purely compressive forcing ($\zeta = 0$). They approximated the regime of mixtures with a heuristic

[1]Note that Passot & Vázquez-Semadeni (1998) suffers from a number of typographical errors as a result of last-minute change of notation. Please see Mac Low et al. (2005, footnote 5) for a number of corrections.

model, which had a linear dependence of b on ζ:

$$\tilde{b} = 1 + \left(\frac{1}{D} - 1\right)\zeta = \begin{cases} 1 - \frac{2}{3}\zeta, & \text{for } D = 3 \\ 1 - \frac{1}{2}\zeta, & \text{for } D = 2 \\ 1, & \text{for } D = 1\,. \end{cases} \tag{4.20}$$

Here, we refine this model based on eleven additional simulations with $\zeta = [0, 1]$ separated by $\Delta\zeta = 0.1$ for RMS Mach numbers of 5 in 2D and 3D. These simulations allow us to test eleven different mixtures of forcing controlled by the parameter ζ (see eq. 4.9). The models were run at a numerical resolution of 256^3 and 1024^2 grid points in 3D and 2D, respectively. We use a lower resolution in 3D, because using our standard resolution of 1024^3 would be too computationally intensive. However, as shown in section 4.3.4, the standard deviation of the density is fairly well reproduced at 256^3, as is the RMS Mach number $\mathcal{M}$ (Federrath et al., 2009, Fig. 2), which allows a reasonably accurate determination of b. The results are plotted in Figure 4.8 as diamonds for 3D (top panel) and 2D (bottom panel). We used equation (4.18) to measure b, because unlike equation (4.19), this version of the standard deviation–Mach number relation does not rest on the assumption of a log-normal PDF. In fact, if equation (4.19) was used to derive b for models with $\zeta < 0.5$, b would be overestimated significantly (by up to an order of magnitude for $\zeta = 0$), because the deviations from the perfect log-normal distribution are stronger for $\zeta < 0.5$ (cf. section 4.3.2; see also Schmidt et al. (2009)).

Figure 4.8 shows that the dependence of b on ζ is non-linear. For 3D turbulence the parameter b increases smoothly from $b \approx 1/3$ for $\zeta = 1$ to $b \approx 1$ for $\zeta = 0$, and for 2D turbulence from $b \approx 1/2$ for $\zeta = 1$ to $b \approx 1$ for $\zeta = 0$. However, there is an apparent break at $\zeta \approx 0.5$, which represents the natural forcing mixture used in many previous studies. For $\zeta \gtrsim 0.5$ the b-parameter remains close to the value obtained for purely solenoidal forcing, i.e. $b \approx 0.3 - 0.4$ in 3D and $b \approx 0.5$ in 2D. The flat part of the data in Figure 4.8 for $\zeta > 0.5$ explains why in previous studies with a natural forcing mixture (e.g., Mac Low et al., 1998; Klessen et al., 2000; Li et al., 2003; Kritsuk et al., 2007; Glover et al., 2009), the turbulence statistics were close to the purely solenoidal forcing case (e.g., Padoan et al., 1997; Stone et al., 1998; Boldyrev et al., 2002; Padoan & Nordlund, 2002; Kowal et al., 2007; Lemaster & Stone, 2008; Burkhart et al., 2009). In contrast, b increases much more strongly for $\zeta \lesssim 0.5$, until it reaches $b \approx 1$ for purely compressive forcing (e.g., Passot & Vázquez-Semadeni, 1998; Federrath et al., 2008b; Schmidt et al., 2009).

Equation (4.20) thus needs to be refined to account for the non-linear dependence of b on the forcing. Moreover, equation (4.20) was based on the analytic expression of the forcing parameter ζ (cf. section 4.2.1). However, the numerical estimate of b depends on how well the code can actually induce compression through the build-up of divergence in the velocity field. Thus, different codes can produce slightly different values of b for the same forcing parameter ζ. This is because of the varying efficiency of codes to convert the energy provided by a given forcing into actual velocity fluctuations (e.g. Kitsionas et al., 2009; Price & Federrath, 2010). To construct a refined model for b that does not directly rest on the analytic forcing parameter ζ and that accounts for the non-linear dependence on the forcing, we recall that b is a normalized measure of compression. Compression is caused by converging flows and shocks, which have a finite magnitude of velocity divergence. A normalized measure of compression is thus also provided by dividing the power in longitudinal modes of the velocity field by the total power of all modes in the velocity field,

$$\langle\Psi\rangle = \frac{E_{\rm long}}{E_{\rm tot}}\,. \tag{4.21}$$

We therefore expect a dependence of b on $\langle\Psi\rangle$.

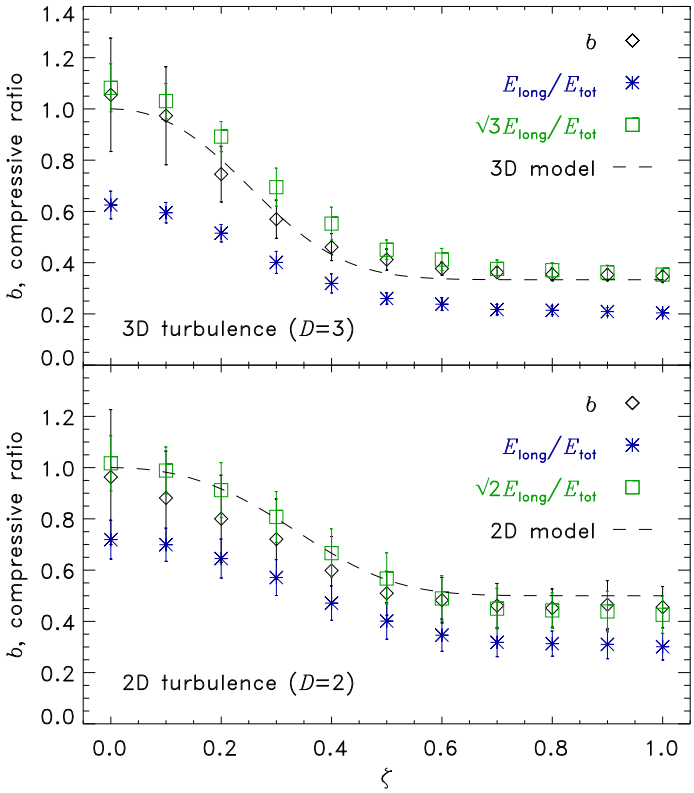

Figure 4.8: *Diamonds:* The proportionality parameter b in the density dispersion–Mach number relation, eq. (4.18), computed as $b = \sigma_\rho / (\langle\rho\rangle \mathcal{M})$ for eleven 3D models at numerical resolution of 256^3 grid cells (*top panel*) and eleven 2D models at numerical resolution of 1024^2 grid cells (*bottom panel*), ranging from purely compressive forcing ($\zeta = 0$) to purely solenoidal forcing ($\zeta = 1$). The parameter b decreases smoothly from $b \approx 1$ for compressive forcing to $b \approx 1/3$ in 3D and $b \approx 1/2$ in 2D for solenoidal forcing. *Stars:* Ratio $\langle\Psi\rangle = E_{\rm long}/E_{\rm tot}$ of longitudinal to total power in the velocity power spectrum (see section 4.6.1). This quantity provides a measure for the relative amount of compression induced by the turbulent velocity field, and appears to be correlated with the standard deviation of the density PDF. *Squares:* Same as stars, but multiplied by the geometrical factor $\sqrt{D}$ with $D = 3$ for the three-dimensional case and $D = 2$ for the two-dimensional case. The quantity $\sqrt{D}\,\langle\Psi\rangle$ provides a good numerical estimate of the PDF parameter b. The dashed lines show model fits using equation (4.23) for $D = 3$ (*top panel*) and $D = 2$ (*bottom panel*).

Figure 4.8 shows $\langle\Psi\rangle$ as a function of ζ (plotted as stars) for 3D and 2D turbulence. It is indeed correlated with b, however, $\langle\Psi\rangle$ is less than b by a factor of roughly $\sqrt{3}$ in 3D and $\sqrt{2}$ in 2D. The squares in Figure 4.8 show $\sqrt{3}\,\langle\Psi\rangle$ in 3D and $\sqrt{2}\,\langle\Psi\rangle$ in 2D, which seems to provide a good estimate of b. The factor $\sqrt{3}$ is a geometrical factor for 3D turbulence (the diagonal in a cube of size unity). It is $\sqrt{2}$ in 2D turbulence (the diagonal in a square of size unity), and $\sqrt{1}$ in 1D. The latter in particular is trivial, because in 1D only longitudinal modes can exist, and thus $\sqrt{1}\,\langle\Psi\rangle = 1$ for any value of ζ (cf. Fig. 4.1). The larger geometrical factors in 2D and 3D account for the fact that the longitudinal velocity fluctuations, which induce compression occupy only one of the available spatial directions (two in 2D and three in 3D) on average. For the general case of supersonic turbulence in $D = 1, 2$ and 3 dimensions, these ideas lead to

$$\tilde{b} = \sqrt{D}\,\langle\Psi\rangle \ , \tag{4.22}$$

which is solely based on the ratio of the power in longitudinal modes in the velocity field to the total power of all modes in the velocity field, $\langle\Psi\rangle$.

In addition to the refined model based on the compressive ratio $\langle\Psi\rangle$ in equation (4.22), we provide a fit function for b based on the forcing parameter ζ. The dashed lines in Figure 4.8 show

$$\tilde{b}(\zeta) = \frac{1}{D} + \frac{D-1}{D}\left(\frac{F_{\rm long}(\zeta)}{F_{\rm tot}(\zeta)}\right)^3 \ . \tag{4.23}$$

The forcing ratio $F_{\rm long}/F_{\rm tot}$ is given by equation 4.9. The first summand in equation (4.23) is the expected ratio of longitudinal modes (compression) in a supersonic turbulent medium for a purely solenoidal forcing, i.e. a forcing that does not directly induce compression. The second summand is the contribution to the compression directly induced by the forcing. The model equation (4.23) is similar to equation (4.20), but with a non-linear dependence of b on the forcing parameter ζ.

We suggest that the dependence of b on the forcing solves a puzzle reported by Pineda et al. (2008). They provided measurements of velocity dispersions and ^{12}CO excitation temperatures for the six subregions in the Perseus MC. The molecular excitation temperatures serve as a guide for the actual gas temperature, from which the sound speed can be estimated. From these values, the local RMS Mach numbers are computed as the ratio of the local velocity dispersion to the local sound speed. Goodman et al. (2009) and Pineda et al. (2008) pointed out that there is clearly *no* correlation of the form suggested by equation (4.19) for a *fixed* parameter b across the investigated subregions in the Perseus MC. For instance, the Shell region exhibits an intermediate to small velocity dispersion derived from ^{12}CO and ^{13}CO observations, while its density dispersion is the largest in the Perseus MC. This provides additional support to our suggestion that the Shell in Perseus is dominated by compressive turbulence forcing for which b takes a higher value compared to solenoidal forcing. The apparent lack of density dispersion–Mach number correlation reported by Pineda et al. (2008) and Goodman et al. (2009) for a fixed parameter b can thus be explained, because b is in fact *not* fixed across different subregions in the Perseus MC.

We plan to measure b in different regions of the ISM in future studies. However, the main problem in a quantitative analysis of equation (4.18) with observational data is that the column density dispersion is typically smaller than the 3D density dispersion (compare Tab. 4.1 and Tab. 4.3). The relation between the column density PDF and the volumetric density PDF is non-trivial and depends on whether the column density tracer is optically thin or optically thick and on the scale of the turbulence driving. However, Brunt et al. (2010b) developed a promising technique to estimate the 3D density variance from 2D observations with an accuracy of about 10%.

4.4 Intermittency

Intermittency manifests itself in

i) non-Gaussian (often exponential) wings of PDFs of quantities involving density and/or velocity, its derivatives (e.g., vorticity) and combinations of density and velocity (e.g., $\rho^{1/2}v$ and $\rho^{1/3}v$ as discussed in section 4.8),

ii) anomalous scaling of the higher-order structure functions of the velocity field (e.g., Anselmet et al., 1984) and centroid velocity increments (Lis et al., 1996; Hily-Blant et al., 2008), and

iii) coherent structures of intense vorticity ($\nabla \times \mathbf{v}$) (see Vincent & Meneguzzi, 1991; Moisy & Jiménez, 2004, for results of incompressible turbulence), and of strong shocks and rarefaction waves ($\nabla \cdot \mathbf{v}$).

Filamentary coherent structures of vorticity (intermittency item *iii*) are indeed observed in our two supersonic models. In Figure 4.2 (middle panel), we show the projected vorticity for solenoidal and compressive forcing, respectively. Most of the filaments of high vorticity coincide with the positions of shocks and therefore also with high density and negative divergence in the velocity field (Figure 4.2, bottom panel). This is furthermore inferred from observations of the Ursa Majoris Cloud by Falgarone et al. (1994) and is consistent with the results of weakly compressible decaying turbulence experiments by Porter et al. (1992a) and Porter et al. (1994), who concluded that intense vorticity is typically associated with intermittency.

4.4.1 The probability distribution of centroid velocity increments

Since there is evidence of filamentary coherent structures in the vorticity (intermittency item *iii*) of our models, and because there is additional evidence of non-Gaussian tails in the density PDFs (intermittency item *i*) discussed in section 4.3, we now proceed to examine the PDFs and the scaling of centroid velocity increments (intermittency item *ii*) to assess the strength of the intermittency. We compare centroid velocity increments (CVIs) for solenoidal and compressive forcing and discuss the interpretation of observations based on that comparison. Following the analysis by Lis et al. (1996), who discuss CVIs computed for the turbulence simulation by Porter et al. (1994), and following the CVI analysis of the Polaris Flare and of the Taurus MC by Hily-Blant et al. (2008), the centroid velocity increment is defined as

$$\delta C_\ell(\mathbf{r}) = \langle C(\mathbf{r}) - C(\mathbf{r}+\ell) \rangle \ , \tag{4.24}$$

where the angle average $\langle \ \ \rangle$ is computed over all possible directions of the vector ℓ in the plane perpendicular to the line-of-sight. Thus, $\delta C_\ell(\mathbf{r})$ only depends on the norm of the lag vector $\ell = |\ell|$, which separates two points $\mathbf{r} = (x, y)$ and $\mathbf{r} + \ell$ in the plane of the sky (x, y). The normalized centroid velocity, $C(\mathbf{r})$ in equation (4.24) is defined as

$$C(\mathbf{r}) = \frac{\int \rho(\mathbf{r}, z)\, v_z(\mathbf{r}, z)\, \mathrm{d}z}{\int \rho(\mathbf{r}, z)\, \mathrm{d}z} \ . \tag{4.25}$$

The variable $v_z(\mathbf{r}, z)$ denotes the line-of-sight velocity in z-direction. We have however computed $C(\mathbf{r})$ separately along each of the three principal lines-of-sight x, y and z of our Cartesian domain in order to examine the effects of varying the projection. Also note that we have computed normalized centroid velocities (Lazarian & Esquivel, 2003), since we want to compare to Hily-Blant et al. (2008). Another point to mention here is that the centroid velocities, $C(\mathbf{r})$ are typically computed using an intensity weighting instead of a density weighting. This is because the gas density cannot be measured directly, whereas the emission intensity is accessible to

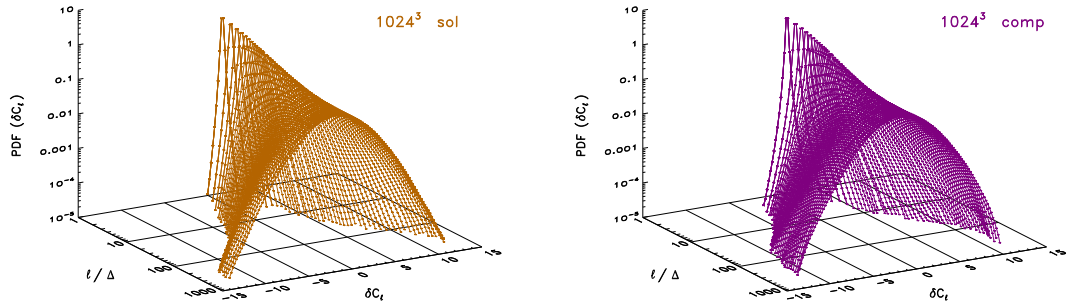

Figure 4.9: PDFs of centroid velocity increments, computed using equations (4.24) and (4.25) are shown as a function of lag ℓ in units of grid cells $\Delta = L/1024$ for solenoidal forcing (*left*) and compressive forcing (*right*). The PDFs are very close to Gaussian distributions for long lags, whereas for short lags, they develop exponential tails, which is a manifestation of intermittency (e.g., Hily-Blant et al., 2008, and references therein).

observations. By using density weighting we implicitly assume optically thin emission. For optically thick emission, uniform weighting would be more appropriate (Lis et al., 1996).

Figure 4.9 shows the PDFs of $\delta C_\ell(\mathbf{r})$ computed for varying lag ℓ in units of the numerical cell size $\Delta = L/1024$. They should be compared to Hily-Blant et al. (2008, Fig. 4-6). The PDFs are mainly Gaussian for large lags, whereas for smaller separations, they develop exponential tails, indicating intermittent behavior. This result is consistent with the numerical simulation analyzed by Lis et al. (1996), and with observations of the ρ Oph Cloud, the Orion B and the Polaris Flare by Lis et al. (1998), Miesch et al. (1999) and Hily-Blant et al. (2008), respectively.

Following the analysis by Hily-Blant et al. (2008), we computed the kurtosis $\mathcal{K}$ of the PDFs of CVIs using the definition in equations (4.13). Note that $\mathcal{K} = 3$ corresponds to a Gaussian distribution, and $\mathcal{K} = 6$ corresponds to an exponential function. The kurtosis of the CVI PDFs is shown in Figure 4.10 as a function of spatial lag ℓ, and can be directly compared to Hily-Blant et al. (2008, Fig. 7). Both forcing types exhibit nearly Gaussian values of the kurtosis at lags $\ell \gtrsim 100\Delta$. On the other hand, for $\ell \lesssim 100\Delta$, both forcing types produce non-Gaussian PDFs. Solenoidal forcing approaches the exponential value $\mathcal{K} = 6$ for $\ell \lesssim 10\Delta$. Compressive forcing yields exponential values already for lags $\ell \approx 40\Delta$, while solenoidal forcing has $\mathcal{K} \approx 4$ on these scales. This indicates stronger intermittency in the case of compressive forcing. For $\ell \lesssim 30\Delta$, compressive forcing yields even super-exponential values of $\mathcal{K}$. For both solenoidal and compressive forcings, we show later in section 4.6 that $\ell \lesssim 30\Delta$ is in the dissipation range for numerical turbulence. Compressive velocity modes dominate in this regime (see Fig. 4.15), which may result artificially in extreme intermittency. For $\ell \approx 30\Delta$, compressive forcing gives $\mathcal{K} = 6.0 \pm 1.0$, which is roughly 35% larger than the Polaris Flare observations at their resolution limit. The solenoidal case on the other hand gives $\mathcal{K} \approx 4.3 \pm 0.5$, which is in very good agreement with the IRAM and KOSMA data discussed by Hily-Blant et al. (2008, Fig. 7). Depending on the actual lag used for the comparison, both solenoidal and compressive forcing seem to be consistent with the observations. However, it should be noted that the lags cannot be easily compared for the real clouds and the simulations, because simulated and observed fields have different spatial resolution. Moreover, the simulated fields have periodic boundaries, while the true fields don't. Nevertheless, the similarity of the observed and the numerically simulated CVIs indicates that turbulence intermittency plays an important role in both our simulations and in real molecular clouds.

The Polaris Flare has a very low star formation rate and is therefore appropriate for study-

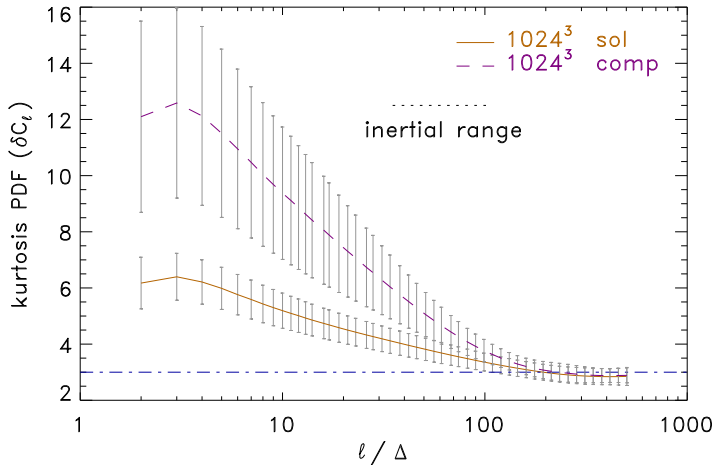

Figure 4.10: Kurtosis $\mathcal{K}$ of the PDFs of centroid velocity increments shown in Fig. 4.9 as a function of the lag ℓ in units of grid cells $\Delta = L/1024$ for solenoidal and compressive forcing. Note that a kurtosis value of 3 (horizontal dot-dashed line) corresponds to the value for a Gaussian distribution. Non-Gaussian values of the kurtosis are obtained for $\ell \lesssim 100\Delta$. The error bars contain both snapshot-to-snapshot variations as well as the variations between centroid velocity increments computed by integration along the x, y and z axes. This figure can be compared to observations of the Polaris Flare and Taurus MC (see Fig. 7 of Hily-Blant et al., 2008).

ing the statistics of interstellar supersonic turbulence without contamination by internal energy sources. In contrast, the Taurus MC is actively forming stars. Against our expectations, the Taurus MC data display very *weak* intermittent behavior and the kurtosis remains at the Gaussian values $\mathcal{K} \approx 3$ in Hily-Blant et al. (2008, Fig. 7). However, the Taurus field studied by Hily-Blant et al. (2008) is located far from star-forming regions in a translucent part of the Taurus MC (E. Falgarone 2009, private communication). This may explain why the Taurus field displays only very weak intermittency. It would be interesting to repeat the analysis of centroid velocity increments for regions of confirmed star formation, including regions with winds, outflows and ionization feedback from young stellar objects to see whether these regions indeed display stronger intermittency.

4.4.2 The structure function scaling of centroid velocity increments

In this section, we discuss the scaling of the pth order structure function of CVIs, defined as

$$\mathrm{CVISF}_p(\ell) = \langle |\delta C_\ell(\mathbf{r})|^p \rangle_{\mathbf{r}} \ . \tag{4.26}$$

We have averaged over a large enough sample of independent increments $\delta C_\ell(\mathbf{r})$ that increasing the sample size produced no change in the value of $\mathrm{CVISF}_p(\ell)$ for $p \leq 6$, which is demonstrated in section 4.4.3. Figure 4.11 shows the CVI structure functions for solenoidal and compressive forcing. The CVI structure functions were fit to power laws of the form

$$\mathrm{CVISF}_p(\ell) \propto \ell^{\zeta_p} \tag{4.27}$$

within the inertial range[2], defined equivalently to the study in Federrath et al. (2009). The value

[2]By its formal definition for *incompressible* turbulence studies (e.g., Frisch, 1995), the inertial range is the range

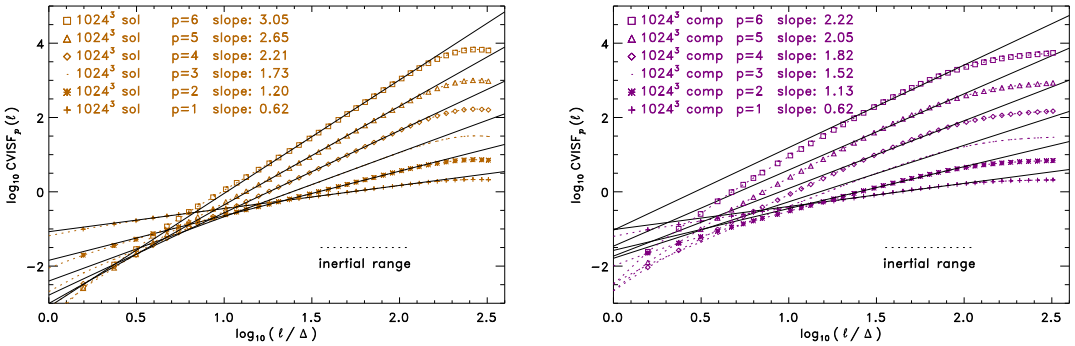

Figure 4.11: Scaling of the structure functions of centroid velocity increments defined in equation (4.26) for solenoidal forcing (*left*) and compressive forcing (*right*) up to the 6th order. Scaling exponents obtained using power-law fits following equation (4.27) within the inertial range are indicated in the figures and summarized in Tab. 4.4.

Absolute Scaling Exponents	ζ_1	ζ_2	ζ_3	ζ_4	ζ_5	ζ_6
CVI SFs (1024^3 sol)	0.62	1.20	1.73	2.21	2.65	3.05
CVI SFs (1024^3 comp)	0.62	1.13	1.52	1.82	2.05	2.22
Relative Scaling Exponents	$\widetilde{\zeta}_1$	$\widetilde{\zeta}_2$	$\widetilde{\zeta}_3$	$\widetilde{\zeta}_4$	$\widetilde{\zeta}_5$	$\widetilde{\zeta}_6$
CVI SFs using ESS [a] (1024^3 sol)	0.36	0.70	1.00	1.27	1.51	1.72
CVI SFs using ESS [a] (1024^3 comp)	0.38	0.72	1.00	1.23	1.41	1.56
Polaris Flare [b]	0.37	0.70	1.00	1.27	1.53	1.77
Polaris Flare [c]	0.38	0.71	1.00	1.28	1.54	1.80
Intermittency Model SL94 [d]	0.36	0.70	1.00	1.28	1.54	1.78
Intermittency Model B02 [e]	0.42	0.74	1.00	1.21	1.40	1.56

[a] Using extended self-similarity (ESS) (Benzi et al., 1993).

[b] Measurement of CVI structure functions by Hily-Blant et al. (2008).

[c] Measurement of CVI structure functions by Hily-Blant et al. (2008) using ^{12}CO(2–1) data by Bensch et al. (2001).

[d] Intermittency model $\widetilde{\zeta}_p = p/9 + \mathcal{C}\left(1 - (1 - 2/(3\mathcal{C}))^{p/3}\right)$ defined in eq. (4.28) using a fractal co-dimension $\mathcal{C} = 2$ (She & Leveque, 1994), which corresponds to filamentary structures ($\mathcal{D} = 1$).

[e] Same as [d], but for co-dimension $\mathcal{C} = 1$ (Boldyrev, 2002; Boldyrev et al., 2002) corresponding to sheet-like structures ($\mathcal{D} = 2$).

Table 4.4: Scaling of the structure functions of centroid velocity increments.

for each power-law exponent is indicated in Figure 4.11 and summarized in Table 4.4.

For a direct comparison of CVI structure functions with the study by Hily-Blant et al. (2008, Fig. 8), we apply the extended self-similarity (ESS) hypothesis (Benzi et al., 1993), which states that the inertial range scaling may be extended beyond the inertial range, such that power-law fits can be applied over a larger dynamic range. The ESS hypothesis is used by plotting the pth order $\mathrm{CVISF}_p(\ell)$ against the 3rd order $\mathrm{CVISF}_3(\ell)$ (Benzi et al., 1993). These plots are shown in

of scales for which the turbulence statistics are not directly influenced by the forcing acting on scales larger than the inertial range, and not directly influenced by the viscosity acting on scales smaller than the inertial range. The inertial range is typically very small in numerical experiments, because of the high numerical viscosity caused by the discretization scheme, given the resolutions achievable with current computer technology (see also section 4.6 and section 4.6.3).

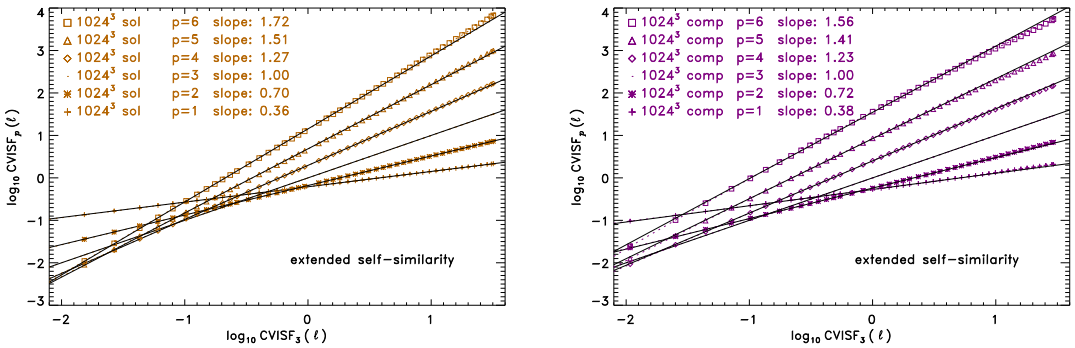

Figure 4.12: Same as Fig. 4.11, but using the extended self-similarity hypothesis (Benzi et al., 1993), allowing for a direct comparison of the scaling exponents of centroid velocity increments with the study by Hily-Blant et al. (2008) for the Polaris Flare and Taurus MC (see Tab. 4.4).

Figure 4.12. Indeed, the scaling range is drastically increased using ESS. All ESS data points are consistent with a single power law for each CVI structure function order $p \leq 6$. We summarize the scaling exponents with and without using the ESS hypothesis in Table 4.4.

Table 4.4 furthermore provides the ESS scaling exponents obtained for the Polaris Flare (Hily-Blant et al., 2008, Tab. 3), as well as the scaling exponents obtained from intermittency models of the structure function scaling exponents

$$\widetilde{\zeta}_p \equiv \frac{\zeta_p}{\zeta_3} = \frac{p}{9} + \mathcal{C}\left(1 - \left(1 - \frac{2}{3\mathcal{C}}\right)^{p/3}\right) \tag{4.28}$$

by She & Leveque (1994) ($\mathcal{C} = 2$) and Boldyrev (2002) ($\mathcal{C} = 1$). In these models, the fractal co-dimension $\mathcal{C}$ is related to the fractal dimension of the most intermittent structures $\mathcal{D}$ by $\mathcal{C} = 3-\mathcal{D}$. The She & Leveque (1994) model assumes 1D vortex filaments as the most intermittent structures ($\mathcal{D} = 1$), whereas the Boldyrev (2002) model assumes sheet-like structures with $\mathcal{D} = 2$.

For solenoidal forcing, the scaling of the CVI structure functions using ESS is very similar to the She & Leveque (1994) model. This model is appropriate for *incompressible* turbulence, for which the most intermittent structures are expected to be filaments (She & Leveque, 1994, $\mathcal{D} = 1$). Interestingly, their model seems to be consistent with the measurements in the Polaris Flare by Hily-Blant et al. (2008) and with our solenoidal forcing case. In contrast, the scaling exponents derived for compressive forcing are better consistent with the intermittency model by Boldyrev (2002, $\mathcal{D} = 2$). This direct comparison indicates that turbulence in the Polaris Flare observed by Hily-Blant et al. (2008) behaves like solenoidally forced turbulence. However, it does not imply that turbulence in the Polaris Flare is close to incompressible, since our numerical models are clearly supersonic in the inertial range (see section 4.6). It rather means that CVI scaling is different from the absolute scaling exponents following from the intermittency models by She & Leveque (1994) and Boldyrev (2002). This is mainly because of two reasons: First, these models do not account for density fluctuations (see however Schmidt et al., 2008), and second, CVIs are 2D projections of the 3D turbulence. The statistics derived from CVIs is a convolution of density and velocity statistics projected onto a 2D plane. As shown by Ossenkopf et al. (2006) and Esquivel et al. (2007), CVI statistics differ significantly from pure velocity statistics, if the ratio of density dispersion to mean density is high. This is usually the case in supersonic flows, and is also the case for both our numerical experiments (see Table 4.1). It explains the difference between the structure functions derived from the pure velocity statistics compared to convolved velocity–density statistics (Schmidt et al., 2008). The deviations from the Kolmogorov (1941)

scaling ($\widetilde{\zeta_p} = p/3$) for the 3D data analyzed in Schmidt et al. (2008) are significantly larger than those derived via CVI in 2D, revealing a significant loss in the signatures of intermittency in the projected CVI data (see also Brunt et al., 2003; Brunt & Mac Low, 2004, for a discussion of projection effects). This also means that direct tests of the theoretical models will be very difficult to achieve, unless a means of relating the CVI-based moments to the 3D moments is developed. Moreover, the fractal dimension of structures changes in a non-trivial way upon projection (Stutzki et al., 1998; Sánchez et al., 2005; Federrath et al., 2009), which severely limits the comparison of CVI statistics with the 3D intermittency models by She & Leveque (1994), Boldyrev (2002) and Schmidt et al. (2008).

Nevertheless, a *direct* comparison of CVI structure function scaling obtained in numerical experiments and observations can provide useful information to distinguish between different parameters of the turbulence, as for instance different turbulence forcings.

4.4.3 Convergence test for the structure functions of centroid velocity increments

For an accurate and reliable determination of the structure function scaling, it must be verified that the number of data pairs used for sampling the structure functions was high enough to yield converged results. There is no general rule to determine a priori the number of data pairs necessary, because the required number of data pairs depends on the underlying statistics of the measured variable itself and on the desired structure function order. However, convergence can be tested by increasing the number of data pairs used for computing the structure functions. Showing that the computed structure functions do not change significantly by further increasing the number of data pairs demonstrates convergence. Furthermore, if convergence is verified for the highest order under consideration, then the structure functions of lower order are also converged. This is because the higher-order structure functions of a variable q reflect the statistics of higher powers of q than the lower order structure functions. This is reflected in the definition of the pth order structure function in equation (4.26).

Figure 4.13 demonstrates convergence for the structure functions of CVIs with orders $p \leq 6$ discussed in section 4.4.2. We only show the compressive forcing case for clarity, but we also verified convergence for the solenoidal forcing case with the same method. Figure 4.13 shows that sampling each structure function with roughly 1.7×10^{10} data pairs is sufficient to yield converged results. The total number of data pairs used to construct the CVI structure functions shown in Figures 4.11 and 4.12 was thus roughly $81 \times 3 \times 1.7 \times 10^{10} \approx 4.1 \times 10^{12}$ from averaging over 81 realizations of the turbulence and three projections along the x, y and z-axes for each of these realizations.

4.5 Principal component analysis

Principal component analysis (PCA) is a multivariate tool (Murtagh & Heck, 1987) introduced by Heyer & Schloerb (1997) for measuring the scaling of interstellar turbulence. It has been used for studying the structure and scaling in several molecular cloud regions, simulations and synthetic images (Brunt & Heyer, 2002a,b; Brunt et al., 2003; Heyer & Brunt, 2004; Heyer et al., 2006). PCA can be used to characterize structure on different scales. For best comparison with observations, we choose to work in position-position-velocity (PPV) space. Since our simulation data are typically stored in position-position-position (PPP) space, we transformed our PPP cubes into PPV space prior to PCA. As for the CVIs discussed in the previous section, we use the approximation of optically thin radiative transfer to derive radiation intensity. This means that we essentially assume that the emission is proportional to the gas density. The PPV data therefore represent a simulated measured intensity $T(x_i, y_i, v_{z,j}) \equiv T_{ij}$ at spatial position

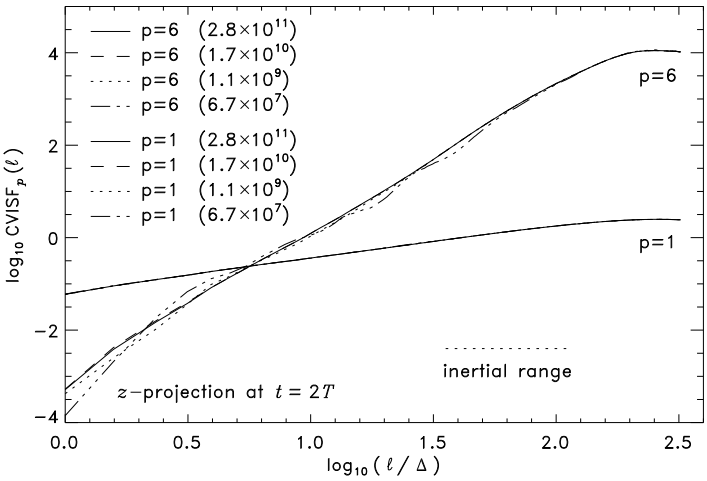

Figure 4.13: The 1st ($p = 1$) and 6th ($p = 6$) order structure functions of the centroid velocity increments sampled with different numbers of data pairs is shown for a single snapshot at time $t = 2\,T$ in z-projection for the case of compressive forcing. The number of data pairs used for sampling is given in brackets. The structure functions of centroid velocity increments are statistically converged for $p \leq 6$ for sample sizes of at least 1.7×10^{10} data pairs per turbulent realization and per projection as used throughout this study.

$\mathbf{r}_i = (x_i, y_i)$ and spectral position $v_{z,j}$. The indices i and j thus represent the spatial and spectral coordinates respectively. A detailed description of the PCA technique is given by Heyer & Schloerb (1997) and Brunt & Heyer (2002a). The most important steps necessary to derive the characteristic length scales and corresponding velocity scales using PCA are described below. First, the covariance matrix

$$U_{jk} = \frac{1}{N_x N_y}\, T_{ij}\, T_{ik} \tag{4.29}$$

is constructed by summation over all spatial points N_x and N_y. Solving the eigenvalue equation

$$\underline{U}\,\mathbf{u}^{(l)} = \lambda^{(l)}\,\mathbf{u}^{(l)} \tag{4.30}$$

yields the l th eigenvalue $\lambda^{(l)}$ and the l th eigenvector $\mathbf{u}^{(l)}$ of the covariance matrix. The subsequent projection

$$I_i^{(l)} = T_{ik}\; u_k^{(l)} \tag{4.31}$$

onto the eigenvectors yields the l th eigenimage $I_i^{(l)}$. Autocorrelation functions (ACFs) are then computed for each of the eigenimages and eigenvectors. The spatial scale on which the two-dimensional ACF of the l th eigenimage falls off by $1/e$ defines the l th characteristic spatial scale. Following the same procedure, the corresponding characteristic velocity scale is determined from the ACF of the l th eigenvector, which contains the spectral information.

Figure 4.14 shows our time- and projection-averaged set of spatial and velocity scales obtained with PCA. We have fitted power laws to the PCA data, which yielded PCA scaling exponents $\alpha_{\rm PCA}$ for solenoidal and compressive forcing respectively. For solenoidal forcing we find $\alpha_{\rm PCA} = 0.66 \pm 0.05$ and for compressive forcing we find $\alpha_{\rm PCA} = 0.76 \pm 0.09$ (see Table 4.5). The different PCA slopes $\alpha_{\rm PCA}$ derived for solenoidal and compressive forcing suggest that by using PCA, differences in the mixture of transverse and longitudinal modes of the velocity field can be detected. However, the difference between solenoidal and compressive forcing is only at the 1-σ

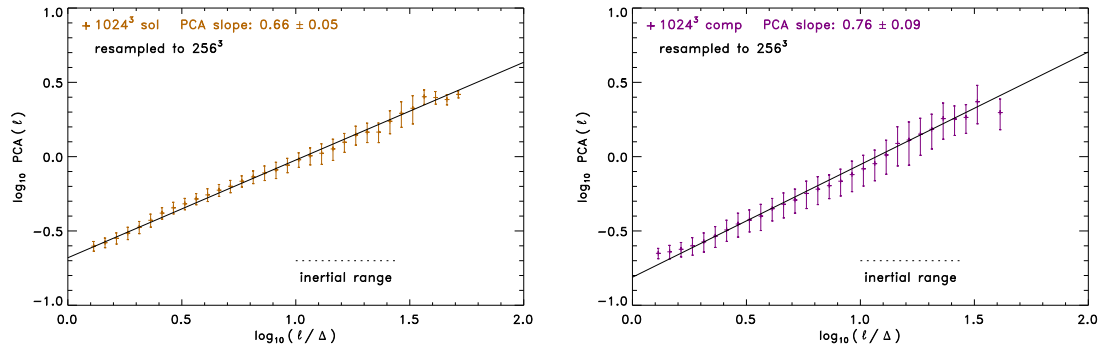

Figure 4.14: Principal component analysis (PCA) for solenoidal (*left*) and compressive forcing (*right*). The PCA slopes obtained for solenoidal and compressive forcings are summarized and compared with observations by Heyer et al. (2006) in Table 4.5. The error bars contain the contribution from temporal variations and from three different projections along the x, y and z-axes. The data were re-sampled from 1024^3 to 256^3 grid points prior to PCA. The re-sampling speeds up the PCA and has virtually no effect on the inertial range scaling (see e.g., Padoan et al., 2006; Federrath et al., 2009).

	1024^3 sol	1024^3 comp	Rosette I [a]	Rosette II [b]	G216-2.5 [c]
$\alpha_{\rm PCA}$	$0.66^{\pm0.05}$	$0.76^{\pm0.09}$			
$\alpha_{\rm PCA}$, ^{12}CO(1–0)			$0.79^{\pm0.06}$	$0.66^{\pm0.06}$	$0.63^{\pm0.04}$
$\alpha_{\rm PCA}$, ^{13}CO(1–0)			$0.86^{\pm0.09}$	$0.67^{\pm0.12}$	$0.56^{\pm0.02}$

[a] PCA by Heyer et al. (2006) of the interior of an H II region in the Rosette MC.

[b] Same as [a], but exterior of the H II region.

[c] PCA by Heyer et al. (2006) for G216-2.5 (Maddalenas's Cloud).

Table 4.5: Comparison of measured PCA scaling slopes.

level.

Heyer et al. (2006) applied PCA to the Rosette MC and to G216-2.5 (Maddalenas's Cloud). These two clouds are quite different in dynamical and evolutionary state, although they exhibit roughly the same turbulence Mach number. Heyer et al. (2006) measured the Mach number $\mathcal{M}_{1\rm pc}\approx4-5$ on a scale of 1 pc for both clouds. The Rosette MC exhibits confirmed massive star formation, whereas G216-2.5 has a low star formation rate, similar to the Polaris Flare discussed in the previous section. Heyer et al. (2006) measured PCA slopes for both clouds and additionally provided the PCA slopes in two distinct subregions of the Rosette MC. The first subregion is inside the H II region (Zone I) surrounding the massive star cluster NGC 2244[3], while the other subregion is outside of this H II region (Zone II). The measured PCA slopes obtained from ^{12}CO and ^{13}CO observations are summarized in Table 4.5 together with our estimates for solenoidal and compressive forcing. The PCA scaling exponent for solenoidal forcing is very close to the PCA scaling exponents derived from the ^{12}CO observations in the G216-2.5 ($\alpha_{\rm PCA}=0.63\pm0.04$) and in Zone II of the Rosette MC ($\alpha_{\rm PCA}=0.66\pm0.06$). In contrast, the PCA slope derived

[3]The formation of the star cluster XA in the Rosette MC was likely triggered by the accumulation of material in the expanding shell surrounding the OB star cluster NGC 2244 (Wang et al., 2008, 2009). This emphasizes the importance of expanding H II regions in triggering subsequent star formation by compression of gas in expanding shells (Elmegreen & Lada, 1977).

from ^{12}CO observations in Zone I of the Rosette MC ($\alpha_{\rm PCA} = 0.79 \pm 0.06$) is better consistent with our compressive forcing case. This indicates that Zone I contains more kinetic energy in compressive modes than Zone II and G216-2.5. The corresponding ^{13}CO observations reported in Heyer et al. (2006) yield slightly larger differences between the PCA scaling exponents derived for Zone I on the one hand, and Zone II and G216-2.5 on the other hand (see also Table 4.5). This supports the idea that Zone I in the Rosette MC, and Zone II as well as G216-2.5 contain quite different amounts of compressive modes in the velocity field, which may be the result of different turbulence forcing mechanisms, similar to the differences obtained in purely solenoidal and compressive forcings.

4.6 Fourier spectra

4.6.1 Velocity Fourier spectra

Fourier spectra of the velocity field $E(k)$ are typically used to distinguish between Kolmogorov (1941) turbulence, $E(k) \propto k^{-5/3}$ and Burgers (1948) turbulence, $E(k) \propto k^{-2}$. For highly compressible, isothermal, supersonic, turbulent flow, it has been shown that the inertial range scaling is close to Burgers turbulence. For instance, Kritsuk et al. (2007) found $E(k) \propto k^{-1.95}$ and Schmidt et al. (2009) obtained $E(k) \propto k^{-1.87}$ from high-resolution numerical simulations.

The Fourier spectrum of a quantity provides a measure of the scale dependence of this quantity. Velocity Fourier spectra are thus defined as

$$E(k)\,\mathrm{d}k = \frac{1}{2} \int \widehat{\mathbf{v}} \cdot \widehat{\mathbf{v}}^* \, 4\pi k^2 \,\mathrm{d}k \;, \tag{4.32}$$

where $\widehat{\mathbf{v}}$ denotes the Fourier transform of the velocity field (e.g., Frisch, 1995). The total Fourier spectrum can be separated into transverse ($\mathbf{k} \perp \widehat{\mathbf{v}}$) and longitudinal ($\mathbf{k} \parallel \widehat{\mathbf{v}}$) parts by applying a Helmholtz decomposition. Note that integrating the transverse energy spectrum yields the kinetic energy in transverse (rotational) modes, while integration of the longitudinal energy spectrum yields the kinetic energy in longitudinal (compressible) modes. Furthermore, by integrating the velocity spectrum from k_1 to k_2, one obtains the kinetic energy content on length scales corresponding to the wavenumber interval $[k_1, k_2]$. Since the mean velocity is zero in our simulations, integration of the total velocity Fourier spectrum $E(k)$ over all wavenumbers yields the total variance of velocity fluctuations σ_v^2:

$$\int_1^{k_\mathrm{c}} E(k)\,\mathrm{d}k = \frac{1}{2}\,\sigma_v^2 \;. \tag{4.33}$$

The upper bound of the integral is the cutoff wavenumber $k_\mathrm{c} = N$ for a cubic dataset with N^3 data points. Thus, $k_\mathrm{c} = 1024$ for our standard resolution of 1024^3 grid cells.

In Figure 4.15 we show the total velocity Fourier spectra $E(k)$ as defined in equation (4.32) together with its decomposition into transverse $E_{\rm trans}$ and longitudinal $E_{\rm long}$ parts for solenoidal and compressive forcing respectively. The prominent signature of the different forcings on the main driving scale, $k = 2$ is clearly noticeable: Solenoidal forcing excites mostly transverse modes, whereas compressive forcing excites mostly longitudinal modes in the velocity field at $k = 2$. However, the forcing has direct influence only for $1 < k < 3$ (see section 4.2.1). Further down the cascade, the turbulent flow develops its own statistics as a result of non-linear interactions in the inertial range $5 \lesssim k \lesssim 15$. We emphasize that this scaling range was chosen very carefully, since turbulence simulations will only provide a small inertial range even at resolutions of 1024^3 grid cells (see, e.g., Klein et al., 2007; Lemaster & Stone, 2009). This is mainly caused by the

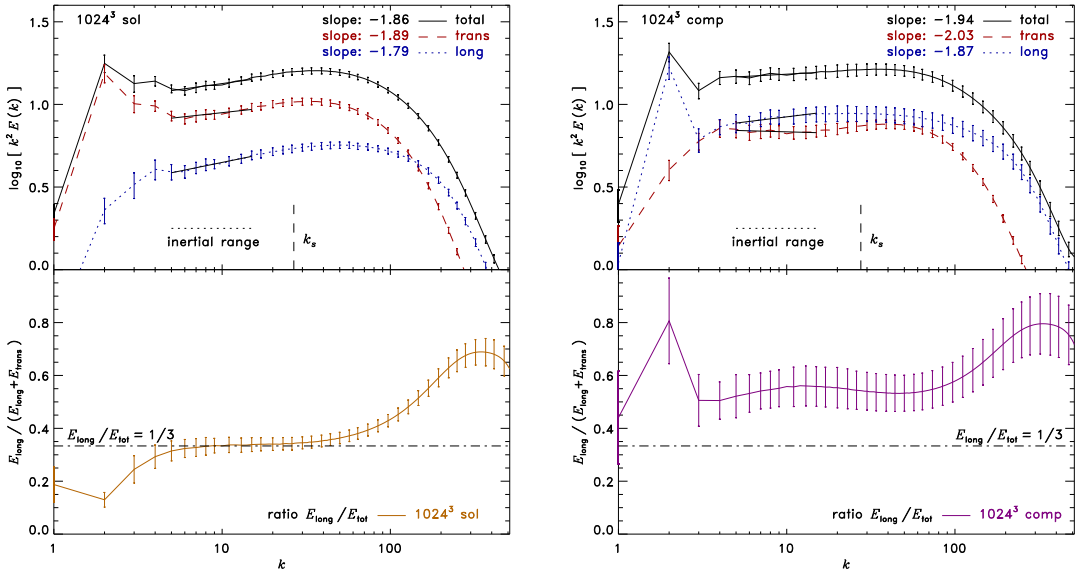

Figure 4.15: *Top panels:* Total, transverse (rotational) and longitudinal (compressible) velocity Fourier spectra $E(k)$ defined in equation (4.32) and compensated by k^2 for solenoidal (*left*) and compressive forcing (*right*). Error bars indicate temporal variations, which account for an uncertainty of roughly ± 0.05 of all scaling slopes reported for the inertial range $5 \lesssim k \lesssim 15$. The inferred inertial range scaling exponents for both solenoidal and compressive forcing are consistent with independent numerical simulations and with observations of the size–linewidth relation (see text). Note that the transverse part, $E_{\rm trans}$ falls off more steeply than the longitudinal part, $E_{\rm long}$ for both forcing types in the inertial range. *Bottom panels:* Ratio of the energy in longitudinal velocity modes $E_{\rm long}$ to the total energy in velocity modes $E_{\rm tot} = E_{\rm trans} + E_{\rm long}$. For solenoidal forcing, we obtain $E_{\rm long}/E_{\rm tot} \approx 1/3$ in the inertial range (horizontal dash-dotted line), because compression can only occur in one of the three spatial dimensions on average (Elmegreen & Scalo, 2004; Federrath et al., 2008b). For compressive forcing, this ratio is roughly 1/2, which corresponds to an equipartition of longitudinal and transverse velocity modes. Note however that compressive forcing can compress the gas in all three spatial dimensions *directly*, whereas solenoidal forcing can only induce compression *indirectly* through the velocity field (Federrath et al., 2008b). The excess of longitudinal modes at high wavenumbers $k \gtrsim 40$ stems from numerical dissipation, which is more effectively dissipating transverse than longitudinal modes on small scales due to the discretization onto a grid. This suggests that roughly 30 grid cells are needed to accurately resolve a vortex, while a shock is typically resolved with roughly 3 grid cells using the piecewise parabolic method (Colella & Woodward, 1984). However, for a numerical resolution of 1024^3 grid cells, we find that wavenumbers $k \lesssim 40$ are almost unaffected by the discretization and by the parameters of the numerical scheme (see section 4.6.3).

bottleneck phenomenon (e.g., Porter et al., 1994; Dobler et al., 2003; Haugen & Brandenburg, 2004; Schmidt et al., 2006; Kritsuk et al., 2007), which may slightly affect the Fourier spectra in the dissipation range. However, the bottleneck phenomenon had no significant impact on the turbulence statistics in our numerical study for wavenumbers $k \lesssim 40$. This is demonstrated in section 4.6.3, where we present the resolution dependence of the Fourier spectra and the dependence on parameters of the PPM numerical scheme. We conclude that the statistical quantities derived for wavenumbers $k \lesssim 40$ are not significantly affected by the numerical scheme or limited resolution applied in the present study.

We apply power-law fits to the inertial range data with the resulting slopes indicated in Figure 4.15 (top panels). Both solenoidal and compressive forcing yield slopes consistent with size–linewidth relations inferred from observations (e.g., Larson, 1981; Myers, 1983; Perault et al., 1986; Solomon et al., 1987; Falgarone et al., 1992; Miesch & Bally, 1994; Ossenkopf & Mac Low, 2002; Padoan et al., 2003; Heyer & Brunt, 2004; Padoan et al., 2006; Ossenkopf et al., 2008b; Heyer et al., 2009), and with the results of independent numerical simulations (e.g., Klessen et al., 2000; Boldyrev et al., 2002; Padoan et al., 2004b; Kritsuk et al., 2007; Schmidt et al., 2009). Note that size–linewidth relations of the form $\sigma_v \propto l^{\gamma}$ with scaling exponents $\gamma = 0.4$–0.5 correspond to Fourier spectra $E(k) \propto k^{-\beta}$ with scaling exponents in the range $\beta = 1.8-2.0$, because $\gamma = (\beta - 1)/2$. However, it must be emphasized that the relation between scaling exponents obtained from observational maps of centroid velocities (as discussed in section 4.4.2) and 3D velocity fields from simulations is non-trivial, because of projection-smoothing and intensity-weighting. Projection-smoothing increases the scaling exponents of the 2D projection of a 3D field such that $\gamma_{\rm 2D} = \gamma_{\rm 3D} + 1/2$ (e.g., Stutzki et al., 1998; Brunt & Mac Low, 2004). However, Brunt & Mac Low (2004) showed that the effect of projection-smoothing is compensated statistically (but not identically) by intensity-weighting of observed centroid velocity maps. Thus, our measurements of velocity scaling seem consistent with observations.

It is important to note that the transverse parts $E_{\rm trans}(k)$ fall off more steeply than the longitudinal parts $E_{\rm long}(k)$ for both forcing types within the inertial range. For solenoidal forcing, we find $E_{\rm trans}(k) \propto k^{-1.89}$ and $E_{\rm long}(k) \propto k^{-1.79}$, and for compressive forcing, $E_{\rm trans}(k) \propto k^{-2.03}$ and $E_{\rm long}(k) \propto k^{-1.87}$. This result indicates that longitudinal modes can survive down to small scales, such that compression may not be neglected anywhere in the turbulent cascade. Lemaster & Stone (2009, Fig. 9, 10) obtain $E_{\rm trans}(k) \propto k^{-2.0}$ and $E_{\rm long}(k) \propto k^{-1.8}$ for their hydrodynamical model with solenoidal forcing at a resolution of 1024^3 grid points in the Athena code. This is consistent with our findings for the scale dependence of the transverse and longitudinal parts and shows that the kinetic energy in longitudinal modes must not be neglected within the inertial range.

In order to quantify the relative importance of compression over rotation in the turbulent motions, we present plots of the ratio

$$\Psi(k) = \frac{E_{\rm long}(k)}{E_{\rm long}(k) + E_{\rm trans}(k)} = \frac{E_{\rm long}(k)}{E_{\rm tot}(k)} \tag{4.34}$$

in the bottom panels of Figure 4.15. Solenoidal forcing yields $\Psi \approx 1/3$ in the inertial range. We emphasize that the ratio $\Psi \approx 1/3$ was expected from the fact that compression can only occur in one of the three available spatial dimensions on average in the case of supersonic flow driven by a purely solenoidal force field (Elmegreen & Scalo, 2004; Federrath et al., 2008b). This is the fundamental idea on which the heuristic model of the density dispersion–Mach number relation given by equation (4.20) was based. For compressive forcing, we find $\Psi \approx 1/2$ in the inertial range as a result of the direct compression induced by compressive forcing. Thus, solenoidal and compressive forcing produce quite similar amounts of compressive modes in the velocity field ($\Psi \approx 1/3$ versus $\Psi \approx 1/2$). This means that even fully compressive forcing can behave very similar to solenoidal forcing in the inertial range, as far as pure velocity statistics are concerned.

However, we show in the next section that the density statistics are very different in the inertial range. The same is true for combined density–velocity statistics (see section 4.8 below).

We also note here that the rise of Ψ at $k \gtrsim 40$ for both forcing types is a numerical effect, which comes from the discretization of the velocity field onto a grid with finite resolution. This shows that energy in rotational modes cannot be accounted for accurately if vortices are smaller than roughly 30 grid cells in each direction, whereas longitudinal modes (i.e. shocks) may still be well resolved. As a result, the transverse kinetic energy is underestimated for $k \gtrsim 40$ up to the resolution limit $k_\mathrm{c} = 1024$. However, the plateau of almost constant Ψ for $k \lesssim 40$ indicates that the discretization had no significant influence on scales with wavenumbers $k \lesssim 40$. The effect of underestimating the transverse kinetic energy due to the discretization of fluid variables is also observed in the ZEUS-3D simulations by Pavlovski et al. (2006, Fig. 2) for wavenumbers $k \gtrsim 10$ at numerical resolution of 256^3 grid cells. In section 4.6.3, we furthermore demonstrate that our results for the Fourier spectra are not affected by the specific choice of parameters of the numerical scheme for wavenumbers $k \lesssim 40$.

4.6.2 Logarithmic density Fourier spectra

In analogy to the velocity Fourier spectra $E(k)$, we define logarithmic density fluctuation spectra

$$S(k)\,\mathrm{d}k = \int (\widehat{s - \langle s \rangle})\,(\widehat{s - \langle s \rangle})^* \, 4\pi k^2 \,\mathrm{d}k \; . \tag{4.35}$$

We subtract the mean logarithmic density prior to the Fourier transformation such that $S(k)$ is a measure of density fluctuations as a function of scale. Therefore, integrating $S(k)$ over all scales yields the square of the logarithmic density dispersion σ_s

$$\int_1^{k_\mathrm{c}} S(k)\,\mathrm{d}k = \sigma_s^2 \; . \tag{4.36}$$

Furthermore, integrating $S(k)$ over the wavenumber range $[k_1, k_2]$ yields the typical density fluctuations on length scales corresponding to this range of scales.

Figure 4.16 (left) shows the logarithmic density fluctuation spectra $S(k)$ together with the total velocity Fourier spectra $E(k)$ in one plot. In contrast to the scaling of the velocity $E(k)$, the scaling of $S(k) \propto k^{-\beta}$ is significantly different for solenoidal ($\beta = 1.56 \pm 0.05$) and compressive forcing ($\beta = 2.32 \pm 0.09$) in the inertial range.

4.6.3 Resolution study of the Fourier spectra and their dependence on the numerical scheme

The resolution and type of numerical method adopted to model supersonic turbulence are expected to critically affect the scaling of Fourier spectrum functions in the inertial range (e.g., Klein et al., 2007; Kritsuk et al., 2007; Padoan et al., 2007). In this section, we investigate the dependence of our Fourier spectra on the numerical resolution and on the numerical scheme used in the present study.

Resolution study

Figure 4.17 shows velocity Fourier spectra $E(k)$ defined in equation (4.32) for numerical resolutions of 256^3, 512^3 and 1024^3 grid points. The inertial range scaling is indeed affected by the numerical resolution. For solenoidal forcing, the inertial range scaling exponent β at resolution of 256^3 grid cells is roughly 13% higher than the scaling exponent at a resolution of 1024^3. However,

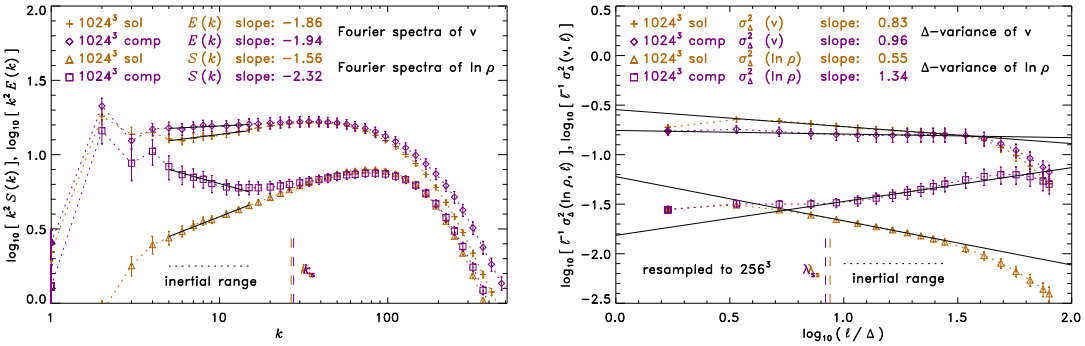

Figure 4.16: *Left panel:* Fourier spectra of the velocity, $E(k)$ defined in eq. (4.32) (crosses and diamonds) and Fourier spectra of the logarithmic density fluctuations, $S(k)$ defined in eq. (4.35) (triangles and squares) for solenoidal and compressive forcing, respectively. Both $E(k)$ and $S(k)$ are compensated by k^2 allowing for a better determination of the inertial range scaling. The density fluctuation power spectra differ significantly in the inertial range $5 \lesssim k \lesssim 15$ with $S(k) \propto k^{-1.56}$ for solenoidal and $S(k) \propto k^{-2.32}$ for compressive forcing. The scale on which the density fluctuation spectra from solenoidal and compressive forcing cross each other and where the slope obtained in compressive forcing breaks and approaches the shallower slope of the solenoidal forcing case roughly coincides with the sonic wavenumber k_s (vertical dashed lines) defined in eq. (4.40). *Right panel:* Same as left panel, but instead of using Fourier spectra to determine the inertial range scaling, we use the Δ-variance method to derive the scaling slopes in physical space. Note that the scaling slopes α obtained with the Δ-variance technique are related to the slopes β of the Fourier spectra by $\beta = \alpha + 1$ (Stutzki et al., 1998). Error bars denote 1-σ temporal fluctuations.

the difference between the inertial range scaling at 512^3 and 1024^3 is less than 3% for solenoidal forcing. For compressive forcing, the difference between the inertial range scaling exponents at resolutions of 512^3 and 1024^3 grid cells is less than 1%. This result indicates that the systematic dependence of the inertial range scaling on the numerical resolution is less than 3% for both solenoidal and compressive forcings. It should be emphasized that variance effects introduced by different realizations of the turbulence are typically on the order of 5–10% (see error bars in Figure 4.16), which is higher than the systematic errors introduced by resolution effects, as long as the numerical resolution is at least 512^3 grid cells.

Dependence on parameters of the piecewise parabolic method

We used the piecewise parabolic method (PPM) (Colella & Woodward, 1984) to integrate the equations of hydrodynamics (eqs. 4.2 and 4.3). PPM improves on the finite-volume scheme originally developed by Godunov (1959) by representing the flow variables with piecewise parabolic functions, which makes the PPM second-order accurate in smooth flows. However, PPM is also particularly suitable for the accurate modeling of turbulent flows involving sharp discontinuities, such as shocks and contact discontinuities. For that purpose, PPM uses a lower artificial viscosity controlled by the PPM diffusion parameter K. In three simulations with resolutions of 512^3 grid cells, we varied the PPM diffusion parameter K between 0.0, 0.1 and 0.2. Note that $K = 0.1$ is the value recommended by Colella & Woodward (1984), which was used for all production runs throughout this study. The PPM algorithm furthermore includes a steepening mechanism to keep contact discontinuities from spreading over too many cells. In one additional run at 512^3, we switched off the PPM steepening algorithm to check its influence on our results.

Figure 4.18 shows that the velocity spectra $E(k)$ decrease faster with increasing diffusion parameter K for wavenumbers $k \gtrsim 40$. It is expected that the scheme dissipates more kinetic

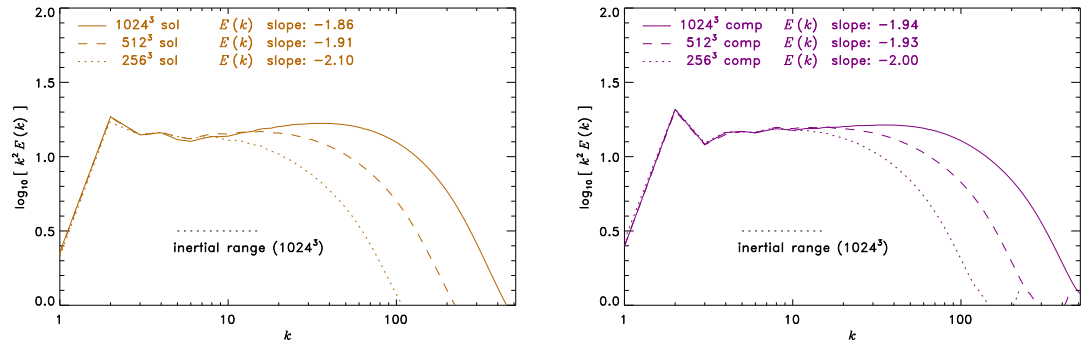

Figure 4.17: Time-averaged velocity Fourier spectra $E(k)$ defined in equation (4.32) for numerical resolutions of 256^3, 512^3 and 1024^3 grid points obtained with solenoidal forcing (*left*) and compressive forcing (*right*). The inferred inertial range scaling is converged to within less than 3% at the typical resolution of 1024^3 grid points used throughout this study for both types of forcing.

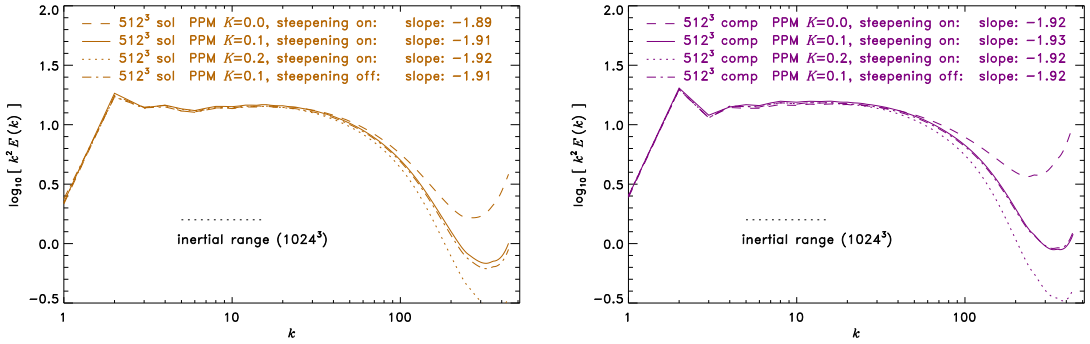

Figure 4.18: Dependence of the time-averaged velocity Fourier spectra $E(k)$ on parameters of the piecewise parabolic method (PPM) (Colella & Woodward, 1984) at fixed resolution of 512^3 grid cells. Varying the PPM diffusion parameter K between 0.0, 0.1 and 0.2 affects the dissipation range at wavenumbers $k \gtrsim 40$. However, the effect of varying the PPM diffusion parameter is negligible for $k \lesssim 40$. Switching off the PPM steepening algorithm for contact discontinuities has also virtually no effect on the Fourier spectra at $k \lesssim 40$.

energy on small scales with increasing K, because the PPM diffusion algorithm is designed to act on shocks only (Colella & Woodward, 1984, eq. 4.5). In contrast, Figure 4.18 demonstrates that the Fourier spectra at wavenumbers $k \lesssim 40$ are hardly affected by the PPM diffusion algorithm for both solenoidal and compressive forcings. Note that Kritsuk et al. (2007) reported that their results for the inertial range scaling are highly sensitive to the choice of PPM diffusion parameter in the ENZO code. However, our results demonstrate that the choice of PPM diffusion parameter only affects the inertial range scaling within less than 1%, which is clearly less than the influence of the numerical resolution and less than the typical snapshot-to-snapshot variations. Figure 4.18 furthermore demonstrates that the PPM contact discontinuity steepening has negligible effects for simulations of supersonic turbulence.

The results obtained here support our conclusion in section 4.6 that the Fourier spectra at resolutions of 1024^3 grid cells are robust for wavenumbers $k \lesssim 40$.

4.7 Δ-variance of the velocity and density

The Δ-variance technique provides a complementary method for measuring the scaling exponent of Fourier spectra in the physical domain using a wavelet transformation (Stutzki et al., 1998). We apply the Δ-variance to our simulation data using the tool developed and provided by Ossenkopf et al. (2008a). This tool implements an improved version of the original Δ-variance (Stutzki et al., 1998; Bensch et al., 2001). The Δ-variance measures the amount of structure on a given length scale ℓ by filtering the dataset $q(\mathbf{r})$ with an up-down-function $\bigodot_\ell$ (typically a French-hat or Mexican-hat filter) of size ℓ, and computing the variance of the filtered dataset. The Δ-variance is defined as

$$\sigma_\Delta^2(\ell) = \left\langle \left(q(\mathbf{r}) * \bigodot_\ell(\mathbf{r}) \right)^2 \right\rangle_{\mathbf{r}} , \tag{4.37}$$

where the average is computed over all data points at positions $\mathbf{r} = (x, y, z)$. The operator $*$ stands for the convolution. We use the original French-hat filter with a diameter ratio of 3.0 as in previous studies using the Δ-variance technique (e.g., Stutzki et al., 1998; Mac Low & Ossenkopf, 2000; Ossenkopf et al., 2001; Ossenkopf & Mac Low, 2002; Ossenkopf et al., 2006).

Figure 4.16 (right panel) shows that the inertial range scaling obtained with the Δ-variance technique is in very good agreement with the scaling measured in the Fourier spectra. Note that the scaling exponents β of Fourier spectra are ideally related to the scaling exponents α of the Δ-variance by $\alpha = \beta - 1$ (Stutzki et al., 1998). The small deviations from this analytical relation are caused by the finite size of the dataset, the re-sampling procedure prior to the Δ-variance analysis applied here and the choice of the filter function (Ossenkopf et al., 2008a). However, these deviations are on the order of 4% and therefore smaller than the average snapshot-to-snapshot variations.

For the Δ-variance of the velocity field, $\sigma_\Delta^2(v, \ell) \propto \ell^\alpha$, we find scaling exponents $\alpha = 0.83 \pm 0.05$ for solenoidal forcing and $\alpha = 0.96 \pm 0.05$ for compressive forcing. This translates into size-linewidth relations $\sigma_\Delta(v, \ell) \propto \ell^\gamma$ with scaling exponents $\gamma = \alpha/2$. Thus, we find $\gamma = 0.42 \pm 0.03$ for solenoidal forcing and $\gamma = 0.48 \pm 0.03$ for compressive forcing. Ossenkopf & Mac Low (2002) found a common power-law slope $\gamma = 0.5 \pm 0.04$ for the Polaris Flare, ranging over three orders of magnitude in length scale from about 50 pc down to roughly 0.05 pc. This scaling exponent is roughly consistent with both our solenoidal and compressive forcing data, but slightly better consistent with compressive forcing. Note that the centroid velocity analysis by Ossenkopf & Mac Low (2002) is also subject to the combined effects of projection-smoothing and intensity-weighting discussed in Brunt & Mac Low (2004) and discussed in section 4.6.1. Thus, the comparison of 3D scaling of the velocity with 2D observations should always be made with the caution that projection-smoothing and intensity-weighting roughly cancel each other out in a statistical sense (Brunt & Mac Low, 2004).

We are not aware of any observational study considering the scaling of *logarithmic* intensity. The use of logarithmic density is useful in isothermal simulations, because the equations of hydrodynamics, equations (4.2) and (4.3), are invariant under transformations in $s = \ln(\rho/\langle\rho\rangle)$. In observations however, the intensity, T is measured instead of the density, but the intensity can be transformed into $s' = \ln(T/\langle T\rangle)$, which gives a normalized quantity similar to $s = \ln(\rho/\langle\rho\rangle)$. This enables a straightforward comparison of simulation and observational data (yet with the limitations listed in section 4.10). It is also interesting to look at logarithmic density and intensity scaling, because this scaling parameter is used in analytic models of the mass distribution of cores and stars by Hennebelle & Chabrier (2008, 2009).

Unlike a *logarithmic* scaling analysis, the scaling of the *linear* integrated intensity, $\sigma_\Delta(\rho, \ell) \propto \ell^\gamma$ was analyzed by Stutzki et al. (1998) and Bensch et al. (2001). They found $\gamma \approx 0.5-0.9$ for the Polaris Flare, in good agreement with the scaling exponent $\gamma = 0.8 \pm 0.1$ obtained from solenoidal

forcing in Federrath et al. (2009). In contrast, the scaling exponent obtained for compressive forcing is significantly higher ($\gamma = 1.4 \pm 0.3$). Bensch et al. (2001) measured scaling exponents $\gamma \approx 1.0$–1.5 in small-scale maps ($\ell \lesssim 0.1\,\mathrm{pc}$) of the Polaris Flare and in Perseus/NGC1333, which are consistent with our estimates for compressive forcing (Federrath et al., 2009, Tab. 1). Since both solenoidal and compressive forcings display strong intermittency at short lags (see Fig. 4.10), intermittency appears to be primarily measurable on scales smaller than the turbulence injection scale. Taking together the results by Bensch et al. (2001) with ours for solenoidal and compressive forcing indicates that interstellar turbulence is driven primarily on large scales, potentially with a significant amount of compressive modes present on the forcing scale (see also Brunt et al., 2009).

4.8 Fourier spectra and Δ-variance scaling of the combined quantities $\rho^{1/2}v$ and $\rho^{1/3}v$

In this section we present the Fourier spectra and Δ-variance results for the combined quantities $\rho^{1/2}v$ and $\rho^{1/3}v$. Usually, the pure velocity scaling is considered without density weighting. However, for highly supersonic turbulence it is interesting to investigate the scaling of combinations of density and velocity. Note that CVIs (section 4.4) and PCA (section 4.5) also analyze convolutions of density and velocity statistics. Figure 4.19 (top panel) shows a repetition of Figure 4.16 (scaling of v) together with the scaling of $\rho^{1/2}v$ (middle panel) and $\rho^{1/3}v$ (bottom panel) for direct comparison. Since Fourier spectra and Δ-variance analyses always represent the mean squares of these quantities, $\rho^{1/2}v$ corresponds to the scaling of the kinetic energy density $\rho\, v^2$. As shown by Kritsuk et al. (2007) (see also Henriksen, 1991; Fleck, 1996), $\rho^{1/3}v$ corresponds to a constant energy flux within the inertial range. This idea was first proposed by Lighthill (1955). Using the eddy turnover time t_ℓ as the typical evolution timescale of a turbulent fluctuation on scale ℓ, the constancy of energy flux in the inertial range is defined as

$$\frac{\rho v^2}{t_\ell} \propto \frac{\rho v^2}{\ell/v} \propto \frac{\rho v^3}{\ell} \propto \mathrm{const}\,, \tag{4.38}$$

which leads to the original Kolmogorov (1941) scaling (but now including density variations),

$$\rho^{1/3}v \propto \ell^{1/3} \tag{4.39}$$

for the quantity $\rho^{1/3}v$. Using the extended self-similarity hypothesis (Benzi et al., 1993), we showed in Schmidt et al. (2008) that the relative scaling exponents of $\rho^{1/3}v$ provide a more universal scaling compared to the velocity scaling without density weighting. Figure 4.19 (bottom panel) shows that the absolute scaling inferred from the Fourier spectra of $\rho^{1/3}v$ is indeed close to the Kolmogorov (1941) scaling (scaling proportional to $k^{-5/3}$) for solenoidal forcing, which is in agreement with the results obtained in Kritsuk et al. (2007). However, compressive forcing yields significantly steeper scaling (also for $\rho^{1/2}v$), which is close to Burgers (1948) turbulence (scaling proportional to k^{-2}). The corresponding results inferred from the Δ-variance analyses are compatible with the Fourier spectra to within the uncertainties. Both quantities $\rho^{1/2}v$ and $\rho^{1/3}v$ show breaks in the scaling close to the sonic wavenumber k_s for compressive forcing.

4.9 The sonic scale

The velocity Fourier spectra $E(k)$ discussed in section 4.6.1 can be described as power laws $E(k) \propto k^{-\beta}$ with negative power-law exponents, $\beta > 1$. This means that the typical velocity

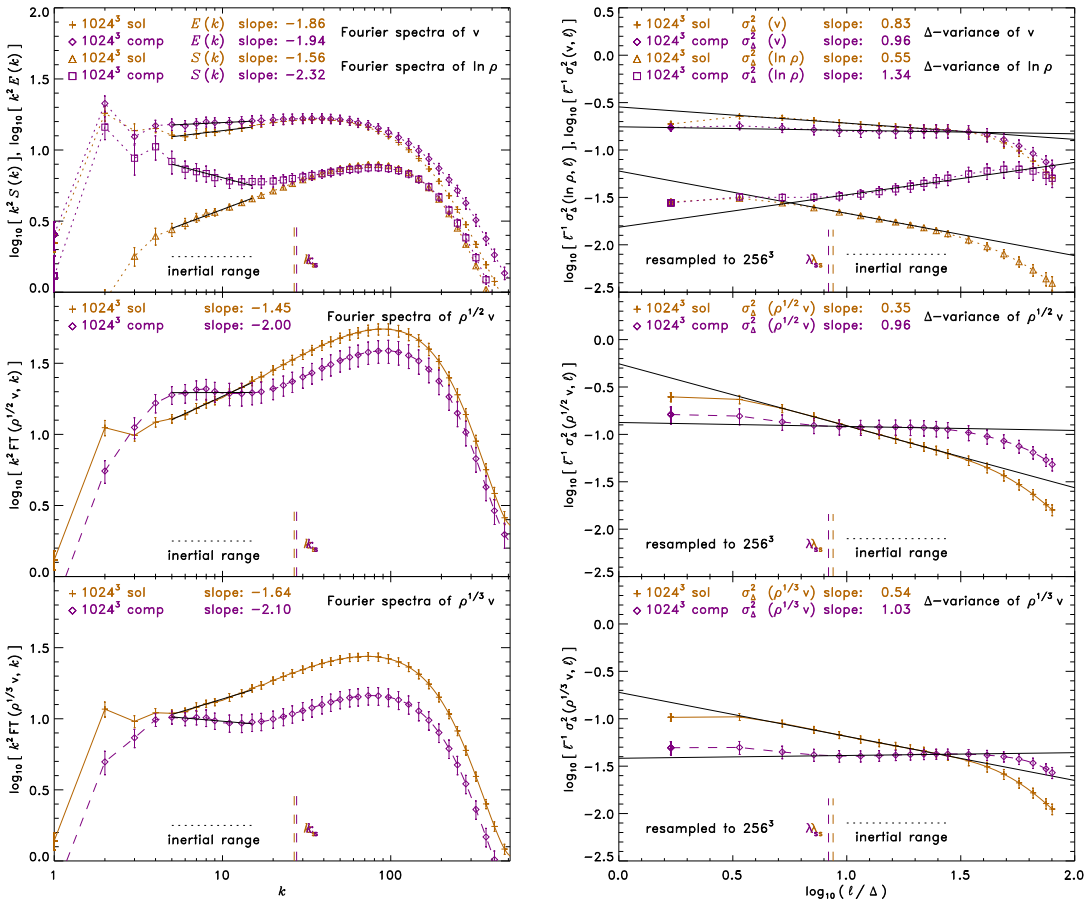

Figure 4.19: *Top panels:* Same as Figure 4.16. *Middle panels:* Same as top panels, but instead of the Fourier spectra and Δ-variances of v, the Fourier spectra and Δ-variances of the density-weighted velocity $\rho^{1/2}v$ are shown. The quantity $\rho^{1/2}v$ has physical reference to kinetic energy. *Bottom panels:* Same as middle panels, but the Fourier spectra and Δ-variances of the density-weighted velocity $\rho^{1/3}v$ are shown. The quantity $\rho^{1/3}v$ has physical reference to a constant kinetic energy dissipation within the inertial range (Kritsuk et al., 2007; Schmidt et al., 2008).

fluctuations are decreasing when going to smaller scales. The value of the integral $\int_{k_1}^{k_c} E(k)\,\mathrm{d}k$ over a finite range of wavenumbers with k_1 as the lower bound and the cutoff wavenumber k_c as the upper bound therefore becomes smaller with increasing k_1. Thus, the turbulent flow is expected to change from a supersonic to a subsonic flow on a certain length scale. This scale separates the supersonic regime on large scales, where the velocity fluctuations are supersonic from the subsonic regime, which is located on smaller scales, where the typical velocity fluctuations are small compared to the thermal motions of the gas. This transition scale is called the *sonic scale* λ_s. Following Schmidt et al. (2009), the corresponding *sonic wavenumber* k_s in Fourier space is defined by solving the equation

$$\int_{k_s}^{k_c} E(k)\,\mathrm{d}k \simeq \frac{1}{2}\,c_s^2 \tag{4.40}$$

implicitly for k_s. The sonic scale is thus defined as the scale on which the mean square velocity fluctuations become comparable to the mean square of the sound speed.

We solved equation (4.40) for the sonic wavenumbers k_s for both the solenoidal and compressive forcing cases. The sonic wavenumbers for solenoidal and compressive forcings are indicted in Figure 4.16 (left) as vertical dashed lines. We find $k_\mathrm{s} = 26$ for solenoidal forcing and $k_\mathrm{s} = 27$ for compressive forcing. The corresponding sonic scales λ_s are also indicated in Figure 4.16 (right) as vertical dashed lines.

The Fourier spectra $S(k)$ shown in Figure 4.16 (left) and the corresponding Δ-variance curves shown in Figure 4.16 (right) for solenoidal and compressive forcing cross each other roughly at the sonic wavenumber and on the sonic scale, respectively. For compressive forcing $S(k)$ is significantly steeper on scales larger than the sonic scale ($k \lesssim k_\mathrm{s}$) compared to scales $k \gtrsim k_\mathrm{s}$. $S(k)$ for compressive forcing approaches the shallower slope of $S(k)$ for solenoidal forcing at $k \approx k_\mathrm{s}$. For $k \gtrsim k_\mathrm{s}$ there are neither significant differences between the density spectra $S(k)$ nor the velocity spectra $E(k)$ for solenoidal and compressive forcings.

The strong break in the logarithmic density fluctuation spectra $S(k)$ for compressive forcing around k_s appears to be linked to the transition from supersonic motions on large scales to subsonic motions on scales smaller than the sonic scale. In order to quantify this, we estimated the typical density fluctuations on supersonic scales ($k < k_\mathrm{s}$) by evaluating $\sigma_s^2(k<k_\mathrm{s}) = \int_1^{k_\mathrm{s}} S(k)\,\mathrm{d}k$. We obtain $\sigma_s(k<k_\mathrm{s}) \approx 1.22$ for solenoidal and $\sigma_s(k<k_\mathrm{s}) \approx 3.05$ for compressive forcing, which is on the order of the logarithmic density dispersions σ_s found from the density PDFs (see Table 4.1). This means that most of the power in density fluctuations is located on scales larger than the sonic scale. In contrast, on scales smaller than the sonic scale the typical density fluctuations can be estimated by solving $\sigma_s^2(k>k_\mathrm{s}) = \int_{k_\mathrm{s}}^{k_\mathrm{c}} S(k)\,\mathrm{d}k$. We obtain $\sigma_s(k>k_\mathrm{s}) \approx 0.45$ for both types of forcing. This shows that density fluctuations on scales below the sonic scale are small compared to the typical density fluctuations in the supersonic regime at $k < k_\mathrm{s}$ (see also Vázquez-Semadeni et al., 2003). Moreover, Figure 4.16 shows that the typical logarithmic density fluctuations are similar for both solenoidal and compressive forcings on scales smaller than the sonic scale. Note that the sum of logarithmic density fluctuations on all scales is

$$\left[\sigma_s^2(k<k_\mathrm{s}) + \sigma_s^2(k>k_\mathrm{s})\right]^{1/2} \approx 1.30 \tag{4.41}$$

for solenoidal forcing and

$$\left[\sigma_s^2(k<k_\mathrm{s}) + \sigma_s^2(k>k_\mathrm{s})\right]^{1/2} \approx 3.08 \tag{4.42}$$

for compressive forcing. As expected from equation (4.36), these values are in excellent agreement with the total logarithmic density dispersions σ_s, obtained from the density PDFs shown in Table 4.1.

A spatial representation of the structures exhibiting subsonic velocity dispersions is shown in Figure 4.20 (bottom panel). These structures are identified in slices through the local Mach number M as regions with $M \lesssim 1$. Figure 4.20 (top panel) displays the corresponding density slices. The density–Mach number correlations are quite weak, as expected for isothermal turbulence (cf. section 4.3.6). However, Figure 4.5 shows that high-density regions exhibit lower Mach numbers on average. In real molecular clouds, the sonic scale is expected to be located on length scales $\lambda_\mathrm{s} \approx 0.1\,\mathrm{pc}$ within factors of a few (e.g., Falgarone et al., 1992; Barranco & Goodman, 1998; Goodman et al., 1998; Schnee et al., 2007). For instance, Heyer et al. (2006) found $\lambda_\mathrm{s} \approx 0.3-0.4\,\mathrm{pc}$ for the Rosette MC and $\lambda_\mathrm{s} \approx 0.1-0.2\,\mathrm{pc}$ for G216-2.5. Furthermore, the sonic scale may be associated with the transition to coherent cores (Goodman et al., 1998; Ballesteros-Paredes et al., 2003; Klessen et al., 2005). Recent simulations of turbulent core formation by Smith et al. (2009) also suggest that star-forming cores typically exhibit transonic to subsonic velocity dispersions. This can be understood if cores form close to the sonic scale in a globally supersonic turbulent medium. Figure 4.20 suggests that regions with subsonic ve-

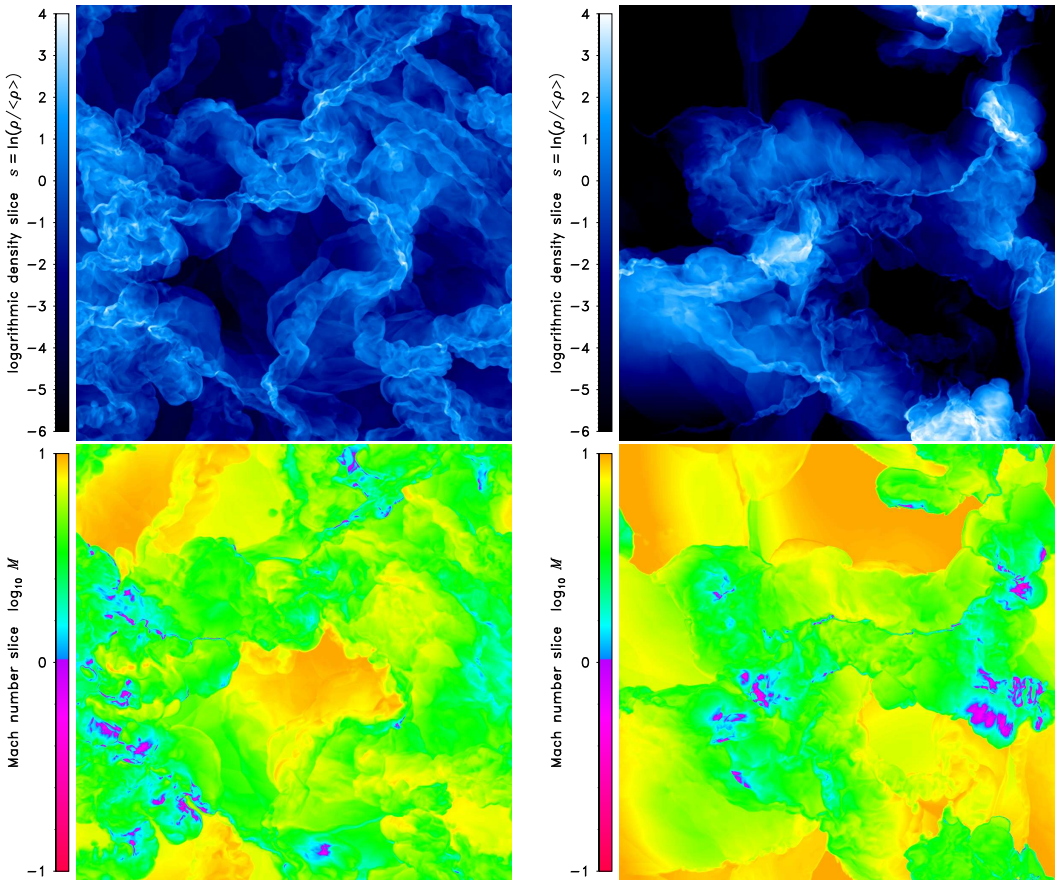

Figure 4.20: z-slices through the local density (*top panels*) and Mach number fields (*bottom panels*) at $z = 0$ and $t = 2\,T$ for solenoidal forcing (*left*), and compressive forcing (*right*). Regions with subsonic velocity dispersions (Mach < 1) are distinguished from regions with supersonic velocity dispersions (Mach > 1) in the color scheme. The correlation between density and Mach number is quite weak. However, as shown in Fig. 4.5, high-density regions exhibit lower Mach numbers on average. Thus, dense cores might naturally exhibit transonic to subsonic velocity dispersions, because their sizes are expected to be comparable to the sonic scale. The sonic scale may be the transition scale to coherent cores (e.g., Goodman et al., 1998). Although many of these 'cores' here are transient, some of them are dense enough to become gravitationally bound, and accumulate enough mass to decouple from the overall supersonic turbulent flow.

locity dispersions have different shapes and sizes for both solenoidal and compressive forcings. These structures are transient objects, forming and dissolving in the turbulent flow (e.g., see also Vázquez-Semadeni et al., 2005b). If we had included self-gravity in the present study, some of these regions would have likely collapsed gravitationally, because turbulent support becomes insufficient in some of these subsonic cores (e.g., Mac Low & Klessen, 2004).

4.10 Limitations

As a result of the simplicity of the hydrodynamic simulations presented in this thesis, comparisons with observational data are limited and should be considered with caution. These limitations

are listed below:

- We assume an isothermal equation of state, so our models are strictly speaking only applicable to molecular gas of low enough density to be optically thin to dust cooling. Variations in the equation of state can lead to changes in the density statistics (e.g., Passot & Vázquez-Semadeni, 1998; Li et al., 2003; Audit & Hennebelle, 2009). The results of the present study apply primarily to the dense interstellar molecular gas for which an isothermal equation of state is an adequate approximation (Wolfire et al., 1995; Ferrière, 2001; Pavlovski et al., 2006; Glover et al., 2009).

- The numerical resolution of our simulations is limited. As shown in Figure 4.6, the high-density tails of the PDFs systematically shift to higher densities (see also Hennebelle & Audit, 2007; Kitsionas et al., 2009; Glover et al., 2009; Price & Federrath, 2010). However, the mean and the dispersions are well converged at the numerical resolutions of 256^3, 512^3 and 1024^3 grid points used in this study. The inertial scaling range is very small even at resolutions of 1024^3 grid cells. However, the systematic difference in the inertial range scaling between resolutions of 512^3 and 1024^3 grid points is less than 3% (see section 4.6.3), which is less than the typical temporal variations between different realizations of the turbulent velocity and density fields.

- Our simulations adopt periodic boundary conditions. This implies that our simulations can only be representative of a subpart of a molecular cloud, for which we study turbulence statistics with high-resolution numerical experiments. However, we cannot take account of the boundary effects in real molecular clouds. Simulations of large-scale colliding flows (e.g., Heitsch et al., 2006; Vázquez-Semadeni et al., 2006; Hennebelle et al., 2008; Banerjee et al., 2009) are more suitable for studying the boundary effects during the formation of molecular clouds.

- We only analyzed driven turbulence. However, there is ongoing debate about whether turbulence is driven or decaying (e.g., Stone et al., 1998; Mac Low, 1999; Lemaster & Stone, 2008; Offner et al., 2008). We are aware of the possibility that turbulence may in fact be excited on scales larger than the size of molecular clouds (e.g., Brunt et al., 2009), but may be globally decaying (if not replenished by a mechanism acting on galactic scales). As discussed in section 4.2.1, this large-scale decay can however act as an effective turbulence forcing on smaller scales, because kinetic energy is transported from large to small scales through the turbulence cascade.

- Centroid velocity and principal component analysis were applied to PPV cubes constructed from the simulated velocity and density fields assuming optically thin radiation transfer to estimate the intensity of emission lines. This approximation will of course not hold for optically thick tracers. A full radiative transfer calculation taking account of the level population (e.g., Keto et al., 2004; Steinacker et al., 2006; Pinte et al., 2009; Hauschildt & Baron, 2009; Baron et al., 2009) of self-consistently formed and evolved chemical tracer molecules (e.g., Glover & Mac Low, 2007a,b; Glover et al., 2009) would be needed to advance on this issue.

- We neglected magnetic fields. In order to test the role of magnetic fields in star formation (e.g., Crutcher et al., 2009; Lunttila et al., 2008), we would have to include the effects of magnetic fields and ambipolar diffusion. For instance, the IMF model by Padoan & Nordlund (2002) requires magnetic fields to explain the present-day mass function, while it is still not clear whether magnetic fields are dynamically important for typical molecular clouds. However, Heyer et al. (2008) showed that magnetohydrodynamic turbulence in the Taurus MC may lead to an alignment of flows along the field lines.

- The present study did not include the effects of self-gravity, because we specifically focus on the pure turbulence statistics obtained in solenoidal and compressive forcings. In a follow-up study, we will include self-gravity and sink particles (e.g., Bate et al., 1995; Krumholz et al., 2004; Jappsen et al., 2005; Federrath et al., 2010a) to study the influence of the different forcings on the mass distributions of sink particles. First results indicate that the sink particle formation rate is at least one order of magnitude higher for compressive forcing compared to solenoidal forcing. Vázquez-Semadeni et al. (2003) argue that the star formation efficiency is mainly controlled by the RMS Mach number and the sonic scale of the turbulence (cf. section 4.9). However, our preliminary results of simulations including self-gravity show that the star formation efficiency measured at a given time (i.e., the star formation rate) is much higher for compressive forcing than for solenoidal forcing with the *same* RMS Mach number *and* sonic scale. This provides additional support to our main conclusion that the type of forcing must be taken into account in any theory of turbulence-regulated star formation. This needs to be investigated in future, high-resolution numerical experiments including self-gravity and sink particles.

4.11 Summary and conclusions

We presented high-resolution hydrodynamical simulations of driven isothermal supersonic turbulence, which showed that the structural characteristics of turbulence forcing significantly affect the density and velocity statistics of turbulent gas (see also Schmidt et al., 2009). We compared solenoidal (divergence-free) forcing with compressive (curl-free) turbulence forcing. Five different analysis techniques were used to compare our simulation data with existing observational data reported in the literature: probability density functions (PDFs), centroid velocity increments, principal component analysis, Fourier spectrum functions, and Δ-variances. We find that different regions in the turbulent ISM exhibit turbulence statistics consistent with different combinations of solenoidal and compressive forcing. Varying the forcing parameter $\zeta \in [0,1]$ in equation (4.9), we showed that a continuum of turbulence statistics exists between the two limiting cases of purely solenoidal ($\zeta = 1$) and purely compressive forcing ($\zeta = 0$). For $\zeta > 0.5$, turbulence behaves almost like in the case of purely solenoidal forcing, while for $\zeta < 0.5$, turbulence is highly sensitive to changes in ζ (cf. 4.8). Note that $\zeta = 0.5$ represents the natural forcing mixture used in many previous turbulence simulations. Because the behavior of all forcing mixtures with $\zeta > 0.5$ is similar to that of purely solenoidal turbulence with $\zeta = 1$ (see 4.8), turbulence statistics is biased towards finding solenoidal-like values. However, observations of regions around massive stars that drive swept-up shells into the surrounding medium (e.g., the shell in the Perseus MC and in the Rosette MC) seem better consistent with models of mainly compressive forcing ($\zeta < 0.5$). Note that expanding H II regions around massive stars, and supernova explosions typically create such swept-up shells, which are considered to be important drivers of interstellar turbulence (Mac Low & Klessen, 2004; Breitschwerdt et al., 2009)[4]. A detailed list of our results is provided below:

1. The standard deviation (dispersion) of the probability distribution function (PDF) of the gas density is roughly three times larger for compressive forcing than for solenoidal forcing. This holds for both the 3D density distributions (Figure 4.4 and Table 4.1) and the 2D column density distributions (Figure 4.7 and Table 4.3). We extended the density dispersion–Mach number relations, equation (4.18) and (4.19) originally investigated by Padoan et al. (1997) and Passot & Vázquez-Semadeni (1998). Based on the varying degree of compression obtained by solenoidal and compressive forcing, we developed a heuristic model for the proportionally constant b in the density dispersion–Mach number relation,

[4]See also Tamburro et al. (2009) for an observational study.

which takes account of the forcing parameter ζ (Federrath et al., 2008b). In the case of compressive forcing the proportionality constant b is close to $b \approx 1$, which confirms the result by Passot & Vázquez-Semadeni (1998). In contrast, solenoidal forcing yields $b \approx 1/3$, which is in excellent agreement with recent independent high-resolution numerical simulations using solenoidal forcing (e.g., Beetz et al., 2008).

2. A parameter study of eleven models with varying forcing parameter $\zeta = [0, 1]$, separated by $\Delta\zeta = 0.1$ showed that the heuristic model given by equation (4.20) can only serve as a first-order approximation to the forcing dependence of b (cf. Fig. 4.8). We showed that b scales with the normalized power of compressible modes in the velocity field, $\langle\Psi\rangle$. A good approximation for b is given by $b \approx \sqrt{D}\,\langle\Psi\rangle$, where $D = 3$ in 3D turbulence.

3. We compared the density PDFs in our models with observations in the Perseus MC by Goodman et al. (2009). Goodman et al. (2009) obtained the largest density dispersion in all of the Perseus MC within a region that they call the Shell region. This Shell surrounds the massive star HD 278942 suggesting that the Shell is an expanding H II region. Swept-up shells represent geometries that can be associated with compressive turbulence forcing, because an expanding spherically symmetric shell is driven by a fully divergent velocity field. This may explain why the Shell region in the Perseus MC exhibits the largest density dispersion among all of the subregions in the Perseus MC investigated by Goodman et al. (2009). We emphasize that the Shell region does not exhibit the highest RMS Mach number, but has an intermediate value among the examined subregions in the Perseus MC (Pineda et al., 2008). Furthermore, as pointed out by Goodman et al. (2009) the density dispersion–Mach number relation of the form given by equation (4.19) for a fixed parameter b is *not* observed for the Perseus MC. This apparent contradiction with equation (4.19) for a fixed parameter b is resolved, if different turbulence forcing mechanisms operate in different subregions of the Perseus MC, such that b is a function of the mixture of solenoidal and compressive modes ζ as shown in Figure 4.8.

4. The turbulent density PDF is a key ingredient for the analytical models of the core mass function (CMF) and the stellar initial mass function (IMF) by Padoan & Nordlund (2002) and Hennebelle & Chabrier (2008, 2009), as well as for the star formation rate models by Krumholz & McKee (2005), Krumholz et al. (2009) and Padoan & Nordlund (2009), and the star formation efficiency model by Elmegreen (2008). We showed that the dispersion of the density probability distribution is not only a function of the RMS Mach number, but also depends on the nature of the turbulence forcing. All the analytical models above rely on integrals over the density PDF. Since the dispersion of the density PDF is highly sensitive to the turbulence forcing, we conclude that star formation properties derived in those analytical models are strongly affected by the assumed turbulence forcing mechanism.

5. The PDFs $p_s(s)$ of the logarithm of the density $s = \ln(\rho/\langle\rho\rangle)$ are roughly consistent with log-normal distributions for both solenoidal and compressive forcings. However, the distributions clearly exhibit non-Gaussian higher-order moments, which are associated with intermittency. Including higher-order corrections represented by skewness and kurtosis is absolutely necessary to obtain a good analytic approximation for the PDF data, because the constraints of mass conservation (eq. 4.11) and normalization (eq. 4.12) of the PDF must always be fulfilled. Even stronger deviations from perfect log-normal distributions are expected if the gas is non-isothermal (e.g., Passot & Vázquez-Semadeni, 1998; Scalo et al., 1998; Li et al., 2003), magnetized (e.g., Li et al., 2008) or self-gravitating (e.g., Klessen, 2000; Li et al., 2004; Federrath et al., 2008a; Kainulainen et al., 2009), which often leads to exponential wings or to power-law tails in the PDFs.

6. Non-Gaussian wings of the density PDFs are a signature of intermittent fluctuations, which we further investigated using centroid velocity increments (CVIs). We find strong non-Gaussian signatures for small spatial lags ℓ in the PDFs of the CVIs (Figure 4.9). These PDFs exhibit values of the kurtosis significantly in excess of that expected for a Gaussian (see Figure 4.10). Figure 4.10 can be compared with Hily-Blant et al. (2008, Fig. 7), who analyzed CVIs in the Taurus MC and in the Polaris Flare. The values of the kurtosis $\mathcal{K}$ measured in the Polaris Flare are consistent with exponential values ($\mathcal{K} = 6$) for short spatial lags, which is also compatible with the results of solenoidal forcing. In contrast, compressive forcing yields values of the kurtosis twice as large at small lags, which indicates that compressive forcing exhibits stronger intermittency. The scaling of the CVI structure functions supports the conclusion that compressive forcing exhibits stronger intermittency compared to solenoidal forcing (see Figure 4.12 and Table 4.4). The scaling exponents of the CVI structure functions obtained for solenoidal forcing are in good agreement with the results by Hily-Blant et al. (2008) obtained in the Polaris Flare for the CVI structure functions up to the 6th order using the extended self-similarity hypothesis.

7. We applied principal component analysis (PCA) to our models. A comparison of the PCA scaling exponents $\alpha_{\rm PCA}$ with the PCA study in the Rosette MC and in G216-2.5 by Heyer et al. (2006) showed that solenoidal forcing is consistent with the PCA scaling measured in G216-2.5 and with the PCA scaling measured in the *outside* of the H II region (Zone II) surrounding the OB star cluster NGC 2244 in the Rosette MC. On the other hand, the PCA scaling *inside* this H II region (Zone I) is in good agreement with the PCA scaling obtained for compressive forcing (Table 4.5). Similar to the Shell region in the Perseus MC, the H II region in the Rosette MC (Zone I) displays signatures of mainly compressive forcing. Recent numerical simulations by Gritschneder et al. (2009) also show that ionization fronts driven by massive stars can efficiently excite compressible modes in the velocity field.

8. The Fourier spectra of the velocity fluctuations showed that they follow power laws in the inertial range with $E(k) \propto k^{-1.86\pm0.05}$ for solenoidal forcing and $E(k) \propto k^{-1.94\pm0.05}$ for compressive forcing. Both types of forcing are therefore compatible with the scaling of velocity fluctuations inferred from observations and independent numerical simulations. The Fourier spectra of the logarithmic density fluctuations scale as $S(k) \propto k^{-1.56\pm0.05}$ for solenoidal forcing and $S(k) \propto k^{-2.32\pm0.09}$ for compressive forcing in the inertial range.

9. The inertial range scaling of the velocity and logarithmic density fluctuations inferred from the Fourier spectra was confirmed using the Δ-variance technique.

10. We computed the sonic scale by integrating the velocity Fourier spectra. The sonic scale separates supersonic turbulent fluctuations on large scales from subsonic turbulent fluctuations on scales smaller than the sonic scale. We found a break in the density fluctuation spectrum $S(k)$ for compressive forcing roughly located on the sonic scale. The typical density fluctuations computed by integration of $S(k)$ over scales larger than the sonic scale are consistent with the logarithmic density dispersions derived from the probability density functions for solenoidal and compressive forcings. On the other hand, the typical density fluctuations on scales smaller than the sonic scale are significantly smaller for both forcing types, which may reflect the transition to coherent cores (e.g., Goodman et al., 1998). Indeed, observations show that cores typically have transonic to subsonic internal velocity dispersions (e.g., Benson & Myers, 1989; André et al., 2007; Kirk et al., 2007; Ward-Thompson et al., 2007; Lada et al., 2008; Foster et al., 2009; Friesen et al., 2009; Beuther & Henning, 2009). This can be understood if cores form near the sonic scale at the stagnation points of shocks in a globally supersonic turbulent ISM (cf. section 4.9).

11. We found that the correlations between the local densities and the local Mach numbers are typically quite weak (Figures 4.5 and 4.20). However, this weak correlation shows that the local Mach number M decreases with increasing density as $M(\rho) \propto \rho^{-0.06}$ for solenoidal forcing and $M(\rho) \propto \rho^{-0.05}$ for compressive forcing for densities above the mean density. This means that dense gas tends to have smaller velocity dispersions on average, consistent with observations of dense protostellar cores.

Chapter 5

Modeling collapse and accretion in turbulent gas clouds: implementation and comparison of sink particles in AMR and SPH

Star formation is such a complex process that accurate numerical tools are needed to quantitatively examine the mass distribution and accretion of fragments in collapsing, turbulent, magnetized gas clouds. To enable a numerical treatment of this regime, I implemented sink particles in the adaptive mesh refinement (AMR) hydrodynamics code FLASH, the details of which are described in this Chapter. Sink particles are created in regions of local gravitational collapse, and their trajectories and accretion can be followed over many dynamical times. We perform a series of tests including the time integration of circular and elliptical orbits, the collapse of a Bonnor-Ebert sphere and a rotating, fragmenting cloud core. We compare the collapse of a highly unstable singular isothermal sphere to the theory by Shu (1977), and show that the sink particle accretion rate is in excellent agreement with the theoretical prediction. To model eccentric orbits and close encounters of sink particles accurately, we show that a very small timestep is often required, for which we implemented subcycling of the N-body system. We emphasize that a sole density threshold for sink particle creation is insufficient in supersonic flows, if the density threshold is below the opacity limit. In that case, the density can exceed the threshold in strong shocks that do not necessarily lead to local collapse. Additional checks for bound state, gravitational potential minimum, Jeans instability and converging flows are absolutely necessary for a meaningful creation of sink particles. We apply our new sink particle module for FLASH to the formation of a stellar cluster, and compare to a smoothed particle hydrodynamics (SPH) code with sink particles. Our comparison shows encouraging agreement of gas properties, indicated by column density distributions and radial profiles, and of sink particle formation times and positions. We find excellent agreement in the number of sink particles formed, and in their accretion and mass distributions. The results of this Chapter are published in Federrath et al. (2010a).

5.1 Introduction

Molecular clouds are turbulent, magnetized, self-gravitating objects. Supersonic turbulence, in particular, plays an important role in shaping the cloud structure, and in controlling star formation, because it creates the seeds for local gravitational collapse (Elmegreen & Scalo, 2004; Scalo & Elmegreen, 2004; Mac Low & Klessen, 2004; McKee & Ostriker, 2007). Due to the filamentary, fractal structure of the interstellar medium, and due to the large density contrasts, star formation in turbulent molecular clouds proceeds in multiple regions at the same time in

parallel, reflecting the hierarchical and fractal nature of the gas density probability distribution (e.g., Scalo, 1990; Vázquez-Semadeni, 1994; Elmegreen & Falgarone, 1996; Klessen et al., 2000; Federrath et al., 2008b; Goodman et al., 2009; Federrath et al., 2009). Moreover, stars typically form in clusters (Lada & Lada, 2003), showing similar fractal patterns as the gas clouds from which they form (Sánchez & Alfaro, 2009).

To model this complex interplay of turbulence and gravity that eventually leads to cloud fragmentation and to stellar birth with a well-defined initial mass function, it is necessary to follow the freefall collapse of each individual fragment, while keeping track of the global evolution of the entire cloud at the same time. The fundamental numerical difficulty with this approach is that the freefall timescale $t_{\rm ff}$ decreases with increasing density,

$$t_{\rm ff} = \left(\frac{3\pi}{32G\rho}\right)^{1/2} . \tag{5.1}$$

Following the freefall collapse from typical molecular cloud densities up to stellar densities requires the numerical scheme to cover about ten orders of magnitude in timescales. Modeling each individual collapse over such an enormous dynamic range, and following the large-scale evolution over several global freefall times in a single hydrodynamical simulation is beyond the capabilities of modern numerical schemes and supercomputers. Thus, if one wants to model the large-scale evolution of the molecular cloud alongside the collapse of individual regions far beyond the collapse of the first object, the individual runaway collapse must be cut-off in a controlled way, and replaced by a subgrid model.

There are two different subgrid models to tackle this problem in numerical simulations. The first approach is to heat up the gas that exceeds a given density threshold, $\rho_{\rm res}$, which is necessarily related to the achievable numerical resolution. We call this procedure 'Jeans heating'. This relative heating of the gas is often modeled by changing the effective equation of state above the density threshold (e.g., by setting the adiabatic exponent to $\gamma > 4/3$ for $\rho > \rho_{\rm res}$). Heating up the gas above a density threshold increases the sound speed locally and thus increases the Jeans length,

$$\lambda_{\rm J} = \left(\frac{\pi c_{\rm s}^2}{G\rho}\right)^{1/2} , \tag{5.2}$$

until the gas is stabilized against gravitational collapse. The problem with the Jeans heating approach is that any parcel of gas above a given density threshold is heated artificially, although the actual gas equation of state should still be close to isothermal so long as the density threshold is below the opacity limit. This is the case for density thresholds smaller than about $10^{-14}\,{\rm g\,cm^{-3}}$ (e.g., Larson, 1969; Penston, 1969; Larson, 2005; Jappsen et al., 2005, and references therein). Moreover, gas can become denser than the threshold value in shocks that do not necessarily lead to the formation of a gravitationally bound structure. Thus, shocked gas not going into freefall collapse will be heated up artificially. An additional problem of the Jeans heating approach is that the increasing sound speed in the heated regions can reduce the Courant timestep (see section 5.2.6) to prohibitively small values.

The second type of subgrid model is to use so called 'sink particles', a method invented by Bate, Bonnell, & Price (1995) for smoothed particle hydrodynamics (SPH), and first adopted for Eulerian, Adaptive Mesh Refinement (AMR) by Krumholz, McKee, & Klein (2004). If the gas has reached a given density, a sink particle is introduced, which can accrete the gas exceeding the threshold, without altering the thermal physics. However, sink particles are supposed to represent bound objects that are/or will be going into freefall collapse, and thus, a density threshold for their creation is insufficient. As for the 'Jeans heating', shock compression can temporarily create local densities larger than the threshold *without* triggering gravitational collapse in that region. Previous grid-based implementations of sink particles are mostly based on a density threshold

criterion. If the density threshold for sink particle creation is smaller than the opacity limit (about $10^{-14}\,\mathrm{g\,cm^{-3}}$), we show that spurious sink particles are created in shocks that did not create a gravitationally bound and collapsing structure. Here, we present an implementation of sink particles for the Eulerian, AMR code FLASH that avoids this problem by using a series of checks for gravitational collapse similar to Bate et al. (1995) prior to sink particle creation, such that only gravitationally bound and collapsing gas is turned into sink particles.

We show that the star formation efficiency and the number of fragments is overestimated, if additional, physical checks (e.g., checks for a gravitationally bound and collapsing state) in addition to a density threshold are ignored prior to sink particle formation. We believe that it is also crucial to investigate the resulting mass distribution of the sink particles, because any successful numerical and analytical model of cloud collapse and star formation is expected to account for the observed mass distribution of cores and stars, i.e., the clump, core and stellar initial mass functions (e.g., Klessen et al., 1998; Klessen, 2001; Kroupa, 2001; Padoan & Nordlund, 2002; Chabrier, 2003; Mac Low & Klessen, 2004; Elmegreen & Scalo, 2004; Larson, 2005; Bonnell & Bate, 2006; McKee & Ostriker, 2007; Krumholz & Bonnell, 2007; Hennebelle & Chabrier, 2008, 2009). The sink particle implementation presented here enables us to address the star formation efficiency and rate, as well as the mass distribution of fragments obtained in numerical experiments in a robust and quantitative way.

We test our sink particle implementation against a number of standard fragmentation and orbit integration tests. Since stars typically form in dense cluster, close encounters of stars are common, and thus we dedicate significant attention to testing our scheme for its ability to capture close orbits and close encounters. Moreover, in the densest existing star clusters, even merging of stars might be possible (Zinnecker & Yorke, 2007). Our scheme also supports sink particle merging for such extreme cases.

We compare our sink particles with the original sink particle implementation of Bate et al. (1995) in their SPH code. It is a standard SPH code, and most SPH implementations of sink particles are based on their approach (e.g., Jappsen et al., 2005). We find that FLASH and SPH show encouraging agreement in the obtained mass distribution of sink particles. This code comparison strengthens our confidence in numerical calculations of collapse and fragmentation, using AMR on the one hand and SPH on the other hand. Here, we primarily introduce the new sink particle module for FLASH and present a series of initial tests for follow-up studies using sink particles. For instance, there are various SPH studies with sink particles of purely hydrodynamic collapse. Our comparison with SPH shows that these results are robust. However, one would also like to test the influence of magnetic fields and ambipolar diffusion on star formation as well. The first significant steps toward this were taken in SPH simulations of magnetized turbulent clouds recently (Price & Bate, 2008). However, the numerical representation of tangled and wound-up magnetic fields in SPH turbulence simulations is (still) limited (Brandenburg, 2010; Price, 2010). Our grid-based approach of sink particles should allow a refined modeling of collapsing, turbulent, magnetized clouds in follow-up studies, including additional physical processes like ambipolar diffusion and self-consistent jet and outflow formation.

In section 5.2 the new sink particle implementation for the AMR code FLASH is explained in detail. A series of simple and more complex tests of the sink particle implementation is presented in section 5.3. In section 5.4 we analyze the formation of a star cluster, and compare column density images, radial profiles, and mass distributions of sink particles obtained with the FLASH code and with a standard SPH code. In section 5.5, we summarize our results and discuss the importance of checks for gravitational instability in addition to a density threshold to avoid spurious creation of sink particles, and to avoid overestimating the star formation efficiency and rate.

5.2 Numerical implementation of sink particles in FLASH

5.2.1 The basic FLASH code

The FLASH code[1] (Fryxell et al., 2000; Dubey et al., 2008) is an adaptive mesh refinement (AMR) code (Berger & Colella, 1989). For purely hydrodynamic studies, it uses the piecewise parabolic method (Colella & Woodward, 1984) by default to integrate the equations of hydrodynamics. For magnetohydrodynamical (MHD) studies, FLASH provides an 8-wave Roe solver. In addition, a new approximate Riemann solver for ideal-MHD (Bouchut et al., 2007, 2009), which preserves positive states in highly supersonic MHD turbulence was recently developed for FLASH by Waagan (2009). The corresponding scheme for preserving positive states in purely hydrodynamic studies has been tested successfully in Klingenberg et al. (2007). Moreover, Duffin & Pudritz (2008) have recently developed a non-ideal MHD scheme to model ambipolar diffusion. This module is also implemented in the FLASH code and works (like all other physics modules) within the AMR framework. FLASH is parallelized with MPI, and output files are written in the versatile HDF5 format. The self-gravity of the gas is treated with an iterative multigrid solver (here we use the multigrid solver implemented in FLASH v2.5, recently refined for v3 by Ricker, 2008). Moreover, a tree-based gravity solver was developed for FLASH (Richard Wünsch 2009, priv. comm.), which is currently being modified to run on graphics processing units. Our sink particle implementation is compatible with existing FLASH modules, i.e., it can be used with the different hydrodynamical and magnetohydrodynamical schemes, including the ambipolar diffusion module, and with either the multigrid or the tree gravity solver. FLASH has been extensively tested against laboratory experiments (Calder et al., 2002) and other codes (Dimonte et al., 2004; Heitmann et al., 2005; Agertz et al., 2007; Tasker et al., 2008; Kitsionas et al., 2009).

For the implementation of the new sink particle module, we made use of the N-body capabilities of FLASH. Once created, sink particles are free to move within the Cartesian computational domain, independent of the underlying grid, i.e., they move in the Lagrangian frame of reference, while the grid points are fixed in space (Eulerian frame of reference). The outer boundary conditions, i.e., *outflow*, *reflecting*, or *periodic* also apply to the sink particles in the simulation box.

5.2.2 Sink particle creation

Prior to sink particle creation, it is necessary to perform a number of tests, since we want to avoid creating spurious sink particles in regions that are not undergoing freefall collapse. The basic idea is to first check each computational cell for whether it exceeds a given density threshold $\rho_{\rm res}$. If this is the case, a roughly spherical region with a given radius $r_{\rm acc}$ centered on that cell is temporarily created from the gas. This radius is usually the same as the accretion radius of the sink particle, so we will also call it $r_{\rm acc}$ in the following (see section 5.2.3 for the implementation of accretion). We denote the region surrounding the cell with $\rho > \rho_{\rm res}$ the control volume V. It is defined such that it covers all computational cells with integer indexes (i, j, k), such that

$$V = \sum_{ijk} \Delta V(i, j, k) \tag{5.3}$$

for all $(i\Delta x)^2 + (j\Delta y)^2 + (k\Delta z)^2 \leq r_{\rm acc}^2$. The central cell of each temporary control volume is at $(i, j, k) = (0, 0, 0)$, and $\Delta V(i, j, k) = \Delta x \Delta y \Delta z$ is the computational cell volume at spatial position (i, j, k). It is then checked whether the gas in the control volume V

[1] `http://flash.uchicago.edu/website/home/`

- is on the highest level of refinement,
- is converging,
- has a central gravitational potential minimum,
- is Jeans-unstable,
- is bound,
- is not within $r_{\rm acc}$ of an existing sink particle.

These checks are similar to the checks introduced in Bate et al. (1995) prior to sink particle formation in SPH. Only after these conditions are fulfilled altogether, a sink particle is formed from the gas within the control volume and placed in the center of mass of the gas from which the particle forms. Each of the criteria for sink particle creation is discussed at more detail in the following. The order in which these checks are performed does not matter, however, during code development and tests it became clear that it is useful to do the least computationally expensive checks first to make a preselection of cells prior to the more expensive checks.

Density threshold

We introduced sink particles in the FLASH code to follow collapse calculations for many dynamical times without violating the Truelove criterion for the gas density (Truelove et al., 1997). The Truelove criterion states that in order to avoid spurious fragmentation in numerical collapse calculations in grid codes, the Jeans length (eq. 5.2) must be resolved with at least four grid cells, $\lambda_{\rm J}/\Delta x \geq 4$ (Truelove et al., 1997). For MHD calculations, Heitsch et al. (2001) find that more than four cells are required. It should be emphasized that the resolution criteria by Truelove et al. (1997) and Heitsch et al. (2001) are only meaningful in regions that are undergoing self-gravitational collapse (further discussed in section 5.2.2). Usually, adaptive mesh refinement (AMR) is used to guarantee that the resolution is always sufficient to satisfy these criteria. However, for collapse calculations involving multiple collapsing regions the pure AMR approach only works for the first object going into collapse. This is because freefall collapse is a runaway process in which the first gravitationally bound over-density collapses the fastest. Due to the Courant condition (see section 5.2.6), this leads to smaller and smaller timesteps, which stalls the evolution of the entire simulation. Introducing sink particles in regions that are going into freefall collapse on the highest level of refinement provides a way for cutting-off this runaway process in a controlled fashion. However, as discussed in the introduction, it is insufficient to form sink particles solely based on a density threshold in supersonically turbulent gas. Additional checks are necessary.

Refinement check

The Jeans refinement criterion discussed in the previous subsection is also used to resolve the Jeans length of the gas up to the highest level of the AMR grid hierarchy. Only when the Jeans refinement reaches the highest AMR level, sink particles are allowed to form. Since the accretion radius $r_{\rm acc}$ of a sink particle is coupled to the grid resolution criterion (see section 5.4.2), sink particles should always be located on the highest level of the AMR hierarchy. This is taken care of by an additional refinement criterion for sink particles, which guarantees that any grid cell located inside the accretion radius of any existing sink particle will always be adaptively refined up to the highest AMR level.

Converging flow check

In order to guarantee that the gas supposed to form a sink particle is in freefall collapse, we introduced a check for convergence of the flow toward the center of the control volume, $\nabla \cdot \mathbf{v} < 0$. Unlike Krumholz et al. (2004) we implemented this criterion such that not just the total divergence toward the central cell must be negative, but also that the flows along each of the principal axes must be directed toward the center. The converging flow check alone is insufficient, because $\nabla \cdot \mathbf{v} < 0$ can also be fulfilled by a localized collision of multiple shocks that do not necessarily produce a gravitationally bound structure. Thus, here we use the converging flow check primarily as a preselection of cells that are considered for sink particle formation, before other, more computationally expensive checks are performed below. Only the combination of the converging flow check with the gravitational potential minimum, bound state and Jeans-instability checks actually guarantees that the gas is in freefall collapse.

Gravitational potential minimum check

We guarantee that sink particles can only be created if the central cell of the control volume V defined in equation (5.3) is the minimum of the local gravitational potential ϕ inside the control volume. The central cell $(i, j, k) = (0, 0, 0)$ must fulfill the constraint

$$\phi(0, 0, 0) = \min_{ijk} [\phi(i, j, k)] \tag{5.4}$$

for sink particle creation.

Jeans instability check

If the converging flow check and the potential minimum criterion are fulfilled, the control volume is checked for Jeans-instability. The thermal energy $E_{\rm th}$ and the gravitational energy $E_{\rm grav}$ of the gas in the control volume are calculated as follows:

$$E_{\rm th} = \frac{1}{2} \sum_{ijk} M(i, j, k) c_{\rm s}^2(i, j, k) \tag{5.5}$$

$$E_{\rm grav} = \sum_{ijk} M(i, j, k) \phi(i, j, k) \,, \tag{5.6}$$

where $c_{\rm s}(i, j, k)$ is the sound speed, $\phi(i, j, k)$ is the gravitational potential due to the gas mass inside the control volume and

$$M(i, j, k) = \rho(i, j, k)\, \Delta V(i, j, k) \tag{5.7}$$

is the mass inside each cell (i, j, k). The relation

$$|E_{\rm grav}| > 2E_{\rm th} \tag{5.8}$$

must hold for sink particle creation, which means that the gas exceeds the Jeans mass within the control volume. In the case of magnetic fields this criterion is modified such that the magnetic pressure is taken into account as well. The magnetic energy,

$$E_{\rm mag} = \frac{1}{8\pi} \sum_{ijk} |\mathbf{B}(i, j, k)|^2 \, \Delta V(i, j, k) \,, \tag{5.9}$$

is computed and added to the right hand side of equation (5.8) to get a modified version of the Jeans criterion, which takes into account the additional pressure provided by magnetic field fluctuations.

Check for bound state

For successful sink particle creation, the total gas energy inside the control volume must be negative,

$$E_{\rm grav} + E_{\rm th} + E_{\rm kin} + E_{\rm mag} < 0\,. \tag{5.10}$$

The gravitational, thermal, and magnetic energies are computed from equations (5.6), (5.5) and (5.9). The kinetic energy

$$E_{\rm kin} = \frac{1}{2}\sum_{ijk} M(i,j,k)\,|\mathbf{v}(i,j,k) - \mathbf{v}_{\rm cm}|^2 \tag{5.11}$$

is determined from the velocity dispersion of the gas, where the center of mass motion,

$$\mathbf{v}_{\rm cm} = \frac{\sum_{ijk} M(i,j,k)\,\mathbf{v}(i,j,k)}{\sum_{ijk} M(i,j,k)} \tag{5.12}$$

is subtracted. Only if equation (5.10) holds, the gas within the control volume is a bound system.

Proximity check

A new sink particle cannot be created within the accretion radius of an already existing sink particle. Gas that exceeds the density threshold within the accretion radius of an existing particle is accreted by that particle, if the gas passes the accretion checks as explained in the following section.

Comparison with other sink particle implementations

Except for the refinement and potential minimum checks, all checks used here are analogous to the sink particle implementation by Bate et al. (1995) for SPH. Test simulations showed that the potential minimum check prevents almost all spurious sink particles (particles not representing bound and collapsing gas) from forming. However, the Jeans instability and bound state checks are still required in regions of large velocity dispersions, occurring in supersonic, shock-dominated flows. Moreover, magnetic effects are not taken into account by the potential minimum check, but are covered with the Jeans instability and bound state checks (as in Bate et al., 1995, except for our inclusion of the magnetic energy).

The Eulerian, AMR implementations of sink particles by Krumholz et al. (2004) and Wang et al. (2010), and the Eulerian, uniform grid implementation by Padoan & Nordlund (2009) use the density threshold check, the refinement check (only Krumholz et al., 2004; Wang et al., 2010) and the converging flow check (only the total divergence is required to be negative, which is implicitly covered by the density threshold check), but no check for potential minimum, Jeans instability, bound state and proximity of existing sink particles. Thus, a significantly larger number of sink particles is typically created, which requires subsequent merging in Krumholz et al. (2004) and Wang et al. (2010). This merging of sink particles is used as an effective accretion in addition to their Bondy-Hoyle accretion model, while Padoan & Nordlund (2009) use no merging of sink particles, but direct accretion from the grid based on the density threshold.

It is important to note here that our sink particle implementation (as the implementation by Bate et al., 1995) allows the density to exceed the density threshold set by the Truelove et al.

(1997) criterion in some cases. However, this does not mean that our implementation violates the Truelove criterion. By definition, the Truelove criterion only applies to gravitationally bound gas in freefall collapse, for which the density reached the threshold due to gravitational collapse, but not due to purely hydrodynamical compression alone, typically occurring in supersonic turbulent flows. In such supersonic flows, the gas can reach and exceed the density threshold in strong shocks (e.g., in isothermal gas the postshock density increases proportional to the square of the Mach number). Thus, supersonic turbulent density fluctuations can cause the gas to exceed the density threshold. Some of those shocks are dominated by the velocity dispersion and *not* by self-gravity. In such cases it is important to avoid spurious creation of sink particles, because they would not represent gravitationally bound and collapsing objects. Our sink particle implementation avoids spurious creation of sink particles by explicitly testing the gas for local gravitational collapse. It should be noted that the additional checks to the density threshold are only necessary, if sink particles are created at densities below the opacity limit (about $10^{-14}\,\mathrm{g\,cm^{-3}}$), when the gas is still in the roughly isothermal regime, as for instance in the large-scale simulations of colliding flows by Banerjee et al. (2009) and in the turbulent box calculations by Padoan & Nordlund (2009), where sink particles are formed at much lower densities to represent clusters of stars rather than individual stars.

5.2.3 Gas accretion

As soon as a sink particle was created, it can gain further mass by accreting gas from the grid. The combined gravitational attraction of the sink particle and the gas typically lead to an increase of the gas density over the density threshold ρ_{res} within the accretion radius r_{acc} of an existing particle. If a cell (i, j, k) within r_{acc} exceeds ρ_{res}, the mass increment

$$\Delta M = [\rho(i, j, k) - \rho_{\mathrm{res}}]\,\Delta V(i, j, k) \tag{5.13}$$

is calculated. If ΔM is bound to the collective mass of the central sink particle and the remaining gas within r_{acc}, ΔM is accreted by that particle. To verify that ΔM is bound to the particle, the kinetic energy of ΔM is calculated in the reference frame of the particle and compared to its gravitational binding energy. We furthermore check that ΔM is moving toward the sink particle, i.e., the radial velocity of ΔM must be negative. This additional check will also allow us to model mass-loaded protostellar jets from within the control volume in follow-up studies.

If the mass increment ΔM is located inside a region of overlapping multiple sink accretion radii (which can happen due to particle motion), the gravitational binding energy of ΔM for each of these particles is calculated, and ΔM is accreted by the particle to which it is most strongly bound.

Gas exceeding the density threshold ρ_{res} within a given inner accretion radius will always be accreted without further checks for a bound state and convergence. The inner accretion radius, however, is always set such that accretion without further checks only applies to the single central cell in which the particle is located. This is only to avoid numerical problems like division by zero and infinite gravitational energies during the default checks.

If the gas mass ΔM has successfully passed all the aforementioned tests for accretion, it is accreted by the central particle, such that mass, linear momentum, and angular momentum are conserved (see the next section for a discussion of angular momentum conservation). The accreting particle is moved to the center of mass of the particle–gas configuration before the accretion step.

5.2.4 Conservation laws during accretion of gas

We briefly discuss the conservation laws during accretion of gas onto sink particles. The index i can be used to denote both the multiple gas portions to be accreted and the sink particle onto which these gas portions are being accreted within a single accretion step. Thus, mass and linear momentum conservation during accretion or merging of sink particles are given by the following equations:

$$M = \sum_i m_i \tag{5.14}$$

$$M\,\mathbf{v}_{\rm cm} = \sum_i m_i\,\mathbf{v}_i\ . \tag{5.15}$$

The last equation determines the center of mass velocity $\mathbf{v}_{\rm cm}$ to conserve linear momentum during an accretion or merging step. However, if these two conservation laws apply, then angular momentum conservation is generally broken in the process of accretion. To see that, consider the angular momentum before the accretion process

$$\mathbf{L} = \sum_i m_i\,\mathbf{r}_i \times \mathbf{v}_i\,. \tag{5.16}$$

The angular momentum after accretion is

$$\mathbf{L}' = M\,\mathbf{R} \times \mathbf{v}_{\rm cm}\,. \tag{5.17}$$

To fulfill angular momentum conservation $\mathbf{L} = \mathbf{L}'$, the following equation needs to be solved for the position $\mathbf{R}$ of the accreted gas plus sink particle:

$$\mathbf{R} \times \mathbf{v}_{\rm cm} = \frac{1}{M}\,\mathbf{L}\,. \tag{5.18}$$

However, this equality *cannot* be fulfilled in the general case, because $\mathbf{L}$ and $\mathbf{v}_{\rm cm}$ are generally *not* orthogonal. Thus, it is impossible to construct a position vector $\mathbf{R}$, such that angular momentum conservation holds. Furthermore, if $\mathbf{R}$ is given by the center of mass

$$\mathbf{R}_{\rm cm} = \frac{1}{M}\sum_i m_i\,\mathbf{r}_i\,, \tag{5.19}$$

angular momentum conservation is also typically broken, because eq. (5.18) does not generally hold true. This is the case for any implementation of accreting sink particles. The only way to restore angular momentum conservation is to introduce an intrinsic angular momentum (spin) for each sink particle (see Bate et al., 1995; Krumholz et al., 2004; Jappsen et al., 2005). This spin compensates the deviation from global angular momentum conservation caused by accretion or merging of sink particles. It can also be used to determine the axis along which a bipolar outflow or jet would be launched in a subgrid model of stellar feedback.

5.2.5 Gravitational interactions

We compute four different contributions to the gravitational interactions between the gas on the grid and the sink particles:

1. gas–gas (g–g)
2. gas–sinks (g–s)
3. sinks–gas (s–g)

4. sinks–sinks (s–s)

The modeling of these interactions is described in detail in the following sections. In the code, these interactions are computed in the order given above, so we also present them in this order below. Physically, however, the order does not matter.

Gas–gas

The self-gravity of the gas is computed using the standard Poisson solver in FLASH. It is an iterative multigrid solver that cycles over the AMR hierarchy to solve Poisson's equation

$$\nabla^2 \Phi_{\rm gas} = 4\pi\, G\, \rho_{\rm gas} \tag{5.20}$$

for the gas distribution on the grid. A tree-based gravity solver was developed for FLASH recently (Richard Wünsch 2009, priv. comm.), which can also be used to calculate the gravitational potential instead of the multigrid solver.

The Poisson solver returns the gravitational potential $\Phi_{\rm gas}$ in each grid cell, which is due to the whole gas distribution only (without the sink particle contribution). The gravitational acceleration of the gas, $\mathbf{g}_{\rm g-g}$ is then computed for each grid cell as

$$\mathbf{g}_{\rm g-g} = -\nabla \Phi_{\rm gas}\ . \tag{5.21}$$

Gas–sinks

Equation (5.21) is used to calculate the gravitational acceleration for the sink particles due to the gas component only. The acceleration $\mathbf{g}_{\rm g-g}$ is interpolated from the grid onto the sink particles with a first-order cloud-in-cell method at each position of a sink particle n, which yields $\mathbf{g}_{{\rm g-s},\,n}$. A higher-order interpolation scheme like the triangular-shaped cloud method or the tri-cubic interpolation (e.g., Lekien & Marsden, 2005) does not yield significantly different results, because the gravitational acceleration of the gas is relatively smooth, and a linear interpolation scheme is sufficient.

Sinks–gas

Due to their mass the sink particles can exert an appreciable gravitational acceleration onto the gas as well. This acceleration is computed by a direct sum involving all computational cells and all sink particles. For each computational cell center (i, j, k), the distance $\mathbf{r}_n$ to each particle n is calculated and the acceleration that the particles with masses M_n exert onto the gas in each cell is then computed as

$$\mathbf{g}_{\rm s-g}(i,j,k) = -\sum_n \frac{GM_n}{|\mathbf{r}_n(i,j,k)|^3}\, \mathbf{r}_n(i,j,k)\ . \tag{5.22}$$

Computing the acceleration of the gas due to the sinks thus involves a nested sum over all grid cells and all particles. This can become computationally expensive, because this operation scales as the number of grid cells times the number of particles. However, even for sink particle numbers up to 10^3, the nested sum hardly affected the overall computational cost, which always remained dominated by the computation of the self-gravity of the gas component (eq. 5.20).

For cell centers (i, j, k) very close to sink particles, the acceleration computed via equation (5.22) can become very large and goes to infinity when a sink particle is exactly located in the center of a cell. It is thus necessary to use gravitational softening of the acceleration within a softening radius of each sink particle, which is discussed in section 5.2.5.

The acceleration of the gas due to the sink particles, $\mathbf{g}_{\mathrm{s-g}}$ is added to the gas–gas acceleration $\mathbf{g}_{\mathrm{g-g}}$ to yield the total gravitational acceleration for the gas:

$$\mathbf{g}_{\mathrm{gas}}(i,j,k) = \mathbf{g}_{\mathrm{g-g}}(i,j,k) + \mathbf{g}_{\mathrm{s-g}}(i,j,k) \tag{5.23}$$

Sinks–sinks

The gravitational acceleration for sink particle n due to all other sink particles in the domain is computed as a direct sum involving all other sink particles m with masses M_m:

$$\mathbf{g}_{\mathrm{s-s},\,n} = -\sum_{m\neq n} \frac{GM_m}{|\mathbf{r}_{nm}|^3}\,\mathbf{r}_{nm}\,, \tag{5.24}$$

where $\mathbf{r}_{nm} = \mathbf{r}_m - \mathbf{r}_n$, is the relative distance vector between two sink particles n and m.

The sink–sink acceleration is added to the grid-interpolated acceleration caused by the gas (cf. section 5.2.5) to yield the total gravitational acceleration for sink particle n:

$$\mathbf{g}_{\mathrm{sinks},\,n} = \mathbf{g}_{\mathrm{g-s},\,n} + \mathbf{g}_{\mathrm{s-s},\,n} \tag{5.25}$$

Equation (5.24) is also subject to gravitational softening as explained in the next section.

Gravitational softening

The basic problem in computing the gravitational acceleration following equations (5.22) and (5.24) is that it can yield extremely large values, if the distance between sink particles and cell centers or between adjacent sink particles becomes small. If the distance goes to zero, the acceleration becomes infinite. Hence, the timestep given by equation (5.30) goes to zero and the simulation grinds to a halt. It is therefore necessary to apply gravitational softening for distances smaller than a given softening radius r_{soft}, such that the acceleration smoothly approaches zero as the distance between particles goes to zero. There are different approaches for gravitational softening. One of the standard softening types is the Plummer softening, $\mathbf{g}(\mathbf{r}) \propto (|\mathbf{r}|^2 + r_{\mathrm{soft}}^2)^{-3/2}\,\mathbf{r}$. In the case of Plummer softening the acceleration approaches Newton's acceleration for a point mass $g \propto 1/r^2$ in the limit $r \gg r_{\mathrm{soft}}$. Instead of Plummer softening, we use a type of spline softening that is typically used in SPH and N-body simulations to soften the gravitational forces (e.g., Monaghan & Lattanzio, 1985; Price & Monaghan, 2007). The functional form of the cubic spline softening used here is

$$\mathbf{g}(\mathbf{r}) \propto \begin{cases} \frac{4}{r_{\mathrm{soft}}^2}\left[\frac{8}{3}\left(\frac{r}{r_{\mathrm{soft}}}\right) - \frac{48}{5}\left(\frac{r}{r_{\mathrm{soft}}}\right)^3 + 8\left(\frac{r}{r_{\mathrm{soft}}}\right)^4\right]\frac{\mathbf{r}}{r} \\ \quad \text{for} \quad 0 \le \frac{\mathrm{r}}{\mathrm{r_{soft}}} < \frac{1}{2} \\ \frac{4}{r_{\mathrm{soft}}^2}\left[\frac{16}{3}\left(\frac{r}{r_{\mathrm{soft}}}\right) - 12\left(\frac{r}{r_{\mathrm{soft}}}\right)^2 + \frac{48}{5}\left(\frac{r}{r_{\mathrm{soft}}}\right)^3 - \frac{8}{3}\left(\frac{r}{r_{\mathrm{soft}}}\right)^4 - \frac{1}{60}\left(\frac{r_{\mathrm{soft}}}{r}\right)^2\right]\frac{\mathbf{r}}{r} \\ \quad \text{for} \quad \frac{1}{2} \le \frac{\mathrm{r}}{\mathrm{r_{soft}}} < 1 \\ \frac{\mathbf{r}}{r^3} \\ \quad \text{for} \quad \mathrm{r} \ge \mathrm{r_{soft}}\,, \end{cases} \tag{5.26}$$

where $r = |\mathbf{r}|$ and r_{soft} is the softening radius.

Figure 5.1 shows a comparison of Plummer softening and spline softening, equation (5.26). For Plummer softening, the gravitational acceleration is modified for all distances r. In contrast, the spline softening exactly follows the asymptotic solution $g \propto 1/r^2$ for $r \ge r_{\mathrm{soft}}$ and smoothly

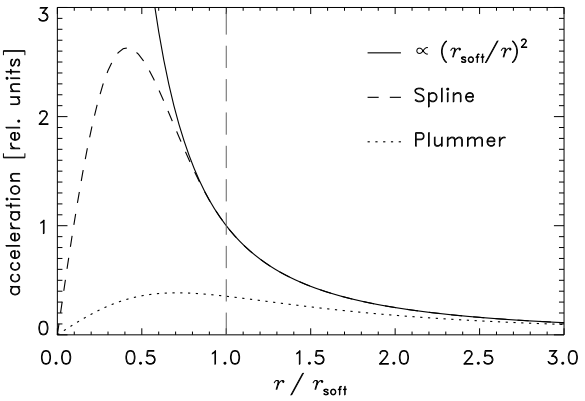

Figure 5.1: Plummer softening versus spline softening: The sink particle implementation presented here uses spline softening, equation (5.26) for the gravitational accelerations between sink particles and grid cell centers, and between adjacent sink particles.

approaches zero for $r < r_{\rm soft}$.

5.2.6 Particle timestep and subcycling

Sink particles are evolved using a variable-timestep leapfrog integration scheme. We consider four timestep constraints to guarantee a stable numerical solution:

$$\Delta t_{\rm CFL} = C_{\rm CFL} \min_{i,j,k} \left(\frac{\Delta x}{\max(|\mathbf{v}(i,j,k)|, c_{\rm s})} \right) \tag{5.27}$$

$$\Delta t_{\rm gg} = C_{\rm gg} \min_{i,j,k} \left(\frac{\Delta x}{|\mathbf{g}_{\rm gas}(i,j,k)|} \right)^{1/2} \tag{5.28}$$

$$\Delta t_{\rm vs} = C_{\rm vs} \min_{n} \left(\frac{\Delta x}{2|\mathbf{v}_n|} \right) \tag{5.29}$$

$$\Delta t_{\rm gs} = C_{\rm gs} \min_{n,m} \left(\frac{\min(|\mathbf{r}_{nm}|, \Delta x)}{|\mathbf{g}_{{\rm sinks},\,n}|} \right)^{1/2} , \tag{5.30}$$

with $C_{\rm CFL}$, $C_{\rm gg}$, $C_{\rm vs}$, $C_{\rm gs} < 1$, and Δx is the smallest linear cell size in the computational domain. The smallest of the first three timestep constraints applies to the hydrodynamic solver to guarantee a stable hydrodynamical evolution of the gas. Equation (5.27) is the Courant-Friedrichs-Lewy condition (Courant, Friedrichs, & Lewy, 1928). A modified version of this is used for magnetohydrodynamic studies, which takes into account the fastest possible magnetosonic wave. By solving equation (5.28), we also consider the gravitational forces of the self-gravity of the gas, and the gravitational forces of the sink particles exerted onto the gas. Equation (5.29) ensures that sink particles cannot cross more than half a grid cell ($\Delta x/2$) within a single timestep when they move with a velocity $\mathbf{v}_n$. The latter two constraints guarantee that the gravitational forces exerted by the sink particles onto the gas are consistently taken into account for the evolution of the hydrodynamics.

Since the sink particles are always moved within a hydrodynamical timestep, the sink particle timestep can never become larger than the smallest of the hydrodynamical timesteps given by equations (5.27), (5.28) and (5.29). However, these three constraints are insufficient to guarantee a stable and accurate time integration of sink particles, because the sink particle timestep

can become significantly smaller than the hydrodynamical timestep for close encounters of sink particles. One additional timestep constraint that captures closely approaching sink particles is needed.

The last timestep constraint given by equation (5.30) takes into account the total gravitational acceleration, $|\mathbf{g}_{\mathrm{sinks},\,n}|$ onto each sink particle (eq. 5.25), and the minimum distance $|\mathbf{r}_{nm}|$ between all sink particles n and m. In the course of code development and initial tests of the scheme, it turned out that fulfilling equation (5.30) is extremely important to avoid inaccurate time integration and artificial acceleration, especially in cases of closely approaching or orbiting sink particles. In test simulations and applications, Δt_{gs} became up to three orders of magnitude smaller than the timestep given by any of the three constraints of equations (5.27), (5.28) and (5.29). To avoid prohibitive small timesteps for the hydrodynamical evolution, we use subcycling for the time integration of sink particles, while keeping the hydrodynamical gas distribution fixed (similar to Krumholz et al., 2004). During subcycling, sink particles cannot change their positions by more than half a grid cell due to equation (5.29), and thus they remain almost fixed relative to the grid. However, subcycling is absolutely necessary to guarantee accurate integration of sink particle orbits as shown in a series of N-body tests in the next section.

5.3 Tests

In the following sections we describe a series of test simulations to analyze the performance of our sink particle scheme. In particular, we test the accuracy of the time integration of pure particle systems and systems involving gas-sink interactions as well as dynamical sink particle creation and their accretion.

5.3.1 N-body tests

As described in section 5.2.5 we modified the gravitational interactions of gas and particles compared to the standard FLASH implementation. Therefore, we test our new approach with the following setups.

Circular orbits

In the simplest tests we initialize two sink particles with equal masses of $1\,\mathrm{M}_{\odot}$ at a distance of 1 AU, and let them orbit around their common center of mass. There are 8x8x8 grid cells in this test. However, the gas density was set small enough, so that this setup purely tests the N-body integration scheme. The results are shown in Figure 5.2. The trajectory of the particles are plotted including all positions up to 1000 orbits around their common center of mass at $(x, y, z) = (0, 0, 0)$. The orbit is maintained circular for these 1000 orbits, and it is not expected to deviate significantly for longer integration times. This is because the leapfrog time-integration scheme is symplectic for constant timesteps. The scheme thus conserves energy and preserves time-reversibility in this test, such that the symmetry of the system is maintained to machine precision.

Elliptical orbits

A more demanding test is the integration of an elliptical orbit. In this case the leapfrog integrator takes variable timesteps depending on the distance and gravitational acceleration according to the timestep criterion, equation (5.30). For this test we use the same initial conditions as for the circular orbit test, but rotate the initial velocity vectors by 45° from the tangent of the circular orbit of the previous test. The system thus has the same total energy, but the sink particles move on elliptical orbits around their common center of mass. The results are shown in Figure 5.3. The

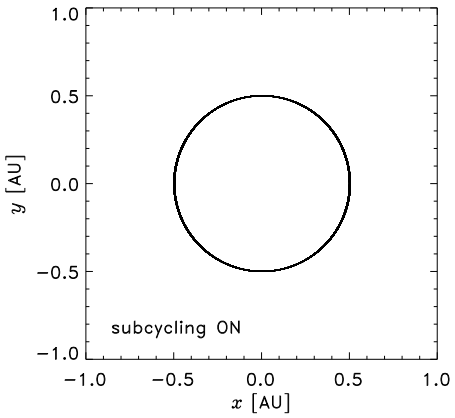

Figure 5.2: Trajectory of two point masses on circular orbits around their common center of mass after 1000 orbits of time integration. The leapfrog integrator is symplectic for constant timesteps, and thus the circular orbits remain numerically stable.

left panel shows the default time integration with subcycling, which means that equations (5.27), (5.28), (5.29) and (5.30) are all used in combination to determine the timestep. The right panel shows the same, but only taking into account the first three of these timestep constraints. It is important to note that equation (5.29) was the only additional timestep constraint for simulations with particles in the FLASH code before our modifications. Figure 5.3 (right panel) shows that using equations (5.27), (5.28) and (5.29) is clearly insufficient, if close orbits are to be accurately reproduced. Even within a single orbit, a significant amount of artificial angular momentum is added to the particles if no subcycling is performed, and after ten orbits they have accumulated an artificial perihel shift of about 21°. In contrast, ten orbits are accurately followed without a noticeable shift with our present scheme. It should be noted however that even when using subcycling, the symplectic property of the leapfrog integrator is broken, and after roughly 100 elliptical orbits, an error leading to a perihel shift of about 1° shows up.

Gravitational softening and subcycling test

This setup tests the gravitational softening introduced in section 5.2.5. We use the same computational domain as in the two previous tests with two $1\,\mathrm{M}_\odot$ sink particles separated by 1 AU. One particle is initially located at $(x, y, z) = (-1.0, +0.5, 0.0)\,\mathrm{AU}$, and the other one is at $(-1.0, -0.5, 0.0)\,\mathrm{AU}$. Both particles have zero initial velocities in the y-direction, such that they accelerate toward each other by their mutual gravitational attraction. While approaching each other, the timestep drops according to the constraints given by equations (5.29) and (5.30). Due to the softening, however, the timestep does not go to zero as the particle distance goes to zero (cf. Fig. 5.1). This allows the two particles to pass through each other smoothly. By the time they pass through the point of zero distance, they have converted their initial potential energy completely into kinetic energy. The softening affects the specific value of this energy but nevertheless, the energy must be conserved. Thus, after one passage both particles have exactly exchanged their initial positions. This process then starts again and the system oscillates for an infinite time. In order to make these oscillations visible, we apply an initial constant velocity in x-direction to both particles. The result is shown in Figure 5.4. The left panel shows both particle trajectories after 1000 oscillations. Using subcycling, the system easily conserves energy during these 1000 oscillations. In contrast, if the timestep constraint given by equation (5.30) is

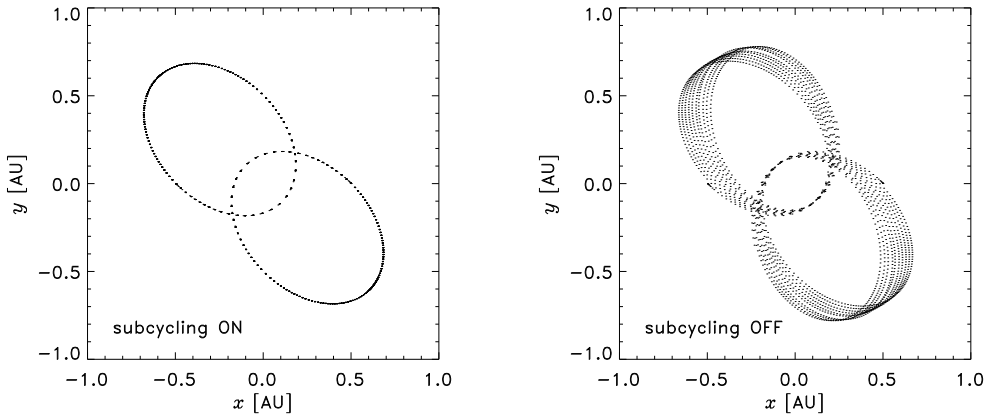

Figure 5.3: Trajectories of two point masses on elliptical orbits around their common center of mass after 10 orbits. The symplectic property of the leapfrog integrator is broken due to variable timesteps in this type of problem. However, 10 orbits are reproduced quite accurately with subcycling turned ON, while for subcycling turned OFF (right), large errors occur already for single orbits, and a significant amount of artificial angular momentum is introduced.

ignored, energy conservation is broken already during the first oscillation as shown in Figure 5.4 (right panel). Both particles gain energy artificially until they leave the domain. In the current test, this happens after about 68 oscillations. Scattering experiments have shown that violating the timestep condition given by equation (5.30), i.e., *not* using subcycling can lead to enormous artificial accelerations already during a single close encounter of two particles.

5.3.2 Gas–sinks gravity and refinement test

The following setup tests the accuracy of the time integration of sink particles orbiting in the gravitational potential of a static gas distribution. We create a singular isothermal sphere with the following density profile on the AMR grid:

$$\rho(r) = \rho(r_0) \left(\frac{r_0}{r}\right)^2 , \tag{5.31}$$

where $r_0 = 5 \times 10^{16}\,\mathrm{cm}$ and $\rho(r_0) = 3.82 \times 10^{-18}\,\mathrm{g\,cm^{-3}}$. The sphere thus has a mass of roughly $3\,\mathrm{M}_\odot$ for $r \leq r_0$. We place three sink particles at radii of $r = 1,\, 2,\, 3 \times 10^{16}\,\mathrm{cm}$ with masses of $10^{-10}\,\mathrm{M}_\odot$. The particles thus represent test particles in a gravitational potential caused by the gas only, such that sink particle interaction is negligible. Since the singular isothermal gas distribution would immediately collapse and form a new sink particle in the center, we deliberately switch off the hydrodynamical evolution, and keep the density distribution and associated potential artificially static. However, we keep the AMR scheme and the Poisson solver fully operational, and adaptively refine on Jeans length and sink particles as discussed in section 5.2.2. We use a base grid of 32^3 grid cells plus two levels of refinement with isolated boundary conditions for the gravity. The Jeans length is resolved with 6 grid cells for this test, while de-refinement is triggered as soon as the Jeans length is resolved with more than 12 grid cells. The initial density and sink particle distributions are shown in Figure 5.5 (left).

The three sink particles were given an initial velocity in the y-direction, such that they should remain on circular orbits around the center of the gas sphere. It is easy to determine this velocity

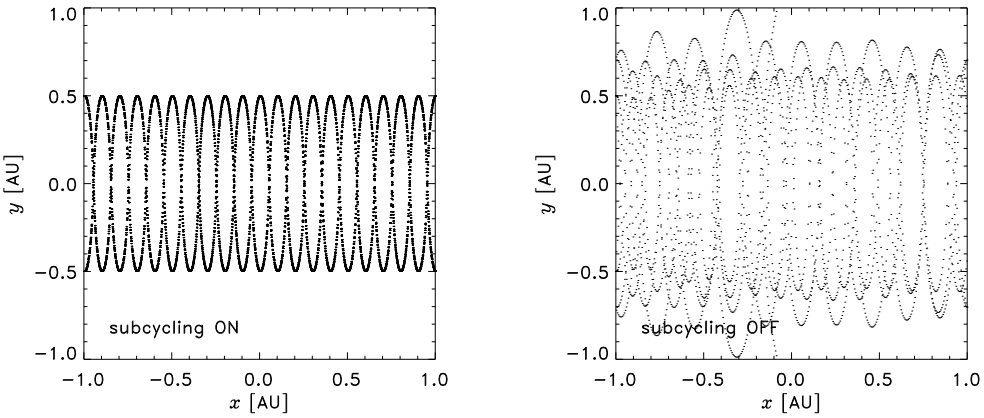

Figure 5.4: Gravitational softening and subcycling test: The trajectories of two point masses starting with zero velocity along the y-axis, but with an initial velocity along the x-axis are shown. The two masses oscillate around their common center of mass, and draw a sine function. The boundary conditions are set to *outflow* for the y-direction and to *periodic* for the x-direction. The frequency of the oscillation in y and the initial velocity in x were chosen such that the two particles leaving on one side of the domain will exactly connect to their previous trajectories. Each sweep through x contains 20 oscillations and a total number of 1000 oscillations is shown (left). When – for the same setup – subcycling is turned OFF (right) the sink particles get artificial accelerations during their close encounters, and energy conservation is broken. Already after roughly 68 oscillations, they have artificially gained enough energy to leave the domain at $x \approx -0.1\,\mathrm{AU}$.

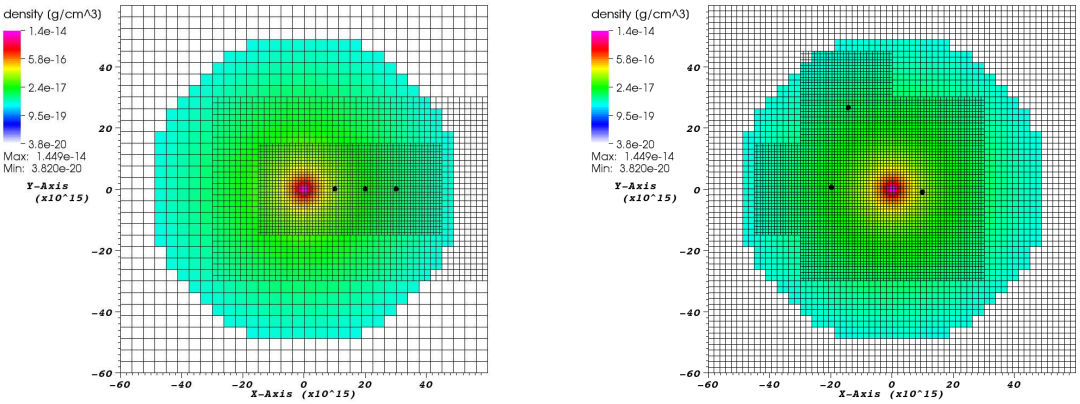

Figure 5.5: Three sink particles orbiting a static spherical gas density profile with $\rho \propto r^{-2}$. Note that the hydrodynamical evolution was switched-off deliberately for this test, while the gravity solver and the AMR scheme remained fully operational. The left image shows the initial conditions and the right image shows the sink particle positions after the innermost particle has completed roughly one full orbit. Adaptive mesh refinement is used to keep the sink particles at the highest level of refinement allowed in this setup. The particle on the middle orbit has completed half an orbit, while the outermost particle has completed 1/3 of an orbit at the time shown in the right-hand image. Figure 5.6 shows the full particle trajectories after one, ten and 100 orbits of the innermost sink particle.

analytically from the density distribution, equation (5.31). The result is a Keplerian velocity of

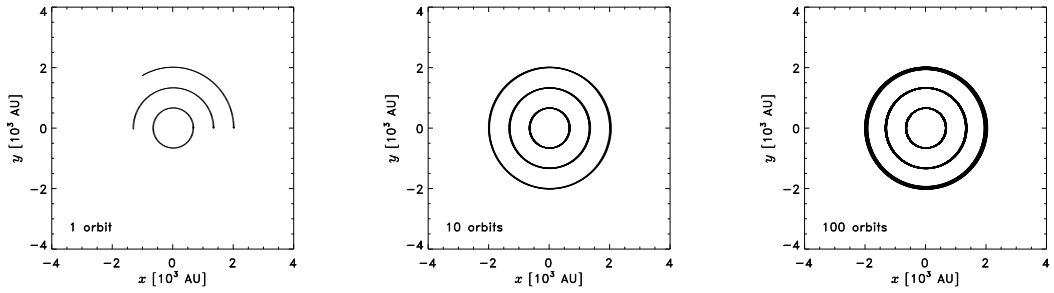

Figure 5.6: Sink particle trajectories of the setup shown in Figure 5.5 after one (left), ten (middle) and 100 (right) completed orbits of the innermost particle. The time in the left plot is equivalent to the image shown in Figure 5.5 (right). Ten orbits (middle) are quite accurately followed. After 100 orbits of the innermost sink particle (right), the intermediate particle has finished 50 orbits, while the outermost sink particle has finished about 33 orbits. The outermost sink particle shows some deviation from a perfect spherical orbit, seen as a slight broadening of its circular trajectory, which is due to the accumulation of small time-integration errors, and due to deviations from spherical symmetry toward the edges of the Cartesian domain.

$v_{\rm K} = \sqrt{GM(r)/r} = 0.895\,{\rm km\,s^{-1}}$ for each sink particle, independent of the radius. However, since the sphere is not singular in the center due to the finite resolution of the grid, the actual velocities necessary to keep the sink particles on circular orbits are slightly smaller than the analytical solution (by roughly 1-2%).

Figure 5.5 (right) shows the AMR hierarchy and the sink particle positions after the innermost particle has finished roughly one orbit. At this time, the sink particle on the intermediate orbit with $r = 2 \times 10^{16}\,{\rm cm}$ has finished almost half an orbit, and the outer sink particle has completed one third of an orbit. The grid is refined according to the position of the sink particles. The Jeans refinement criterion keeps the central part at the highest level of refinement and the outer parts at a resolution such that the Jeans length is refined with at least 6 grid cells. De-refinement to the base grid resolution was not triggered in the outer parts, because the Jeans length was resolved with 6-12 grid cells there.

We evolved this configuration for 100 orbits of the innermost sink particle. The trajectories of all three sink particles are shown in Figure 5.6 after 1, 10, and 100 orbits of the innermost sink particle (from left to right). After 100 orbits of the innermost sink particle, the intermediate particle has finished 50 orbits, while the outermost sink particle has finished about 33.3 orbits. The latter orbit as well as to a smaller degree also the intermediate orbit are slightly broadened, and they are not as accurately reproduced as the innermost orbit. This is because the Poisson solver introduces slight deviations from the spherical gravitational potential mainly in regions close to the boundaries of the Cartesian domain at the coarse grid resolution used in this test. For such a configuration and setup that incorporates the multigrid solver and the full AMR scheme, it is hard to maintain perfect spherical symmetry for more than 10-100 sink particle orbits.

5.3.3 Collapse of a Bonnor-Ebert sphere

The collapse of supercritical Bonnor-Ebert spheres (Ebert, 1955; Bonnor, 1956), is a well-studied problem (e.g. Larson, 1969; Foster & Chevalier, 1993; Banerjee et al., 2004; Aikawa et al., 2005), and thus represents a good test case for our sink particle implementation. A Bonnor-Ebert sphere can be described by the following dimensionless parameters for the radius, time, mass, and mass

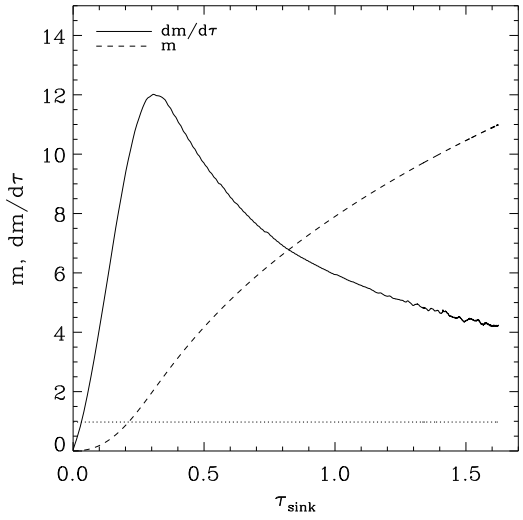

Figure 5.7: Time evolution of the mass accretion rate, $\mathrm{d}m/\mathrm{d}\tau$, and of the accreted mass, m, of the central sink particle in the case of a collapsing Bonnor-Ebert sphere. The quantities are given in dimensionless units (see text). The mass accretion rate increases rapidly until about 12% of the gas mass is accreted onto the sink particle (the total mass of the Bonnor-Ebert sphere is $m = 17.3$). Here, the density threshold for sink particle accretion was set to $10^2\,\rho_0$, which corresponds to an effective accretion radius of $\xi = 0.1$. The time $\tau_{\rm sink} = 0$ corresponds to the time when the sink particle starts to accrete.

accretion, respectively:

$$\xi = \frac{r}{c_{\rm s}/\sqrt{4\pi\,G\,\rho_0}} \tag{5.32}$$

$$\tau = \frac{t}{1/\sqrt{4\pi\,G\,\rho_0}} \tag{5.33}$$

$$m = \frac{M}{c_{\rm s}^3/\sqrt{4\pi\,G^3\,\rho_0}} \tag{5.34}$$

$$\dot{m} = \frac{\dot{M}}{c_{\rm s}^3/G}\,, \tag{5.35}$$

where $c_{\rm s}$ is the sound speed and ρ_0 is the central density of the sphere. In the hydrostatic configuration of such a sphere, the dimensionless mass can be written as $m = \xi^2\,\phi'$, where $\phi' = -\mathrm{d}\ln(\rho/\rho_0)/\mathrm{d}\xi$ is the gravitational acceleration. The sphere becomes supercritical if its dimensionless radius exceeds the critical value $\xi_{\rm crit} = 6.451$. To trigger the collapse, we set the initial value to $\xi_{\rm max} = 7.0$, which gives a total mass, $m = 17.3$ in dimensionless units. We follow the collapse with two different density thresholds for sink particle creation and accretion: $\rho_{\rm res} = 10^2\,\rho_0$ and $\rho_{\rm res} = 10^4\,\rho_0$. These two density thresholds correspond to accretion radii of $\xi = 0.1$ and $\xi = 10^{-2}$, respectively.

Figure 5.7 shows the mass accretion history of the sink particle in the case of the low density threshold, $\rho_{\rm res} = 10^2\,\rho_0$. Initially, when the sink particle starts to accrete at $\tau_{\rm sink} = 0$, the accretion rate increases quickly until it reaches a maximum. The accretion rate peaks at $\tau_{\rm sink} \approx 0.3$ when about 12% of the total mass of the sphere is accreted onto the sink particle. After that, the accretion rate decreases while the envelope runs out of gas. At $\tau_{\rm sink} = 1.62$ about 64% of the total gas mass has been accreted onto the sink particle.

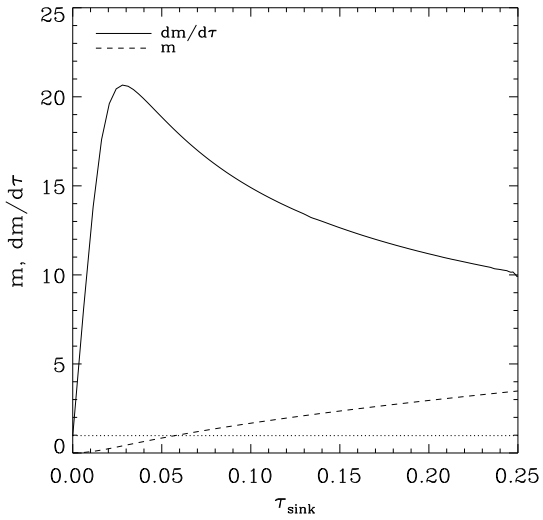

Figure 5.8: Same as Fig. 5.7 but in the case of $\rho_{\rm res} = 10^4\,\rho_0$, corresponding to an effective accretion radius of $\xi = 10^{-2}$, ten times smaller than in the previous test. The peak accretion rate is thus reached ten times faster than in Fig. 5.7.

The time evolution of the accretion rate is similar in the case of a higher density threshold ($\rho_{\rm res} = 10^4\,\rho_0$) for the sink particle accretion. Figure 5.8 shows the mass evolution for this case. Here, the effective accretion radius is smaller by a factor of ten compared to the $\rho_{\rm res} = 10^2\,\rho_0$ case, and thus the peak accretion rate is reached ten times faster.

The time evolution of the mass accretion is in qualitative agreement with 1D simulations by Foster & Chevalier (e.g., 1993), and with various analytical (e.g., Hunter, 1977; Whitworth & Summers, 1985) and numerical models of protostellar collapse, which predict a peak in the accretion followed by a smoothly declining accretion rate (see also Schmeja & Klessen, 2004, and references therein).

5.3.4 Collapse of a singular isothermal sphere

The collapse of a singular isothermal sphere with a $\rho(r) \propto r^{-2}$ density profile produces a constant flux of mass through spherical shells, i.e. a constant accretion rate (see e.g. Shu, 1977). We compute the collapse of a singular isothermal sphere to test whether our model of sink particle accretion reflects this collapse behavior. The sphere has a truncation radius of $R = 5 \times 10^{16}\,{\rm cm}$, a density at this radius of $\rho(R) = 3.82 \times 10^{-18}\,{\rm g\,cm^{-3}}$, and therefore a total mass of $3.02\,{\rm M_\odot}$. The sphere is at a temperature of 10 K corresponding to a sound speed of $0.166\,{\rm km\,s^{-1}}$. With these values the sphere has a large instability parameter of $A = 29.3$, where $A = 4\pi G\,\rho(R)\,R^2/c_{\rm s}^2$ (Shu, 1977).

Figure 5.9 shows the mass and the mass accretion rate onto the sink particle during the collapse of the singular isothermal sphere. As the gas of the sphere is initially at rest, the mass accretion reaches a close to constant value of about $1.5 \times 10^{-4}\,{\rm M_\odot\,yr^{-1}}$, until the entire gas of the sphere is accreted onto the central sink particle at $t \sim 2 \times 10^4\,{\rm yr}$.

For comparison of the accretion history of the sink particle, we show the time evolution of radial profiles of the gas sphere in Figure 5.10. As expected, the density profile of the sphere evolves from r^{-2} to $r^{-1.5}$ (see e.g., Shu, 1977; Ogino et al., 1999). The collapse proceeds highly supersonically ($\mathcal{M} > 15$) with increasing infall velocities toward the collapse center (Fig. 5.10, middle panel).

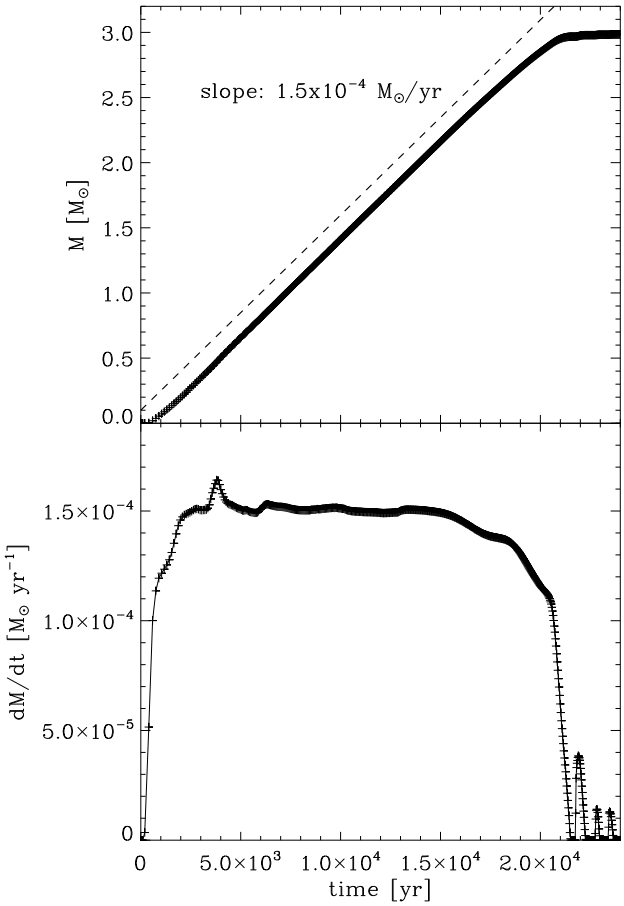

Figure 5.9: Mass accretion of the central sink particle during the collapse of a singular isothermal gas sphere. The mass accretion rate onto the sink particle is roughly constant in time with a value of $\dot{M} \approx 1.5 \times 10^{-4} \mathrm{M}_\odot\,\mathrm{yr}^{-1}$, until the sphere runs out of gas at $t \approx 2 \times 10^4\,\mathrm{yr}$. The collapse is highly supersonic due to the large instability parameter $A = 4\pi G\,\rho(R)\,R^2/c_\mathrm{s}^2 = 29.3$. Therefore, the mass accretion rate reaches values much larger than the expansion-wave collapse solution by Shu (1977) that would give $m_0 c_\mathrm{s}^3/G = 1.06 \times 10^{-6}\,\mathrm{M}_\odot\,\mathrm{yr}^{-1}$ for the asymptotic solution: $A = 2$ and $m_0 = 0.975$ (see Shu, 1977, Tab. 1). For our case, $A = 29.3$ and $m_0 \approx 133$, Shu (1977) predicts an accretion rate of $\dot{M} \approx 1.45 \times 10^{-4}\,\mathrm{M}_\odot\,\mathrm{yr}^{-1}$, which is in excellent agreement with our numerical estimate of the central sink particle accretion rate.

The mass accretion, i.e. the mass flux through spherical shells of radius r is constant in time as well as independent of the radial position with a value of $\dot{M} \approx 1.5 \times 10^{-4}\,\mathrm{M}_\odot\,\mathrm{yr}^{-1}$. It is the exact same amount of gas that flows through these spherical shells into the control volume of the sink particle, where it is finally accreted. A comparison of the sink particle accretion rate in Figure 5.9 with the mass flux through spherical shells in Figure 5.10 (bottom panel) shows the high accuracy of the sink particle accretion mechanism.

For comparison, we calculated the mass accretion rate predicted by Shu (1977). The constant accretion rate often referred to in many studies citing Shu (1977) is

$$\dot{M} = m_0\,\frac{c_\mathrm{s}^3}{G} \tag{5.36}$$

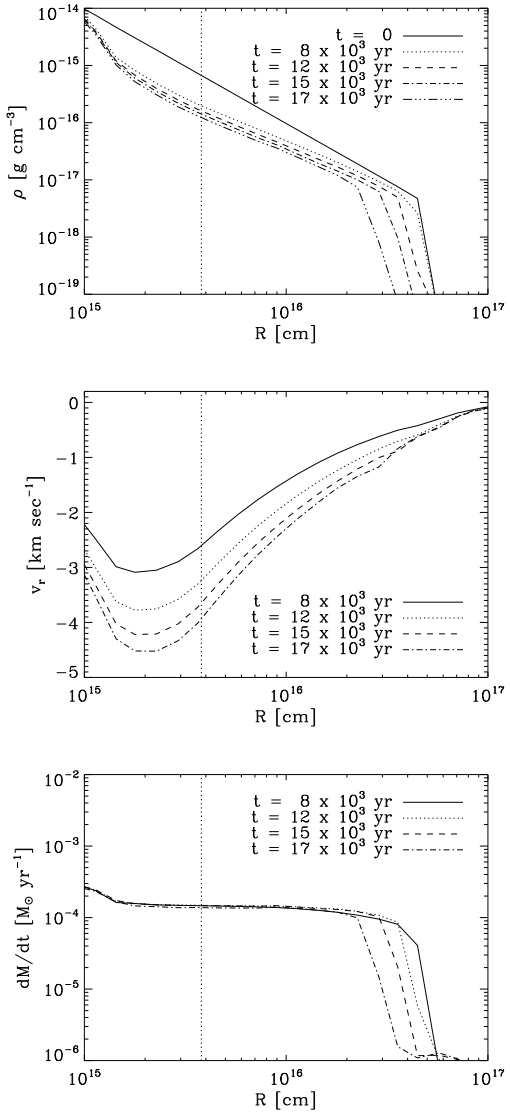

Figure 5.10: Time evolution of the radial density profile (top panel), infall velocity (middle panel) and mass flux through radial shells (bottom panel) for the collapse of a singular isothermal sphere. The vertical dotted line marks the accretion radius of the sink particle. The density profile evolves from the initial r^{-2} profile to $r^{-1.5}$ when the mass of the sink particle starts to dominate the gravitational potential (see e.g. Shu, 1977; Ogino et al., 1999). As expected for a highly unstable sphere the collapse proceeds with highly supersonic speeds (note that $c_\mathrm{s} = 0.166\,\mathrm{km\,s^{-1}}$). The mass flux of gas through spherical shells of radius r is constant in time. It is exactly the mass accretion rate of the central sink particle, $\dot{M} \approx 1.5 \times 10^{-4} \mathrm{M}_\odot\,\mathrm{yr}^{-1}$ (cf. Fig. 5.9).

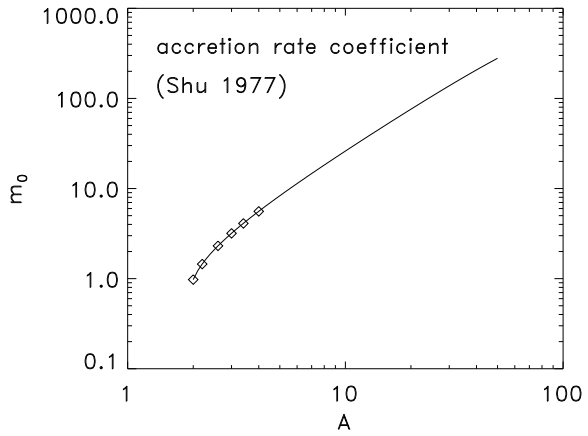

Figure 5.11: Coefficient m_0 for the accretion rate in equation (5.36) as a function of the instability parameter $A = 4\pi G\,\rho(R)\,R^2/c_\mathrm{s}^2$ for the collapse of a singular isothermal sphere. The diamonds show tabulated values by Shu (1977, Tab. 1). For $A = 29.3$ as in the collapse test shown in Figures 5.9 and 5.10, the accretion rate is more than two orders of magnitude higher than c_s^3/G, in excellent agreement with the predicted accretion rate by Shu (1977).

with $m_0 = 0.975$, which is the appropriate value for an instability parameter close to $A = 2$ (see Shu, 1977, Tab. 1). The accretion rate depends on the coefficient m_0, which is controlled by A. Numerical integration of the dimensionless, one-dimensional equations of hydrodynamics gives the solutions of m_0 for given instability parameters A as in Shu (see 1977, Tab. 1). There, Shu only tabulated values up to $A = 4$. Since our singular isothermal sphere has a much larger instability parameter ($A = 29.3$), we repeated the numerical analysis by Shu (1977) to find solutions for instability parameters up to $A = 50$. The result for the coefficient m_0 of the Shu accretion rate in equation (5.36) is plotted as a function of the instability parameter A in Figure 5.11. The parameter m_0 increases from $m_0 = 0.975$ for $A = 2$ to $m_0 = 279$ for $A = 50$, more than two orders of magnitude higher! For the instability parameter $A = 29.3$ of the singular isothermal sphere studied here, we obtain $m_0 = 133$. The accretion rate predicted by Shu (1977) is thus $\dot{M} \approx 1.45 \times 10^{-4}\,\mathrm{M}_\odot\,\mathrm{yr}^{-1}$, which is in excellent agreement with our numerical estimate of the sink particle accretion rate (cf. Fig. 5.9).

5.3.5 Rotating cloud core fragmentation test

We now analyze the collapse and fragmentation of a rotating cloud core, also known as the Boss & Bodenheimer (1979) test. It is a standard test for fragmentation in hydrodynamical codes (e.g., Bodenheimer & Boss, 1981; Burkert et al., 1997; Truelove et al., 1997; Commerçon et al., 2008). In particular we use a setup similar to Burkert & Bodenheimer (1993) and Bate & Burkert (1997). The initial parameters for the rotating cloud core are: radius $R = 5 \times 10^{16}\,\mathrm{cm}$, constant density $\rho_0 = 3.82 \times 10^{-18}\,\mathrm{g\,cm^{-3}}$, mass $M = 1\,\mathrm{M}_\odot$, angular velocity $\Omega = 7.2 \times 10^{-13}\,\mathrm{rad\,s^{-1}}$ (ratio of rotational to gravitational energy $\beta = 0.16$), sound speed $c_\mathrm{s} = 0.166\,\mathrm{km\,s^{-1}}$ (ratio of thermal to gravitational energy $\alpha = 0.26$), global freefall time $t_\mathrm{ff} = 1.075 \times 10^{12}\,\mathrm{s} = 3.41 \times 10^4\,\mathrm{yr}$, and a 10% density perturbation with an $m = 2$ mode: $\rho = \rho_0[1 + 0.1\,\cos(2\varphi)]$, where φ is the azimuthal angle. The following polytropic equation of state,

$$P = c_\mathrm{s}^2 \rho^\Gamma \,, \tag{5.37}$$

was used with the polytropic exponent

$$\Gamma = \begin{cases} 1 & \text{for } \rho/(10^{-15}\,\mathrm{g\,cm^{-3}}) \leq 0.25\,, \\ 1.1 & \text{for } 0.25 < \rho/(10^{-15}\,\mathrm{g\,cm^{-3}}) \leq 5.0\,, \\ 4/3 & \text{for } \rho/(10^{-15}\,\mathrm{g\,cm^{-3}}) > 5.0\,. \end{cases} \tag{5.38}$$

The initial rotation ($\beta = 0.16$) forces the gas sphere to collapse to a disk with a central bar due to the $m = 2$ initial density perturbation. Sink particles are allowed to form at densities exceeding $10^{-14}\,\mathrm{g\,cm^{-3}}$. The accretion radius was set to $r_{\mathrm{acc}} = 39\,\mathrm{AU}$ corresponding to 2.5 grid cells at the highest level of refinement.

Figure 5.12 shows a face-on column density projection of the disk at different times along the collapse of the rotating cloud core. Two sink particles form at the location of the two fragments at $t = 1.26\,t_{\mathrm{ff}}$. At $t = 1.29\,t_{\mathrm{ff}}$ a bar forms that connects the two main fragments. A third fragment forms in the center of the cloud core. After that, the two main fragments move toward the central object due to the global collapse of the cloud core. At $t = 1.33\,t_{\mathrm{ff}}$ two of the three fragments merge to a single particle close to the center of the rotating cloud core. Note that sink particle merging was used in this test. Sink particle merging is optional in our implementation in FLASH, and can be activated if desired. If activated, sink particles are only allowed to merge, if they are inside the accretion radii of one another, and if they are gravitationally bound and converging. The merged particle is moved to the center of mass of the merging particles, and their linear and angular momenta are assigned to the merged particle.

The conservation laws during accretion and merging of sink particles are discussed in section 5.2.4. The initial total angular momentum of the rotating cloud core computed from the analytic solution is $L_0 = 1.44 \times 10^{54}\,\mathrm{g\,cm^2\,s^{-1}}$. The numerical solution conserves angular momentum to within 2% for all times including the last snapshot shown in Figure 5.12 when 23% of the mass has been accreted onto sink particles. This is comparable to the typical conservation of angular momentum achieved in numerical simulations of rotating self-gravitating cloud cores (e.g., Commerçon et al., 2008).

5.4 Star cluster formation: AMR vs SPH

To check our sink particle implementation for the AMR code FLASH on a more complex physical problem, we apply it here to the formation of a star cluster. We furthermore want to compare our sink particles against an existing sink particle implementation in a typical SPH code. We compare to the SPH code developed by Bate et al. (1995). Bate et al. (1995) were the first to use sink particles in an SPH code, and thus, most SPH implementations for sink particles are based on their approach (e.g., Jappsen et al., 2005), as is the grid-based implementation presented here. A detailed description of the FLASH code and the our sink particle implementation was given in section 5.2.1. In the following we briefly describe the SPH code used for our sink particle comparison.

5.4.1 The SPH code

Smoothed particle hydrodynamics (SPH, Lucy, 1977; Gingold & Monaghan, 1977) calculations presented in this study were performed using a code based on the version developed by Benz (Benz, 1988, 1990; Benz et al., 1990), which has since been modified by Bate to include individual particle timesteps (Navarro & White, 1993; Hernquist & Katz, 1989) and sink particles (Bate et al., 1995). To capture shocks, the code uses the standard artificial viscosity suggested by Gingold & Monaghan (1983) and Monaghan & Gingold (1983), with $\alpha = 1$ and $\beta = 2$. To

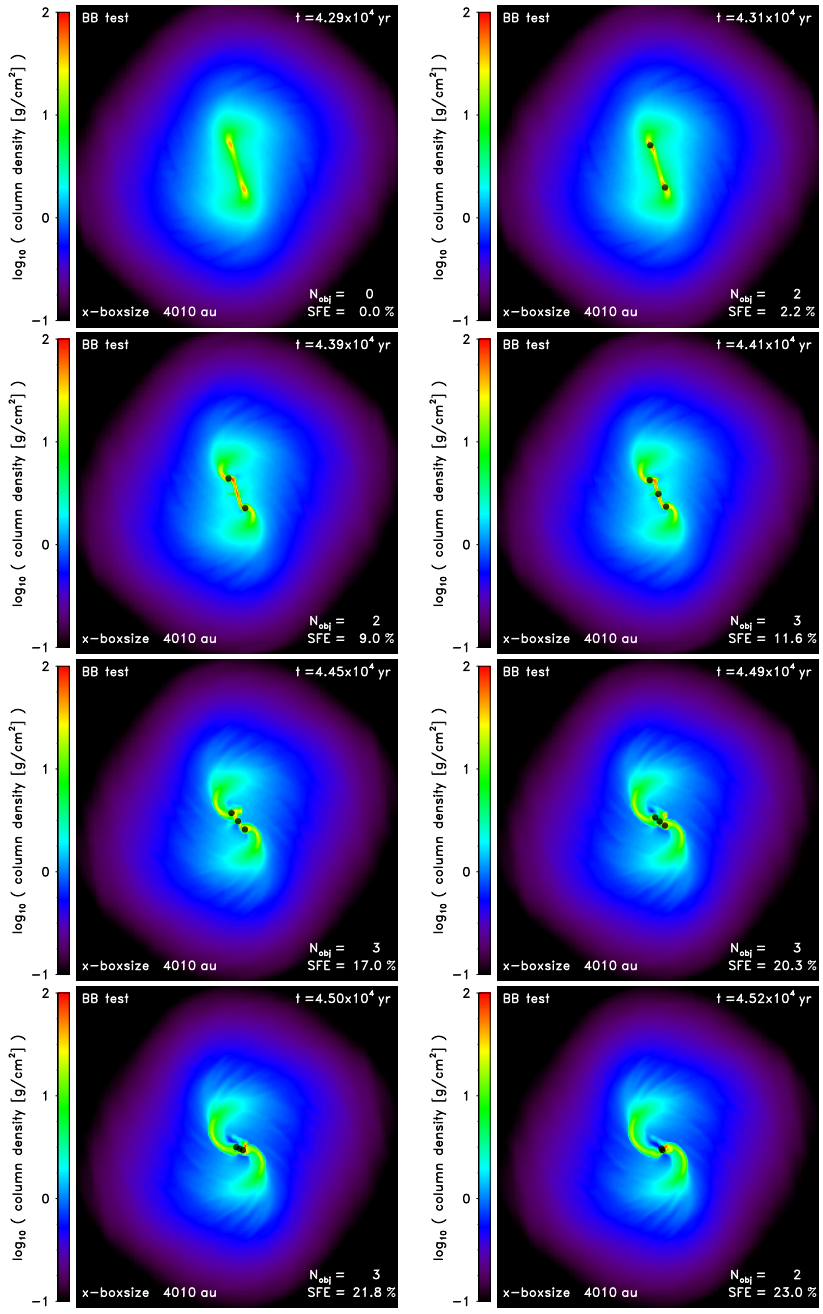

Figure 5.12: Column density time sequence of the inner 4000 AU of a rotating cloud core (see initial conditions in section 5.3.5), the so called 'BB test' (Boss & Bodenheimer, 1979; Bate & Burkert, 1997). Two sink particles form at the location of the two cloud fragments at $t = 4.31 \times 10^4$ yr. At $t = 4.39 \times 10^4$ yr a bar forms that connects the two main fragments, in which a third particle is dynamically created at $t = 4.41 \times 10^4$ yr right in the center. The two main fragments move toward the central object, and at $t = 4.52 \times 10^4$ yr two of the three sink particles merged to a single particle close to the center of the rotating cloud core, because the optional sink particle merging was used in this test. The freefall time of the initial gas distribution is $t_{\rm ff} = 3.41 \times 10^4$ yr. Sink particles are drawn as black circles with a radius of $r_{\rm acc} = 39$ AU in a true-to-scale representation.

provide adaptive resolution, the code allows the SPH smoothing lengths (h) to vary in time and space, with the constraint that each particle maintains a roughly constant number of neighbors (50 ± 10) within a distance $2h$. Gravitational forces are found using a binary tree (Press, 1987; Benz, 1988, and references therein), which is also used to obtain the neighbor lists required by the SPH algorithm. The binary tree opening angle was set to 0.47 in this study, and so returns a more accurate calculation of the gravitational forces than the theoretical limit of 0.57 for 3D binary trees described by Press (1987). Gravitational forces are softened using the spline softening technique, equation (5.26). In the SPH code this softening is used between all particle types. Between the gas-gas interactions, the softening length $r_{\rm soft}$ is given by the mean smoothing length of the particle pair, and so the softening is zero for particles which are not neighbors, since the distance between them is greater than $2h$ by definition. This form of the softening assumes that the standard SPH smoothing kernel (Monaghan & Lattanzio, 1985) describes the radial density profile of the particles, and has been shown to reduce the effects of artificial fragmentation (Bate & Burkert, 1997; Whitworth, 1998; Hubber et al., 2006). For the sink particles, one is free to chose the value of $r_{\rm soft}$ and in our current study this is set to the sink particle accretion radius, $r_{\rm acc}$, as for FLASH. The value of $r_{\rm soft}$ between gas-sink interactions is then set to $(r_{\rm acc} + h)/2$ for each pair-wise force. Finally, the SPH equations and sink particle trajectories are integrated using a second-order Runge-Kutta-Fehlberg integrator. A full description of the timestepping constraints can be found in Bate et al. (1995).

5.4.2 Initial conditions for the code comparison

An isolated gas sphere of radius $R = 5.0 \times 10^{17}\,{\rm cm} = 0.16\,{\rm pc}$ with a uniform density of $\rho_0 = 3.85 \times 10^{-19}\,{\rm g\,cm^{-3}}$ containing $M = 100\,{\rm M_\odot}$ was initialized in both the FLASH and the SPH code. The initial column density structure is shown in Figure 5.13 (top panels) for the FLASH run (left panels) and the SPH run (right panels). An initial random, divergence-free turbulent velocity field was generated on a grid with 128^3 grid cells with a velocity power spectrum $P(k) \propto k^{-4}$, consistent with the observed velocity dispersion-size relation in molecular clouds (e.g., Larson, 1981; Heyer & Brunt, 2004), and consistent with the velocity spectra usually obtained for driven supersonic turbulence (e.g., Federrath et al., 2009; Schmidt et al., 2009; Federrath et al., 2010b). However, in the present study we are not driving the turbulence, i.e., we study decaying turbulence. The velocity dispersion was scaled to $0.89\,{\rm km\,s^{-1}}$, consistent with the observed velocity dispersions in molecular clouds of the size studied here (e.g., Larson, 1981; Falgarone et al., 1992). With the isothermal sound speed of $c_{\rm s} = 0.19\,{\rm km\,s^{-1}}$ (temperature $T = 10\,{\rm K}$, mean molecular weight $\mu = 2.3$), this velocity dispersion corresponds to an initial RMS Mach number of about 4.5. Thus, the ratio of kinetic to gravitational energy of the gas sphere is $E_{\rm kin}/E_{\rm grav} \approx 0.25$. The equation of state is isothermal, and self-gravity is used throughout this code comparison. Sink particles are allowed to form in both codes at densities exceeding $\rho_{\rm res} = 8.0 \times 10^{-17}\,{\rm g\,cm^{-3}}$ with a sink particle accretion radius of $r_{\rm acc} = 7.3 \times 10^{15}\,{\rm cm} = 490\,{\rm AU}$. Both codes used the same spline softening, equation (5.26) for sink particle interactions, with the softening radius set equal to the accretion radius ($r_{\rm soft} = r_{\rm acc}$). The temporal evolution is followed in units of the initial freefall time $t_{\rm ff} = 3.39 \times 10^{12}\,{\rm s} = 1.07 \times 10^5\,{\rm yr}$.

For the FLASH run, we used a cubic computational domain with a boxsize of 0.4 pc, slightly larger than the diameter of the initial gas sphere ($d = 0.32\,{\rm pc}$). To keep the mass outside of the sphere small, the gas density was set two orders of magnitude smaller outside than the uniform density inside the sphere. The additional mass of $2.7\,{\rm M_\odot}$ outside the sphere is about 3% of the total mass, and thus the total mass in the computational domain is 3% larger in the FLASH run than in the SPH run. Pressure equilibrium is provided by keeping the gas outside the sphere at a temperature two orders of magnitude higher than inside.

For the SPH run the initial velocity field was interpolated from the grid to the SPH particles using the standard SPH smoothing kernel (Monaghan & Lattanzio, 1985). The initial density

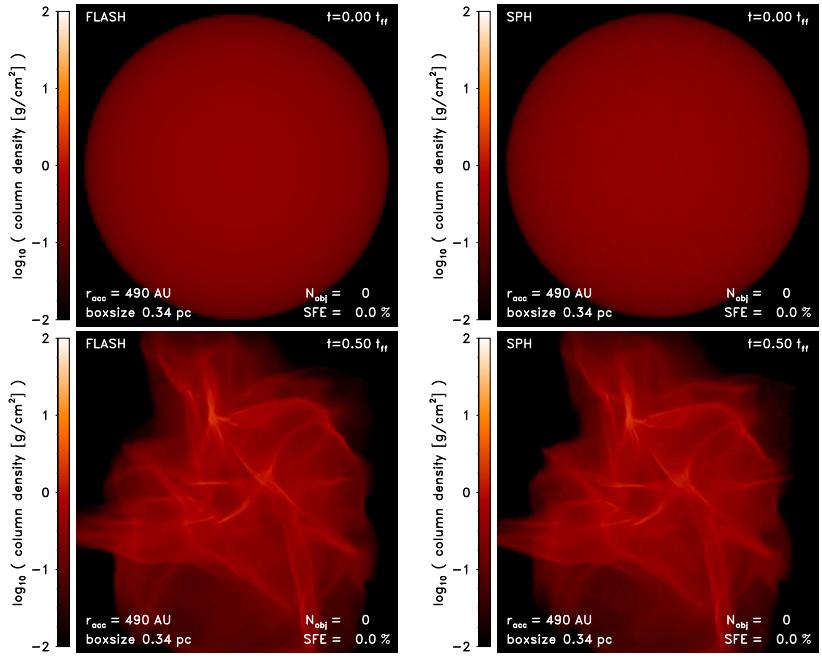

Figure 5.13: Comparison of the column density distributions obtained with the AMR code FLASH (left) and with the SPH code by Bate et al. (1995) (right) at $t = 0.0\,t_{\rm ff}$ (top) and $t = 0.5\,t_{\rm ff}$ (bottom) prior to the formation of a stellar cluster. The initial supersonic, turbulent velocity field creates a complex network of filaments. Some of these shocked regions become gravitationally unstable and collapse, i.e., sink particles are created, while other dense regions are transient features, not leading to local collapse (see Fig. 5.14).

outside the isolated gas sphere is zero for the SPH run since no particles were used there. However, a constant boundary pressure was applied in order to keep the sphere in pressure equilibrium with the surrounding. Both codes used isolated boundary conditions for the computation of the gravitational potential.

The initial conditions used in our comparison provide a more rigorous test of the performance of our codes than those commonly used in the study of cluster formation. Typically, initial conditions are set up with roughly equal kinetic and gravitational energies, $E_{\rm kin} \approx E_{\rm grav}$ (e.g., Bate et al., 2003; Bonnell et al., 2003). These clouds tend to evolve to form several centers of star formation, each producing a small group of fragments that feed from the gas delivered by the large-scale flows in the cloud. Clouds with less kinetic energy, in contrast, have less support against global contraction, and so undergo global collapse. As a result, such clouds tend to produce a single, dense star-forming center that also has a higher rate of star formation (e.g., Clark et al., 2008). As a consequence, the cloud modeled here enters a more violent and chaotic N-body phase, in which it is more difficult to obtain convergence for different numerical methods.

Resolution criterion in FLASH

In order to satisfy the resolution criterion in simulations including self-gravity, the gas density on the grid must not exceed a critical density $\rho_{\rm res}$ in regions of gravitational collapse (Truelove et al., 1997). This density is related to the smallest resolvable Jeans length $\lambda_{\rm J}$ on the highest level of the AMR hierarchy. The density threshold $\rho_{\rm res}$ is obtained by solving equation (5.2) for ρ, and using the Jeans length and sound speed of the gas resolved with AMR on the highest level

of refinement:

$$\rho_{\rm res} = \frac{\pi c_{\rm s}^2}{G\lambda_{\rm J}^2} = \frac{\pi c_{\rm s}^2}{4\,G r_{\rm acc}^2}\ . \tag{5.39}$$

Since the Jeans length should be resolved with at least 4 grid cells in AMR simulations (Truelove et al., 1997), the sink particle accretion radius $r_{\rm acc}$ must not be smaller than 2 grid cells. The sink particle accretion radius is thus determined by the smallest linear cell size Δx that can be resolved with pure AMR. We set $r_{\rm acc} \simeq 2.5\Delta x$ to satisfy the Truelove criterion on the highest level of refinement. The Jeans length $\lambda_{\rm J} = 2r_{\rm acc}$ is thus resolved with 5 grid cells on the top of the AMR hierarchy. However, on all AMR levels smaller than the maximum level of refinement we resolve the Jeans length with at least 12 grid cells to follow features on their way to runaway collapse more accurately. We additionally apply the shock refinement criterion provided in FLASH (Fryxell et al., 2000), and our additional refinement on sink particles (cf. section 5.2.2).

For the comparison test presented here, we used a fixed base grid with 128^3 grid cells plus two levels of AMR resulting in an effective resolution of 512^3 grid cells.

Resolution criterion in SPH

Bate & Burkert (1997) have shown that at least two times the number of SPH neighbors, $2N_{\rm neigh}$ particles are necessary for resolving the minimum Jeans mass to avoid artificial fragmentation in SPH codes. The Jeans mass is defined as

$$M_{\rm J}(\rho) = \frac{4\pi}{3}\left(\frac{\lambda_{\rm J}(\rho)}{2}\right)^3 \rho = \frac{1}{6}\pi^{5/2}\left(\frac{k_{\rm B}T}{G\mu m_{\rm H}}\right)^{3/2} \rho^{-1/2}\,, \tag{5.40}$$

where $k_{\rm B}$, μ and $m_{\rm H}$ are the Boltzmann constant, the mean molecular weight and the mass of a hydrogen atom, respectively. Assuming a number of SPH neighbors of roughly $N_{\rm neigh} \simeq 50$, we can estimate the mass resolution limit for an SPH calculation as $M_{\rm res} \simeq M_{\rm J}(\rho_{\rm res})/100$. The corresponding sink particle accretion radius is $r_{\rm acc} = \lambda_{\rm J}(\rho_{\rm res})/2$.

Since we resolve the Jeans length with 5 grid cells in the FLASH run, we chose to use a similar number of SPH smoothing lengths to resolve the Jeans length in the SPH run. Therefore, we used a total number of 2 million SPH particles for our comparison, which roughly corresponds to resolving the Jeans length with 5 SPH smoothing lengths. Furthermore, the initial velocity field was constructed on a grid with $128^3 \sim 2 \times 10^6$ grid cells. Thus, to accurately sample the initial velocity field with SPH particles, it was reasonable to use a similar number of resolution elements in the SPH code as grid cells for the initial velocity field.

5.4.3 Results of the sink particle code comparison

Column density distributions

Figure 5.13 shows the column density distributions of the FLASH (left) and the SPH run (right) at $t = 0.0\,t_{\rm ff}$ (top) and $t = 0.5\,t_{\rm ff}$ (bottom). The initial supersonic turbulent velocity field has generated a complex network of shocks at $t = 0.5\,t_{\rm ff}$. Some of the shock-compressed gas becomes gravitationally unstable and goes into freefall collapse. This happens at roughly $t = 0.8\,t_{\rm ff}$ as shown in the top panels of Figure 5.14 (left and middle columns for FLASH and SPH, respectively). Five sink particles have formed in both the FLASH and the SPH run, containing a total mass of $0.9\,{\rm M}_\odot$ and $0.7\ {\rm M}_\odot$, respectively. They form at roughly the same locations in the gas distribution with slight differences in the exact positions. These differences are mainly due to the slightly different hydrodynamic evolution of the gas prior to sink particle formation in the FLASH and SPH runs. There is striking agreement between the FLASH and SPH runs at $t = 0.9\,t_{\rm ff}$, indicated by the number of sink particles (15 versus 17) and their accreted mass ($4.9\,{\rm M}_\odot$).

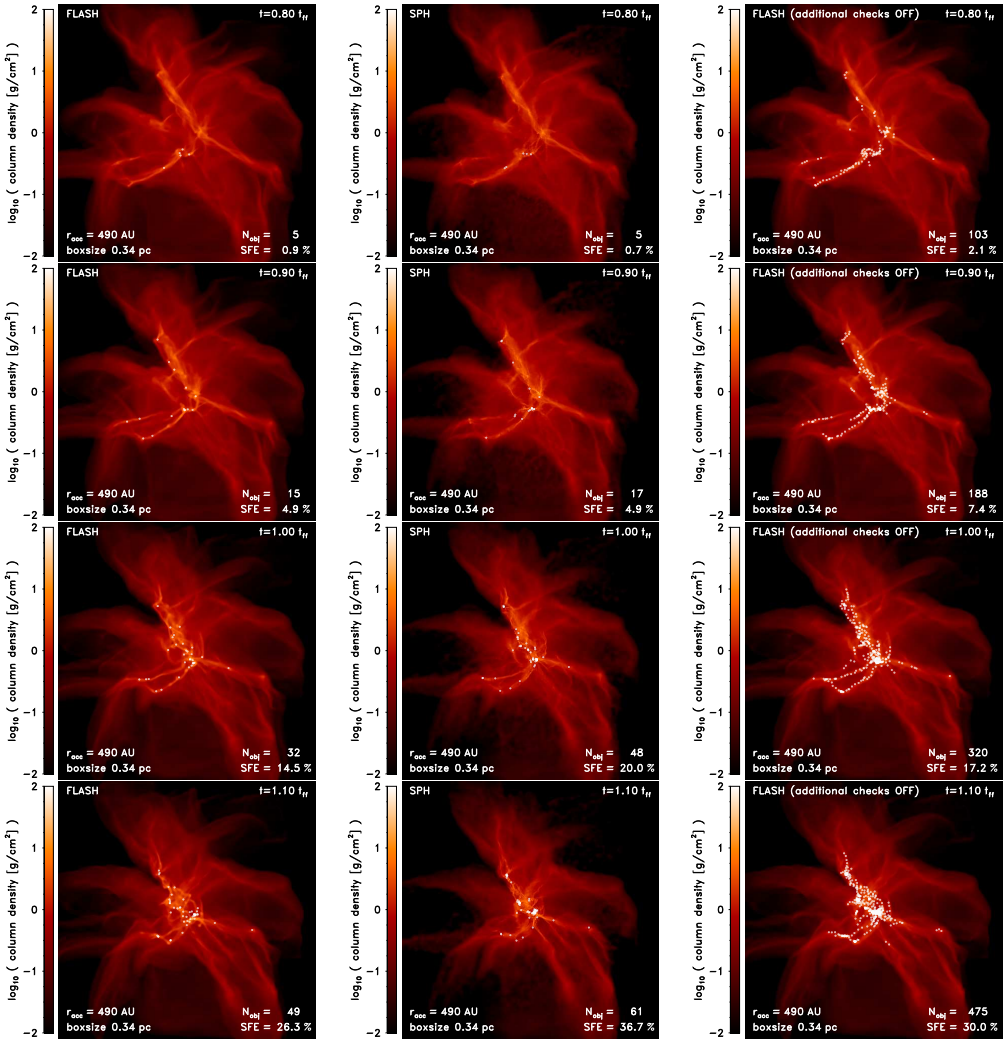

Figure 5.14: Same as Figure 5.13, but white filled circles show the projected position of sink particles obtained with FLASH (left panels) and SPH (middle panels) as a function of the global freefall time ($t/t_{\rm ff}$ = 0.8, 0.9, 1.0, 1.1, from top to bottom). Sink particles form at roughly the same positions in the FLASH and SPH runs. The number and mass of sink particles is in excellent agreement for $t < 1\,t_{\rm ff}$. At later times ($t > 1\,t_{\rm ff}$), the stellar cluster produced in the SPH run collapses on slightly smaller timescales than the FLASH cluster, and is more centrally condensed at $t = 1.1\,t_{\rm ff}$. The right panels show the effect of *only* using a density threshold for sink particle creation with FLASH, compared to the default FLASH run (left panels), for which *all* sink particle creation checks (see Section 5.2.2) were used. Without additional checks for converging flows, gravitational potential minimum, bound state, and Jeans instability, a significant number of spurious sink particles are created, which do not represent collapsing objects. Most of the sink particles in the right hand panels were formed in transient density peaks caused by shocks that did not accumulate enough mass to create gravitationally bound and collapsing objects. The much larger number of particles created in that case may be reduced by some sort of merging algorithm, but the accreted mass in sink particles would still be overestimated, in particular at early times (by 133%, 51%, 19% and 14% compared to the default FLASH run at $t/t_{\rm ff}$ = 0.8, 0.9, 1.0 and 1.1, respectively), if a sole density threshold was used for sink particle creation at densities below the opacity limit. In contrast, the sink particles in the left hand plots (default FLASH runs) represent gravitationally bound and collapsing objects, as in the SPH run (middle panels).

At $t = 0.9\,t_{\rm ff}$, the gas distribution has already started to collapse globally due to the decay of the initial turbulence. At $t = 1.0\,t_{\rm ff}$, 32 sink particles containing a total of $14.5\,{\rm M}_\odot$ have formed in the FLASH run, while the SPH run has produced 48 sink particles with $20.0\,{\rm M}_\odot$. Thus, the FLASH and SPH runs start to diverge at $t = 1.0\,t_{\rm ff}$. The star cluster produced in the SPH run is slightly denser than in the FLASH run. This trend continues to the last snapshot at $t = 1.1\,t_{\rm ff}$ when the FLASH run has produced 49 sink particles with $26.3\,{\rm M}_\odot$, while the SPH run has produced 61 with $36.7\,{\rm M}_\odot$. The star cluster is clearly denser in the SPH run at this last time. There are still new sink particles forming in the outskirts of the cluster. They from at very similar locations in both the FLASH and the SPH runs. For example, at $t = 1.1\,t_{\rm ff}$ the rightmost sink particle has formed at almost exactly the same location in both codes with respect to the position of the dense core forming there. However, this particular sink particle also forms slightly closer to the center of the star cluster, reflecting the faster global collapse in the SPH run. This is discussed further in the following section.

Radial profiles

To quantify the differences in the FLASH and SPH runs we show radial profiles of the mass, density and radial velocity in Figure 5.15 for times $t = 0.0$, 0.5, 0.8, 0.9, 1.0 and $1.1\,t_{\rm ff}$ (from top to bottom). The initial conditions are compared in the three top panels. The density is constant inside the initial gas sphere with a radius of $R = 5.0 \times 10^{17}\,{\rm cm} = 3.3 \times 10^4\,{\rm AU}$. Thus, the integrated mass grows with the radius r proportional to r^3 inside the sphere until it reaches $M = 100\,{\rm M}_\odot$ at $r = R$. In the FLASH run, the mass grows slightly further for $r > R$ up to about $103\,{\rm M}_\odot$, because of the remaining low-density gas outside of the sphere as discussed in section 5.4.2. In contrast, the density is zero for $r > R$ in the SPH run. Initially, the radial velocity is roughly zero, because the turbulent velocity field was constructed to be isotropic with zero mean.

At $t = 0.5\,t_{\rm ff}$ the radial velocity indicates the onset of global infall with slightly supersonic speeds of $0.5\,{\rm km\,s^{-1}}$ at $r \sim 1 - 2 \times 10^4\,{\rm AU}$. Both the FLASH and the SPH run exhibit similar radial profiles at that time. When the first sink particles have formed ($t = 0.8\,t_{\rm ff}$) the radial density profiles roughly follow $\rho(r) \propto r^{-3/2}$ (see e.g., Shu, 1977) for $2 \times 10^3 \lesssim r/{\rm AU} \lesssim 2 \times 10^4$. At $t = 0.9\,t_{\rm ff}$ the FLASH and SPH run have produced 15 and 17 sink particles, respectively, which is seen as density peaks in the radial density profiles. The infall velocities have reached Mach 5 at that time, and they are roughly consistent between the two codes. However, at $t = 1.0\,t_{\rm ff}$ the SPH run shows slightly larger infall speeds than the FLASH run for $2 \times 10^3 \lesssim r/{\rm AU} \lesssim 2 \times 10^4$. This becomes more prominent at $t = 1.1\,t_{\rm ff}$, reaching down to the cluster center, when the infall speeds in the SPH run are almost twice as large as in the FLASH run. The star cluster produced in the SPH run is denser, which is shown by the mass and density profiles at $t = 1.1\,t_{\rm ff}$. This is consistent with the visual inspection of column density images discussed in the previous section. Thus, the global collapse of the gas cloud proceeds slightly faster in the SPH run compared to the FLASH run.

There are three explanations for this behavior, probably all contributing to the faster collapse speeds in the SPH run. First, the gas mass outside the sphere may contribute to slow down the collapse slightly in the FLASH run. *Inflow* boundary conditions were used for the hydrodynamics in the FLASH run. Thus, low-density gas is streaming in from the boundaries during the global collapse, which further increases the filamentary excess mass outside of the cluster from $3\,{\rm M}_\odot$ to $5\,{\rm M}_\odot$. Secondly, both the FLASH and SPH codes have different dissipation mechanisms. Kitsionas et al. (2009) find that SPH codes tend to dissipate small-scale, random, turbulent motions slightly faster than grid codes. Thus, our SPH run may loose turbulent support faster than our FLASH run, which shifts the onset of global collapse to earlier times in the SPH run. Finally, one must consider that the low-density gas is better resolved in the grid calculation (e.g., Price & Federrath, 2010). This becomes even stronger at later times when the number of SPH

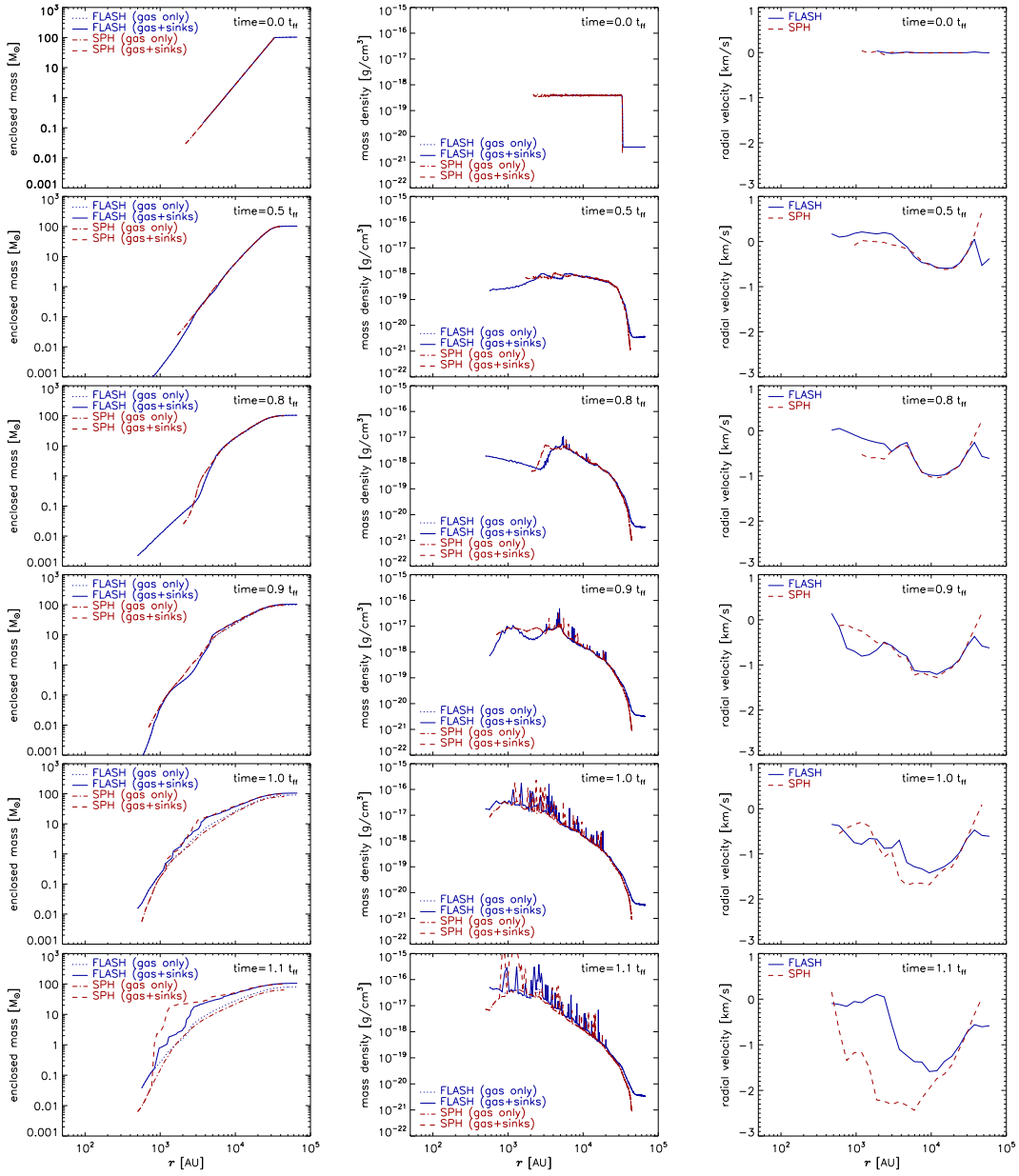

Figure 5.15: Comparison of radial profiles (cumulative mass, density, and radial velocity from left to right), obtained in the FLASH and SPH runs as a function of global freefall time ($t/t_{\rm ff}$ = 0.0, 0.5, 0.8, 0.9, 1.0, 1.1, from top to bottom).

particles decreases due to accretion, and the number of grid cells in the FLASH run increases due to the Jeans refinement and the formation of sink particles (cf. 5.2.2). Therefore, at late times, the numerical resolution of the FLASH run becomes increasingly superior to the SPH run. For the star cluster simulation presented here, lower numerical resolution could lead to somewhat smaller collapse timescales, because small-scale turbulent pressure support is weaker at lower resolution. We conclude that all these three effects may contribute to the slightly faster global collapse in the SPH run compared to the FLASH run.

Mass distributions of fragments

Figure 5.16 shows a comparison of the mass distributions of sink particles obtained in the FLASH and SPH runs at $t = 0.8$, 0.9, 1.0 and $1.1\,t_{\rm ff}$ (from top to bottom). The left panels show the histograms of sink particle mass, while the right panels show the cumulative mass distributions from which the Kolmogorov-Smirnov probability (p-KS) was determined with a KS test. The KS test provides an estimate of the probability that the mass distributions obtained in the FLASH and in the SPH run were drawn from the same basic distribution, and it thus provides an estimate of their similarity.

Figure 5.16 shows that at $t = 0.8\,t_{\rm ff}$ the KS probability is about 70%, which means that the mass distributions obtained in the FLASH and SPH run are very likely drawn from the same distribution. The similarity in the number of particles formed and in the mass accreted onto sink particles taken together with the similarity in the location of sink particles at that time is encouraging. This is an important result, because it shows that two independent implementations of sink particle formation in two fundamentally different hydrodynamic codes give almost identical results for the number, mass and location of formed fragments.

At later times, the KS probability drops to 55%, 40% and 8% at $t = 0.9$, 1.0 and $1.1\,t_{\rm ff}$, respectively. However, the general shape of the mass distributions obtained in the FLASH and SPH runs is similar for all times (although the relatively small number of sink particles does not allow for a detailed comparison of the slope at the high-mass end of the distributions). The peaks of the mass distributions agree well for $t \leq 1.0\,t_{\rm ff}$. However, at $t = 1.1\,t_{\rm ff}$ the peak of the distribution is shifted to slightly higher masses in the SPH run as a result of the faster global collapse in the SPH run (cf. section 5.4.3). The high-mass ends of the FLASH and SPH mass distributions are roughly consistent with the Salpeter (1955) power law, $N \propto M^{-1.35}$, as also found in previous SPH studies. However, our statistical samples are not large enough to draw further quantitative conclusions on the slope of the high-mass end. It should also be noted that the low-mass end is probably affected by our assumption of an isothermal equation of state. Our models did not take into account the effects of radiation transfer, which is expected to suppress fragmentation (Krumholz et al., 2007; Bate, 2009). However, the fact that our sink particle radius is about 500 AU in this simulation does not allow any fragmentation below this scale. Thus, we are more likely underestimating the amount of fragmentation, because we cannot follow possible fragmentation on scales smaller than about 500 AU.

The fact that the KS probability becomes smaller at later times is a result of the faster global collapse in the SPH run. To quantify this further, we compare the mass distributions at the times when the total mass of sink particles is roughly the same in the FLASH and SPH runs. Figure 5.17 shows the mass distribution of FLASH at $t = 1.1\,t_{\rm ff}$ together with the mass distribution of SPH at $t = 1.04\,t_{\rm ff}$ (about 5% earlier) when the sink particle formation efficiency is about 26% in both runs. The mass distributions agree very well for similar sink formation efficiencies, which is indicated by a KS probability of 55%. Moreover, the number of fragments is almost identical in the FLASH and SPH run (49 versus 50). There is striking agreement between the sink particle properties obtained in our FLASH implementation and in the Bate et al. (1995) implementation for SPH albeit the highly complex and chaotic nature of the problem modeled in this code comparison. The fact that two fundamentally different numerical schemes with complementary strengths and weaknesses give the same overall result is very encouraging. It strengthens our confidence in simulations of the turbulent collapse of clouds with AMR on the one hand and SPH on the other hand.

Computational efficiency of FLASH and SPH

We briefly mention the computational efficiency of our FLASH and SPH runs. Both codes were run in a mode of parallel computation on the same supercomputer (HLRB-II: SGI Altix 4700)

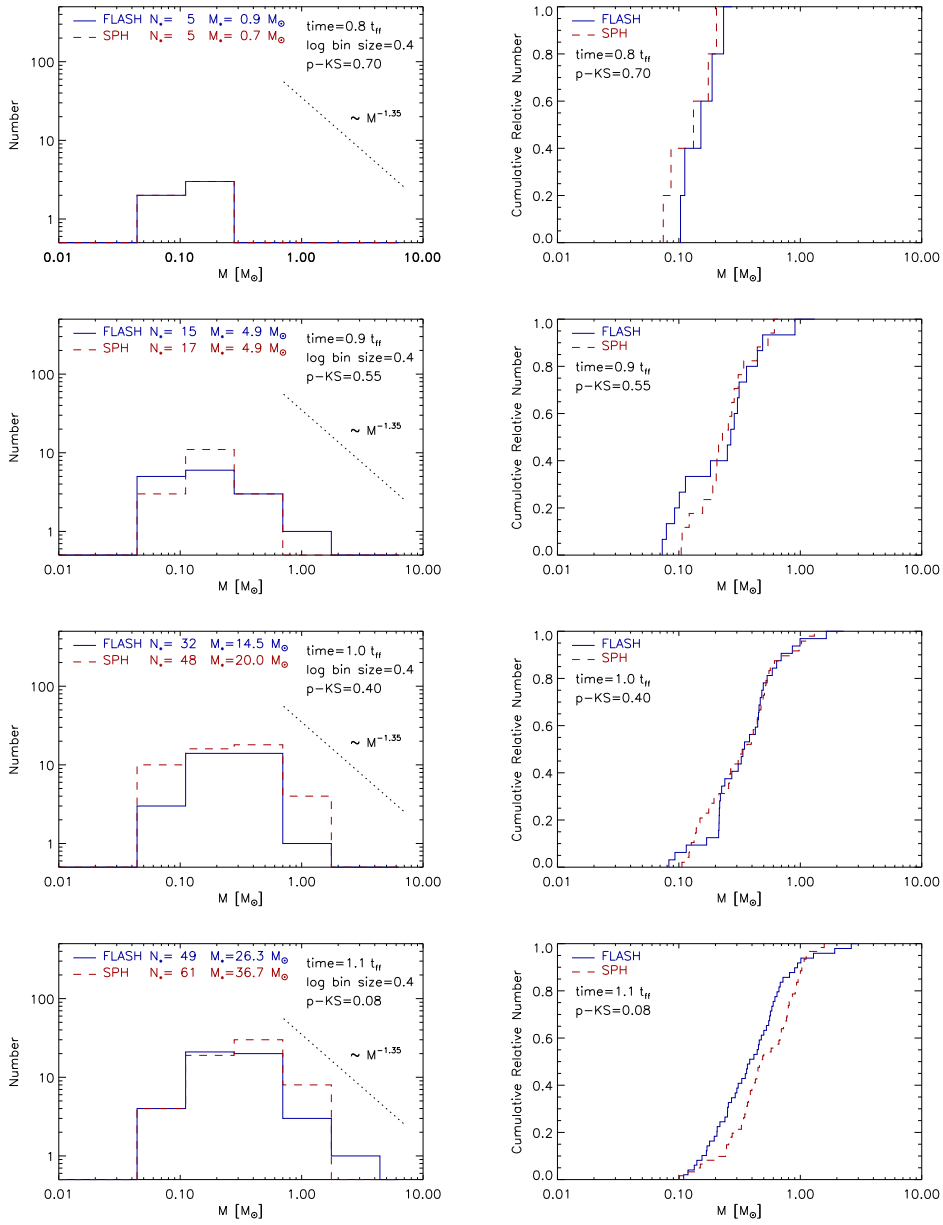

Figure 5.16: Comparison of the sink particle mass distributions (left) and cumulative mass distributions (right), obtained with FLASH and SPH as a function of global freefall time ($t/t_{\rm ff}$ = 0.8, 0.9, 1.0, 1.1, from top to bottom).

at the Leibniz-Rechenzentrum Garching[2]. The FLASH run consumed about 10,300 CPU hours and was run on 128 CPUs. The SPH run consumed roughly 2,400 CPU hours and was run on 16 CPUs, which is 4-5 times faster than the FLASH run. The SPH code automatically increases resolution in high-density regions, without the necessity to increase the number of resolution elements there, because the SPH particles move in the Lagrangian frame. It should be noted

[2] `http://www.lrz-muenchen.de`

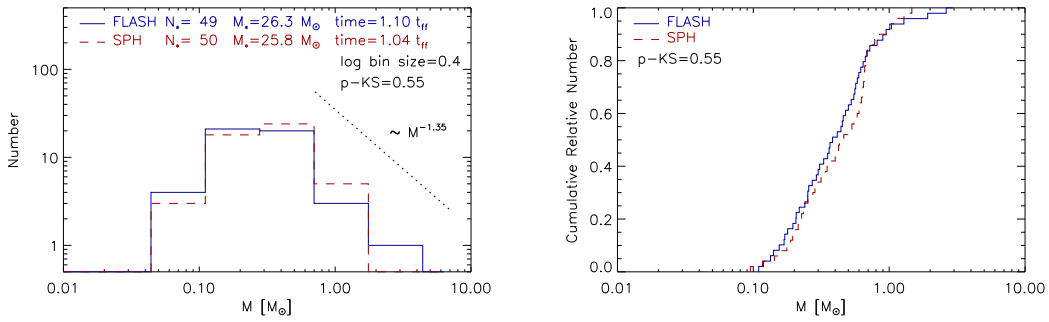

Figure 5.17: Same as the bottom panels of Figure 5.16, but the mass function of FLASH at $t = 1.10\,t_{\rm ff}$ is compared to the mass function of SPH at $t = 1.04\,t_{\rm ff}$, when the accreted gas mass is roughly the same for both runs ($M_\star \sim 26\,{\rm M}_\odot$). The number of fragments (sink particles) is in excellent agreement between the two codes. The mass distributions are also very similar as shown by a Kolmogorov-Smirnov probability of 55%, which indicates that the two samples are likely drawn from the same fundamental distribution.

however that due to accretion of SPH particles onto sink particles, the total number of SPH particles decreases from the initial 2 million to about 1.3 million at $t = 1.1\,t_{\rm ff}$. In contrast, the Eulerian code FLASH refined the grid adaptively in high-density regions. The number of resolution elements (grid cells) thus increases from about 32 million at $t = 0$ to 56 million at $t = 1.1t_{\rm ff}$, which is a factor of about 30 more resolution elements on average in the FLASH run compared to the SPH run. The computational cost per resolution element was thus a factor of 6-8 smaller for FLASH than for SPH. This is roughly consistent with the difference in the average computational efficiency per resolution element measured for typical grid-based and particle-based hydrodynamic codes in the case of non-selfgravitating, supersonic turbulence (e.g., Kitsionas et al., 2009; Price & Federrath, 2010).

5.5 Conclusions

We introduced an implementation of accreting sink particles for the adaptive mesh refinement code FLASH. Sink particles are used as a subgrid model to cut-off local runaway collapse in a controlled way to avoid artificial fragmentation and to avoid prohibitive small timesteps in numerical simulations involving multiple collapse regions. Sink particles interact gravitationally with the gas and with one another, and can accrete bound gas. The gas must pass a series of checks prior to sink particle formation as explained in detail in section 5.2.2. In particular, in our grid-based implementation the gas considered for sink particle creation is not only required to exceed a given density threshold, but this gas must be gravitationally bound and collapsing at the same time, similar to the original sink particle implementation of Bate et al. (1995) for SPH. Figure 5.14 (right panels) shows that spurious sink particles would be created in the star cluster formation run discussed in section 5.4, if a *sole* density threshold was used to determine sink particle creation. The root cause of spurious sink particle creation is that the gas density can exceed the given density threshold in shocks that do not necessarily trigger gravitational collapse. Figure 5.14 (right versus left panels) shows that the number of fragments would be overestimated by more than one order of magnitude, and that the star formation efficiency (total gas mass accreted by sink particles) would also be overestimated by 133%, 51%, 19% and 14% at $t/t_{\rm ff} = 0.8$, 0.9, 1.0 and 1.1, respectively, if the additional checks described in section 5.2.2

are switched off. Some sort of sink particle merging could be used to reduce the overestimated number of sink particles, but the mass accreted onto sink particles would still be overestimated if a sole density threshold was used for sink particle creation at densities below the opacity limit (about $10^{-14}\,\mathrm{g\,cm^{-3}}$).

We performed a series of tests of our sink particle implementation in section 5.3, including the time integration of circular and elliptical orbits, the collapse of a Bonnor-Ebert sphere, and a rotating cloud core fragmentation test. The sink particle accretion rate in the collapse of a singular isothermal sphere showed excellent agreement with the theoretical predictions of the Shu (1977) model. Those tests showed that the dynamical creation, gravitational interaction, motion, timestepping and accretion of sink particles works in a way that enables us to analyze the trajectories, accretion rates and mass distributions of collapsing fragments quantitatively and reliably in follow-up studies that will also include MHD effects.

A comparison calculation of star cluster formation between the SPH code by Bate et al. (1995) and our grid-based FLASH implementation showed encouraging agreement of gas and sink particle properties obtained in the SPH and FLASH runs (cf. section 5.4). Using column density images, we demonstrated that sink particles are created at roughly the same locations and times in both codes. Radial velocity profiles revealed that the global collapse in the SPH run was about 5% faster than in the FLASH run, probably due to the slightly higher numerical dissipation in SPH codes (Kitsionas et al., 2009; Price & Federrath, 2010). After correction for this time lag, we showed that the number of sink particles and their mass distributions in the FLASH and SPH runs are in very good agreement. The agreement of our FLASH and SPH runs is an encouraging result that strengthens our confidence in numerical simulations of gravoturbulent cloud fragmentation and collapse with AMR and SPH.

Chapter 6

Summary and outlook

6.1 Summary

In Chapters 2, 3, and 4, I discussed the density and velocity statistics of compressible, supersonic turbulence in molecular clouds and the relation of turbulence to star formation. In numerical experiments I compared turbulence driven by the frequently applied solenoidal (divergence-free) forcing and driven by a new approach that I called compressive (curl-free) forcing. This systematic forcing comparison provides striking evidence that the nature of the turbulence forcing must be taken into account in any theory of star formation based on the statistics of supersonic turbulence. In fact, this applies to essentially all modern star formation theories (e.g., Padoan & Nordlund, 2002; Krumholz & McKee, 2005; Tassis, 2007; Elmegreen, 2008; Hennebelle & Chabrier, 2008, 2009; Padoan & Nordlund, 2009; Krumholz et al., 2009). In addition, I introduced the sink particle method for the FLASH code to model gravitational collapse and accretion in turbulent gas clouds in Chapter 5. The sink particles will allow us to test and quantify the star formation theories mentioned above in forthcoming works. The main results presented in this thesis are summarized in the following sections.

6.1.1 The density probability distribution in compressible isothermal turbulence: solenoidal vs compressive forcing

In Chapter 2, I investigated the probability density function (PDF) of the gas density in turbulent supersonic flows with high-resolution numerical experiments. The main result of this study is that compressive forcing yields a density PDF with standard deviation about three times larger than in the case of solenoidal forcing for the same RMS Mach number.

6.1.2 The fractal density structure in supersonic isothermal turbulence: solenoidal vs compressive energy injection

Following-up on this study of the PDF, I discussed the scaling of the volume density and the column density of the fractal structures obtained in the simulations of solenoidal and compressive forcing in Chapter 3. The major result is that compressive forcing yields a fractal dimension of about 2.3 ± 0.1, while solenoidal forcing yields 2.6 ± 0.1, which is within the range of fractal dimension estimates inferred from observations ($D \sim 2.0 \ldots 2.7$).

6.1.3 Comparing the statistics of interstellar turbulence in simulations and observations: solenoidal vs compressive turbulence forcing

In Chapter 4, I focused on the comparison of our solenoidal and compressive forcing simulations with observations. In addition, eleven models with different forcing mixtures were analyzed. From this study I concluded that the strong dependence of the density PDF on the type of forcing must be taken into account in any theory using the PDF to predict properties of star formation. I supply a quantitative description of this dependence. I found that different observed regions show evidence of different mixtures of compressive and solenoidal forcing, with more compressive forcing occurring primarily in swept-up shells. Finally, I showed that core formation close to the sonic scale naturally explains the frequently observed subsonic velocity dispersions of protostellar cores.

6.1.4 Modeling collapse and accretion in turbulent gas clouds: implementation and comparison of sink particles in AMR and SPH

In order to enable a quantitative comparison of the star formation rate and the mass distribution of cores and stars, as predicted in analytic theories of star formation, I implemented accreting sink particles in the adaptive mesh refinement (AMR) fluid dynamics code FLASH, the details of which are described in Chapter 5. I applied the sink particle module to the formation of a star cluster, and compared it to a standard smoothed particle hydrodynamics (SPH) code with sink particles. My comparison showed encouraging agreement of gas properties, indicated by column density distributions and radial profiles, and of sink particle formation times and positions. I found excellent agreement in the number of sink particles formed, and in their accretion and mass distributions. I hope that this encouraging result helps to strengthen the confidence in numerical simulations of gravoturbulent cloud fragmentation and collapse with AMR and SPH.

6.2 Outlook and future directions

6.2.1 The star formation rate of supersonic turbulence: solenoidal vs compressive forcing

In the numerical studies of purely driven supersonic turbulence, discussed in Chapters 2, 3, 4, I did not include the effects of self-gravity, because I specifically focused on the pure turbulence statistics obtained in solenoidal and compressive forcings. However, it is the self-gravity of the gas that will eventually lead to the formation of stars. It must be included in studies of star formation, and thus I present preliminary simulations of gravitating turbulence (gravoturbulence) here. As shown in Chapter 5 such numerical studies inevitably require the use of sink particles to follow the collapse of individual objects.

Figure 6.1 (top panels) shows two snapshots of the column density in a gravoturbulent simulation using solenoidal forcing (left) and compressive forcing (right). The time shown corresponds to the time when the sink particles have accreted about 10% of the initial gas mass of $1,850\,\mathrm{M}_\odot$. Turbulence was driven until an RMS Mach number of $\mathcal{M} = 10$ was reached in both cases, then I activated self-gravity and allowed for the formation of sink particles. The driving of the turbulence remained active in the course of the whole simulation. The number of objects formed was roughly the same in both cases at the time when the simulations were stopped, i.e., when the sink formation efficiencies were about 10% in both forcing cases (at $t = 2.80\,\mathrm{Myr}$ and $0.12\,\mathrm{Myr}$ for solenoidal and compressive forcing, respectively). I prefer not to follow the simulation to later times, not only because the simulation becomes computationally expensive, but mainly because radiative and mechanical feedback processes (e.g., jets and outflows, see 6.2.5 below) from

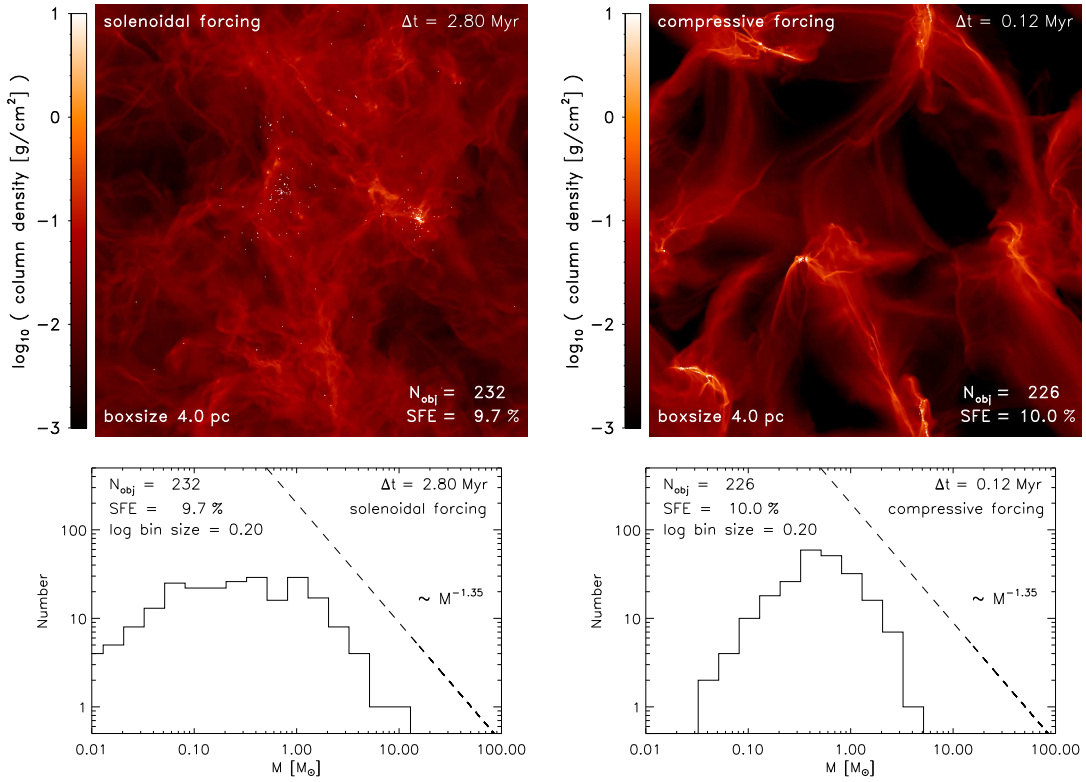

Figure 6.1: *Top panels*: column density snapshots of a simulation of gravoturbulent fragmentation using the standard solenoidal (divergence-free) forcing (*left*) and compressive (curl-free) forcing (*right*) at times when about 10% of the gas had been accreted onto sink particles in both runs. *Bottom panels*: the corresponding mass distribution of the sink particles. Although the Mach number was the same in both runs ($\mathcal{M} = 10$), the star formation rate is about 25 times higher for compressive forcing compared to solenoidal forcing.

the newly formed stars will likely alter the subsequent evolution. Feedback processes were not included in the present numerical experiment. However, Peters et al. (2010) have investigated radiative feedback on core scales, while including both radiative and mechanical feedback on larger scales will be subject of work for the near future.

The most striking result of the systematic comparison shown in Figure 6.1 is that compressive forcing produced the same amount of star formation (i.e., in terms of mass accreted and number of sink particles) about 25 times faster than solenoidal forcing. If the density PDF (see Chapter 2) is indeed the most important ingredient controlling the star formation rate as suggested by e.g., Krumholz & McKee (2005) and Padoan & Nordlund (2009), then the forcing dependence of the density PDF must be taken into account in any successful theory of star formation based on the PDF (see, section 1.2 of the introduction). The quantitative comparison of the analytic theories of star formation (see also, Padoan & Nordlund, 2002; Hennebelle & Chabrier, 2008, 2009) with numerical simulations is one of the most important projects that I will pursue in the near future.

6.2.2 Turbulent molecular cloud formation and comparison with observations

Measuring the density PDF

If we accept that the density PDF is essential for understanding molecular cloud and star formation, we have to find a way to measure it in observations and to compare it with simulations and theory. Measuring the density PDF in observations has been attempted using dust extinction maps (e.g., Lombardi et al., 2006; Kainulainen et al., 2009), dust emission, and ^{13}CO line emission (Goodman et al., 2009). The fundamental difficulty, however, is to relate the column density PDF (which is accessible to observations) to the three-dimensional density PDF (not directly accessible to observations) in order to enable a quantitative comparison with the analytic models of star formation. Brunt et al. (2010b,a) suggested a statistical method to calculate the three-dimensional PDF using only information contained in the projected two-dimensional column density field. They tested the method by applying it to numerical simulations of hydrodynamic and magnetohydrodynamic turbulence in molecular clouds, and showed that the PDF of log(normalized column density) is a compressed, shifted version of the PDF of log(normalized density). This method will facilitate the comparison of observations, simulations and theory of star formation in the future.

The X-factor

To enable realistic comparisons of simulations and observations, we have to model the observed chemical tracers. Among the most commonly observed tracer is carbon monoxide (CO), which is frequently used to infer the gas content of a cloud, i.e., to infer the most abundant molecule, molecular hydrogen (H_2). However, the reliability of CO as a tracer for H_2 has long been questioned in different environments. In particular, to measure the H_2 column density, which is inaccessible to observations (except for gas much hotter than the typical temperature of molecular clouds), the so called X-factor,

$$X_{\rm CO} = \frac{N(\rm H_2)}{W(^{12}\rm CO\ 1 \rightarrow 0)} \tag{6.1}$$

is frequently used, which is the ratio of the H_2 column density, $N(H_2)$, to the line-of-sight integrated emission, W, from the rotational transition, $J = 1 \rightarrow 0$ of the ^{12}CO molecule.

It is just recently that enough computer power and the necessary methods have become available to address the reliability of assuming a constant X-factor in a systematic way through numerical simulations (Glover et al., 2009). Figure 6.2 shows column density distributions of a driven turbulence simulation where we follow the formation and destruction of H_2 and CO alongside 30 other chemical species. CO forms primarily in filaments of dense gas, created by turbulent compression. We find that the ratio of H_2 to CO column density is clearly not constant (see Figure 6.3), indicating that the X-factor is far from being constant, too. This is investigated further by Glover & Mac Low (2010) who find that the scatter of this ratio over more than two orders of magnitude is primarily due to the different formation and destruction mechanisms for H_2 on the one hand, and CO on the other. The abundance of H_2 is primarily determined by the amount of time available for its formation, but rather insensitive to photodissociation, because of its effective self-shielding. CO forms quickly, within a dynamical time, but its abundance depends primarily on photodissociation, with only a weak secondary dependence on H_2 abundance. What does this mean for observations using CO to measure turbulence statistics and star formation properties? Can we come up with a method to correct for the uncertainties introduced by the variations in the abundance ratio of CO and H_2? These questions have to be addressed in order to enable meaningful comparisons of observations with theory and numerical models.

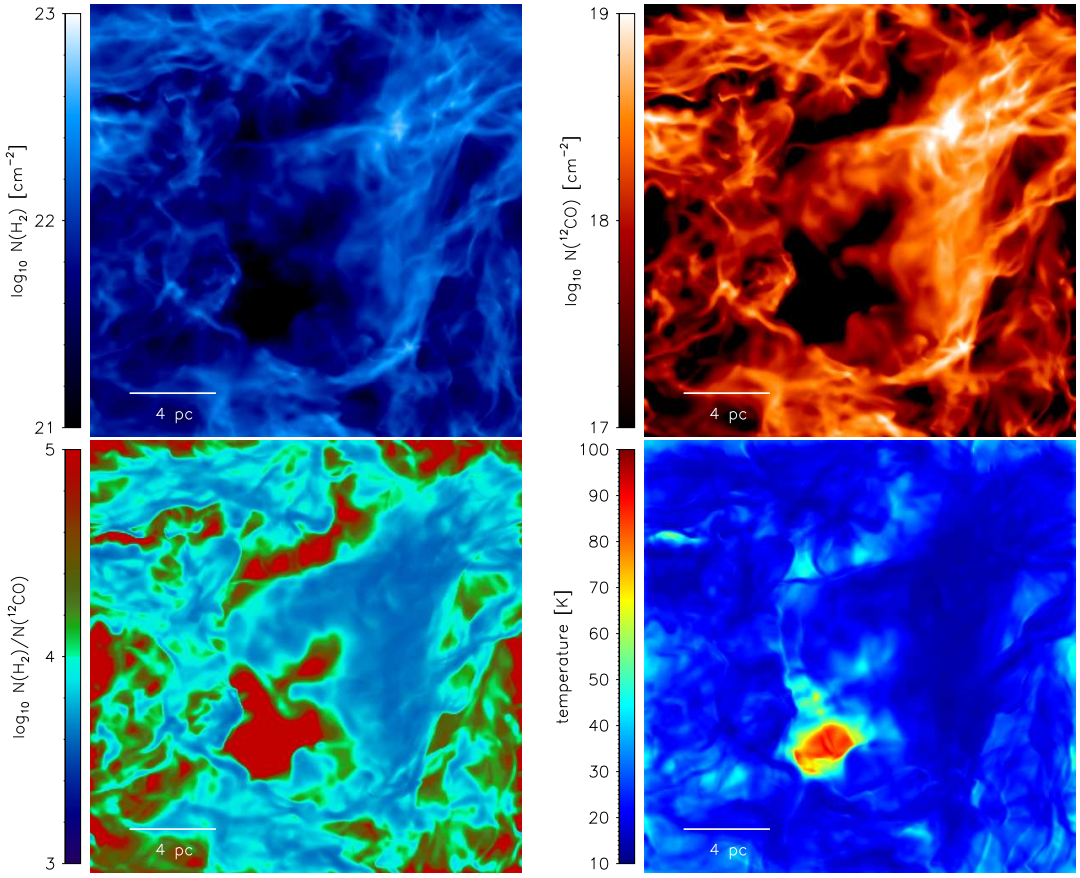

Figure 6.2: Maps of the H_2 column density, $N(H_2)$ (*top left*), the ^{12}CO column density, $N(^{12}CO)$ (*top right*)), the ratio, $N(H_2)/N(^{12}CO)$ (*bottom left*)), and the temperature, $\int \rho T \mathrm{d}z / \int \rho \mathrm{d}z$ (*bottom right*)) for run R3 of Glover et al. (2009) with 256^3 grid zones, at time $t = t_{\mathrm{end}} = 5.7\,\mathrm{Myr}$, viewed along the lines-of-sight parallel to the z axis.

Future directions for including chemistry in numerical models

One of the key results of Glover et al. (2009) is that CO forms rapidly, within a dynamical time. We can thus expect that once a sufficiently strong shock creates an overdensity, such that CO can form quickly, the cloud will be readily observable. However, Glover & Mac Low (2010) show that the formation of H_2 typically needs more time, $t_{\mathrm{form}} \propto n^{-1}$ (Hollenbach et al., 1971), depending sensitively on the number density n. We thus expect compressive forcing to create dense H_2 clouds significantly faster than solenoidal turbulence forcing. Indeed, recent numerical work (M. Milosavljevic et al., in preparation) confirms this expectation, which needs to be quantified further. In any case, it seems likely that molecular clouds are created by compressive turbulence forcing rather than purely solenoidal forcing.

Moreover, I can identify two important extensions of the present chemical network that will be necessary for the study of star formation on scales of individual dense cores in the future. First, we have to include the freeze-out of CO on dust grains at densities $n \gtrsim 10^4\,\mathrm{cm}^{-3}$, a process that can potentially affect the cooling, and thus the fragmentation of dense gas. Moreover, once frozen out on dust grains, the CO will be inaccessible to observations. Second, to facilitate the comparison with observations, following nitrogen-bearing molecules will be useful. It is those ob-

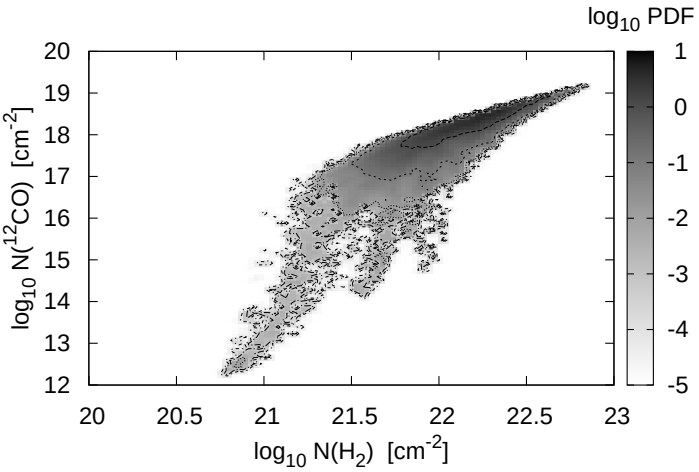

Figure 6.3: Correlation PDF of the column density of ^{12}CO and H_2.

servational tracers (e.g., NH_3) that are frequently used to identify dense cores (e.g., Friesen et al., 2009). However, adding pathways to the formation and destruction of nitrogen-bearing molecules in simulations will increase the complexity and required computational resources significantly, rendering it a very challenging, but promising study for the more distant future.

6.2.3 Turbulent mixing

The role of turbulent mixing prior to star formation has been investigated by e.g., Klessen & Lin (2003) and Federrath et al. (2008a). They found that even in strongly self-gravitating environments, turbulence is efficiently mixing gas of high density with low density material, within fractions of a dynamical time. This points towards a state of well-mixed gas in molecular clouds prior to star formation. Glover & Mac Low (2007b) also found that H_2 that formed at high density is quickly transported to lower density gas. Observations also indicate that gas is well-mixed prior to star formation. For instance, stars that formed from the same molecular cloud in the Pleiades cluster have nearly identical metal abundance Wilden et al. (2002).

An important task of future simulations is to quantify the mixing of gas prior to star formation. This would ideally require modeling the chemical evolution of the species of interest, as in e.g., Glover & Mac Low (2007a,b) and Glover et al. (2009). In addition, however, we need to follow individual fluid parcels to capture their trajectories and chemical evolution along this trajectory. Using tracer particles seems a promising way to follow individual fluid parcels in the Lagrangian frame, while evolving the hydrodynamics in the Eulerian frame of reference simultaneously. The tracer particles provide information on the density and velocity fluctuations (L. Konstandin et al., in preparation), as well as the time evolution of shielding from the background radiation in the Lagrangian frame of reference. In a set of simulations with the ENZO code we have this information already. However, the problem with this dataset is that we neither had the chemical network nor the sink particles available at that time. One of the most important future developments will be to include the chemical network introduced by Glover et al. (2009) into simulations of self-gravitating collapse with sink particles *and* tracer particles. FLASH v2.5 will soon provide support for a chemical network to follow H_2 and CO formation (M. Milosavljevic et al., in preparation), and it supports sink particles (Federrath et al., 2010a). However, FLASH

v2.5 does not support multiple particle types yet. Implementing support for multiple particle types will thus enable us to perform simulations including sink particles and tracer particle simultaneously, which will be a key-development for future projects.

6.2.4 Control of star formation by magnetic fields vs turbulence

Ambipolar diffusion

Crutcher et al. (2009) have recently argued that observations of molecular cores are more consistent with the turbulence-regulated star formation picture. Their argument is based on the prediction of the magnetic field-regulated star formation theory: The mass-to-magnetic-flux ratio should be larger in the center of the molecular cloud core than in its envelope. This is because the magnetic field-regulated star formation theory predicts that the gas should slowly diffuse through the initially stabilizing magnetic field from the envelope to the cloud core, a process called 'ambipolar diffusion'. Their measurements of four nearby molecular cloud cores, however, revealed the opposite. Using the numerical setup of the formation of a star cluster described in section 5.4 in combination with a new ambipolar diffusion module (Duffin & Pudritz, 2008) will allow us to directly compare the magnetic field- and turbulence-regulated star formation scenarios. A systematic comparison of purely hydrodynamic (without magnetic fields), ideal magnetohydrodynamic (the case where the gas is perfectly coupled to the magnetic field), and full ambipolar diffusion turbulent star cluster formation calculations are already under way (D. Duffin et al., in preparation). First results indicate that the star formation rate is slightly lower in ideal MHD than in purely hydrodynamical collapse. In the ambipolar diffusion case, however, we expect the star formation rate to be in between the ideal MHD and the hydrodynamic case. With this systematic study we hope to quantify the relative importance of magnetic fields compared to turbulence in the most realistic, self-consistent model of star cluster formation available today.

Turbulent dynamos

Magnetic fields are ubiquitous in molecular clouds, but it remains controversial whether these fields have an influence on the cloud dynamics (e.g., Mac Low & Klessen, 2004). However, there is some observational evidence that the galactic field direction tends to be preserved during the process of molecular cloud formation (Li et al., 2006). These authors also argue that interstellar turbulence is close to Alfvénic or even slightly sub-Alfvénic, which points towards a significant influence of the magnetic field on the internal cloud motions. Although the role of magnetic fields on giant molecular cloud scales remains a controversial issue, it is widely accepted that magnetic fields play a significant role on the scales of protostellar cores, where they lead to the generation of spectacular jets and outflows, launched from the protostellar disks (as discussed in the next section).

It is likely that the magnetic pressure can become comparable to the thermal pressure in dense cores due to the amplification of the magnetic field through first, compression of magnetic field lines, and second, due to the winding, twisting and folding of the field lines by vorticity, a process called turbulent dynamo (see, Brandenburg & Subramanian, 2005, for a comprehensive review of turbulent dynamo action in astrophysical systems). Magnetic field amplification in the early universe is discussed analytically by e.g., Schleicher et al. (2010), showing that the magnetic pressure can reach levels of about 20% of the thermal pressure in primordial mini-halos, thus potentially influencing the fragmentation of the gas. In present-day star formation the influence of magnetic fields on the scales of dense cores were investigated in numerical work by e.g., Price & Bate (2007) and Hennebelle & Teyssier (2008), both concluding that magnetic fields strongly affect fragmentation of dense gas. Understanding the magnetic field growth due to the turbulent

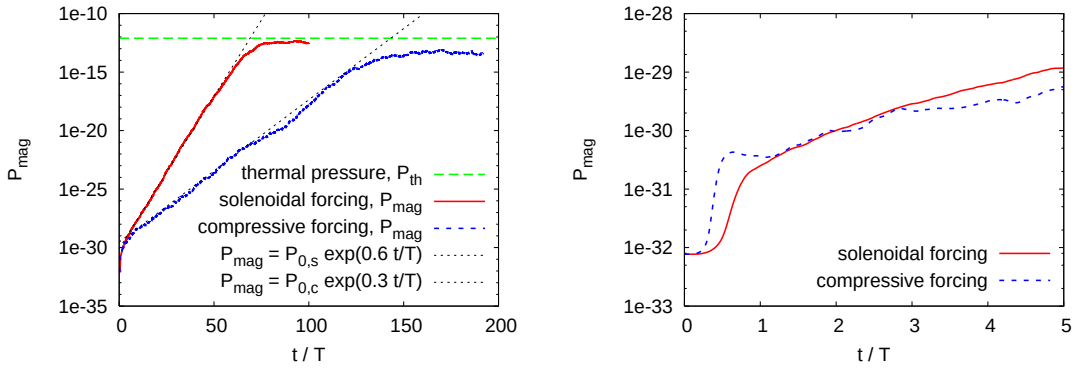

Figure 6.4: *Left:* Shows the magnetic pressure as a function of time (for 200 eddy turnover times, T) for solenoidal forcing (solid line) and compressive forcing (short-dashed line). The long-dashed horizontal line shows the thermal pressure. The turbulent dynamo works with an exponential growth rate of about $0.6/T$ for solenoidal forcing and $0.3/T$ for compressive forcing. For comparison, e.g., Schekochihin et al. (2004) find an amplification rate of about $0.5/T$ for subsonic, solenoidally driven turbulence. *Right:* Same as *left*, but only the first 5 eddy turnover times are shown. The magnetic pressure increases more steeply than a simple exponential within the first turnover time.

dynamo is thus crucial for future studies of star formation. Many studies have focused on subsonic turbulence (e.g., Schekochihin et al., 2004), with only very little contributions on the supersonic regime. For instance, Haugen et al. (2004) only studied the turbulent dynamo for mildly supersonic Mach numbers, $\mathcal{M} \lesssim 2.5$. For molecular clouds however, the highly supersonic regime is more relevant.

Figure 6.4 shows a preliminary study of the turbulent dynamo operating in the supersonic case (RMS Mach 5) for both solenoidal and compressive forcing, which is an example of a larger parameter study of the Mach number and turbulence forcing dependence of the dynamo action in the highly supersonic regime (S. Sur et al., in preparation). The figure shows that the turbulent dynamo leads to an exponential growth of the magnetic pressure over more than 15 orders of magnitude within about 100 large-scale eddy turnover times, T. The dynamo growth rate is about twice as large for solenoidal forcing ($\approx 0.6/T$) as for compressive forcing ($\approx 0.3/T$), which is likely due to the higher average vorticity generated by solenoidal forcing. The dynamo saturates after about 70 and 140 T for solenoidal and compressive forcing, respectively. The saturation level is close to the thermal pressure in both cases. For compressive forcing the saturated magnetic pressure is about 5% of the thermal pressure, while for solenoidal forcing it reaches 40% of the thermal pressure. This preliminary numerical result indicates that the turbulent dynamo can act as a very efficient way to amplify small initial magnetic fields to values that could potentially affect the gas dynamics and the fragmentation of dense gas in the context of star formation. However, given the long timescales (several tens of eddy turnover times) that are required to reach the saturated state of the dynamo, it remains unclear whether the dynamo action can indeed significantly alter the dynamics of a single population of molecular clouds. Molecular clouds are not likely to survive for more than a few large-scale turnover times, because they are dispersed by mechanical and radiative feedback within just a few turnover times (see, e.g., the discussion of molecular cloud timescales in Klessen et al., 2009). However, the presented-day, galactic magnetic field may have been build up by the dynamo action over long timescales, such that present-day star formation may be significantly affected by magnetic fields (see next section).

The right panel of Figure 6.4 shows a zoomed-in version of the left panel of the same figure,

focusing on the first 5 eddy turnover times. The most conspicuous part is the super-exponential rise within the first turnover time. Some combination of compression and folding of the initially weak field seems to lead to an extremely fast growth of the magnetic pressure. It is likely an out-of-equilibrium process that leads to this enormous field amplification, since turbulence is not yet fully established within the first turnover time. Although hard to quantify with statistical methods, this phenomenon deserves further study.

6.2.5 Outflow-regulated star formation

The means by which kinetic energy is supplied to sustain the observed turbulent motions in molecular clouds remains poorly understood. Although turbulence is likely driven on large scales and with a significant amount of compressible energy as shown in this thesis, there is an ongoing debate in the community about the importance of protostellar outflows and jets for driving turbulent motions in star-forming molecular clouds. Protostellar objects drive high-speed jets into the surrounding molecular cloud material, a process that may be capable of sustaining the observed supersonic turbulence. Moreover, this would have a significant influence on subsequent star formation occurring in the cloud. It was shown that single jets are insufficient to drive supersonic turbulence (Banerjee et al., 2007). However, Cunningham et al. (2009) argue that multiple jets in young stellar clusters can inject enough kinetic energy to sustain the level of observed turbulence in the clouds. Nakamura & Li (2008), as well as Wang et al. (2010), even go one step beyond that, and argue that star formation regulates itself by outflow feedback. However, a serious limitation of those two numerical studies is that they used an artificial model to inject jets and outflows with arbitrary power, and did not resolve the self-consistent formation of jets from magnetohydrodynamic effects. Magnetic fields are likely important on scales of the dense star-forming gas though, when they get twisted and amplified in a rotating gas disk around the central protostar, thereby launching powerful bipolar jets and outflows along the rotation axis. Although quite powerful, it is still controversial whether these jets can efficiently drive and sustain the observed level of supersonic turbulent motions in interstellar star-forming clouds.

In Figure 6.5, I show a preliminary snapshot from an isolated collapse of a rotating cloud core (D. Seifried et al., in preparation). This model includes a central sink particle to represent a protostar in the center of the rotating disk. The sink particle is used to model the collapse and mass growth during the gravitational collapse of the central dense object.

With the recent implementation of sink particles introduced in Chapter 5, we should be able to test the scenario of outflow-regulated star formation in a self-consistent magnetohydrodynamical simulation. The sink particle technique works in concert with the magnetohydrodynamic solver and allows the formation of protostellar jets to be launched self-consistently from individual sites of star formation. Although sink particles have been available for 15 years in smoothed particle hydrodynamics (SPH) codes (sink particles were invented by Bate et al., 1995, for SPH), it is only very recently that researchers have started to include the effects of magnetic fields in star cluster formation simulations using SPH (e.g., Price & Bate, 2008). However, there is one significant limitation of SPH studies that include magnetic fields: none of them was able to produce a self-consistent jet or outflow during the collapse of a magnetized rotating disk so far. This limitation is related to the SPH method used to model the magnetic field. Modelers have so far not been successful to represent wound-up magnetic field configurations in SPH simulations due to limitations of the magnetic field discretization in SPH (e.g., Price & Federrath, 2009; Brandenburg, 2010; Price, 2010). The twisted, wound-up magnetic fields are however essential for the self-consistent formation of a jet (e.g., Blandford & Payne, 1982; Pudritz & Norman, 1983; Shibata & Uchida, 1985, 1986; Contopoulos, 1995; Lynden-Bell, 2003; Duffin & Pudritz, 2009). With the sink particle module developed for FLASH, we hope to combine soon the advantages of sink particles with the magnetohydrodynamic capabilities of grid codes to model self-consistent feedback from jets and outflows, launched from individual protostellar disks in a

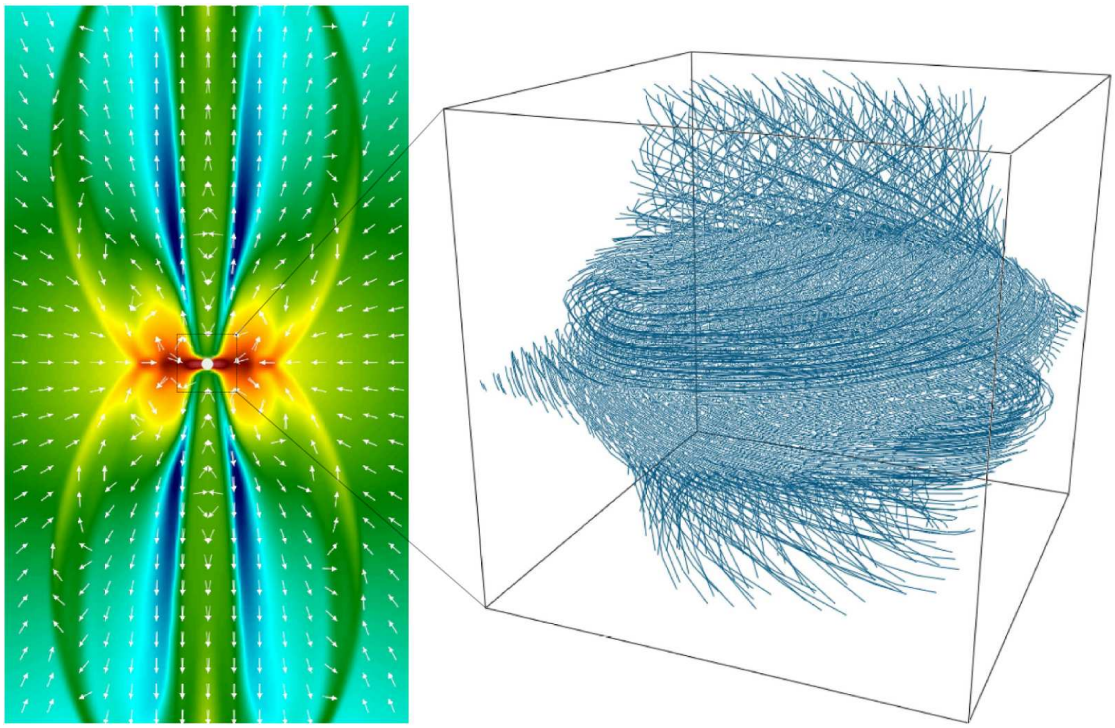

Figure 6.5: *Left:* Perpendicular slice through the gas density of a rotating, star-forming disk (high-density gas is shown in red, low-density gas in blue). At the evolutionary stage shown, two bipolar outflows (velocity vectors are overlaid on the density slice) have formed and propagated roughly 5,000 AU from the disk midplane. The disk has a diameter of about 1,250 AU, while the central sink particle has a radius of 80 AU (white circle in the center of the disk). *Right:* Shows the three-dimensional magnetic field structure in the inner 800 AU of the disk. The magnetic field lines are wound up strongly due to the disk rotation, which leads to the launch of the bipolar outflows shown in the left image. Simulation Credit: Daniel Seifried.

global calculation of a forming star cluster.

Acknowledgement

Mein größter Dank gilt Ralf Klessen für sein Engagement bei der Betreuung meiner Arbeit. Die vielen Diskussionen mit ihm haben mir geholfen die interstellare Turbulenz und die Physik der Sternentstehung besser zu verstehen. Ganz besonders wichtig waren vor allem seine zahlreichen Anregungen und Vorschläge für interessante Projekte, die diese Arbeit ganz wesentlich bereichert haben, seine Offenheit für neue Ideen, sowie die aktive Unterstützung bei der Zusammenarbeit mit Experten außerhalb des Instituts.

Die Zusammenarbeit mit anderen Mitgliedern des ITA war für diese Arbeit von besonderer Bedeutung. Dies gilt vor allem Robi Banerjee, der mir sowohl mit seinem physikalischen Verständnis, als auch mit seiner unschätzbaren Erfahrung in numerischen Simulationen stets geholfen hat. Gerade der offene und aktive Austausch von Ideen war die Grundlage für unsere gemeinsame Implementierung der 'Sink Teilchen' in FLASH. Ganz besonderer Dank gilt auch Paul Clark für sein Engagement bei der Durchführung der Vergleichsstudie zu den Sink Teilchen mit SPH und für die zahlreichen Diskussionen zu analytischen Sternentstehungsmodellen. Ebenso dankbar bin ich Simon Glover für die kontinuierliche Zusammenarbeit an der Chemie und am Strahlungstransport in Molekülwolken, eine Zusammenarbeit, die bis zu meiner Diplomarbeit zurückreicht.

Von ebenso großer Bedeutung für mich war die gemeinsame Arbeit mit Experten außerhalb des Instituts. Dies gilt vor allem Wolfram Schmidt (Göttingen), auf dessen ursprünglicher Idee die numerische Untersuchung des komprimierenden Treibens beruht. Besonders danken möchte ich Mordecai Mac Low (AMNH), der meine Arbeit an vielen Stellen kritisch hinterfragt hat und damit wesentlich zur Verbesserung beigetragen hat. Außerdem danke ich ihm für seine Unterstützung bei meinem dreimonatigen Forschungsaufenthalt am AMNH in New York und dafür, dass er sich bereit erklärt hat, das Zweitgutachten für diese Arbeit zu erstellen. Besonderer Dank gilt auch Rainer Spurzem (ARI) und Rosemary Mardling (Monash), durch die ich einen Monat an der Monash Universität in Melbourne verbringen durfte. Dieser Aufenthalt förderte die enge Zusammenarbeit mit Daniel Price (Monash), durch den ich sehr viel über SPH und Magnetfelder lernen konnte. Ebenso danken möchte ich Chris Brunt (Exeter) für sein Interesse an meiner Arbeit und für die kritischen Diskussionen zu Beobachtungsmethoden. Besonderer Dank gilt auch Henrik Beuther (MPIA), Julia Duval (STScI) und Nicola Schneider (CNRS), durch die ich mehr über die Beobachtung von Molekülwolken lernen konnte. Ganz besonders hilfreich für mein Verständnis der Sternentstehung waren auch die Diskussionen mit Ralph Pudritz und Dennis Duffin (McMaster) über Magnetfelder und protostellare Jets, sowie mit Gilles Chabrier und Patrick Hennebelle zu analytischen Sternentstehungsmodellen.

Für wertvolle Hinweise beim Schreiben dieser Arbeit danke ich Robi Banerjee, Ingo Berentzen, Ralf Klessen, Daniela Sacher und Dominik Schleicher. Außerdem danke ich Robi Banerjee, Matthias Bartelmann, Ingo Berentzen, Paul Clark, Gustavo Dopcke, Philipp Girichidis, Simon Glover, Thomas Greif, Ralf Klessen, Lukas Konstandin, Milica Milosavljevic, Faviola Molina, Thomas Peters, Dominik Schleicher, Stefan Schmeja, Daniel Seifried, Rahul Shetty, Rowan Smith, Sharanya Sur, Bernd Voelkl und Anna Zacheus für viele spannende Diskussionen und für die angenehme und lebhafte Arbeitsatmosphäre am ITA. Ganz besonderer Dank gilt auch Christian Fendt für die Koordinierung von IMPRS, sowie Matthias Bartelmann für seine Unterstützung in Form von Empfehlungsschreiben und für seine Beteiligung in meiner Prüfungskommission.

Am meisten möchte ich mich schließlich bei meinen Eltern und bei meinen beiden Brüdern bedanken, die mich immer unterstützen und die mir geholfen haben meine Interessen zu entfalten. Ebenso danke ich Daniela Sacher, die mich im Laufe meiner Doktorarbeit immer liebevoll unterstützt hat.

Bibliography

Agertz, O., Moore, B., Stadel, J., Potter, D., Miniati, F., Read, J., Mayer, L., Gawryszczak, A., Kravtsov, A., Nordlund, Å., Pearce, F., Quilis, V., Rudd, D., Springel, V., Stone, J., Tasker, E., Teyssier, R., Wadsley, J., & Walder, R. 2007, MNRAS, 380, 963

Aikawa, Y., Herbst, E., Roberts, H., & Caselli, P. 2005, ApJ, 620, 330

Alves, J., Lombardi, M., & Lada, C. J. 2007, A&A, 462, L17

André, P., Belloche, A., Motte, F., & Peretto, N. 2007, A&A, 472, 519

Anselmet, F., Gagne, Y., Hopfinger, E. J., & Antonia, R. A. 1984, Journal of Fluid Mechanics, 140, 63

Audit, E., & Hennebelle, P. 2009, A&A, accepted (arXiv:0911.0748)

Azzalini, A. 1985, Scand. J. Statist., 12, 171

Ballesteros-Paredes, J., Gazol, A., Kim, J., Klessen, R. S., Jappsen, A.-K., & Tejero, E. 2006, ApJ, 637, 384

Ballesteros-Paredes, J., Klessen, R. S., & Vázquez-Semadeni, E. 2003, ApJ, 592, 188

Banerjee, R., Klessen, R. S., & Fendt, C. 2007, ApJ, 668, 1028

Banerjee, R., Pudritz, R. E., & Holmes, L. 2004, MNRAS, 355, 248

Banerjee, R., Vázquez-Semadeni, E., Hennebelle, P., & Klessen, R. S. 2009, MNRAS, 398, 1082

Baron, E., Hauschildt, P. H., & Chen, B. 2009, A&A, 498, 987

Barranco, J. A., & Goodman, A. A. 1998, ApJ, 504, 207

Bate, M. R. 2009, MNRAS, 392, 1363

Bate, M. R., Bonnell, I. A., & Bromm, V. 2003, MNRAS, 339, 577

Bate, M. R., Bonnell, I. A., & Price, N. M. 1995, MNRAS, 277, 362

Bate, M. R., & Burkert, A. 1997, MNRAS, 288, 1060

Bazell, D., & Desert, F. X. 1988, ApJ, 333, 353

Beech, M. 1987, Ap&SS, 133, 193

—. 1992, Ap&SS, 192, 103

Beetz, C., Schwarz, C., Dreher, J., & Grauer, R. 2008, Physics Letters A, 372, 3037

Bensch, F., Stutzki, J., & Ossenkopf, V. 2001, A&A, 366, 636

Benson, P. J., & Myers, P. C. 1989, ApJS, 71, 89

Benz, W. 1988, Computer Physics Communications, 48, 97

Benz, W. 1990, in Numerical Modelling of Nonlinear Stellar Pulsations Problems and Prospects, ed. J. R. Buchler, 269

Benz, W., Cameron, A. G. W., Press, W. H., & Bowers, R. L. 1990, ApJ, 348, 647

Benzi, R., Ciliberto, S., Tripiccione, R., Baudet, C., Massaioli, F., & Succi, S. 1993, Phys. Rev. E, 48, 29

Berger, M. J., & Colella, P. 1989, Journal of Computational Physics, 82, 64

Beuther, H., & Henning, T. 2009, A&A, 503, 859

Blandford, R. D., & Payne, D. G. 1982, MNRAS, 199, 883

Bodenheimer, P., & Boss, A. P. 1981, MNRAS, 197, 477

Boldyrev, S. 2002, ApJ, 569, 841

Boldyrev, S., Nordlund, Å., & Padoan, P. 2002, ApJ, 573, 678

Bonnell, I. A., & Bate, M. R. 2006, MNRAS, 370, 488

Bonnell, I. A., Bate, M. R., & Vine, S. G. 2003, MNRAS, 343, 413

Bonnor, W. B. 1956, MNRAS, 116, 351

Boss, A. P., & Bodenheimer, P. 1979, ApJ, 234, 289

Bouchut, F., Klingenberg, C., & Waagan, K. 2007, Numerische Mathematik, 108, 7

—. 2009, Numerische Mathematik, accepted

Brandenburg, A. 2010, MNRAS, 401, 347

Brandenburg, A., & Subramanian, K. 2005, Phys. Rep., 417, 1

Breitschwerdt, D., de Avillez, M. A., Fuchs, B., & Dettbarn, C. 2009, Space Science Reviews, 143, 263

Brunt, C. M., Federrath, C., & Price, D. J. 2010a, in press (arXiv:1003.4151)

—. 2010b, MNRAS, 403, 1507

Brunt, C. M., & Heyer, M. H. 2002a, ApJ, 566, 276

—. 2002b, ApJ, 566, 289

Brunt, C. M., Heyer, M. H., & Mac Low, M. 2009, A&A, 504, 883

Brunt, C. M., Heyer, M. H., Vázquez-Semadeni, E., & Pichardo, B. 2003, ApJ, 595, 824

Brunt, C. M., & Mac Low, M. 2004, ApJ, 604, 196

Burgers, J. M. 1948, Adv. Appl. Mech., 1, 171

Burkert, A., Bate, M. R., & Bodenheimer, P. 1997, MNRAS, 289, 497

Burkert, A., & Bodenheimer, P. 1993, MNRAS, 264, 798

Burkhart, B., Falceta-Gonçalves, D., Kowal, G., & Lazarian, A. 2009, ApJ, 693, 250

Calder, A. C., Fryxell, B., Plewa, T., Rosner, R., Dursi, L. J., Weirs, V. G., Dupont, T., Robey, H. F., Kane, J. O., Remington, B. A., Drake, R. P., Dimonte, G., Zingale, M., Timmes, F. X., Olson, K., Ricker, P., MacNeice, P., & Tufo, H. M. 2002, ApJS, 143, 201

Chabrier, G. 2003, PASP, 115, 763

Chandrasekhar, S. 1949, ApJ, 110, 329

—. 1951a, Royal Society of London Proceedings Series A, 210, 18

—. 1951b, Royal Society of London Proceedings Series A, 210, 26

Chappell, D., & Scalo, J. 2001, ApJ, 551, 712

Cho, J., Lazarian, A., & Vishniac, E. T. 2002, ApJ, 564, 291

Clark, P. C., Bonnell, I. A., & Klessen, R. S. 2008, MNRAS, 386, 3

Clark, P. C., Glover, S. C. O., Bonnell, I. A., & Klessen, R. S. 2009, ApJ, submitted (arXiv:0904.3302)

Colella, P., & Woodward, P. R. 1984, Journal of Computational Physics, 54, 174

Commerçon, B., Hennebelle, P., Audit, E., Chabrier, G., & Teyssier, R. 2008, A&A, 482, 371

Contopoulos, J. 1995, ApJ, 450, 616

Courant, R., Friedrichs, K., & Lewy, H. 1928, Mathematische Annalen, 100, 32

Crutcher, R. M., Hakobian, N., & Troland, T. H. 2009, ApJ, 692, 844

Cunningham, A. J., Frank, A., Carroll, J., Blackman, E. G., & Quillen, A. C. 2009, ApJ, 692, 816

Dib, S., Brandenburg, A., Kim, J., Gopinathan, M., & André, P. 2008, ApJ, 678, L105

Dib, S., Kim, J., Vázquez-Semadeni, E., Burkert, A., & Shadmehri, M. 2007, ApJ, 661, 262

Dickman, R. L., Horvath, M. A., & Margulis, M. 1990, ApJ, 365, 586

Dimonte, G., Youngs, D. L., Dimits, A., Weber, S., Marinak, M., Wunsch, S., Garasi, C., Robinson,

A., Andrews, M. J., Ramaprabhu, P., Calder, A. C., Fryxell, B., Biello, J., Dursi, L., MacNeice, P., Olson, K., Ricker, P., Rosner, R., Timmes, F., Tufo, H., Young, Y.-N., & Zingale, M. 2004, Physics of Fluids, 16, 1668

Dobler, W., Haugen, N. E. L., Yousef, T. A., & Brandenburg, A. 2003, Phys. Rev. E, 68, 026304

Dubey, A., Fisher, R., Graziani, C., Jordan, IV, G. C., Lamb, D. Q., Reid, L. B., Rich, P., Sheeler, D., Townsley, D., & Weide, K. 2008, in Astronomical Society of the Pacific Conference Series, Vol. 385, Numerical Modeling of Space Plasma Flows, ed. N. V. Pogorelov, E. Audit, & G. P. Zank, 145

Dubinski, J., Narayan, R., & Phillips, T. G. 1995, ApJ, 448, 226

Duffin, D. F., & Pudritz, R. E. 2008, MNRAS, 391, 1659

—. 2009, ApJ, 706, L46

Ebert, R. 1955, Zeitschrift für Astrophysik, 37, 217

Elmegreen, B. G. 2002, ApJ, 577, 206

—. 2008, ApJ, 672, 1006

Elmegreen, B. G. 2009, in IAU Symposium, Vol. 254, IAU Symposium, ed. J. Andersen, J. Bland-Hawthorn, & B. Nordström, 289–300

Elmegreen, B. G., & Falgarone, E. 1996, ApJ, 471, 816

Elmegreen, B. G., Klessen, R. S., & Wilson, C. D. 2008, ApJ, 681, 365

Elmegreen, B. G., & Lada, C. J. 1977, ApJ, 214, 725

Elmegreen, B. G., & Scalo, J. 2004, ARA&A, 42, 211

Esquivel, A., & Lazarian, A. 2005, ApJ, 631, 320

Esquivel, A., Lazarian, A., Horibe, S., Cho, J., Ossenkopf, V., & Stutzki, J. 2007, MNRAS, 381, 1733

Eswaran, V., & Pope, S. B. 1988, Computers and Fluids, 16, 257

Falgarone, E., Lis, D. C., Phillips, T. G., Pouquet, A., Porter, D. H., & Woodward, P. R. 1994, ApJ, 436, 728

Falgarone, E., & Phillips, T. G. 1990, ApJ, 359, 344

Falgarone, E., Phillips, T. G., & Walker, C. K. 1991, ApJ, 378, 186

Falgarone, E., Puget, J.-L., & Perault, M. 1992, A&A, 257, 715

Federrath, C., Banerjee, R., Clark, P. C., & Klessen, R. S. 2010a, ApJ, 713, 269

Federrath, C., Glover, S. C. O., Klessen, R. S., & Schmidt, W. 2008a, Phys. Scr. T, 132, 014025

Federrath, C., Klessen, R. S., & Schmidt, W. 2008b, ApJ, 688, L79

—. 2009, ApJ, 692, 364

Federrath, C., Roman-Duval, J., Klessen, R. S., Schmidt, W., & Mac Low, M. 2010b, A&A, 512, A81, (arXiv:0905.1060)

Ferrière, K. M. 2001, Reviews of Modern Physics, 73, 1031

Fleck, Jr., R. C. 1996, ApJ, 458, 739

Foster, J. B., Rosolowsky, E. W., Kauffmann, J., Pineda, J. E., Borkin, M. A., Caselli, P., Myers, P. C., & Goodman, A. A. 2009, ApJ, 696, 298

Foster, P. N., & Chevalier, R. A. 1993, ApJ, 416, 303

Friesen, R. K., Di Francesco, J., Shirley, Y. L., & Myers, P. C. 2009, ApJ, 697, 1457

Frisch, U. 1995, Turbulence (Cambridge Univ. Press)

Fryxell, B., Olson, K., Ricker, P., Timmes, F. X., Zingale, M., Lamb, D. Q., MacNeice, P., Rosner, R., Truran, J. W., & Tufo, H. 2000, ApJS, 131, 273

Gingold, R. A., & Monaghan, J. J. 1977, MNRAS, 181, 375

—. 1983, MNRAS, 204, 715

Glover, S. C. O., Federrath, C., Mac Low, M.-M., & Klessen, R. S. 2009, MNRAS, in press (arXiv:0907.4081)

Glover, S. C. O., & Mac Low, M. 2010, MNRAS, submitted (arXiv:1003.1340)

Glover, S. C. O., & Mac Low, M.-M. 2007a, ApJS, 169, 239

—. 2007b, ApJ, 659, 1317

Godunov, S. K. 1959, Math. Sbornik, 47, 271

Goodman, A. A., Barranco, J. A., Wilner, D. J., & Heyer, M. H. 1998, ApJ, 504, 223

Goodman, A. A., Pineda, J. E., & Schnee, S. L. 2009, ApJ, 692, 91

Goodwin, S. P., & Kouwenhoven, M. B. N. 2009, MNRAS, 397, L36

Gritschneder, M., Naab, T., Walch, S., Burkert, A., & Heitsch, F. 2009, ApJ, 694, L26

Haugen, N. E., & Brandenburg, A. 2004, Phys. Rev. E, 70, 026405

Haugen, N. E. L., Brandenburg, A., & Mee, A. J. 2004, MNRAS, 353, 947

Hauschildt, P. H., & Baron, E. 2009, A&A, 498, 981

Heitmann, K., Ricker, P. M., Warren, M. S., & Habib, S. 2005, ApJS, 160, 28

Heitsch, F., Mac Low, M.-M., & Klessen, R. S. 2001, ApJ, 547, 280

Heitsch, F., Slyz, A. D., Devriendt, J. E. G., Hartmann, L. W., & Burkert, A. 2006, ApJ, 648, 1052

Hennebelle, P., & Audit, E. 2007, A&A, 465, 431

Hennebelle, P., Banerjee, R., Vázquez-Semadeni, E., Klessen, R. S., & Audit, E. 2008, A&A, 486, L43

Hennebelle, P., & Chabrier, G. 2008, ApJ, 684, 395

—. 2009, ApJ, 702, 1428

Hennebelle, P., & Teyssier, R. 2008, A&A, 477, 25

Henriksen, R. N. 1991, ApJ, 377, 500

Hernquist, L., & Katz, N. 1989, ApJS, 70, 419

Hetem, Jr., A., & Lepine, J. R. D. 1993, A&A, 270, 451

Heyer, M., Gong, H., Ostriker, E., & Brunt, C. 2008, ApJ, 680, 420

Heyer, M., Krawczyk, C., Duval, J., & Jackson, J. M. 2009, ApJ, 699, 1092

Heyer, M. H., & Brunt, C. M. 2004, ApJ, 615, L45

Heyer, M. H., & Schloerb, F. P. 1997, ApJ, 475, 173

Heyer, M. H., Williams, J. P., & Brunt, C. M. 2006, ApJ, 643, 956

Hily-Blant, P., Falgarone, E., & Pety, J. 2008, A&A, 481, 367

Hollenbach, D. J., Werner, M. W., & Salpeter, E. E. 1971, ApJ, 163, 165

Hubber, D. A., Goodwin, S. P., & Whitworth, A. P. 2006, A&A, 450, 881

Hunter, C. 1977, ApJ, 218, 834

Jappsen, A.-K., Klessen, R. S., Larson, R. B., Li, Y., & Mac Low, M.-M. 2005, A&A, 435, 611

Kainulainen, J., Beuther, H., Henning, T., & Plume, R. 2009, A&A, 508, L35

Keto, E., Rybicki, G. B., Bergin, E. A., & Plume, R. 2004, ApJ, 613, 355

Kim, S., Staveley-Smith, L., Dopita, M. A., Sault, R. J., Freeman, K. C., Lee, Y., & Chu, Y.-H. 2003, ApJS, 148, 473

Kirk, H., Johnstone, D., & Tafalla, M. 2007, ApJ, 668, 1042

Kissmann, R., Kleimann, J., Fichtner, H., & Grauer, R. 2008, MNRAS, 391, 1577

Kitsionas, S., Federrath, C., Klessen, R. S., Schmidt, W., Price, D. J., Dursi, L. J., Gritschneder, M., Walch, S., Piontek, R., Kim, J., Jappsen, A., Ciecielag, P., & Mac Low, M. 2009, A&A, 508, 541

Klein, R. I., Inutsuka, S.-I., Padoan, P., & Tomisaka, K. 2007, in Protostars and Planets V, ed. B. Reipurth, D. Jewitt, & K. Keil, 99–116

Klessen, R. S. 2000, ApJ, 535, 869

—. 2001, ApJ, 556, 837

Klessen, R. S., Ballesteros-Paredes, J., Vázquez-Semadeni, E., & Durán-Rojas, C. 2005, ApJ, 620, 786

Klessen, R. S., Burkert, A., & Bate, M. R. 1998, ApJ, 501, L205

Klessen, R. S., Heitsch, F., & Mac Low, M.-M. 2000, ApJ, 535, 887

Klessen, R. S., Krumholz, M. R., & Heitsch, F. 2009, Advanced Science Letters, submitted (arXiv:0906.4452)

Klessen, R. S., & Lin, D. N. 2003, Phys. Rev. E, 67, 046311

Klingenberg, C., Schmidt, W., & Waagan, K. 2007, Journal of Computational Physics, 227, 12

Kolmogorov, A. N. 1941, Dokl. Akad. Nauk SSSR, 32, 16

Kowal, G., & Lazarian, A. 2007, ApJ, 666, L69

Kowal, G., Lazarian, A., & Beresnyak, A. 2007, ApJ, 658, 423

Kravtsov, A. V. 2003, ApJ, 590, L1

Kritsuk, A. G., Norman, M. L., & Padoan, P. 2006, ApJ, 638, L25

Kritsuk, A. G., Norman, M. L., Padoan, P., & Wagner, R. 2007, ApJ, 665, 416

Kroupa, P. 2001, MNRAS, 322, 231

Krumholz, M. R., & Bonnell, I. A. 2007, to be published in "Structure Formation in the Universe", ed. G. Chabrier, (arXiv:0712.0828)

Krumholz, M. R., Klein, R. I., & McKee, C. F. 2007, ApJ, 656, 959

Krumholz, M. R., & McKee, C. F. 2005, ApJ, 630, 250

Krumholz, M. R., McKee, C. F., & Klein, R. I. 2004, ApJ, 611, 399

Krumholz, M. R., McKee, C. F., & Tumlinson, J. 2009, ApJ, 699, 850

Lada, C. J., & Lada, E. A. 2003, ARA&A, 41, 57

Lada, C. J., Muench, A. A., Rathborne, J., Alves, J. F., & Lombardi, M. 2008, ApJ, 672, 410

Larson, R. B. 1969, MNRAS, 145, 271

—. 1981, MNRAS, 194, 809

—. 2005, MNRAS, 359, 211

Lazarian, A., & Esquivel, A. 2003, ApJ, 592, L37

Lee, Y. 2004, Journal of Korean Astronomical Society, 37, 137

Lekien, F., & Marsden, J. E. 2005, International Journal for Numerical Methods in Engineering, 63, 455

Lemaster, M. N., & Stone, J. M. 2008, ApJ, 682, L97

—. 2009, ApJ, 691, 1092

Li, H., Griffin, G. S., Krejny, M., Novak, G., Loewenstein, R. F., Newcomb, M. G., Calisse, P. G., & Chuss, D. T. 2006, ApJ, 648, 340

Li, P. S., McKee, C. F., Klein, R. I., & Fisher, R. T. 2008, ApJ, 684, 380

Li, P. S., Norman, M. L., Mac Low, M.-M., & Heitsch, F. 2004, ApJ, 605, 800

Li, Y., Klessen, R. S., & Mac Low, M.-M. 2003, ApJ, 592, 975

Lighthill, M. J. 1955, in IAU Symposium, Vol. 2, Gas Dynamics of Cosmic Clouds, 121

Lis, D. C., Keene, J., Li, Y., Phillips, T. G., & Pety, J. 1998, ApJ, 504, 889

Lis, D. C., Pety, J., Phillips, T. G., & Falgarone, E. 1996, ApJ, 463, 623

Lombardi, M., Alves, J., & Lada, C. J. 2006, A&A, 454, 781

Lucy, L. B. 1977, AJ, 82, 1013

Lunttila, T., Padoan, P., Juvela, M., & Nordlund, Å. 2008, ApJ, 686, L91

Lynden-Bell, D. 2003, MNRAS, 341, 1360

Mac Low, M.-M. 1999, ApJ, 524, 169

Mac Low, M.-M., Balsara, D. S., Kim, J., & de Avillez, M. A. 2005, ApJ, 626, 864

Mac Low, M.-M., & Klessen, R. S. 2004, Reviews of Modern Physics, 76, 125

Mac Low, M.-M., Klessen, R. S., Burkert, A., & Smith, M. D. 1998, Physical Review Letters, 80, 2754

Mac Low, M.-M., & Ossenkopf, V. 2000, A&A, 353, 339

Mandelbrot, B. B. 1983, The fractal geometry of nature (New York: Freeman)

Mandelbrot, B. B., & Frame, M. 2002, Fractals (San Diego, Calif.: Encyclopedia of Physical Science and Technology, Academic Press)

Matzner, C. D., & McKee, C. F. 2000, ApJ, 545, 364

McKee, C. F., & Ostriker, E. C. 2007, ARA&A, 45, 565

Miesch, M. S., & Bally, J. 1994, ApJ, 429, 645

Miesch, M. S., Scalo, J., & Bally, J. 1999, ApJ, 524, 895

Moisy, F., & Jiménez, J. 2004, Journal of Fluid Mechanics, 513, 111

Monaghan, J. J., & Gingold, R. A. 1983, Journal of Computational Physics, 52, 374

Monaghan, J. J., & Lattanzio, J. C. 1985, A&A, 149, 135

Muench, A. A., Lada, E. A., Lada, C. J., & Alves, J. 2002, ApJ, 573, 366

Murtagh, F., & Heck, A., eds. 1987, Astrophysics and Space Science Library, Vol. 131, Multivariate Data Analysis

Myers, P. C. 1983, ApJ, 270, 105

Nakamura, F., & Li, Z. 2008, ApJ, 687, 354

Navarro, J. F., & White, S. D. M. 1993, MNRAS, 265, 271

Nordlund, Å., & Padoan, P. 1999, in Interstellar Turbulence, ed. J. Franco & A. Carraminana, 218

Offner, S. S. R., Klein, R. I., & McKee, C. F. 2008, ApJ, 686, 1174

Ogino, S., Tomisaka, K., & Nakamura, F. 1999, PASJ, 51, 637

Ossenkopf, V., Esquivel, A., Lazarian, A., & Stutzki, J. 2006, A&A, 452, 223

Ossenkopf, V., Klessen, R. S., & Heitsch, F. 2001, A&A, 379, 1005

Ossenkopf, V., Krips, M., & Stutzki, J. 2008a, A&A, 485, 917

—. 2008b, A&A, 485, 719

Ossenkopf, V., & Mac Low, M.-M. 2002, A&A, 390, 307

Ostriker, E. C., Gammie, C. F., & Stone, J. M. 1999, ApJ, 513, 259

Ostriker, E. C., Stone, J. M., & Gammie, C. F. 2001, ApJ, 546, 980

Padoan, P., Boldyrev, S., Langer, W., & Nordlund, Å. 2003, ApJ, 583, 308

Padoan, P., Jimenez, R., Juvela, M., & Nordlund, Å. 2004a, ApJ, 604, L49

Padoan, P., Jimenez, R., Nordlund, Å., & Boldyrev, S. 2004b, Physical Review Letters, 92, 191102

Padoan, P., Juvela, M., Kritsuk, A., & Norman, M. L. 2006, ApJ, 653, L125

Padoan, P., & Nordlund, Å. 2002, ApJ, 576, 870

Padoan, P., & Nordlund, A. 2009, ApJ, submitted (arXiv:0907.0248)

Padoan, P., Nordlund, Å., & Jones, B. J. T. 1997, MNRAS, 288, 145

Padoan, P., Nordlund, Å., Kritsuk, A. G., Norman, M. L., & Li, P. S. 2007, ApJ, 661, 972

Passot, T., Pouquet, A., & Woodward, P. 1988, A&A, 197, 228

Passot, T., & Vázquez-Semadeni, E. 1998, Phys. Rev. E, 58, 4501

Pavlovski, G., Smith, M. D., & Mac Low, M.-M. 2006, MNRAS, 368, 943

Peitgen, H.-O., Jürgens, H., & Saupe, D. 2004, Chaos and fractals - new frontiers of science (New York; Berlin; Heidelberg: Springer)

Penston, M. V. 1969, MNRAS, 144, 425

Perault, M., Falgarone, E., & Puget, J. L. 1986, A&A, 157, 139

Peters, T., Banerjee, R., Klessen, R. S., Mac Low, M., Galván-Madrid, R., & Keto, E. R. 2010, ApJ, 711, 1017

Pineda, J. E., Caselli, P., & Goodman, A. A. 2008, ApJ, 679, 481

Pinte, C., Harries, T. J., Min, M., Watson, A. M., Dullemond, C. P., Woitke, P., Ménard, F., & Durán-Rojas, M. C. 2009, A&A, 498, 967

Porter, D. H., Pouquet, A., & Woodward, P. R. 1992a, Theoretical and Computational Fluid Dynamics, 4, 13

—. 1992b, Physical Review Letters, 68, 3156

—. 1994, Physics of Fluids, 6, 2133

Press, W. H. 1987, in The Use of Supercomputers in Stellar Dynamics, ed. P. Hut & S. L. W. McMillan, 267

Press, W. H., Flannery, B. P., Teukolsky, S. A., & Vetterling, W. T. 1986, Numerical recipes (Cambridge University Press), 818 S.

Price, D. J. 2010, MNRAS, 401, 1475

Price, D. J., & Bate, M. R. 2007, MNRAS, 377, 77

—. 2008, MNRAS, 385, 1820

Price, D. J., & Federrath, C. 2009, proceedings of "ASTRONUM-2009", Chamonix, eds. Pogorelov & Audit, (arXiv:0910.0285)

—. 2010, MNRAS, accepted (arXiv:1004.1446)

Price, D. J., & Monaghan, J. J. 2007, MNRAS, 374, 1347

Pudritz, R. E., & Norman, C. A. 1983, ApJ, 274, 677

Reipurth, B., & Schneider, N. 2008, Star Formation and Young Clusters in Cygnus, ed. Reipurth, B., 36–+

Ricker, P. M. 2008, ApJS, 176, 293

Ridge, N. A., Schnee, S. L., Goodman, A. A., & Foster, J. B. 2006, ApJ, 643, 932

Salpeter, E. E. 1955, ApJ, 121, 161

Sánchez, N., & Alfaro, E. J. 2009, ApJ, 696, 2086

Sánchez, N., Alfaro, E. J., & Pérez, E. 2005, ApJ, 625, 849

—. 2007, ApJ, 656, 222

Scalo, J. 1990, in Astrophysics and Space Science Library, Vol. 162, Physical Processes in Fragmentation and Star Formation, ed. R. Capuzzo-Dolcetta, C. Chiosi, & A. di Fazio, 151–176

Scalo, J., & Elmegreen, B. G. 2004, ARA&A, 42, 275

Scalo, J., Vázquez-Semadeni, E., Chappell, D., & Passot, T. 1998, ApJ, 504, 835

Schekochihin, A. A., Cowley, S. C., Taylor, S. F., Maron, J. L., & McWilliams, J. C. 2004, ApJ, 612, 276

Schleicher, D. R. G., Banerjee, R., Sur, S., Arshakian, T. G., Klessen, R. S., Beck, R., & Spaans, M. 2010, MNRAS, submitted (arXiv:1003.1135)

Schmeja, S., & Klessen, R. S. 2004, A&A, 419, 405

Schmidt, W., Federrath, C., Hupp, M., Kern, S., & Niemeyer, J. C. 2009, A&A, 494, 127

Schmidt, W., Federrath, C., & Klessen, R. 2008, Phys. Rev. Lett., 101, 194505

Schmidt, W., Hillebrandt, W., & Niemeyer, J. C. 2006, Computers and Fluids, 35, 353

Schmidt, W., Kern, S. A. W., Federrath, C., & Klessen, R. S. 2010, A&A, submitted (arXiv:1002.2359)

Schnee, S., Caselli, P., Goodman, A., Arce, H. G., Ballesteros-Paredes, J., & Kuchibhotla, K. 2007, ApJ, 671, 1839

Schneider, N., Bontemps, S., Simon, R., Ossenkopf, V., Federrath, C., Klessen, R., Motte, F., & Brunt, C. 2010, A&A, submitted (arXiv:1001.2453)

She, Z.-S., & Leveque, E. 1994, Physical Review Letters, 72, 336

Shibata, K., & Uchida, Y. 1985, PASJ, 37, 31

—. 1986, PASJ, 38, 631

Shu, F. H. 1977, ApJ, 214, 488

Smith, R. J., Clark, P. C., & Bonnell, I. A. 2009, MNRAS, 396, 830

Solomon, P. M., Rivolo, A. R., Barrett, J., & Yahil, A. 1987, ApJ, 319, 730

Stahler, S. W., & Palla, F. 2004, The formation of stars (Weinheim: Wiley-VCH)

Steinacker, J., Bacmann, A., & Henning, T. 2006, ApJ, 645, 920

Stone, J. M., Ostriker, E. C., & Gammie, C. F. 1998, ApJ, 508, L99

Stutzki, J., Bensch, F., Heithausen, A., Ossenkopf, V., & Zielinsky, M. 1998, A&A, 336, 697

Tamburro, D., Rix, H.-W., Leroy, A. K., Low, M.-M. M., Walter, F., Kennicutt, R. C., Brinks, E., & de Blok, W. J. G. 2009, AJ, 137, 4424

Tasker, E. J., Brunino, R., Mitchell, N. L., Michielsen, D., Hopton, S., Pearce, F. R., Bryan, G. L., & Theuns, T. 2008, MNRAS, 390, 1267

Tassis, K. 2007, MNRAS, 382, 1317

Truelove, J. K., Klein, R. I., McKee, C. F., Holliman, II, J. H., Howell, L. H., & Greenough, J. A. 1997, ApJ, 489, L179

Vázquez-Semadeni, E. 1994, ApJ, 423, 681

Vázquez-Semadeni, E., Ballesteros-Paredes, J., & Klessen, R. S. 2003, ApJ, 585, L131

Vázquez-Semadeni, E., Kim, J., & Ballesteros-Paredes, J. 2005a, ApJ, 630, L49

Vázquez-Semadeni, E., Kim, J., Shadmehri, M., & Ballesteros-Paredes, J. 2005b, ApJ, 618, 344

Vázquez-Semadeni, E., Ryu, D., Passot, T., González, R. F., & Gazol, A. 2006, ApJ, 643, 245

Vincent, A., & Meneguzzi, M. 1991, Journal of Fluid Mechanics, 225, 1

Vogelaar, M. G. R., & Wakker, B. P. 1994, A&A, 291, 557

Vogelaar, M. G. R., Wakker, B. P., & Schwarz, U. J. 1991, in IAU Symposium, Vol. 147, Fragmentation of Molecular Clouds and Star Formation, ed. E. Falgarone, F. Boulanger, & G. Duvert, 508

von Weizsäcker, C. F. 1951, ApJ, 114, 165

von Weizsäcker, C. F. V. 1943, Zeitschrift fur Astrophysik, 22, 319

Waagan, K. 2009, Journal of Computational Physics, 228, 8609

Wang, J., Feigelson, E. D., Townsley, L. K., Román-Zúñiga, C. G., Lada, E., & Garmire, G. 2009, ApJ, 696, 47

Wang, J., Townsley, L. K., Feigelson, E. D., Broos, P. S., Getman, K. V., Román-Zúñiga, C. G., & Lada, E. 2008, ApJ, 675, 464

Wang, P., Li, Z., Abel, T., & Nakamura, F. 2010, ApJ, 709, 27

Ward-Thompson, D., André, P., Crutcher, R., Johnstone, D., Onishi, T., & Wilson, C. 2007, in Protostars and Planets V, ed. B. Reipurth, D. Jewitt, & K. Keil, 33–46

Westpfahl, D. J., Coleman, P. H., Alexander, J., & Tongue, T. 1999, AJ, 117, 868

Whitworth, A., & Summers, D. 1985, MNRAS, 214, 1

Whitworth, A. P. 1998, MNRAS, 296, 442

Wilden, B. S., Jones, B. F., Lin, D. N. C., & Soderblom, D. R. 2002, AJ, 124, 2799

Wolfire, M. G., Hollenbach, D., McKee, C. F., Tielens, A. G. G. M., & Bakes, E. L. O. 1995, ApJ, 443, 152

Zinnecker, H., & Yorke, H. W. 2007, ARA&A, 45, 481

Zuckerman, B., & Evans, II, N. J. 1974, ApJ, 192, L149